Cumhuriyet University

ISSN : 2587-2680

e-ISSN : 2587-246X

Cumhuriyet Science Journal

Volume : 40 Number : 4 Year : 2019

ISSN: 2587-2680
e-ISSN:2587-246X
Period: Quarterly
Founded: 2002
Publisher: Cumhuriyet University

Cumhuriyet Science Journal (CSJ)

Derginin Eski Adı: Cumhuriyet Üniversitesi Fen-Edebiyat Fakültesi Fen Bilimleri Dergisi

Eski ISSN: 1300-1949

Akademik Dizin / Abstracted/Indexed in

Ulakbim TR-Dizin

Akademik Dizin

Arastirmax Bilimsel Yayın İndeksi

Bielefeld Academic Search Engine (BASE)

Directory of Open Access Journals (DOAJ)

Directory of Research Journal Indexing (DRJI)

Google Scholar

Index Copernicus

Research Gate

Thomson Reuters Zoological

WorldCat

CUMHURİYET SCIENCE JOURNAL

Publication Type. Peer Reviewed Journal

Cite Type: Cumhuriyet Sci. J.

Contact Information

Faculty of Science Cumhuriyet University 58140
Sivas- TURKEY
Phone: +90(346)2191010-1522
Fax: +90(346)2191186
e-mail: csj@cumhuriyet.edu.tr
http://dergipark.gov.tr/csj

CONTENTS *PAGES*

Cumhuriyet Science Journal
CSJ

e-ISSN: 2587-246X
ISSN: 2587-2680

Cumhuriyet Sci. J., Vol.40-4 (2019) 784-791

The Regularized Trace Formula Of A Second Order Differentıal Equation Given With Anti-Perıodic Boundary Conditions

Seda KIZILBUDAK ÇALIŞKAN [1] ***Leyla ÖZEN*** [1]

[1] *Yıldız Technical University, Faculty of Arts and Science, Department of Mathematics, (34210), Davutpaşa, İstanbul,TURKEY*

Received: 09.11.2018; Accepted: 24.10.2019 *http://dx.doi.org/10.17776/csj.480810*

Abstract. In this study, we examined the formula of the regularized trace of the self-adjoint operator which is formed by

$\ell(y) = -y'' + p(x)y$

differential expression and

$y(0) + y(\pi) = 0$

$y'(0) + y'(\pi) = 0$

anti-periodic boundary condition.

Keywords**:** Regularized trace, Eigenvalues, Eigen functions.

Ters Periyodik Sınır Koşulları İle Verilmiş İkinci Mertebeden Diferansiyel Denklemin Düzenli İz Formülü

Özet. Bu çalışmada,

$\ell(y) = -y'' + p(x)y$

diferansiyel ifadesi ve

$y(0) + y(\pi) = 0$

$y'(0) + y'(\pi) = 0$

ters periyodik sınır koşulları ile oluşturulmuş kendine eş operatörün düzenli iz formülü incelenmiştir.

Anahtar Kelimeler: Düzenli iz, Öz değer, Öz fonksiyon.

1. INTRODUCTION

$p(x)$ is a real valued, continuous function in$[0,\pi]$, L_0 and L get two self-adjoint operators generated by the following expressions

$$\ell_0(y) = -y''$$

and

$$\ell(y) = -y'' + p(x)y \tag{1}$$

* Corresponding author. *Email address:* *skizilb@yildiz.edu.tr*

with the same boundary conditions

$$y(0) + y(\pi) = 0$$

$$y'(0) + y'(\pi) = 0 \tag{2}$$

respectively, in the space $L_2[0,\pi]$. The spectrum of operator L_0 coincides with the set $\{(2n+1)^2\}_{n=0}^{\infty}$. Every point of the spectrum is an eigenvalue with multiplicity two.

Let

$$\mu_k = \begin{cases} k^2, \ if\ k\ is\ odd \\ (k-1)^2, \ if\ k\ is\ even \end{cases} \qquad (k = 1,2,\dots)$$

is the eigenvalues of operator L_0 and

$$\psi_1 = \sqrt{\frac{2}{\pi}}\sin x\,, \psi_2 = \sqrt{\frac{2}{\pi}}\cos x\,, \psi_3 = \sqrt{\frac{2}{\pi}}\sin 3x, \psi_4 = \sqrt{\frac{2}{\pi}}\cos 3x, \dots$$

are the orthonormal eigenfunctions corresponding to this eigenvalues.

Also we showed the eigenvalues of operator L by $\lambda_1 \le \lambda_2 \le \lambda_3 \le \cdots \le \lambda_k \le \cdots$ and corresponding orthonormal eigenfunctions by $\varphi_0, \varphi_1, \varphi_2, \dots, \varphi_k, \dots$

In this study, we obtained a formula for the sum of series by Dikii's method,

$$\sum_{n=1}^{\infty}(\lambda_n - \mu_n)$$

which is called the formula of regularized trace of operator L.

The regularized trace theory, which was first examined by Gelfand and Levitan and they derived the formula of regularized trace for the Sturm-Liouville operator [1], attracted the attention of many authors. Dikii [2] provided and developed Gelfand and Levitan's formulas by their own method. Later, Levitan [6] suggested one more method for computing the traces of the Sturm–Liouville operator. There are numerous investigations on the calculation of the regularized trace of differential operator equations [3-17].

2. CALCULATION

Let us show the following equation

$$\lim_{N\to\infty}\sum_{n=1}^{N}[(\varphi_n, L\varphi_n) - (\psi_n, L\psi_n)] = 0 \tag{3}$$

which will be used later. For this we consider the transfer matrix $(u_{ik})_{i,k=1}^{\infty}$ from the orthonormal basis $\{\varphi_k\}$ to orthonormal basis $\{\psi_k\}$ as in [2] :

$$\psi_k = \sum_{i=1}^{\infty} u_{ik}\varphi_i \qquad (k = 1,2,\dots)$$

where $u_{ik} = (\varphi_i, \psi_k)$ and $(u_{ik})_{i,k=1}^{\infty}$ are the unitary matrix, that is

$$\sum_{i=1}^{\infty} u_{ik}^2 = 1 \qquad (k = 1,2, \dots)$$

Let us give some limitations for u_{ik} . It is clear that

$$L\psi_k = \mu_k \psi_k + p\psi_k \tag{4}$$

If we multiply both side of equality (4) by φ_i we obtain

$$(L\psi_k, \varphi_i) = (\mu_k \psi_k, \varphi_i) + (p\psi_k, \varphi_i)$$

Or

$$\lambda_i(\psi_k, \varphi_i) = \mu_k(\psi_k, \varphi_i) + (p\psi_k, \varphi_i)$$

and

$$(\lambda_i - \mu_k)(\psi_k, \varphi_i) = (p\psi_k, \varphi_i)$$

.

With respect to [2] taking the square of both sides of the last equality and summing from 1 to ∞ respect to i we obtain

$$\sum_{i=1}^{\infty} (\lambda_i - \mu_k)^2 (\psi_k, \varphi_i)^2 = \sum_{i=1}^{\infty} (p\psi_k, \varphi_i) = \|p\psi_k\|^2 = \int_0^{\pi} [p(x)\psi_k(x)]^2 dx \le p_0^2 \tag{5}$$

where $p_0 = max_{0 \le x \le \pi} |p(x)|$.

Suppose that the following conditions hold:

1. For the eigenvalues and the eigenfunctions of the *L* operator holds the asymptotic formulas

$$\lambda_k = \mu_k + O\left(\frac{1}{k}\right) \ , \quad \varphi_k = \psi_k + O\left(\frac{1}{k}\right) \qquad [10].$$

2. $\int_0^{\pi} p(x)\, dx = 0$.

Hence

$$\sum_{i=N+1}^{\infty} (\lambda_i - \mu_k)^2 u_{ik}^2 < C \qquad (C = const.) \ (k < N) \ . \tag{6}$$

We will use condition 1 in the inequalities we will obtain.

Obviously,

$$\sum_{i=N+1}^{\infty} (\lambda_i - \mu_k) u_{ik}^2 < C \ \Rightarrow \ \sum_{i=N+1}^{\infty} (\lambda_i - \mu_k)(\lambda_i - \lambda_k) u_{ik}^2 < C$$

$$\Rightarrow \sum_{i=N+1}^{\infty} (\lambda_i - \lambda_k)^2 u_{ik}^2 < C$$

is obtained for all integer N from equation (6)

And we obtain

$$\sum_{i=N+1}^{\infty}(\lambda_i-\lambda_k)u_{ik}^2 \le \frac{C}{\lambda_{N+1}-\mu_k} \qquad (k<N). \tag{7}$$

Now let us prove the equation (3).

$$(\psi_k, L\psi_k)=\left(\sum_{i=1}^{\infty}u_{ik}\varphi_i\,,\sum_{i=1}^{\infty}\lambda_i u_{ik}\varphi_i\right)=\sum_{i=1}^{\infty}\lambda_i u_{ik}^2$$

If we take the sum on k from 1 to N on both sides of this equation we get

$$\sum_{k=1}^{N}(\psi_k, L\psi_k)=\sum_{k=1}^{N}\sum_{i=1}^{\infty}\lambda_i u_{ik}^2\,.$$

Since $\sum_{i=1}^{\infty}u_{ki}^2=1$ we get

$$\sum_{k=1}^{N}(\varphi_k, L\varphi_k)=\sum_{k=1}^{N}\lambda_k=\sum_{k=1}^{N}\sum_{i=1}^{\infty}\lambda_k u_{ki}^2$$

So now we need to prove

$$\lim_{N\to\infty}\left(\sum_{k=1}^{N}\sum_{i=1}^{\infty}\lambda_i u_{ik}^2-\sum_{k=1}^{N}\sum_{i=1}^{\infty}\lambda_k u_{ki}^2\right)=0. \tag{8}$$

$$\sum_{k=1}^{N}\sum_{i=1}^{\infty}\lambda_i u_{ik}^2-\sum_{k=1}^{N}\sum_{i=1}^{\infty}\lambda_k u_{ki}^2=\sum_{k=1}^{N}\sum_{i=N+1}^{\infty}(\lambda_i-\lambda_k)u_{ik}^2+\sum_{k=1}^{N}\sum_{i=N+1}^{\infty}\lambda_k\left(u_{ik}^2-u_{ki}^2\right). \tag{9}$$

Let us calculate first sum on the right side of equality (9). For convenience while let $N+1$ be even number then we have

$$\sum_{k=1}^{N}\sum_{i=N+1}^{\infty}(\lambda_i-\lambda_k)u_{ik}^2=\sum_{k=1}^{N-1}\sum_{i=N+1}^{\infty}(\lambda_i-\lambda_k)u_{ik}^2+(\lambda_{N+1}-\lambda_N)u_{(N+1)N}^2+\sum_{i=N+2}^{\infty}(\lambda_i-\lambda_N)u_{iN}^2 \tag{10}$$

Let us calculate first and third sum on the right side of equality (10) by inequality (7), for $N\to\infty$

$$\sum_{k=1}^{N}\sum_{i=N+1}^{\infty}(\lambda_i-\lambda_k)u_{ik}^2<\frac{1}{4N}+\frac{1}{2(N+1)}\left[\ln\frac{N^2+N}{N-1}\right]\to 0 \tag{11}$$

and

$$\sum_{i=N+2}^{\infty}(\lambda_i-\lambda_N)u_{iN}^2 \le \frac{C}{\lambda_{N+2}-\mu_N} \le \frac{C}{4N+4} \to 0 \tag{12}$$

Now we shall calculate the second term on the right side of equality (10) when $N \to \infty$. Suppose that $N+1$ is even , we have

$$(\lambda_{N+1}-\lambda_N)u_{(N+1)N}^2 \le N^2 + O\left(\frac{1}{N+1}\right) - N^2 - O\left(\frac{1}{N}\right) \to 0 \qquad (N \to \infty) \tag{13}$$

In this way, for even number $N+1$ from the expressions (10), (11), (12) and (13) we have

$$\lim_{N\to\infty}\sum_{k=1}^{N}\sum_{i=N+1}^{\infty}(\lambda_i-\lambda_k)u_{ik}^2 = 0. \tag{14}$$

Formula (14) can also calculated for odd number $N+1$.

Now we shall calculate second sum on the right side of equality (9).

$$u_{ik}+u_{ki} = (\varphi_i,\psi_k)+(\varphi_k,\psi_i) = -(\varphi_i-\psi_i,\varphi_k-\psi_k) \tag{15}$$

By equality (15) and condition 1., we have

$$|u_{ik}+u_{ki}| \le \|\varphi_i-\psi_i\|\,\|\varphi_k-\psi_k\| < \frac{C}{ik}\,. \tag{16}$$

According to Cauchy-Schwarz inequality we have

$$\sum_{i=N+1}^{\infty}(\lambda_i-\mu_k)\left|u_{ik}^2-u_{ki}^2\right| = \sum_{i=N+1}^{\infty}(\lambda_i-\mu_k)\left|u_{ik}-u_{ki}\right|\left|u_{ik}+u_{ki}\right|$$

$$\le \sqrt{\sum_{i=N+1}^{\infty}\left|u_{ik}-u_{ki}\right|^2}\sqrt{\sum_{i=N+1}^{\infty}(\lambda_i-\mu_k)^2\left|u_{ik}-u_{ki}\right|^2}$$

$$< \frac{C}{(k-1)\sqrt{N+1}}\,. \tag{17}$$

Hence

$$\sum_{i=N+1}^{\infty}\left|u_{ik}^2-u_{ki}^2\right| < \frac{C}{(k-1)\sqrt{N+1}[N^2-(k-1)^2]} \tag{18}$$

Now we shall evaluate the second sum on the right side of equality (9),

$$\sum_{k=1}^{N}\lambda_k\sum_{i=N+1}^{\infty}\left|u_{ik}^2-u_{ki}^2\right| = \lambda_N\sum_{i=N+1}^{\infty}\left|u_{iN}^2-u_{Ni}^2\right| + \sum_{k=1}^{N-1}\lambda_k\sum_{i=N+1}^{\infty}\left|u_{ik}^2-u_{ki}^2\right|$$

$$= \lambda_N \left|u_{N+1N}^2 - u_{NN+1}^2\right| + \lambda_N \sum_{i=N+2}^{\infty} \left|u_{iN}^2 - u_{Ni}^2\right| + \sum_{k=1}^{N-1} \lambda_k \sum_{i=N+1}^{\infty} \left|u_{ik}^2 - u_{ki}^2\right| \qquad (19)$$

By inequality (16) we have

$$\lambda_N \left|u_{N+1N}^2 - u_{NN+1}^2\right| = \lambda_N \left|u_{N+1N} - u_{NN+1}\right| \left|u_{N+1N} + u_{NN+1}\right|$$

$$< \frac{CN^2}{N^2(N+1)^2} \left|u_{N+1N} - u_{NN+1}\right| \to 0 \qquad (N \to \infty) \qquad (20)$$

By the expression (18) we evaluate the second and third sum on the right side of equality (19)

$$\lambda_N \sum_{i=N+2}^{\infty} \left|u_{iN}^2 - u_{Ni}^2\right| < \frac{CN^2}{(N-1)\sqrt{N+2}[(N+2)^2 - (N+1)^2]} \to \infty \ (N \to \infty) \qquad (21)$$

and

$$\sum_{k=1}^{N-1} \lambda_k \sum_{i=N+1}^{\infty} \left|u_{ik}^2 - u_{ki}^2\right| < \frac{CN}{\sqrt{N+1}} \sum_{k=2}^{N} \frac{1}{N^2 - (k-1)^2} \sim C \frac{\ln N}{\sqrt{N}} \to 0 \ (N \to \infty). \qquad (22)$$

From the expressions (19), (20),(21) and (22) we have

$$\lim_{N\to\infty} \sum_{k=1}^{N} \sum_{i=N+1}^{\infty} \lambda_k \left(u_{ik}^2 - u_{ki}^2\right) = 0 \qquad (23)$$

Thus from the expressions (9), (14), and (23) we obtain formula (8). Therefore formula (3) have proved.

3. CONCLUSION

$$(\varphi_k, L\varphi_k) = \lambda_k \qquad \text{and} \qquad (\psi_k, L\psi_k) = \mu_k + (\psi_k, p\psi_k).$$

If we use these into formula (3) then we obtain

$$\sum_{k=1}^{N} [(\psi_k, L\psi_k) - (\varphi_k, L\varphi_k)] = \sum_{k=1}^{N} (\mu_k - \lambda_k) + \sum_{k=1}^{N} (\psi_k, p\psi_k) \to 0\,, \qquad (N \to \infty). \qquad (24)$$

Now we shall calculate

$$\lim_{N\to\infty} \sum_{k=1}^{N} (\psi_k, p\psi_k).$$

According to condition 2. we have for even number N

$$\sum_{k=1}^{N}(\psi_k, p\psi_k) = \frac{1}{\pi}\int_0^{\pi} p(x)\ dx + \frac{N}{\pi}\int_0^{\pi} p(x)\ dx = 0 \qquad (25)$$

Similarly we have for odd number N

$$\sum_{k=1}^{N}(\psi_k, p\psi_k) = -\frac{1}{\pi}\int_0^{\pi} p(x)\cos 2Nx\ dx \to 0\,, \qquad (N \to \infty)\,. \qquad (26)$$

From the expressions (25) and (26) we have

$$\lim_{N\to\infty}\sum_{k=1}^{N}(\psi_k, p\psi_k) = 0$$

Hence from the expressions (24) and (26) we have

$$\lim_{N\to\infty}\sum_{k=1}^{N}(\lambda_k - \mu_k) = 0.$$

So we have proved the following theorem.

THEOREM : The following formula is true when we considered $p(x)$ is a continuous function and conditions 1.,2. are fulfilled

$$\sum_{n=1}^{\infty}(\lambda_n - \mu_n) = 0\ . \qquad (27)$$

REFERENCES

[1] Gelfand, I. M. and Levitan, B. M., On a formula for eigenvalues of a differential operator of second order. Dokl. Akad. Nauk SSSR, 88-4 (1953) 593-596.

[2] Dikii, L. A., On a Formula of Gelfand–Levitan. Usp. Mat. Nauk, 8-2 (1953) 119-123.

[3] Gelfand, I. M., About an identity for eigenvalues of a differential operator of second order. Usp. Mat. Nauk, 11(67) (1956) 191-198.

[4] Fadeev, L.D., On the Expression for the Trace of the Difference of Two Singular Differential Operators of the Sturm–Liouville Type. Dokl. Akad. Nauk SSSR, 115-5 (1957) 878–881.

[5] Dikii, L. A., Trace formulas for differential operators of Sturm- Liouville. Uspeki Matem. Nauk, 13-3 (1958) 111-143.

[6] Levitan, B.M., Calculation of the Regularized Trace for the Sturm–Liouville Operator. Uspekhi Mat. Nauk, 19-1 (1964) 161–165.

[7] Sadovnichii,V.A.,On the trace of the difference of two high-order ordinary differential operators. Differents, Uravneniya, 2-12 (1966) 1611-1624.

[8] Cao, C.W. and Zhuang, D.W., Some trace formulas for the Schr¨odinger equation with energy-dependent potential, Acta Math. Sci.(in Chinese), 5 (1985) 233-236.

[9] Bayramoğlu, M., On the regularized trace formula of th differential equation with unbounded Coefficient. Spectral Theory and Its Applications, 7 (1987) 15-40.

[10] Lax P. D., Trace formulas for the Schroeding operator. Commun. Pure Appl. Math., 47- 4 (1994) 503-512.

[11] Papanicolaou, V.G., Trace formulas and the behavior of large eigenvalues, SIAM J. Math. Anal., 26 (1995), 218-237.

[12] Adıgüzelov, E. E., Baykal, O. and Bayramov, A., On the spectrum and regularized trace of the Sturm-Liouville problem with spectral parameter on the boundary condition and with the operator coefficient. International Journal of Differential Equations and Applications, 2-3 (2001) 317-333.

[13] Savchuk, A.M., Shkalikov, A.A., Trace formula for Sturm-Liouville Operators with Singular Potentials. Mathematical Notes, 69-3 (2001).

[14] Bayramov, A., Öztürk Uslu, S. and Kızılbudak Çalışkan, S., On the trace formula of second order differential equation given with non-seperable boundary conditions. Sigma Journal of Engineering and Natural Sciences, 4 (2005) 57-64.

[15] Guliyev, N.J., The regularized trace formula for the Sturm-Liouville equation with spectral parameter in the boundary condition. Proceedins of IMM of NAS of Azerbaijan, 22 (2005) 99-102.

[16] Sadovnichii, V.A. and Podol'skii, V.E., Traces of Differential Operators. Differential Equations, 45- 4 (2009) 477-493

[17] Wang, Y.P., Koyunbakan H. and Yang, C.F., A Trace Formula for Integro-differential Operators on the Finite Interval, Acta Mathematicae Applicatae Sinica (English Series) 33-1 (2017) 141-146.

Cumhuriyet Science Journal
CSJ

e-ISSN: 2587-246X
ISSN: 2587-2680

Cumhuriyet Sci. J., Vol.40-4 (2019) 792-801

3-Zero-Divisor Hypergraph with Respect to an Element in Multiplicative Lattice

Gülşen ULUCAK [1]

[1] *Department of Mathematics, Gebze Technical University, P.K 41400, Gebze-Kocaeli, TURKEY*

Received: 19.11.2018; Accepted: 23.10.2019 *http://dx.doi.org/10.17776/csj.485085*

Abstract. Let L be a multiplicative lattice and z be a proper element of L. We introduce the 3-zero-divisor hypergraph of L with respect to z which is a hypergraph whose vertices are elements of the set $\left\{x_1 \in L-\{z\} \middle| \begin{matrix} x_1x_2x_3 \leq z \Rightarrow x_1x_2 \nleq z,\ x_2x_3 \nleq z \text{ and } x_1x_3 \nleq z \\ \text{for some } x_2, x_3 \in L-\{z\} \end{matrix} \right\}$ where distinct vertices x_1, x_2 and x_3 are adjacent, that is, $\{x_1, x_2, x_3\}$ is a hyperedge if and only if $x_1x_2x_3 \leq z \Rightarrow x_1x_2 \nleq z, x_2x_3 \nleq z \text{ and } x_1x_3 \nleq z$. Throughout this paper, the hypergraph is denoted by $H_3(L, z)$. We investigate many properties of the hypergraph over a multiplicative lattice. Moreover, we find a lower bound of diameter of $H_3(L, z)$ and obtain that $H_3(L, z)$ is connected.

Keywords**:** 3-Zero-Divisor Hypergraph, Complete n-partite Hypergraph.

Çarpımsal Kafeslerde Bir Eleman ile İlgili 3-lü Sıfır Bölen Hipergrafı

Özet. L bir çarpımsal kafes ve z, L nin bir has elemanı olsun. z ile ilgili L nin 3-lü sıfır bölen hipergrafını tanıttık öyle ki bu hipergrafın köşeleri $\left\{x_1 \in L-\{z\} \middle| \begin{matrix} x_1x_2x_3 \leq z \Rightarrow x_1x_2 \nleq z,\ x_2x_3 \nleq z \text{ ve } x_1x_3 \nleq z \\ \text{herhangi } x_2, x_3 \in L-\{z\} \text{ için} \end{matrix} \right\}$ kümesinin elemanlarıdır ki burada x_1, x_2 ve x_3 komşudur, yani, $\{x_1, x_2, x_3\}$ bu hipergarfin bir hiperkenarıdır ancak ve ancak $x_1x_2x_3 \leq z \Rightarrow x_1x_2 \nleq z, x_2x_3 \nleq z \text{ ve } x_1x_3 \nleq z$. Bu çalışma boyunca, bu hipergrafı $H_3(L, z)$ ile göstereceğiz. Çarpımsal bir kafes üzerinde bu hipergrafın birçok özelliğini araştırdık. Ayrıca, $H_3(L, z)$ nin diametresinin bir alt sınırını bulduk ve bu hipergrafın bağlantılı olduğunu gösterdik.

Anahtar Kelimeler**:** 3-lü Sıfır Bölen Hipergraf, n-parçalı Tam Hipergraf.

1. INTRODUCTION

A complete lattice L is called multiplicative lattice if there exists a commutative, associative, completely join distributive product on the lattice with the compact greatest element 1_L, which is the multiplicative identity, and the least element 0_L. It can be easily seen that $L/a = \{b \in L | a \leq b\}$ is a multiplicative lattice with the product $x \circ y = xy \vee a$ where L is multiplicative lattice and $a \in L$. Note that $0_{L/z} = z$. D.D. Anderson and the current authors have studied on multiplicative lattices in a series of articles [1-4]. An element $a \in L$ is said to be proper if $a < 1_L$. A proper element $p \in L$ is called a prime element if $ab \leq p$ implies $a \leq p$ or $b \leq p$, where $a, b \in L$. Then p is called 2-absorbing element of L if $x_1x_2x_3 \leq p$ for some x_1, x_2 and x_3 in L, then $x_1x_2 \leq p$ or $x_1x_3 \leq p$ or $x_2x_3 \leq p$.

Let a finite set V be a vertex set and $E(V) = \{(u, v) | u, v \in V, u \neq v\}$. A pairwise $G = (V, E)$ is called a graph on V where $E \subseteq E(V)$. The elements of V are the vertices of G, and those of E the

* Corresponding author. *Email address:* *gulsenulucak@gtu.edu.tr*

edges of G. Consider that the edges (x, y) and (y, x) denote the same edge (For more information, see [3-8].

A hypergraph H is a pair (V, E) of disjoint sets, where the elements of E are nonempty subsets of V. The elements of V are called the vertices of H and the elements of E are called the hyperedges of H. If the size of any hyperedge e in the hypergraph H is n, then H is called n-uniform hypergraph. Let H be an n-uniform hypergraph. An alternating sequence of distinct vertices and hyperedges is called a path with the form $v_1, e_1, v_2, e_2, \dots, v_m$ such that v_i, v_{i+1} are in e_i for all $1 \leq i \leq m-1$. The length of a path is the number of hyperedges of it. The distance $d(x, y)$ between two vertices x and y of H is the length of the shortest path from x to y. If no such path between x and y exists, then $d(x, y) = \infty$. The diameter $diam(H)$ of H is the greatest distance between any two vertices. The hypergraph H is said to be connected if $diam(H) < \infty$. A cycle in a hypergraph H is an alternating sequence of distinct vertices and hyperedges of the form $v_1, e_1, v_2, e_2, \dots, v_m, e_m, v_1$ such that $v_i, v_{i+1} \in e_i$ and $v_m, v_1 \in e_m$ for all $1 \leq i \leq m$. The girth $gr(H)$ of a hypergraph H containing a cycle is the smallest size of the length of cycles of H. (For more information, see [5]). A hypergraph H is called trivial if it has a single vertex and also it is called empty if it has no hyperedges.

The concept of a zero-divisor graph of a commutative ring was first introduced in [6]. Let R be a commutative ring and $k \geq 2$ be an integer. A nonzero nonunit element x_1 in R is said to be a k-zero-divisor in R if there are $k-1$ distinct nonunit elements $x_2, x_3, \dots, x_k$ in R different from x_1 such that $x_1 x_2 x_3 \dots x_k = 0$ and the product of no elements of any proper subset of $A = \{x_1, x_2, x_3, \dots, x_k\}$ is zero. The set of k-zero divisor elements of R is denoted by $Z_k(R)$. Let I be a proper ideal of R. The 3-zero-divisor hypergraph of R with respect to I, denoted by $H_3(R, I)$, is the hypergraph whose vertices are the set $\{x_1 \in R \backslash I | x_1 x_2 x_3 \in I \text{ for some } x_2, x_3 \in R \backslash I \text{ such that } x_1 x_2 \notin I, x_2 x_3 \notin I \text{ and } x_1 x_3 \notin I\}$ where distinct vertices x_1, x_2 and x_3 are adjacent if and only if $x_1 x_2 x_3 \in I, x_1 x_2 \notin I, x_2 x_3 \notin I \text{ and } x_1 x_3 \notin I$ (See [9]). Let I be a proper ideal of R. Recall that I is called a 2-absorbing ideal of R if $x_1 x_2 x_3 \in I$ for some x_1, x_2 and x_3 in R, then $x_1 x_2 \in I$ or $x_2 x_3 \in I$ or $x_1 x_3 \in I$ (For more information, see [10]). Hence $H_3(R, I)$ is not empty if and only if I is not a 2-absorbing ideal of R (see Proposition 1 in [9]).

Let z be a proper element of L. A proper element a_1 of L is called n-zero divisor element with respect to z in L if there are $n-1$ distinct elements $a_2, a_3, \dots, a_n$ in L different from a_1 such that $a_2 a_3 \dots a_n \leq z$ and the product of no elements of any proper subset of $A = \{a_1, a_2, \dots, a_n\}$ is less than or equals to z. The set of all n-zero divisor element with respect to z in L is denoted by $Z_n(L, z)$. For example, consider the lattice of ideals of $\mathbb{Z}$, $L = \mathrm{I}(\mathbb{Z})$ the set of all ideals of $\mathbb{Z}$. The ideal (2) is a 3-zero-divisor with respect to (8) in L since $(2)(3)(6) \subseteq (8)$, and the product of no elements of any proper subset of $\{(2), (3), (6)\}$ is contained by (8).

Throughout this paper, we assume that a lattice L is a multiplicative lattice. Let z be a proper element of L. The 3-zero-divisor hyper-graph of L with respect to z, denoted by $H_3(L, z)$, is a hypergraph whose vertices are elements of the set $\left\{x_1 \in L - \{z\} \middle| \begin{matrix} x_1 x_2 x_3 \leq z \Rightarrow x_1 x_2 \not\leq z, x_2 x_3 \not\leq z \text{ and } x_1 x_3 \not\leq z \\ \text{for some } x_2, x_3 \in L - \{z\} \end{matrix}\right\}$ such that distinct vertices x_1, x_2 and x_3 are adjacent, that is, $\{x_1, x_2, x_3\}$ is a hyperedge if and only if $x_1 x_2 x_3 \leq z \Rightarrow x_1 x_2 \not\leq z$, $x_2 x_3 \not\leq z \text{ and } x_1 x_3 \not\leq z$. It can be seen that $H_3(L, z)$ is a 3-uniform hypergraph. In this paper, we show that $H_3(L, z)$ is empty if and only if z is a 2-absorbing element of L and also, $H_3(L/z)$ is empty

hypergraph if and only if $H_3(L,z)$ is empty hypergraph. Then we give that $H_3(L,z)$ is connected and $diam(H_3(L,z)) \leq 4$. Additionally, we show that $H_3(L,z)$ is a complete 3-partite hypergraph if p_1, p_2 and p_3 are prime elements of L and $z = p_1 \wedge p_2 \wedge p_3 \neq 0_L$ and the converse is true if L is reduced lattice. Finally, we see that $H_3(L,z)$ has no cut-point.

2. ZERO DIVISOR HYPERGRAPH H_3 (L,z) WITH RESPECT TO z

Definition 1. Let z be a proper element of L. The 3-zero-divisor hypergraph of L with respect to z is a hypergraph whose vertices are elements of the set $\left\{x_1 \in L - \{z\} \middle| \begin{matrix} x_1x_2x_3 \leq z \Rightarrow x_1x_2 \leq z, x_2x_3 \leq z \text{ and } x_1x_3 \leq z \\ \text{for some } x_2, x_3 \in L - \{z\} \end{matrix} \right\}$. Also, distinct vertices x_1, x_2 and x_3 are adjacent, that is, $\{x_1, x_2, x_3\}$ is a hyperedge if and only if $x_1x_2x_3 \leq z \Rightarrow x_1x_2 \leq z,\ x_2x_3 \leq z \text{ and } x_1x_3 \leq z$. Throughout this paper, the hypergraph is denoted by $H_3(L,z)$.

Let $z = 0_L$. Then it is clear that $H_3(L) = H_3(L, 0_L)$ is the hypergraph whose vertices are elements of the set $\left\{x_1 \in Z_3(L) \middle| \begin{matrix} x_1x_2x_3 = 0_L \Rightarrow x_1x_2 \neq 0_L, x_2x_3 \neq 0_L \text{ and } x_1x_3 \neq 0_L \\ \text{for some } x_2, x_3 \in Z_3(L) \end{matrix} \right\}$ where distinct vertices x_1, x_2 and x_3 are adjacent if and only if $x_1x_2x_3 = 0_L \Rightarrow x_1x_2 \neq 0_L, x_2x_3 \neq 0_L \text{ and } x_1x_3 \neq 0_L$.

The hypergraphs $H_3(R)$ in [5] and $H_3(R,I)$ in [10], which are defined on a commutative ring R and a proper ideal I of R, are examples for the hypergraph $H_3(L,z)$.

We obtain the following results with the above definition and the definition of 2-absorbing element in L.

Proposition 1. Let z be a proper element of L. Then the following statements hold:

1) $H_3(L,z)$ is empty hypergraph if and only if z is a 2-absorbing element of L.
2) $H_3(L/z)$ is empty hypergraph if and only if $H_3(L,z)$ is empty hypergraph.

Proof. 1). ($\Rightarrow$): Let $H_3(L,z)$ be empty hypergraph. Suppose that z is not a 2-absorbing element of L. Take $x_1x_2x_3 \leq z$ for some $x_1, x_2, x_3 \in L$. Then we get $x_1x_2 \nleq z,\ x_2x_3 \nleq z$ and $x_1x_3 \nleq z$. Hence $e = \{x_1, x_2, x_3\}$ is a hyperedge of $H_3(L,z)$, a contradiction.

($\Leftarrow$): It is obvious.

2). ($\Rightarrow$): Assume that $H_3(L,z)$ is not an empty hypergraph. Then it has a hyperedge $e = \{x_1, x_2, x_3\}$. Consider $x_1 \vee z, x_2 \vee z, x_3 \vee z \in L/z$. It is clear that $x_1 \vee z, x_2 \vee z, x_3 \vee z$ are different from z. Then we have that $(x_1 \vee z)(x_2 \vee z)(x_3 \vee z) = 0_{L/z}$, $(x_1 \vee z)(x_2 \vee z) \neq 0_{L/z}$, $(x_2 \vee z)(x_3 \vee z) \neq 0_{L/z}$ and $(x_1 \vee z)(x_3 \vee z) \neq 0_{L/z}$. Thus $e' = \{x_1 \vee z, x_2 \vee z, x_3 \vee z\}$ is a hyperedge of $H_3(L/z)$, a contradiction.

($\Leftarrow$): Let $H_3(L/z)$ be not an empty hypergraph. Then it has a hyperedge $e = \{y_1, y_2, y_3\}$ for some $y_1, y_2, y_3 \in V(H_3(L/z))$. Then $y_1 \circ y_2 \circ y_3 = 0_{L/z}$, that is, $y_1y_2y_3 \leq z$ and since $y_1 \circ y_2$, $y_2 \circ y_3$ and $y_1 \circ y_3$ are different from $0_{L/z}$, then $y_1y_2, y_2y_3, y_1y_3 \nleq z$. Therefore, $e = \{y_1, y_2, y_3\}$ is a hyperedge of $H_3(L,z)$, a contradiction.

Theorem 1. Let $H_3(L,z)$ be a 3-zero-divisor hypergraph of L with respect to z. If $x^2 \not\leq z$ for each 3-zero-divisor $x \in L$ with respect to z, then $H_3(L,z)$ is connected and $diam(H_3(L,z)) \leq 4$. Furthermore, if $H_3(L,z)$ has a cycle, then $gr(H_3(L,z)) \leq 9$.

Proof. Let $e_1 = \{x_1, x_2, x_3\}$ and $e_2 = \{y_1, y_2, y_3\}$ be hyperedges of $H_3(L,z)$. If $e_1 \cap e_2 \neq \emptyset$, the proof is completed. Assume that $e_1 \cap e_2 = \emptyset$. We show that there are hyperedges e_3, e_4 such that they satisfy one of the followings:

(1) $\boldsymbol{e_3 \cap e_1 \neq \emptyset, e_3 \cap e_2 \neq \emptyset}$
(2) $e_3 \cap e_1 \neq \emptyset, e_4 \cap e_2 \neq \emptyset, e_4 \cap e_3 \neq \emptyset$

Assume that G is the partite graph such that $V(G) = e_1 \cup \boldsymbol{e_2}$ and $x_i y_j \in E(G)$ if and only if $x_i y_j \leq z$.

Assume that G has two isolated vertices such that one is in e_1 and the other is in e_2. Let $deg_G(x_3) = deg_G(y_3) = 0$. Suppose that there is $a \in \{x_1, x_2, y_1, y_2\}$ where $x_3 y_3 a \leq z$. Then $e_3 = \{x_3, y_3, a\}$ is a hyperedge which holds the condition (1). Let the case not satisfy. If $x_3 y_3 \notin \{x_1, x_2, y_1, y_2\}$, then $e_3 = \{x_1, x_2, x_3 y_3\}$ and $e_4 = \{y_1, y_2, x_3 y_3\}$ are two hyperedges which satisfy the condition (2). In the contrary case, without loss of generality (wlog.), suppose that $x_3 y_3 = x_1$. Hence $e_3 = \{x_1, y_1, y_2\}$ is a hyperedge satisfying the condition (1). Consequently, $H_3(L,z)$ is connected. Now, we show that $diam(H_3(L,z)) \leq 4$. We consider the number of edges G for the rest of the proof.

Case 1. Assume that $|E(G)| \leq 2$. Then G has two isolated vertices such that one is in e_1 and the other is in e_2.

Case 2. Let $|E(G)| = 3$. Take account of the next four different subcases for this case:

Case 2.1: Let $deg_G(a) = 1$ for each vertex a of G. Assume that $E(G) = \{x_1 y_1, x_2 y_2, x_3 y_3\}$. We consider $\{x_1, x_2 y_3, y_1 \vee y_2\}$. If $x_1 = x_2 y_3$, then $x_1 y_2 = x_2 y_3 y_2 \leq z$, a contradiction. If $x_1 = y_1 \vee y_2$, then $y_1 x_2 x_3 \leq z$. Thus $e_3 = \{y_1, x_2, x_3\}$ satisfies the condition (1). If $y_1 \vee y_2 = x_2 y_3$, then $x_1 y_2 x_3 \leq z$ and so the condition (1) is satisfied for $e_3 = \{x_1, y_2, x_3\}$. On the contrary, reconsider $e_3 = \{x_1, x_2 y_3, y_1 \vee y_2\}$. If e_3 is not a hyperedge, then $x_1 x_2 y_3 \leq z$ or $x_2 y_3 (y_1 \vee y_2) \leq z$, that is, $x_2 y_3 y_1 \leq z$. Then $e'_3 = \{x_1, x_2, y_3\}$ is a hyperedge satisfying the condition (1) or $e'_4 = \{x_2, y_3, x_1\}$ is a hyperedge satisfying the condition (1). Let $e_3 = \{x_1, x_2 y_3, y_1 \vee y_2\}$ be a hyperedge. In a similar way, we consider $\{y_1, x_2 y_3, x_1 \vee x_3\}$. If e_4 is not a hyperedge, then $y_1 x_2 y_3 \leq z$ or $x_2 y_3 (x_1 \vee x_3) \leq z$, that is, $x_2 y_3 x_1 \leq z$. Then $e''_3 = \{y_1, x_2, y_3\}$ is a hyperedge satisfying the condition (1) or $e''_4 = \{x_2, y_3, x_1\}$ is a hyperedge satisfying the condition (1). Assume that $e_4 = \{y_1, x_2 y_3, x_1 \vee x_3\}$ is a hyperedge. Then we have two hyperedges $e_3 = \{x_1, x_2 y_3, y_1 \vee y_2\}$ and $e_4 = \{y_1, x_2 y_3, x_1 \vee x_3\}$ with e_3 and e_4 satisfying the condition (2).

Case 2.2. Let $deg_G(a) = 1$ for only an element a of G. Wlog., suppose that $E(G) = \{x_1 y_1, x_1 y_2, x_2 y_3\}$. We consider $\{x_2, x_3 y_1, x_1 \vee y_3\}$. If $x_2 = x_3 y_1$, then $x_1 x_2 \leq z$, is a contradiction. If $x_2 = x_1 \vee y_3$, then $x_2 y_2 y_1 \leq z$ and so the condition (1) is satisfied for $e_3 = \{x_2, y_2, y_1\}$. If $x_1 \vee y_3 = x_3 y_1$, then $x_3 y_1 y_2 y_1 \leq z$. In the circumstances, if $x_3 = y_1 y_2$, then $x_1 x_3 \leq z$, a contradiction. If $y_1 = y_1 y_2$, then $y_1 y_3 \leq z$, a contradiction. Hence, the condition (1) holds for $e_3 = \{x_3, y_1 y_2, y_1\}$. Let the above conditions not hold. If $e_3 = \{x_2, x_3 y_1, x_1 \vee y_3\}$ is not a hyperedge, then $x_2 x_3 y_1 \leq z$ or $x_3 y_1 (x_1 \vee y_3) \leq z$, that is, $x_3 y_1 y_3 \leq z$. Then $e'_3 = \{x_2, x_3, y_1\}$ is a hyperedge satisfying the condition (1) or $e'_4 = \{x_3, y_1, y_3\}$ is a hyperedge satisfying the condition (1). Suppose that $e_3 =$

$\{x_2, x_3y_1, x_1 \vee y_3\}$ is a hyperedge. Now, similarly we consider $\{y_2, x_3y_1, y_3\}$. If $e_4 = \{y_2, x_3y_1, y_3\}$ is not a hyperedge, then $y_2x_3y_1 \leq z$ or $x_3y_1y_3 \leq z$. Then $e''_3 = \{y_2, x_3, y_1\}$ is a hyperedge satisfying the condition (1) or $e'_4 = \{x_3, y_1, y_3\}$ is a hyperedge satisfying the condition (1). Let $\{y_2, x_3y_1, x_1 \vee y_3\}$ be a hyperedge. Then we obtain two hyperedges $e_3 = \{x_2, x_3y_1, x_1 \vee y_3\}$ and $e_4 = \{y_2, x_3y_1, y_3\}$ with e_3 and e_4 satisfying the condition.

Case 2.3. Let $deg_G(a) = deg_G(b) = 2$ for $a, b \in V(G)$. Wlog., suppose that $E(G) = \{x_1y_1, x_1y_2, x_2y_2\}$. Then $deg_G(x_3) = deg_G(y_3) = 0$ and so the proof is completed.

Case 2.4. Let $deg_G(a) = 3$ for only one element a of G. Wlog., suppose that $E(G) = \{x_1y_1, x_1y_2, x_1y_3\}$. Let ${x_1}^2x_2 \nleq z$. Consider $\{x_1x_2 \vee y_1, x_1, x_3\}$. If $x_1x_2 \vee y_1 = x_1$, then $y_2y_1 \leq z$, a contradiction. If $x_1x_2 \vee y_1 = x_3$, then $x_3y_3y_2 \leq z$, a contradiction. Hence $e_3 = \{x_3, y_2, y_3\}$ is a hyperedge satisfying the condition (1). In the other case, $e_3 = \{x_1x_2 \vee y_1, x_1, x_3\}$ is a hyperedge. In a similar way, we consider $\{x_1x_2 \vee y_1, y_2, y_3\}$. Then we have a hyperedge e_3 which satisfies the condition (1) or $e_4 = \{x_1x_2 \vee y_1, y_2, y_3\}$ is a hyperedge with e_3 and e_4 satisfying the condition (2). Let ${x_1}^2x_2 \leq z$. We consider $\{x_1 \vee y_1, x_1, x_2\}$. If $x_1 \vee y_1 = x_2$, then $x_2y_3y_2 \leq z$, a contradiction. Thus $e_3 = \{x_1 \vee y_1, x_1, x_2\}$ is a hyperedge. In a similar way, we consider $\{x_1 \vee y_1, y_2, y_3\}$. Then we have a hyperedge e_3 which satisfies the condition (1) or $e_4 = \{x_1x_2 \vee y_1, y_2, y_3\}$ is a hyperedge with e_3 and e_4 satisfying the condition (2).

Case 3. Assume that $|E(G)| = 4$. Consider four different subcases for this case:

Case 3.1. Let $deg_G(a) = 3$ for only one element a of G. Wlog., suppose that $E(G) = \{x_1y_1, x_1y_2, x_1y_3, x_2y_3\}$. We consider $\{x_3y_1, x_2, x_1 \vee y_3\}$. If $x_3y_1 = x_2$, then $x_3y_3y_1 \leq z$, a contradiction. Thus $e_3 = \{x_3, y_1, y_3\}$ is a hyperedge which holds (1). If $x_3y_1 = x_1 \vee y_3$, then ${x_1}^2 \leq z$, is a contradiction. If $x_2 = x_1 \vee y_3$, then ${y_3}^2 \leq z$, a contradiction. In the other condition, consider again $e_3 = \{x_3y_1, x_2, x_1 \vee y_3\}$. If $e_3 = \{x_3y_1, x_2, x_1 \vee y_3\}$ is not a hyperedge, then $x_2x_3y_1 \leq z$ or $x_3y_1(x_1 \vee y_3) \leq z$, that is, $x_3y_1y_3 \leq z$. Then $e'_3 = \{x_2, x_3, y_1\}$ is a hyperedge satisfying the condition (1) or $e'_4 = \{x_3, y_1, y_3\}$ is a hyperedge satisfying the condition (1). Assume that $e_3 = \{x_3y_1, x_2, x_1 \vee y_3\}$ is a hyperedge. In a similar way, we consider $\{x_3y_1, y_2, y_3\}$. If $e_4 = \{x_3y_1, y_2, y_3\}$ is not a hyperedge, then $x_3y_1y_2 \leq z$ or $x_3y_1y_3 \leq z$. Then $e''_3 = \{y_2, x_3, y_1\}$ is a hyperedge satisfying the condition (1) or $e'_4 = \{x_3, y_1, y_3\}$ is a hyperedge satisfying the condition (1). Suppose that $e_4 = \{x_3y_1, y_2, y_3\}$ is a hyperedge. Then we get two hyperedges $e_3 = \{x_3y_1, x_2, x_1 \vee y_3\}$. and $e_4 = \{x_3y_1, y_2, y_3\}$ with e_3 and e_4 satisfying the condition (2).

Case 3.2. Assume that the degree of four vertices of G equals to two. Wlog., presume that $E(G) = \{x_1y_1, x_1y_2, x_2y_1, x_2y_2\}$. Then $deg_G(x_3) = deg_G(y_3) = 0$ and so the proof is completed.

Case 3.3. Suppose that the degree of three vertices of G is two. Wlog. assume that $E(G) = \{x_1y_1, x_1y_2, x_2y_2, x_2y_3\}$. We consider $\{x_3y_3, x_1, x_2\}$. If $x_3y_3 = x_1$ or $x_3y_3 = x_2$, then $x_3y_3y_2 \leq z$ and so (1) is satisfied for a hyperedge $e_3 = \{x_3, y_2, y_3\}$. In the other case, let us view $e_3 = \{x_3y_3, x_1, x_2\}$. If $e_3 = \{x_3y_3, x_1, x_2\}$ is not a hyperedge, then $x_3y_3x_1 \leq z$ or $x_3y_3x_2 \leq z$. Then $e'_3 = \{x_3, y_3, x_1\}$ is a hyperedge satisfying the condition (1) or $e'_4 = \{x_3, y_3, x_2\}$ is a hyperedge satisfying the condition (1). Let $e_3 = \{x_3y_3, x_1, x_2\}$ be a hyperedge. In a similar way, we consider $\{x_3y_3, y_1, y_2\}$. If $e_4 = \{x_3y_3, y_1, y_2\}$ is not a hyperedge, then $x_3y_3y_1 \leq z$ or $x_3y_3y_2 \leq z$. Then $e''_3 = \{x_3, y_3, y_1\}$ is a hyperedge satisfying the condition (1) or $e''_4 = \{x_3, y_3, y_2\}$ is a hyperedge

satisfying the condition (1). Let $e_4 = \{x_3y_3, y_1, y_2\}$ be a hyperedge. Then we get two hyperedges $e_3 = \{x_3y_3, x_1, x_2\}$ and $e_4 = \{x_3y_3, y_1, y_2\}$ with e_3 and e_4 satisfying the condition (2).

Case 3.4. Let $deg_G(a) = deg_G(b) = 2$ for $a, b \in V\ (G)$. Then, we have two different cases and we can choose one of these sets $E(G) = \{x_1y_1, x_1y_2, x_2y_2, x_3y_3\}$ and $E(G) = \{x_1y_1, x_1y_2, x_2y_3, x_3y_3\}$. In the first choice, we consider $\{x_3y_1, x_2, x_1 \vee y_2\}$. If $x_3y_1 = x_2$, then $x_3y_1y_2 \leq z$ and so $e_3 = \{x_3, y_1, y_2\}$ is an edge satisfying (1). If $x_3y_1 = x_1 \vee y_2$, then ${x_1}^2 \leq z$, a contradiction. If $x_2 = x_1 \vee y_2$, then ${y_2}^2 \leq z$, is a contradiction. In the other case, consider $e_3 = \{x_3y_1, x_2, x_1 \vee y_2\}$. If $e_3 = \{x_3y_1, x_2, x_1 \vee y_2\}$ is not a hyperedge, then $x_3y_1x_2 \leq z$ or $x_3y_1(x_1 \vee y_2) \leq z$, that is, $x_3y_1y_2 \leq z$. Then ${e''}_3 = \{x_3, y_1, y_2\}$ is a hyperedge satisfying the condition (1) or ${e''}_4 = \{x_3, y_1, y_3\}$ is a hyperedge satisfying the condition (1). Let $e_4 = \{x_3y_1, y_2, y_3\}$ be a hyperedge. Then we get two hyperedges $e_3 = \{x_3y_1, x_2, x_1 \vee y_2\}$ and $e_4 = \{x_3y_1, y_2, y_3\}$ with e_3 and e_4 satisfying the condition (2).

In a similar manner, we consider $\{x_1 \vee y_1, x_2, x_3\}$ and $\{x_1 \vee y_1, y_2, y_3\}$ for the second choice. Hence, we have a hyperedge e_3 which holds (1) or two hyperedges e_3 and e_4 which hold the condition (2).

Case 4. Assume that $|E(G)| = 5$. Consider four different subcases for this case:

Case 4.1. Wlog. assume that $E(G) = \{x_1y_1, x_1y_2, x_1y_3, x_2y_1, x_2y_2\}$. We consider $\{x_3y_3, x_2, x_1 \vee y_2\}$. If $x_3y_3 = x_2$, then $x_3y_3x_2 \leq z$, and so the condition (1) is satisfied for a hyperedge $e_3 = \{x_2, x_3, y_3\}$. If $x_3y_3 = x_1 \vee y_2$, then ${x_1}^2 \leq z$, a contradiction. If $x_2 = x_1 \vee y_2$, then $y_1y_2 \leq z$, yielding a contradiction. On the other hand, $e_3 = \{x_3y_3, x_2, x_1 \vee y_2\}$ is a edge in G. In a similar way, we consider $\{x_3y_3, y_1, y_2\}$. If $e_4 = \{x_3y_3, y_1, y_2\}$ is not a hyperedge, then $x_3y_3y_1 \leq z$ or $x_3y_3y_2 \leq z$. Then ${e''}_3 = \{x_3, y_3, y_1\}$ is a hyperedge satisfying the condition (1) or ${e''}_4 = \{x_3, y_3, y_2\}$ is a hyperedge satisfying the condition (1). Let $e_4 = \{x_3y_3, y_1, y_2\}$ be a hyperedge. Then we get two hyperedges $e_3 = \{x_3y_3, x_2, x_1 \vee y_2\}$ and $e_4 = \{x_3y_3, y_1, y_2\}$ with e_3 and e_4 satisfying the condition (2).

Case 4.2. Wlog., presume that $E(G) = \{x_1y_1, x_1y_2, x_1y_3, x_2y_1, x_3y_2\}$. We consider $\{x_1 \vee y_1, x_2, y_2\}$. If $x_1 \vee y_1 = x_2$, then ${y_1}^2 \leq z$, is a contradiction. If $x_1 \vee y_1 = y_2$, then ${x_1}^2 \leq z$, is a contradiction. In the following situations, $e_3 = \{x_1 \vee y_1, x_2, x_3y_3\}$ is a hyperedge of G satisfying (1).

Case 4.3. Wlog., presume that $E(G) = \{x_1y_1, x_1y_2, x_1y_3, x_2y_1, x_3y_2\}$. We consider $\{x_1 \vee y_1, x_2, y_2\}$. If $x_1 \vee y_1 = x_2$ then ${y_1}^2 \leq z$, is a contradiction. If $x_1 \vee y_1 = y_2$ then $x_2x_3y_2 \leq z$. Thus $e_3 = \{x_2, x_3, y_2\}$ is a hyperedge satisfying (1). In the other case, $e_3 = \{x_1 \vee y_1, x_2, y_2\}$ is a hyperedge satisfying (1).

Case 4.4. Wlog., let $E(G) = \{x_1y_1, x_1y_2, x_2y_1, x_2y_2, x_3y_3\}$. We consider $\{x_3 \vee y_1, x_1, y_3\}$. If $x_3 \vee y_1 = x_1$ or $x_3 \vee y_1 = y_3$, then $x_1x_2y_3 \leq z$. Then $e_3 = \{x_1, x_2, y_3\}$ is a hyperedge satisfying the condition (1). In the other case, $e_3 = \{x_3 \vee y_1, x_1, y_3\}$ is a hyperedge satisfying the condition (1).

Case 4.5. Wlog., presume that $E(G) = \{x_1y_1, x_1y_2, x_2y_2, x_2y_3, x_3y_3\}$. We consider $\{x_1 \vee y_2, x_2, y_1\}$. If $x_1 \vee y_2 = x_2$, then ${y_2}^2 \leq z$, is a contradiction. If $x_1 \vee y_2 = y_1$, then ${x_1}^2 \leq z$, is a contradiction. Then $e_3 = \{x_1 \vee y_2, x_2, y_1\}$ is a hyperedge satisfying the condition (1).

Case 5. Let $|E(G)| = 6$. Consider three different subcases for this case:

Case 5.1. Wlog., presume that $E(G) = \{x_1y_1, x_1y_2, x_1y_3, x_2y_1, x_2y_2, x_3y_1\}$.

We consider $\{x_1 \vee y_1, x_2, x_3\}$ and $\{x_1 \vee y_1, y_2, y_3\}$. If $x_1 \vee y_1 = x_2$, then $y_1y_2 \leq z$, a contradiction. If $x_1 \vee y_1 = x_3$, then ${y_1}^2 \leq z$, is a contradiction. If $x_1 \vee y_1 = y_2$ or $x_1 \vee y_1 = y_3$, then ${x_1}^2 \leq z$, is a contradiction. Thus $e_3 = \{x_1 \vee y_1, x_2, x_3\}$ and $e_4 = \{x_1 \vee y_1, y_2, y_3\}$ are hyperedges satisfying the condition (2).

Case 5.2. Wlog., presume that $E(G) = \{x_1y_1, x_1y_2, x_1y_3, x_2y_1, x_2y_2, x_3y_3\}$.

We consider $\{x_1 \vee y_3, x_3, y_1\}$. If $x_1 \vee y_3 = x_3$, then ${y_3}^2 \leq z$, is a contradiction. If $x_1 \vee y_3 = y_1$, then ${x_1}^2 \leq z$, is a contradiction. Thus $e_3 = \{x_1 \vee y_3, x_3, y_1\}$ is a hyperedge satisfying the condition (1).

Case 5.3. Wlog., presume that $E(G) = \{x_1y_1, x_1y_3, x_2y_1, x_2y_2, x_3y_2, x_3y_3\}$. We consider $\{x_1 \vee y_3, x_3, y_1\}$. If $x_1 \vee y_3 = x_3$, then ${y_3}^2 \leq z$, is a contradiction. If $x_1 \vee y_3 = y_1$, then ${x_1}^2 \leq z$, is a contradiction. Thus $e_3 = \{x_1 \vee y_3, x_3, y_1\}$ is a hyperedge satisfying the condition (1).

Case 6. If $7 \leq |E(G)| \leq 9$, then we have two vertices which are degree three in e_1 and the other in e_2. We suppose that $deg_G(x_1) = deg_G(y_1) = 3$. We consider $\{x_1 \vee y_1, x_2, x_3\}$ and $\{x_1 \vee y_1, y_2, y_3\}$. If $x_1 \vee y_1 = x_2$ or $x_1 \vee y_1 = x_3$, then ${y_1}^2 \leq z$, is a contradiction. If $x_1 \vee y_1 = y_2$ or $x_1 \vee y_1 = y_3$, then ${x_1}^2 \leq z$, is a contradiction. Hence $e_3 = \{x_1 \vee y_1, x_2, x_3\}$ and $e_4 = \{x_1 \vee y_1, y_2, y_3\}$ are hyperedges satisfying the condition (2).

By the fact that $gr(H_3(L,z)) \leq 2diam(H_3(L,z)) + 1$, we have that $gr(H_3(L,z)) \leq 9$.

2.1. Complete 3-Partıte Hypergraph

Definition 2. [10] A hypergraph H is called an n-partite if the vertex set V can be partitioned into disjoint subsets $V_1, V_2, \dots, V_n$ of V such that a hyperedge in the hyperedge set E composes of a choice of completely one vertex from each subset of V. Also, a hypergraph H is called a complete n-partite hypergraph if the vertex set V can be partitioned into disjoint subsets $V_1, V_2, \dots, V_n$ of V and each element of V_i for each $1 \leq i \leq n$ creates a hyperedge of H.

Proposition 2. Let $H_3(L,z)$ be a complete 3-partite hypergraph.

If $xy \leq z$, then x and y are contained by same subset V_i for some $i \in \{1,2,3\}$.

Proof. Let $H_3(L,z)$ has disjoint subsets V_1, V_2, V_3 which are partitions of the vertex set V. Let a be a vertex with $xya \leq z$. Without loss of generality, assume that $x \in V_1$ and $a \in V_2$. Then $e = \{x, y, a\}$ is not a hyperedge in $H_3(L,z)$ by our assumption. If $y \in V_3$, then e is a hyperedge since $H_3(L,z)$ is a complete 3-partite hypergraph, a contradiction. If $y \in V_2$, then there is a vertex $b \in V_3$ such that $e' = \{x, y, b\}$. But this contradicts the fact that $xy \leq z$. Therefore, y must be in V_1.

Theorem 2. Let z be a proper element of L. Then the following statements hold:

(1) If p_1, p_2 and p_3 are prime elements of L and $z = p_1 \wedge p_2 \wedge p_3 \neq 0_L$, then $H_3(L,z)$ is a complete 3-partite hypergraph.

(2) Let $a^2 \leq z$ for every 3-zero-divisor $a \in L$ with respect to z and $H_3(L,z)$ be a complete 3-partite hypergraph over the reduced lattice L. Then there exist prime elements p_1, p_2 and p_3 of L such that $p_1 \wedge p_2 \wedge p_3 \leq z$.

Proof. (1). Let $e = \{a,b,c\}$ be a hyperedge of $H_3(L,z)$. Then $abc \leq z = p_1 \wedge p_2 \wedge p_3$, that is, $abc \leq p_1, p_2, p_3$. Since p_i is a prime element for any $i \in \{1,2,3\}$, then $a \leq p_1$ or $b \leq p_1$ or $c \leq p_1$ and $a \leq p_2$ or $b \leq p_2$ or $c \leq p_2$ and $a \leq p_3$ or $b \leq p_3$ or $c \leq p_3$. Additionally, $ab \nleq p_i$ and $bc \nleq p_j$ and $ac \nleq p_k$ for some $i,j,k \in \{1,2,3\}$ since $ab, bc, ac \nleq z = p_1 \wedge p_2 \wedge p_3$. Wlog., we assume $ab \nleq p_1$. Then $a \nleq p_1$ and $b \nleq p_1$. Thus, we have $c \leq p_1$. Indeed, if $ac \nleq p_1$, then $b \leq p_1$, a contradiction. In a similar manner, suppose that $ac \nleq p_2$. Then $a \nleq p_2$ and $c \nleq p_2$. Thus, this yields $b \leq p_2$. Indeed, if $bc \nleq p_1$, then $a \leq p_1$, a contradiction and if $bc \nleq p_2$, then $a \leq p_2$, a contradiction. Thus, it must be $bc \nleq p_3$. Then, we get $a \leq p_3$. We assume that $a \leq p_3$ and $a \nleq p_1, p_2$, $b \leq p_2$ and $b \nleq p_1, p_3$ and $c \leq p_1$ and $c \nleq p_2, p_3$. Consequently, $H_3(L,z)$ is a complete 3-partite hypergraph with parts V_i for any $i \in \{1,2,3\}$ whose vertices must be only less than or equal to p_i.

(2). Let $H_3(L,z)$ be a complete 3-partite hypergraph and it has parts V_1, V_2 and V_3. Set $p_1 = V_1 \vee z, p_2 = V_2 \vee z$ and $p_3 = V_3 \vee z$. Then $x_1x_2x_3 \leq z$ for every $x_i \leq p_i$ for any $i \in \{1,2,3\}$. It is clear that $\left(\bigvee_{x_1 \in V_1} x_1\right)\left(\bigvee_{x_2 \in V_2} x_2\right)\left(\bigvee_{x_3 \in V_3} x_3\right) \vee z \leq z$, that is, $p_1p_2p_3 \leq z$ since L is a multiplicative lattice. As L is reduced, then $p_1 \wedge p_2 \wedge p_3 \leq z$. We assume that p_1 is not a prime element of L, that is, $ab \leq p_1$ and $a, b \nleq p_1$ for some $a, b \in L$. Since $ab \leq p_1 = V_1 \vee z$ then $ab \leq z$ or $ab \in V_1$. We have three cases for this assumption.

Case 1. Let $ab \in V_1$ and $ab \leq z$. This contradicts the definition of vertex set of $H_3(L,z)$.

Case 2. Let $ab \in V_1$ and $ab \nleq z$. Since $ab \in V_1$ and $a \notin V_1$, then $a \in V_2$ or $a \in V_3$. Wlog., assume that $a \in V_2$. So, $\{ab, a, c\}$ must be a hyperedge of $H_3(L,z)$ for any $c \in V_3$. However, since $a^2 \leq z$ for every 3-zero-divisor $a \in L$, then $a^2b \leq z$, contradiction.

Case 3. Let $ab \notin V_1$ and $ab \leq z$. By Proposition 2, a and b must be in the same V_i for any $i = \{2,3\}$. Wlog., let $a, b \in V_2$. Then, $xay \leq z$, $xa \nleq z, xy \nleq z, ay \nleq z$ and $xby \leq z$, $xb \nleq z, xy \nleq z, by \nleq z$ for some $x \in V_1$ and $y \in V_3$. By Proposition 2, we obtain that $xa \in V_3$, $xb \in V_3$, $ay \in V_1$, $by \in V_1$. Therefore, $\{ay, b, xa\}$ must be a hyperedge, since $H_3(L,z)$ is a complete 3-partite hypergraph. However, $a^2yx \leq z$ for $a^2 \leq z$, contradiction. We have a contradiction for each cases. Therefore, a or b must be less than or equal to p_1. Similarly, it can be seen that p_2 and p_3 are prime elements in L.

2.2. Cut Points and Bridge of $H_3(L,z)$

Definition 3. [6] A vertex a of a connected graph G is called a cut-point of G if there are vertices x and y of G with $a \neq x$ and $a \neq y$ such that a is in every path which is from x to y.

Theorem 3. Let $z \in L$ and $S = \{u \in L | u \leq z \; and \; u \nleq a\}$. If $S \neq \emptyset$, then a is not a cut-point in $H_3(L,z)$.

Proof. Let a be in every path which is from x to y with $a \neq x$ and $a \neq y$. We know that $d(x,y) = 2,3$ or 4 by Theorem 1. Consider $a \vee u$. Note that it is a vertex in $H_3(L,z)$ which is different from a. We consider the following cases:

Case 1. Let $d(x,y) = 2$. Then there are two hyperedges $e_1 = \{x, a, c_1\}$ and $e_2 = \{a, y, c_2\}$ for some vertices c_1, c_2 in $H_3(L,z)$ such that $x -_{e_1} a -_{e_2} y$ is a path. Consider $e'_1 = \{x, a \vee u, c_1\}$ and $e'_2 = \{a \vee u, y, c_2\}$.

Let $a \vee u \neq x$, $a \vee u \neq y$ and $a \vee u \neq c_i$ for $i \in \{1,2\}$. It is easily seen that e'_1 and e'_2 are two hyperedges such that $x -_{e'_1} a \vee u -_{e'_2} y$ is a path.

i. If $a \vee u = x$ or $a \vee u = y$, then x and y are adjacent.

ii. Consider $a \vee u = c_1$ or $a \vee u = c_2$. Wlog., assume that $a \vee u = c_1$. Then $e''_1 = \{x, a \vee u, a\}$ and $e'_2 = \{a \vee u, y, c_2\}$ are two hyperedges such that $x -_{e''_1} a \vee u -_{e'_2} y$ is a path.
Thus a is not a cut point.

Case 2. Let $d(x,y) = 3$. Then there are three hyperedges $e_1 = \{x, a, c_1\}$ and $e_2 = \{a, b, c_2\}$ and $e_3 = \{b, y, c_3\}$ for some vertices b, c_1, c_2, c_3 in $H_3(L,z)$ such that $x -_{e_1} a -_{e_2} b -_{e_3} y$ is a path. If $a \vee u$ is different from each of x, b and c_i for $i \in \{1,2,3\}$, then there is a path from x to y which does not contain a. Now, we consider other situations.

i. Let $a \vee u = x$. Then consider $e'_2 = \{a \vee u, b, c_2\}$ and e_3. Note that there is a path $a \vee u -_{e'_2} b -_{e_3} y$. Thus a is not a cut point.

ii. Let $a \vee u = b$. Consider $e'_1 = \{x, a \vee u, c_1\}$ and e_3. Clearly, there is a path $x -_{e'_1} a \vee u -_{e_3} y$. Hence a is not a cut point.

iii. Let $a \vee u = y$. Consider $e'_1 = \{x, a \vee u, c_1\}$. Thus x and y are adjacent. Hence a is not a cut point.

iv. $a \vee u = c_i$ for $i \in \{1,2\}$. It can be seen in a similar way in Case 1 (ii).

v. Let $a \vee u = c_3$. Consider $e'_3 = \{b, y, a \vee u\}$ and $e'_1 = \{x, a \vee u, c_1\}$. Then there is a path such that $x -_{e'_1} a -_{e'_3} y$.

Case 3. Let $d(x,y) = 4$. Then there are four hyperedges $e_1 = \{x, a, c_1\}$ and $e_2 = \{a, b, c_2\}$, $e_3 = \{b, c, c_3\}$ and $e_4 = \{c, y, c_4\}$ for some vertices b, c, c_1, c_2, c_3, c_4 in $H_3(L,z)$ such that $x -_{e_1} a -_{e_2} b -_{e_3} y -_{e_4} c$ is a path. If $a \vee u$ is different from each of x, b, c, y and c_i for $i \in \{1,2,3,4\}$, then there is a path from x to y which does not contain a. Now, we consider other situations.

i. Let $a \vee u = x$. Now, consider $e'_2 = \{a \vee u, b, c_2\}$. Then note that e'_2 is a hyperedge and there is a path $a \vee u -_{e'_2} b -_{e_3} c -_{e_4} y$.

ii. Let $a \vee u = b$ Consider $e'_1 = \{x, a \vee u, c_1\}$ and $e'_3 = \{a \vee u, c, c_3\}$. Then note that e'_1 and e'_3 are two hyperedges and there is a path $x -_{e'_1} a \vee u -_{e'_3} c -_{e_4} y$.

iii. Let $a \vee u = c$. Consider $e'_1 = \{x, a \vee u, c_1\}$ and $e'_4 = \{a \vee u, y, c_4\}$. Then note that e'_4 is a hyperedge and there is a path $x -_{e'_1} a \vee u -_{e'_4} y$.

iv. Let $a \vee u = y$. Consider $e'_1 = \{x, a \vee u, c_1\}$. Note that e'_1 is a hyperedge and x and y are adjacent.

iv. Let $a \vee u = c_i$ for $i \in \{1,2\}$. It can be seen in a similar way in Case 1 (ii).

v. Let $a \vee u = c_i$ for $i \in \{3,4\}$. It can be seen in a similar way in Case 2 (v).

We obtain the following result by the previous theorem.

Corollary 1. Let a be a vertex in $H_3(L,z)$ and $z \not\leq a$. Then a is not a cut-point of $H_3(L,z)$.

Proposition 3. If $H_3(L,z)$ is connected, then $H_3(L,z)$ has not any bridge.

Proof. Let $e = \{a,b,c\}$ be a bridge of $H_3(L,z)$. Then $H_3(L,z)$ is disconnected if e is omitted in hypergraph. Take an element y with $0_L \neq y \not\leq z$. Then $a \vee y, b \vee y, c \vee y \not\leq z$. Also each of $e_1 = \{a \vee y, b, c\}$, $e_2 = \{a, b \vee y, c\}$ and $e_3 = \{a, b, c \vee y\}$ is a hyperedge. Thus, there is a cycle $a -_{e_3} b -_{e_1} c -_{e_2} a$. Indeed if e is omitted in hypergraph, $H_3(L,z)$ is connected. Thus, $H_3(L,z)$ has not any bridge.

REFERENCES

[1] Jayaram C. and Johnson E.W., Some Results on Almost Principal Element Lattices, Period. Math. Hungar, 31 (1995) 33-42.

[2] Anderson D.D., Abstract Commutative Ideal Theory without Chain Condition, Algebra Universalis, 6 (1976) 131-145.

[3] Anderson D.F. and Livingston P.S., The Zero Divisor of a Commutative Ring, J. of Algebra, (1999) 434-447.

[4] Dilworth R.P., Abstract Commutative Ideal Theory, Pacific Journal of Mathematics 12 (1962) 481-498.

[5] Eslahchi Ch. and Rahimi A.M., The k-Zero-Divisor Hypergraph of a Commutative Ring, Int. J. Math. Math. Sci. Art. 50875 (2007) 15.

[6] Beck I., Coloring of Commutative Rings, J. of Algebra, (1988) 208-226.

[7] Selvakumar K. and Ramanathana V., Classification of non-Local Rings with Genus One 3-zero-divisor Hypergraphs, Comm. Algebra, (2016) 275-284.

[8] Akbari S. and Mohammadian A., On the Zero-Divisor Graph of a Commutative Ring, J. Algebra, (2004) 847-855.

[9] Elele A.B. and Ulucak G., 3-Zero-Divisor Hypergraph Regarding an Ideal, 7 th International Conference on Modeling, Simulation, and Applied Optimization (ICMSAO), 2017.

[10] Badawi A., On 2-absorbing Ideals of Commutative Rings, Bull. Austral. Math. Soc.,75 (2007) 417-429.

Cumhuriyet Science Journal
CSJ

e-ISSN: 2587-246X
ISSN: 2587-2680

Cumhuriyet Sci. J., Vol.40-4 (2019) 802-812

Purification and characterization glutathione S-transferase enzyme from quail (Coturnix, coturnix japonica) heart and investigation the effect of some metal ions on enzyme activity

***Barzan Mirza AHMED*[1], *Yusuf TEMEL*[2], *Mehmet ÇİFTCİ*[1,*]**

[1]*Bingol University, Department of Chemistry, Arts and Science Faculty, Bingol, TURKEY*

[2]*Bingol University, Solhan Vocational School of Health Services, Bingol, TURKEY*

Received: 12.12.2018; Accepted: 13.05.2019 *http://dx.doi.org/10.17776/csj.496122*

Abstract. In this study glutathione S-transferase enzyme (EC: 2.5.1.18) from the heart of japonica quail was purified with 34.0 EU/mg specific activity, 10.44% purification yield and 78.29 purification folds and characterized. Purification processes are consist of three steps, firstly homogenate was prepared, and then ammonium sulfate precipitation was performed and finally glutathione-agarose gel affinity column chromatography was performed. To check the purity of GST enzyme used SDS-PAGE method. Then the M.W calculated at approximately 26.3 kDa by SDS-PAGE method. Enzymatic activity was determined spectrofotometrically according to Beutler`s method at 340 nm. Also characterizations study carry out, and the results obtained are stability-pH = 9.0 in Tris/HCL buffer, optimum pH = 8.0 in Tris/HCl buffer, optimum temperature 60 °C, optimum ionic strength was 1.2 M in Tris/HCl buffer. And kinetic studies performed for GST enzyme purified from quail heart by used both glutathione and 1-chloro 2,4-dinitrobenzen as substrate. K_M and V_{max} values are determined as 1.642 mM and 0.502 EU/mL respectively for GSH substrate and 3.880 mM and 0.588 EU/mL respectively for CDNB substrate. In addition, the effect of some metal ions (Cu^{2+}, Cd^{2+}, Fe^{2+}, Fe^{3+} Zn^{2+}, Ag^{+}, Co^{2+}, and Ti^{1+}) were investigated on the GST enzyme activity *in vitro*.

***Keywords*:** Quail, Heart, Glutathione S-transferase, Purification, Characterizations, Metal Ions.

Glutatyon S-transferaz enziminin Japon bıldırcın (Coturnix, coturnix japonica) yürek dokusundan saflaştırılması, karakterizasyonu ve bazı metal iyonlarının enzim aktivitesi üzerine etkilerinin araştırılması

Özet. Bu çalışmada japon bıldırcın yürek dokusundan glutatyon S-transferaz enzimi (EC: 2.5.1.18) 34.0 EU/mg spesifik aktivite ile % 10.44 verimle ve 78.29 kat saflaştırılmıştır. Saflaştırma işlemi üç aşamada gerçekleştirilmiştir. Bu aşamalar homojenatın hazırlanması, amonyum sülfat çöktürmesi ve glutatyon-agaroz jel afinite kolon kromatografisinden oluşmaktadır. Bıldırcın yürek dokusu GST enziminin saflığını test etmek için SDS-PAGE yöntemi kullanılmıştır. Daha sonra SDS-PAGE yöntemi ile enzimin alt birimlerinin molekül kütlesi yaklaşık olarak 26.3 kDa olarak hesaplanmıştır. Enzimatik aktivite 340 nm'de Beutler yöntemine göre spektrofotometrik olarak belirlenmiştir. Yapılan karakterizasyon çalışmalarında enzyme ait optimum pH Tris/HCl tamponu pH = 8.0, stabil pH Tris / HCL tamponu pH = 9.0, optimum sıcaklık 60 °C, optimum iyonik şiddeet Tris/HCl tamponu 1.2 M olarak bulunmuştur. GST enzimi substrat olarak hem glutatyon hem de 1-kloro 2,4-dinitrobenzen kullanmaktadır. Yapılan kinetik çalışmalarda GST enzimi için K_M ve V_{max} değerleri, GSH substratı için sırasıyla 3.880 mM ve 0.588 EU/mL, CDNB substrat için sırasıyla 1.642 mM ve 0.502 EU/mL

* Corresponding author. *Email address:* *mciftci@bingol.edu.tr*

bulunmuştur. Buna ek olarak bazı metal iyonlarının (Cu^{2+}, Cd^{2+}, Fe^{2+}, Fe^{3+} Zn^{2+}, Ag^{+}, Co^{2+} ve Ti^{1+}) GST enzim aktivitesi üzerine *in vitro* etkileri araştırılmıştır.

***Anahtar Kelimeler*:** Bıldırcın, Yürek, Glutatyon S-Transferaz, Karakterizasyon, Metal iyonları.

1. INTRODUCTION

Glutathione S-transeferase (GST-EC: 2.5.1.18) isozymes consist of approximately 223 amino acids are ubiquitously distributed from the nature, can be detect in both prokaryotes and eukaryotes [1]. Being found in organism as diverse as microbes, insect, plants, fish, birds and mammals [2-3]. These cellular detoxification enzymes exist mostly from kidney and liver as well as intestine also present in other tissue such as heart, brain and erythrocyte. GST isoenzymes protect the cell against the harmful effects of toxic chemicals. GST isoenzymes are important antioxidant enzymes that protect cells from the toxic effects of reactive oxygen species (ROS) by detoxifying exogenous and endogenous substances [4]. Transferase enzymes catalyze different types of reactions. Some of these enzymes can catalyze the conjugation of the reduced glutathione (GSH) with compounds containing the electrophilic center. This reaction takes place with the formation of a thioether bond between the GSH and the xenobiotic sulfur atom [5]. A number of GST isoenzymes reveal some GSH-dependent catalytic activities, such as reduction of organic hydroperoxides[6], and isomerization of different types unsaturated compounds [7].

GSTs can catalysis the conjugation of glutathione to different electrophiles and reverse conjugation of various electrophiles compounds with glutathione [8]. By lowering activation energy and increase speed of conjugation that participates in deprotonation of GSH to GS by a tyrosine residue in which as the base catalyst function. The first step from the mercapturic acid pathway is the glutathione conjugation due to elimination of xenobiotic compounds. Evolved GSH by GSTs and are abundant throughout most life forms. Because of GST response of detoxifying both endogenously and exogenously derived toxic compounds [9]. GST isoenzymes are divided into two distinct super-family members: the cytosolic family members and membrane bound microsomal based upon the similarity of amino acid sequence. In which five classes are cytosolic (designated α, μ, π, θ, and κ), so two are membrane-band. The cytosolic family of GSTs are subject to genetic significantly polymorphisms in human populations [10].

Glutathione S-tansferase GSTs have been purified and characterized from different sources such as rat brain cytosol [11], humane kidney [12], human placental tissues [13], and rainbow trout hepatocytes [14], liver of the freshwater fish Monopterus albus [15], rat liver [16], turkey liver [17], muscle tissue of Van Lake fish [18] and quail liver [19]. There have been used different techniques such as the affinity, ion exchange, hydrophobic, and gel filtration chromatography to purification.

Nowadays from the world our environmental was contaminated and polluted through the metal refuses, agriculture practice, industrials, commercials waste and human activity every day. In which any substances such as (drugs, metal ions, poisons, etc.) form *in vivo* and *in vitro* of the living organism cell can inhibition or activation of enzymes. Living organisms are exposed to heavy metals in nature. Nowadays, the toxic effects of heavy metals on living things have been intensively studied by researchers, and this has become a central research area in the toxicological field [20-22], So far, there were not found any encountered study on the purification and characterization glutathione S-tanasferase from the heart tissue of japanese quail and the effect of (Cu^{2+}, Cd^{2+}, Fe^{2+}, Fe^{3+} Zn^{2+}, Ag^{+}, Co^{2+}, and Ti^{+}) metal ions on the quail heart GST activity.

The objective of this study was purification and characterization of GST enzyme from the quail heart and investigation of the any possible effects of metal ions on enzyme activity *in vitro*.

2. MATERIALS AND METHODS

2.1. Materials

Ammonium sulfate, sodium chloride, sodium hydroxide, potassium phosphate, EDTA ethylene diamine tetra acetic acid, Tris (Trihydroxy methyl amino methane), isopropanol, β-mercaptoethanol,

acrylamide, TEMED (N, N, N, N tetramethylethylenediamine), hydrochloric acid, phosphoric acid, glycerin, ethanol, methanol, acetic acid, GSH, glutathione-agarose gel (Sigma company), bromothymol blue, sodium acetate, potassium hydroxide, glycine amino acid and trichloroacetic acid (Merck company), SDS (sodium dodecyl sulfate), Commasie Brilliant Blue G-250, Commasie Brilliant Blue R-250 (Fishcer Scientific), Ammonium persulfate (Chem Solute Bio).

2.2. Methods

2.2.1. Preparation of homogenate

The quail heard tissues were supplied fresh from the Bingol University application farm. It was frozen in deep freeze at -20 °C. In the experiments, the frozen heart 4 g was cut into small pieces and suspended in 12 mL of homogenate buffer (50 mM Tris-HCl pH = 7.5) by homoginezer after that the suspention was centrifuged at 13,000 rpm for one hour and perciptate was discarded. These processes carry out at +4 °C.

2.2.2. Activity determination

Enzyme activity was determined according to Habig method [32].

2.2.3. Ammonium sulfate precipitation

Solid ammonium sulfate precipitation was performed at 0% -20%, 30%, 40%, 50%, 60%, 70%, 80%, 90% and 100% to homogenate and the settling interval was determined. According to the method was performed by Green and Hughes [33].

2.2.4. Glutathione agarose affinity column chromatography

Weighted 1 gram of dry glutathione agarose gel and washed by distillated water for some times to remove impurities also dissolved gel in 200 mL distillated water or equilibration buffer and kept it overnight between 2 ºC and 4 ºC. The gel was swollen, the swollen gelatin air was removed by used water tromp then put into the (1 x 10 cm) column and packed via closed system. The column was equilibrate with 10 mM KH_2PO_4, 150 mM NaCl (pH = 7.4) and sample applied to the glutathione-agarose affinity column. Then the column was washed with 10 mM KH_2PO_4, 0.1M KCl, pH = 8.0, until absorbance difference 0.05 at 340nm by spectrofometrically and then gradient elution was performed in 50 mM Tris-HCl and 1.25-10 mM GSH, pH = 9.5, finally the eluates were collected.

2.2.5. Protein determination

Quantitative protein was determined at 595 nm spectrophotometrically by used bovine serum albumin as a standard according to Bradford 1976 method [34].

2.2.6. Sodium dodecyl sulfate polyacrylamide gel electrophoresis (SDS-PAGE)

To control the purity of the GST enzyme, (SDS-PAGE) was performed at 3% to 15%. According to the Laemmli procedure. Also GST molar mass was determined according to the Laemmli method [35].

2.2.7. Determination optimum pH

To determine the optimal pH of the GST enzyme, two different buffers system were used; potassium phosphate with pHs 5.5 to 8.0 and Tris/HCl with pHs 7.5 to 9.0. With appropriate substrate solution, the GST enzyme activity was determined at 340 nm by spectrophotometrically.

2.2.8. Stable pH determination

To determine the GST enzyme pH-stable, two different buffers system were used; potassium phosphate with pHs 5.5 to 8.0 and Tris/HCl with pHs 7.5 to 9.0. The GST enzyme activity measured at 340 nm by spectrofotometrically. % activity were found as against time (days) at 24 hour intervals for 7 days under optimal conditions.

2.2.9. Optimum ionic strength determination

To determine the optimum ionic strength the GST enzyme, two different buffers system were used; KH_2PO_4 prepared with 0.1-1.0 M and Tris /HCl prepared with 0.1-1.4 M with the pH = 8.0 for all solutions. The GST enzyme activity was measured for each solution at 340 nm by spectrofotometrically.

2.2.10. Optimum temperature determination

To determine optimum temperature of GST enzyme was used water bath. The GST enzyme activity was measured increased temperatures at 10, 20, 30, 40, 50, 60, 70, 75 and 80 °C, respectively.

2.2.11. Kinetic study

To determine the K_M and V_{max} values for GSH and CDNB substrates of GST enzyme, the enzyme activity was measured. In this process used at 5 different concentrations of CDNB and constant GSH concentration. Lineweaver-Burk graph plotted with the obtain data. The values of K_M and V_{max} for CDNB substrate were determined by Lineweaver-Burk graph. In the same way, activity measurement with 5 different concentrations of GSH and constant CDNB concentration. Activity measurements was performed under optimal condition [36].

2.2.12. In vitro effects of metal ions

The following concentrations of metal ions selected for this study; Ag^{+} (0.05 - 1.0 mM), Cu^{2+} (0.1 - 1.0 mM), Cd^{2+} (1.0 - 7.5 mM), Fe^{2+} (0.05 - 1.5 mM), Fe^{3+} (0.001 - 0.007 mM), Co^{2+} (0.5 - 2.5 mM), Zn^{2+} (0.5 - 5.0 mM), Ti^{+} (1 - 7 mM) and Pb^{2+} (0.25 - 1.5 mM) were added to the reaction medium, and GST enzyme activity was measured. The absence of metal ions was used as a control (100% activity). Activity (%) - metal ion concentration graph plotted, to determine the IC_{50} value which is the inhibitor concentration to reduce enzyme activity by half. To determine K_i values, 5 different (GSH) substrate concentrations (0.2, 0.5, 1.0, 2.0, 3.0 mM) and 3 different inhibitor (metal ions) solutions Cu^{2+}, Ag^{+} and Cd^{2+} were added to the reaction cuvette. Lineweaver-Burk graphs (1/V vs 1/[S]) were drawn and K_i constant were calculated.

3. RESULTS

The GST enzyme was purified from the quail heart with the 34.0 EU/mg specific activity, 10.44% purification yield and 78.29 purification folds. The purity of the quail heart GST enzyme was checked by SDS-PAGE (Figure 1). The molecular weight of GST enzyme was determined as approximately 26.3 kDa by SDS-PAGE method (Figure 2).

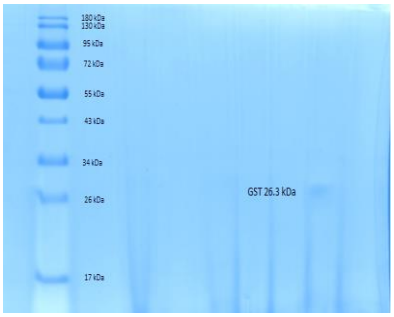

Figure 1. SDS-PAGE photograph: show a single band of GST enzyme.

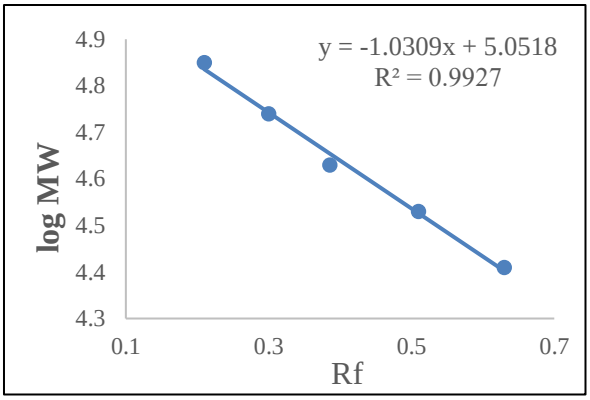

Figure 2. Rf-log M.W calibration curve to determine M.W of GST enzyme.

The pH stability for GST enzyme was determined as 9.0 in Tris-HCl buffer (Figure 3). The optimum pH for GST enzyme was determined as pH = 8.0 in Tris-HCl buffer (Figure 4). Optimum temperature for GST enzyme was determined by measuring the activity for GST enzyme in different temperature started from 0 °C to 80 °C. The obtained result showed the optimum temperature 60 °C (Figure 5). The effect of ionic strength on GST enzyme from the quail heart tissue was determined by the measured GST enzyme activity in 0.1 M to 1.0 M KH_2PO_4 and 0.1 M to 1.4 M Tris /HCl with pH = 8.0 for all solutions. The obtained result showed, the optimum ionic strength 1.2 M Tris/ HCl buffer (Figure 6).

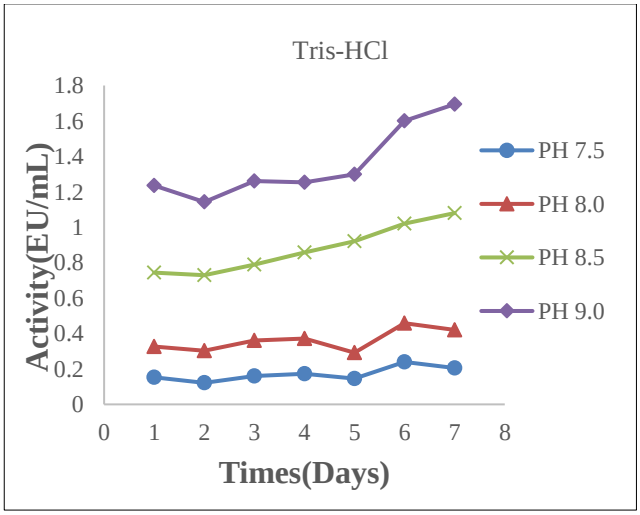

Figure 3. Graphic of stable pH studied with Tris-HCl

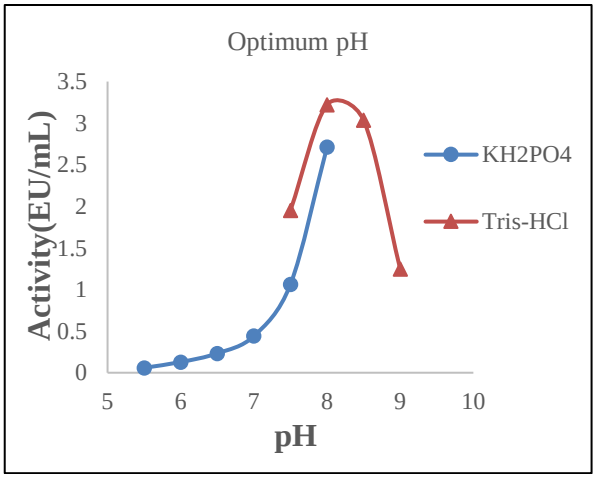

Figure 4. The graphic of optimum pH results.

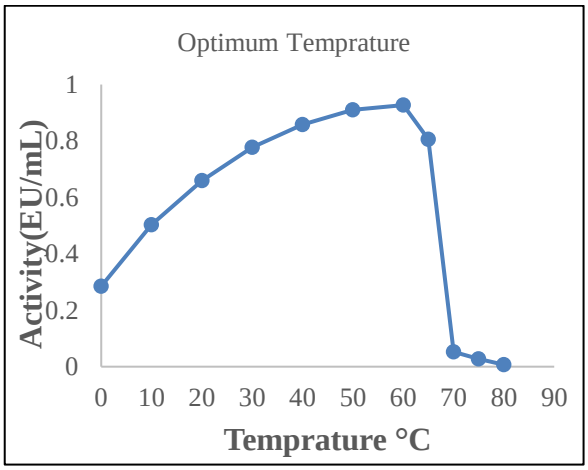

Figure. 5. Result of optimum temperature.

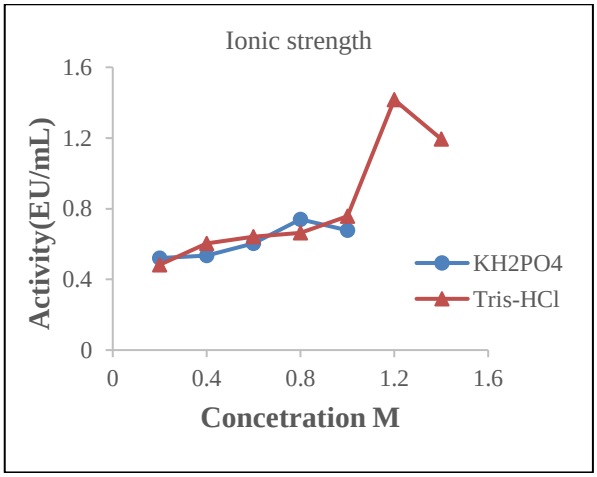

Figure 6. The results of optimum ionic strength (KH_2PO_4 and Tris-HCl buffer).

In addition enzyme kinetic study was performed to determine K_M and V_{max} for glutathione S-transferase purified from the quail heart tissues, and by using both GSH and CDNB as substrate. The results obtained are 1.642 mM and 0.502 EU/mL respectively for GSH substrate (Figure 7), and 3.880 mM and 0.588 EU/mL respectively for CDNB substrate (Figure 8).

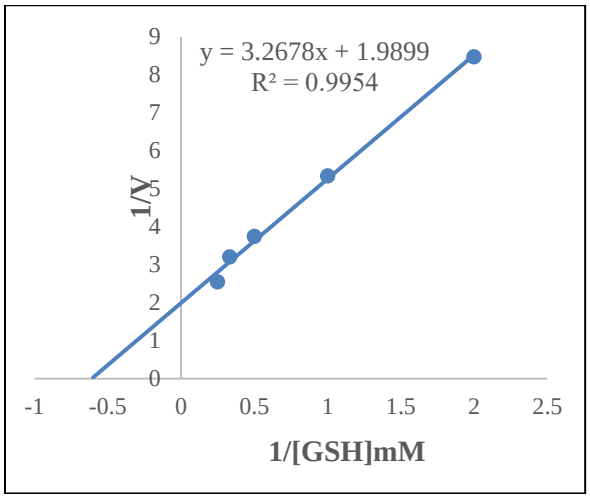

Figure 7. Lineweaver-Burk graphic with five different [GSH].

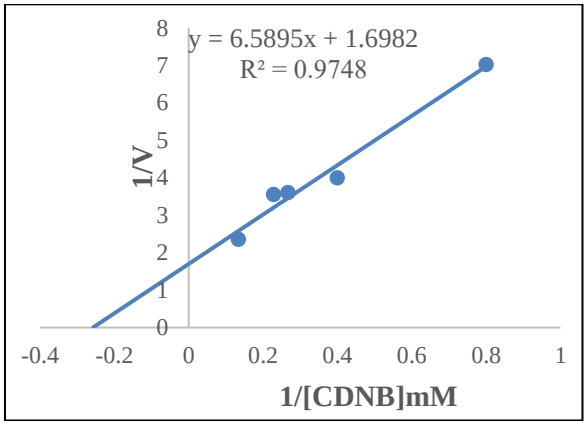

Figure 8. Lineweaver-Burk graphic with five different [CDNB].

The effect of metal ions on the GST enzyme activity were determined. Results show that Co^{2+}, Fe^{2+}, Fe^{3+}, Ti^{+}, Zn^{2+} metal ions increased GST enzyme activity. Those metal ions indicated activator for GST enzyme, (an example Co^{2+} ion, Figure 9), But Cd^{2+}, Cu^{2+}, Ag^{+} have negative effect on the GST enzyme cause the decreased enzyme activity, that indicated those are inhibitors for GST enzyme from quail heart (Figure 10, Figure 11).

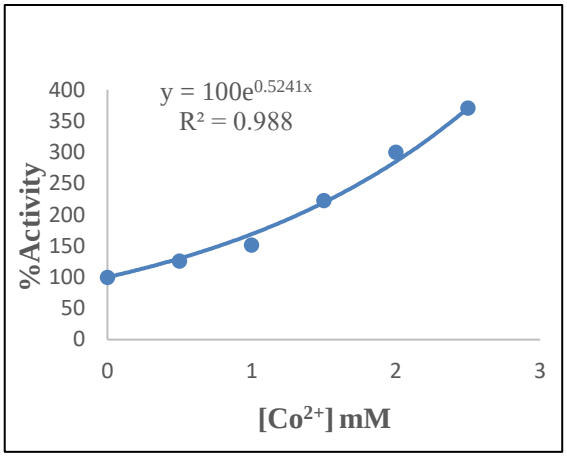

Figure 9. Effect of Co^{2+} on the GST enzyme activity.

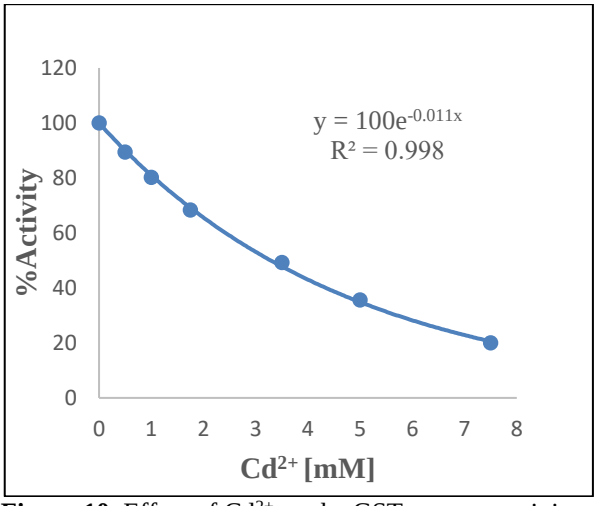

Figure 10. Effect of Cd^{2+} on the GST enzyme activity.

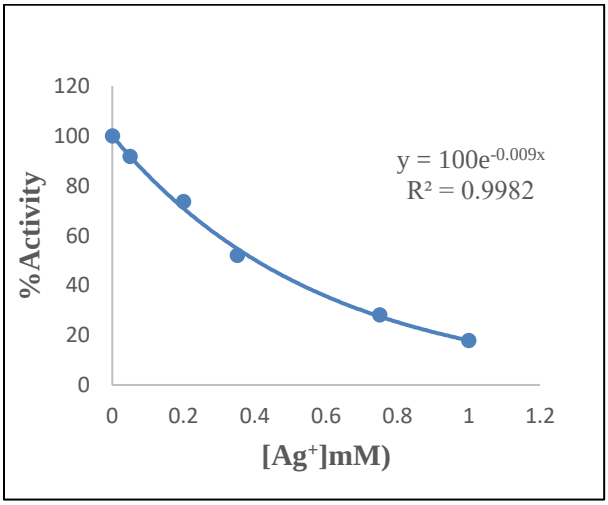

Figure 11. Effect of Ag^{+} on the GST enzyme activity.

4. DISCUSSION

In this study, glutathione S-transferase enzyme for the first time was purified from the japanese quails heart tissue based on the protein purification process with three steps. After purification, characterization studies were carried out. Glutathione agarose affinity column chromatography method was used to purify the GST enzyme. It is available and powerful method because it is an easy process to apply, low cost, less time, single step, potable for bulk amounts of enzymes purified and gives very good purification yields.

GST enzyme purified with specific activity 34.0 EU/mg, purification yield 10.439% and purification fold 78.296 folds in which compared with specific activity of 23.7 EU/mg, 11% yield, 1107-fold purification from the human placental tissues[13], specific activity 1.250 x 10^{-6} unit/mg protein, 56.43% yield and 419.88 fold from the rat liver[16], specific activity of 164.31 U/mg, a yield of 45%, with 252.7-folds from the turkey liver[17], specific activity 29,304 EU / mg protein, purification fold 316,11 folds and purification yield 37.36% from the liver of the Van Lake fish[23], and specific activity of 35,583 EU/mg protein, purification fold 301.5-folds, a purification yield 19.07% from the muscle tissue of Van Lake fish[18], in literature.

To check the enzyme purity, the sodium doduecyl sulfate-polyacrylamaide gel electrophorsis (SDS-PAGE) method was used [35]. Then SDS-PAGE were stained and distained and single band was appeared on the gel, it is an evidence to purified enzymes. The same method were used in rat brain cytosol [11], human placenta [13], human hepatoma [25], rainbow trout hepatocytes [14], filarial worms *Setaria cervi* [26], rat liver [16], turkey liver [17], Van Lake fish liver [23], and muscle tissue of Van Lake fish [18]. SDS-PAGE method is suitable and powerful method to check purity of enzymes with good results by less time and easy to work. So calculate the molar mass of GST enzyme by took the R_f-value for standard protein bands and GST enzyme single band, the result value was drawn plot between R_f-value and logarithm molar mass of standard proteins. The molar mass was determined as approximately 26.3kDa for GST enzyme from the heart tissue of japanese quail, in which compared with heterodimers of MW 26.5 kDa and MW 24.5 kDa subunit in human kidney [12], 25 kDa from the human placental tissues [13], 27 kDa in maize (zea mays pioneer hybrid 3906) [27], 26 kDa from the sorghum cereal [28], 26.7 kDa from catfish intestinal mucosa [29], 26 kDa and 24 kDa from the turkey liver [17] and two subunits as 28 kDa and 33.8 kDa from liver of the van lake fish [23] in literature. This comparison illustrates that GST

isoenzymes have the different molar mass and ubiquitous distributed. In which GST molar mass from quail heart near to the GST in human kidney, turkey liver, sorghum cereal than human placental, liver of the Van Lake fish, mazie (zea mays pioneer hybrid 3906), and catfish intestinal mucosa.

After purification of GST enzyme from quail heart tissues, characterization study was carry out to determine the optimum pH, optimum ionic strength, optimum temperature, pH-stability. Firstly, pH-stability was determined as pH = 9.0 in the Tris/HCl buffer. The result was compared with stable-pH =7.5 in Down syndrome (DS) and normal children erythrocytes [30], stability-pH = 8.5 in turkey liver [17] and stable-pH = 5.5 liver of the Van Lake fish [23], result was closest to the stable pH in turkey liver in literature**,** pH-stability is most important point during the study on all enzymes because of keeping enzymes in stable pH help to have a best results and continues study for a longest interval on target enzymes, since enzymes are not denatured, loss activity and biological functions to a long time. By continuing the study optimum pH was determined as 8.0 in Tris-HCl buffer. Compare to optimum pH = 7.5 – 8.0 from the maize (zea mays pioneer hybrid 3906) [27], optimum pH = 7 from the Down syndrome (DS) and normal children erythrocytes [30], optimum pH = 7.3 from the turkey liver[17] and optimum pH = 7.8 from the liver of the Van Lake fish [23] in the literature in which result was similar to the optimum pH of GST from the liver of the Van Lake fish and maize (zea mays pioneer hybrid 3906). In the living organism cell each enzyme works in specific pH called optimum pH in which it has maximum activity. Since pH is the important factor that have influence on enzyme activity at below and above optimum pH all enzymes loss activity and denatured especially in high acidic and basic medium.

Also temperature is another factor that have effect on enzyme activities, like all reaction enzyme activities increase with increase temperature but for enzyme increasing temperature is limited because at very high temperature all enzymes are denatured this is the lose biological function and lose enzymes activity. In this study optimum temperature was determined as 60 ºC. In which above that degree GST loses activity until the 80 ºC the activity becomes zero. Compared with optimum temperature in range 30 °C– 55 °C from the liver of the freshwater fish Monopterus albus [30], optimum temperature between 25-35ºC from the rat livers [31], optimum temperature 50 °C in turkey liver [17] and optimum temperature 30 °C from the liver of the Van Lake fish [23] in the literature in which result nearest to the optimum temperature of GST from the turkey liver and liver of the freshwater fish Monopterus albus. In continuous study, the effect of ionic-strength on glutathione S-transferase was studied as 1.2 M of Tris-HCl buffer pH = 8.0. The optimum ionic strength for GST 600 mM turkey liver [17], 100 mM in liver Van Lake fish [23], our results were found to be different compared to the literature, the quail heart GST enzyme has maximum activity at that concentration.

In addition, kinetic study was performed to determine K_M and V_{max} for glutathione S-transferase enzyme from the quail heart tissues. The results obtained are 1.642 mM and 0.502 EU/mL respectively for GSH substrate and 3.880 mM and 0.588 EU/mL respectively for CDNB substrate. The results is compare with K_M 0.085 mM for GSH and 2.0 mM for CDNB from the human placental tissues [12], K_M and V_{max} for CDNB are 0.28 mM and 15.68 EU/ml, respectively from the liver of the freshwater fish Monopterus albus [15], $\boldsymbol{K_M}$ values 0.786 mM for GSH and 0.205 mM for CDNB from human erythrocyte [30], $\boldsymbol{K}_M$ and $\boldsymbol{V}_{max}$ values 0.154 mM, 1.803 EU/mL for GSH and 0.380 mM, 2.125 EU/mL for CDNB substrate, respectively for GST enzyme in turkey liver [17], K_M and V_{max} determined as 0.060 mM, 0.562 EU / mL for GSH and 0.891 mM, 1.245 EU / mL for CDNB, respectively from the liver of the Van Lake fish [23], K_M and V_{max} determined as 0.53mM, 1.88 EU/mL for GSH and 1.59 mM, 5.58 EU/mL for CDND, respectively from the muscle tissue of Van Lake fish [18], in the literature. Results illustrated that the quail heart GST enzyme has low affinity for CDNB substrate than GSH substrate because the K_M value for CDNB substrate greater than K_M value for GSH substrate. The result was similar to the GST enzyme in liver and muscle tissue of the Van Lake fish, turkey liver and human placental tissues, but different from human erythrocyte. Also the results illustrated that the V_{max} for both GSH and CDNB are closest value but V_{max} for CDNB substrate was greater than V_{max} for GSH substrate it mean the CDNB substrate concentration has the more influence on the rate of reaction that catalyzed by GST enzyme than GSH substrate concentration, in which results was similar to the GST from turkey liver, muscle tissue of Van Lake fish and liver of the Van Lake fish.

Recent research has been found that various metal ions and organic compounds cause toxicity on enzyme activities purified from different sources [37-41]. The effect of metal ions on the GST enzyme were determined. (Co^{2+}, Fe^{2+}, Fe^{3+}, Ti^{+}, Zn^{2+}) increase activity that indicated those metal ions are activator But (Cd^{2+}, Cu^{2+}, Ag^{+}) decreased enzyme activity that indicated those are inhibitors. Further studied determined the types of inhibition for GST enzyme from quail heart, results obtained Cd^{2+} and Cu^{2+} ions were non-competitive inhibitors, because K_M is constant but V_{max} changed (Figure 12*)* as an example for Cd^{2+}, also for Ag^{+} ion was competitive inhibitor, since K_M is constant and V_{max} was changed (Figure 13) also K_i constant and IC_{50} values were determined for inhibitor metal ions that are the most suitable parameters for seeing inhibitor effects. Which in vitro studies reviled that the enzyme activity was inhibited by Cd^{2+}, Cu^{2+}, and Ag^{+}. IC_{50} values and K_i constants were 0.57±0.236 mM for Cd^{2+}, 0.0028 mM, 0.63±0.224 mM for Cu^{2+} and 0.382 mM, 0.27±0.098 mM for Ag^{+}, respectively (Table 2). In recent studies, the effects of various heavy metals on different enzyme activities have been investigated. In a recent study, have been investigated the inhibitor effects of Ag^{+}, Cd^{2+}, Fe^{3+}, Cu^{2+} and Zn^{2+} ions on turkey liver mitochondrial thioredoxin reductase enzyme [42]. it was reported in different study that Fe^{2+}, Pb^{2+}, Cd^{2+}, Ag^{+} and Zn^{2+} ions inhibitory effect on rat erythrocytes G6PD enzyme activities [43].

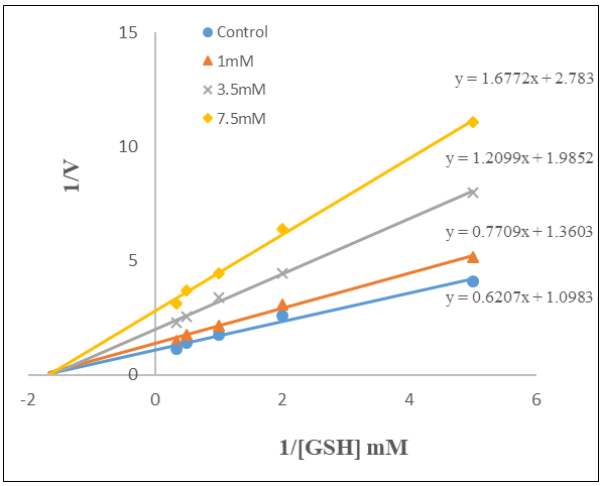

Figure12. Lineweaver-Burk graph of five different GSH concentrations for the determination of K_i in three different concentration of Cd^{2+}.

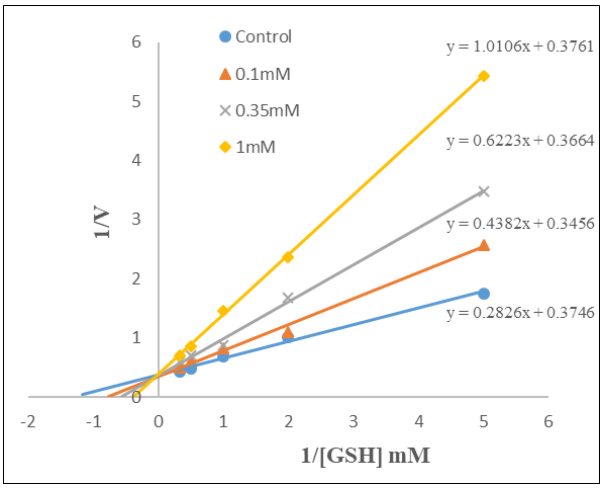

Figure. 13. Lineweaver-Burk graph of five different GSH concentrations for the determination of K_i in three different concentration of Ag^{+}.

Table 1. Quail`s heart tissue Glutathione S-transferase purification results table.

Samples	Volume mL	Activity EU/mL	Total activity EU	Protein content mg/mL	Total protein mg	Specific activity EU/mg	Purification Yield%	Purification fold
Homogenate	10	0.632	6.319	1.455	14.55	0.434	100	1
Ammonium sulfate precipitation	2	1.753	3.506	1.189	2.378	1.474	55.494	3.395
Pure enzyme	2	0.329	0.659	0.0097	0.0194	34.0	10.439	78.296

Table 2. K_i and IC_{50} values obtained from regression analysis graphs for quail heart GST in the presence of different metal ions concentration

Heavy metal	IC_{50} (mM)	K*i*(mM)	Inhibition type
Cd^{2+}	3.127	0.57±0.236	Non-competitive
Cu^{2+}	0.0028	0.63±0.224	Non-competitive
Ag+	0.382	0.27±0.098	Competitive

5. CONCLUSION

In this study, glutathione S-transferase enzyme for the first time was purified from the japanese quails heart tissue based on the protein purification process with three steps. After purification, characterization studies were carried out. In addition the effect of metal ions on the GST enzyme activity were determined. Our study showed that Co^{2+}, Fe^{2+}, Fe^{3+}, Ti^{+}, Zn^{2+} metal ions increased GST enzyme activity, while Cd^{2+}, Cu^{2+} and Ag^{+} ions had an inhibitory effect on enzyme activity.

REFERENCES

[1] Booth J., Boyland E., Sims A.P., An enzyme from rat liver catalysing conjugations with glutathione, Biochem. J., 79 (1961) 516-524.

[2] Sherratt P.H., Hayes J., Glutathione S-Transferases Enzyme System That Metabolise Drugs and Other Xenobiotics. Chichester, UK ., (2001) 1-578.

[3] Hayes J.D., Pulford D.J., The glutathione S-transferase supergene family: regulation of GST and the contribution of the lsoenzymes to cancer chemoprotection and drug resistance, part I. Critic. Rev. Biochem. Mol. Biol., 30 (1995) 445-520.

[4] George S.G., Enzymology and molecular biology of phase II xenobiotic-conjugating enzymes in fish, Aquatic Toxicol. (1994) 37-85.

[5] Mannervik B., Alin P., Guthenbergg C., Jensson H., Tahir M.K., Warholm M., Jornvall H., Identification of three classes of cytosolic glutathione transferase common to several mammalian species: correlation between structural data and enzymatic properties, Proceed National Acad. Sci USA 82 (1985) 7202-206.

[6] Ketterer B., Meyer D.J, Taylor J.B., Pemble S., Coles B., Fraser G., GSTs and protection against oxidative stress. In Glutathione S.Transferase and Drug Resistance, Taylor Francis Bristol, 1990; pp 97-109.

[7] Benson A.M., Talalay P., Keen J.H., Jakoby W.B., Relationship between the soluble glutathione-dependent delta 5-3-ketosteroid isomerase and the glutathione S-transferases of the liver, Proceed National Acad. Sci., 74 (1977) 158-162.

[8] Yu S.J., Insect glutathione S-transferases, Zoological Studies, 35-1 (1996) 9-19.

[9] Cancado G.M., De Rosa V.E., Fernandez J.H., Maron L.G., Jorge R.A., Menossi M., Glutathione S-transferase and aluminum toxicity in maize, Functional Plant. Biol., 32 (2005) 1045–1055.

[10] Townsend D.M., Tew K.D., The role of glutathione-S-transferase in anti-cancer drug resistance, Oncogene 22 (2003) 7369-7375.

[11] Senjo M., Ishibashi T., Purification and characterization of glutathione S-transferase from rat brain cytosol identification of four isozymes and evidence for absence of the Ya subunit, Biomed. Res., 7 (1986) 19-26.

[12] Singh S.V., Leal T., Ansari G.A., Awasthi Y.C., Purification and characterization of glutathione S-transferases of human kidney, Biochem. J., 246 (1987) 179-186.

[13] Kwak S.J, Park S.C., Purification and Characterization of Glutathione S-transferase π from Human Placental Tissues, Seoul J. Med., 29 (1988) 107-118.

[14] Riol M.M., Valinas M.N., Fernandez M.G., Lopez M.P., Glutathione S-transferases from rainbow trout liver and freshly isolated hepatocytes: purification and characterization, Comp. Biochem. Physiol Part C: Toxicol. Pharmacol., 128 (2001) 227-235.

[15] Huang Q., Liang L., Wei T., Zhang D., Zeng Q.Y., Purification and partial characterization of glutathione transferase from the teleost Monopterus albus. Comp Biochem Physiol Part C: Toxicol Pharmacol 147 (2008) 96-100.

[16] Jassim H.A., Ameen F.Z., Al-Jumaily E.F.A., Isolation And Purification Of Glutathione S-Transferasefrom Rat Liver, J Al-Nahrain Univ. Sci., 12 (2009) 137-144.

[17] Akkemik E., Taser P., Bayindir A., Budak H., Ciftci M., Purification and characterization of glutathione S-transferase

from turkey liver and inhibition effects of some metal ions on enzyme activity, Environ. Toxicol. Pharmacol. 34 (2012) 888-894.

[18] Aksoy M., Ozaslan M., Kufrevioglu O., Purification of glutathione S-transferase from Van Lake fish (Chalcalburnus tarichii Pallas) muscle and investigation of some metal ions effect on enzyme activity. J Enzyme Inhib. Med. Chem. 31 (2016) 546-550.

[19] Temel Y., Koçyigit U.M., Taysı M.Ş., Gökalp F., Gürdere M.B., Budak Y., Çiftci M., Purification of glutathione S-transferase enzyme from quail liver tissue and inhibition effects of (3aR, 4S, 7R, 7aS)-2-(4-((E)-3-(aryl) acryloyl) phenyl)-3a, 4, 7, 7a-tetrahydro-1H-4, 7-methanoisoindole-1, 3 (2H)-dione derivatives on the enzyme activity, J. Biochem. Mol. Toxicol. 32 (2018) e22034.

[20] Krewski D., Yokel R.A., Nieboer E., Borchelt D., Cohen J., Harry J., Rondeau V., Human health risk assessment for aluminium, aluminium oxide, and aluminium hydroxide, J. Toxicol. Environ. Health Part B 10 (2007) 1-269.

[21] Kucuk M., Gulcin I., Purification and characterization of the carbonic anhydrase enzyme from Black Sea trout (Salmo trutta Labrax Coruhensis) kidney and inhibition effects of some metal ions on enzyme activity, Environ. Toxicol. Pharm. 44 (2016) 134-139.

[22] Verstraeten S.V., Aimo L., Oteiza P.I., Aluminium and lead: molecular mechanisms of brain toxicity, Arch. Toxicol., 82 (2008) 789-802.

[23] Ozaslan M.S., Ciftci M., Purification of glutathione S-transferase from Van Lake fish (Chalcalburnus tarichii Pallas) liver and investigation of some metal ions effect on enzyme activity. J. Enzyme İnhib. Med. Chem., 31 (2014) 546-550.

[24] Laemmli U.K., Cleavage of structural proteins during assembly of head of bacteriophage T4. Nature 227 (1970) 680–85.

[25] Dierickx P.J., Purification and characterization of glutathione S-transferase from the human hepatoma derived PLC/PRF/5 cell line, Biomed. Res., 10 (1989) 301-306.

[26] Ahmad R., Srivastava A. K., Walter R.D., Purification and biochemical characterization of cytosolic glutathione-S-transferase from filarial worms Setaria cervi, Comp. Biochem. Physiology Part B: Biochem. Mol. Biol., 151 (2008) 237-245.

[27] Fuerst E.P., Irzyk G.P., Miller K.D., Partial characterization of glutathione S-transferase isozymes induced by the herbicide safener benoxacor in maize, Plant Physiol. 102 (1993) 795-802.

[28] Gronwald J.W., Plaisance K.L., Isolation and Characterization of Glutathione S-Transferase Isozymes from Sorghum, Plant Physiol. 17-1(1998) 877-892.

[29] Gadagbui B.K., James M.O., Activities of affinity-isolated glutathione S-transferase (GST) from channel catfish whole intestine, Aquatic Toxicol., 49 (2000) 27-37.

[30] Hamed R.R., Maharem T.M., Abdel-Meguid N., Sabry G.M., Abdalla A.M., Guneidy R.A., Purification and biochemical characterization of glutathione S-transferase from Down syndrome and normal children erythrocytes: A comparative study, Res. Develop. disabilities 32 (2011) 1470-1482.

[31] Lebda M., Taha N., Noeman S., Korshom M., El-Wahab Mandour, A. Purification and Characterization of Glutathione-S-Transferase from Rat′ s Liver: Effect of Carbon Tetrachloride and Camel′ s Milk, J. Chromat. Separation Techniq, 3-4 (2012) 2-8.

[32] Habig W.H., Pabst M.J., Jakoby W.B., Glutathione S-transferases the first enzymatic step in mercapturic acid formation, J. Biol. Chem. 249 (1974) 7130-7139.

[33] Wingfield P., Protein precipitation using ammonium sulfate, Current Prot. Prot. Sci., 53 (2001) A- 3F.

[34] Bradford M.M., Rapid and sensitive method for the quantitation of microgram

quantities of protein utilizing the principle of protein-dye binding, Anal. Biochem., 72 (1976) 248-254.

[35] Laemmli D.K., Cleavage of structural proteins during in assembly of the heat of bacteriophage T4. Nature London, 227 (1970) 680-685.

[36] Lineweaver H., Burk D., The determination of enzyme dissocation constants, J. Am. Chem. Soc., 56-3 (1934) 57-685.

[37] Temel Y., Bengü A.Ş., Akkoyun H.T., Akkoyun M.B., Çiftci M., Effect of astaxanthin and aluminum chloride on erythrocyte G6PD and 6PGD enzyme activities in vivo and on erythrocyte G6PD in vitro in rats, J. Biochem. Mol. Tox. 31 (2017) e21954.

[38] Ceylan M., Kocyigit U.M., Usta N.C., Gürbüzlü B., Temel Y., Alwasel S.H., Gulcin I., Synthesis, carbonic anhydrase I and II iso enzymes inhibition properties, and antibacterial activities of novel tetralone-based 1,4-benzothiazepine deriva tives, J. Biochem. Mol. Tox. 31 (2017) e21872.

[39] Bayındır S., Ayna A., Temel Y., Çiftci M., The synthesis of new oxindoles as analogs of natural product 3,3'-bis(indolyl)oxindole and in vitro evaluation for enzyme activity of G6PD and 6PGD, Turk. J. Chem. 42 (2018) 332- 345.

[40] Bayindir S., Temel Y., Ayna A., Ciftci M., The synthesis of N-benzoylindoles as inhibitors of rat erythrocyte glucose-6-phosphate dehydrogenase and 6-phosphogluconate dehydrogenase, J. Biochem. Mol. Tox. 32 (2018) e22193.

[41] Temel Y., Taher S.S.M., Hamza M.A., Shafeeq I.H., Koçyiğit U.M., Çiftci M., Investigation of the Inhibition Effects of Some Metal Ions on Glutathione Reductase Enzyme From Japanese Quail (Coturnix coturnix japonica) Liver, Cumhuriyet Sci. J. 39 (2018) 3679-687.

[42] Temel Y., Küfrevioğlu Ö.İ., Çiftci M., Investigation of the effects of purification and characterization of turkey (Meleagris gallopavo) liver mitochondrial thioredoxin reductase enzyme and some metal ions on enzyme activity, Turk. J. Chem. 41 (2017) 48-60.

[43] Temel Y. and Kocyigit U.M., Purification of glucose-6-phosphate dehydrogenase from rat (Rattus norvegicus) erythrocytes and inhibition effects of some metal ions on enzyme activity, J. Biochem. Mol. Tox. 31 (2017) e21927.

Cumhuriyet Science Journal
CSJ

e-ISSN: 2587-246X
ISSN: 2587-2680

Cumhuriyet Sci. J., Vol.40-4 (2019) 813-818

The Effects of CO_2, N_2, and H_2O Dilutions on NO Formation of Partially Premixed Synthesis Gas Combustion

Suat OZTURK[1,*]

[1]*Department of Electronic and Automation, Zonguldak Vocational School, Zonguldak Bulent Ecevit University, Zonguldak, Turkey*

Received: 21.03.2019; Accepted: 11.11.2019 *http://dx.doi.org/10.17776/csj.543130*

Abstract. One of the main methods to decrease NO emission during the combustion of gases is the use of diluents. This study is interested in the effects of CO_2, N_2, and H_2O dilutions in the adiabatic, turbulent, partially premixed combustion of synthesis gas. The amounts of NO emissions are computationally determined. The results show that NO maximizes at 1.39 of equivalence ratio under humid burning air conditions. The best reductive effect on NO emissions indicates H_2O dilution followed by CO_2 and N_2. The increase in the dilution rates gradationally reduces NO. The rising pressure enhances NO emissions with/without diluters. The increasing inlet air and premixed mixture temperatures raises NO.

***Keywords*:** Synthesis gas, partially premixed, combustion, nitrogen oxide.

Kısmi Önkarışımlı Sentez Gazı Yanmasının NO Oluşumu Üzerinde CO_2, N_2 ve H_2O Seyreltmelerinin Etkileri

Özet. Gazların yakılmasında NO emisyonunu azaltmak için ana metodlardan biri seyrelticilerin kullanımıdır. Bu çalışma sentez gazının adyabatik, turbülanslı, kısmi önkarışımlı yanmasında CO_2, N_2 ve H_2O seyreltmelerinin etkileri ile ilgilenmektedir. NO emisyonlarının miktarları hesaplamalı olarak saptanmıştır. Sonuçlar, nemli yakma havası şartlarında, NO'in, 1.39 ekivalans oranında maksimize olduğunu göstermektedir. NO emisyonları üzerinde en iyi azaltıcı etkiyi CO_2 ve N_2 tarafından takip edilen H_2O seyrelticisi göstermektedir. Seyreltici oranlarındaki artış derecesel olarak NO'i azaltmaktadır. Yükselen basınç seyreltili veya seyreltisiz NO emisyonlarını artırmaktadır. Artan hava ve önkarıştırılmış karışım giriş sıcaklıkları NO'i yükseltmektedir.

***Anahtar Kelimeler*:**, Sentez gazı, kısmi karışımlı, yanma, nitrojen oksit.

1. INTRODUCTION

Synthesis gas (syngas) is a product obtained by gasification process from coal, tire, biomass, or steam reforming from natural gas. It generally consists of different components as H_2, CH_4, CO, CO_2, H_2O, N_2, H_2S, NH_3, and COS depending on fuel source what it is derived of. Synthesis gas is utilized in industrial furnace and high efficiency gas turbines for power generation after post gasification process removing H_2S and other unwanted contaminants. Its wide presence and appropriate combustion characteristics makes synthesis gas a conspicuous option among gas fuels [1, 2].

NO_x emissions forming because of high temperature reactions of N_2 and O_2 in burning air and fuel also continue to be an environmental problem as a pollutant for synthesis gas combustion. NO_x is the sum of mostly NO and NO_2 from greenhouse gases and countries take common

* Corresponding author. *Email address:* *suatozturk@beun.edu.tr*

precautions to reduce these gas releases [3]. NO_x emerges during the combustion by three different ways called thermal, prompt, and fuel. Thermal NO_x begins to be more effective by the reactions of nitrogen and oxygen at temperatures over 1300 ^oC and is defined by the reactions of $N_2 + O \leftrightarrow NO + N$, $N + O_2 \leftrightarrow NO + O$, $N + OH \leftrightarrow NO + H$. The reactions with nitrogen of both carbon and hydrocarbon derivatives form prompt NO_x in fuel-rich areas. Finally, the oxidation of nitrogen and its compounds in fuel causes fuel NO_x [4].

The partially premixed or diffusion combustion methods are largely preferred to obtain lower NO_x and to get rid of flashback caused by high burning velocity of H_2 in combustion devices burning synthesis gases. Furthermore, the gas diluents as N_2, H_2O, and CO_2 are used to decrease flame temperature and NO_x by adding to air, fuel or unburned fuel/air mixtures and also have effects on flame's stability, extinction, propagation, and fuel flammability [5, 6].

Many studies are interested in the production methods of synthesis gas from different sources. There have been a few studies to investigate the combustion and emission characteristics of premixed or non-premixed synthesis gases under different conditions in literature. Park and Kim detected that H_2O and CO_2 dilutions are more effective than N_2 to reduce NO_x emissions [7]. Parka et al. concluded the increased pressure raises NO_x emissions and fuel side N_2 dilution reduces NO_x for coal based synthesis gas [8]. Williams et al. found oxygen up to 22% in CO_2 is beneficial to decrease NO_x [9]. Huang et al. determined the preheating air causes higher NO_x but lower CO emissions [10]. Tian et al. detected the rising N_2 dilution in dry and humid burning air fades NO_x in dry and humid burning air at a non-premixed combustor and its effect rises with humidification of air [11]. Tran et al. showed CO_2 dilution lowers the adiabatic flame temperature and laminar burning velocity for syngas/air mixture [12]. Giles et al. found CO_2 and H_2O are more effective than N_2 in reducing NO and the most effective is H_2O diluent in airstream for counter-flow diffusion flames [13]. Chan et al. determined CO_2 dilution lower flame temperature and increases the specific heat of the premixed methane/air mixture [14]. Zhang et al. concluded the increasing CO_2 dilution reduces the temperature and NO_x [15].

In this study, the mass fractions of NO emitted at the end of partially premixed combustion of synthesis gas derived from waste tires are computationally determined with dilution effects of CO_2, H_2O, and N_2 mixed in the upstream air under different equivalence ratio, pressure, inlet air and premixed fuel/air temperatures by ANSYS software.

2. MATERIALS AND METHODS

The numerical calculations for evaluating NO mass fractions at the end of partially premixed synthesis gas/air combustion are realized in ANSYS R15.0. Fluent in ANSYS is the computational fluid dynamics software that is used to model turbulence, flow, chemical reactions, heat transfer, aerodynamics, hydrodynamics, combustion, etc. It reaches a solution by solving the equations related to the phenomena under defined conditions on meshed field of a physical model created in Fluent. Moreover, computational fluid dynamics software for investigating the combustion case are preferred more by researchers because of its cheaper, easier manipulation, and lesser time consumption with respect to experimental way.

The meshed field of co-axial combustor used for burning synthesis gas/air mixture is given in Figure 1. The mesh of 2D model of the chamber consists of 11800 elements and 12076 nodes. The composition of synthesis gas derived of waste tires is 24% CH_4, 51.8% H_2, 16.9% CO, and 7.3% CO_2 [16].

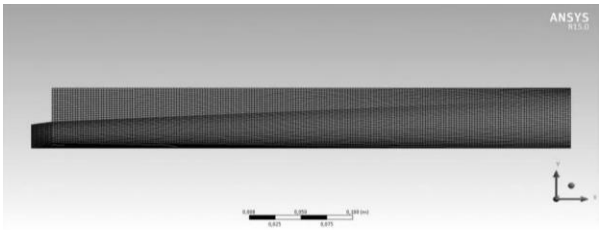

Figure 1. The meshed chamber of co-axial combustor.

The inlet flow rates and temperatures of premixed shale gas/air and air with the dimensions of the co-axial burner are illustrated in Figure 2. If not mentioned any different condition in the text, the premixed shale gas and air enters by 30 m/s rate at 300 K as the upstream air enters into the combustor by 10 m/s rate at 600 K. The air includes humidity at the rate of 1.5%. The diluents of CO_2, H_2O, and N_2 to examine the dilution effects on NO emissions during the combustion are added to the upstream air at changing ratios from 0 to 30%.

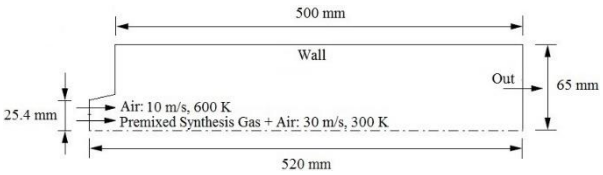

Figure 2. The dimension of co-axial combustor and the inlet flow rates and temperatures [17].

The following model and property options under Fluent Setup are selected for the solutions of partially premixed combustions:

- Viscous Model – k-epsilon (2 eqn), k-epsilon model – standard, Near-Wall Treatment – Standard Wall Functions
- Species Model – Partially Premixed Combustion (Premixed Model – C Equation, Chemical Equilibrium, Adiabatic, and Flame Speed Model – Zimont)
- NO_x Model – On (Thermal, Prompt, and N_2O Intermediate are selected)
- The inlet flow rates, inlet temperatures, and equivalence ratios are entered from Zone of Boundary Conditions, Prompt Tab of NO_x Model and Boundary tab of PDF Table by changing Fuel (shale gas-air mixture) and Oxide (air) ratios for the complete combustions and others.

NO_x emissions are evaluated in terms of NO concentration at the out because NO can be utilized in the place of NO_x consisting of NO and NO_2 owing to an order difference of 10^{-3} mostly between mass fractions of NO and NO_2.

3. RESULTS AND DISCUSSION

The increment of temperature in the combustion chamber always causes to the rise of NO formation at the end of combustion. Figure 3 and 4 represent the contours of temperatures in the co-axial combustor as the equivalence ratio equals to 1 and 1.4. It is seen that there is a difference of 1215 K between the maximum temperatures of ER=1 and 1.4.

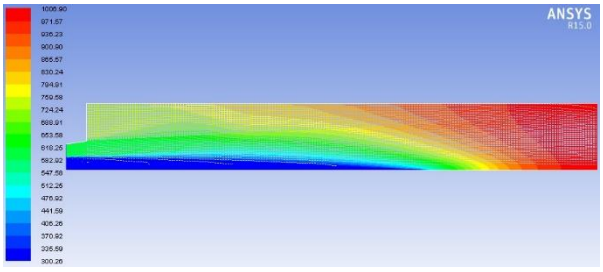

Figure 3. The contours of temperatures during the combustion of synthesis gas at ER=1.

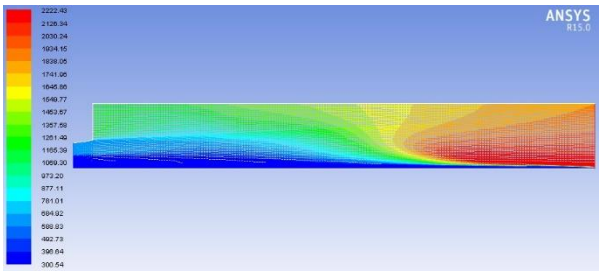

Figure 4. The contours of temperatures during the combustion of synthesis gas at ER=1.4.

NO mass fractions arising at the end of partially premixed combustions of synthesis gases/air at various equivalence ratios (ER) are illustrated in Figure 5. NO roughly reach to the maximum at 1.39 of the equivalence ratio of premixed synthesis gas/air for the all. The highest NO value as 0.000141 kg NO/kg belongs to the synthesis gas/air combustion with non-dilution as expected. It is respectively followed by N_2, CO_2, and H_2O diluted combustions toward to the lowest. It is seen that H_2O dilution indicates the best reductive effect on NO. The difference between NO of the combustion without dilution and 15% N_2, CO_2, and H_2O diluted ones is 13.4%, 14.8%, and 24.8% at ER=1.39. The decrease of the burning air amount in the combustor with rising fuel side equivalence ratio raises causes the incomplete combustion and the descending reaction temperature drops NO emission after a certain point of ER.

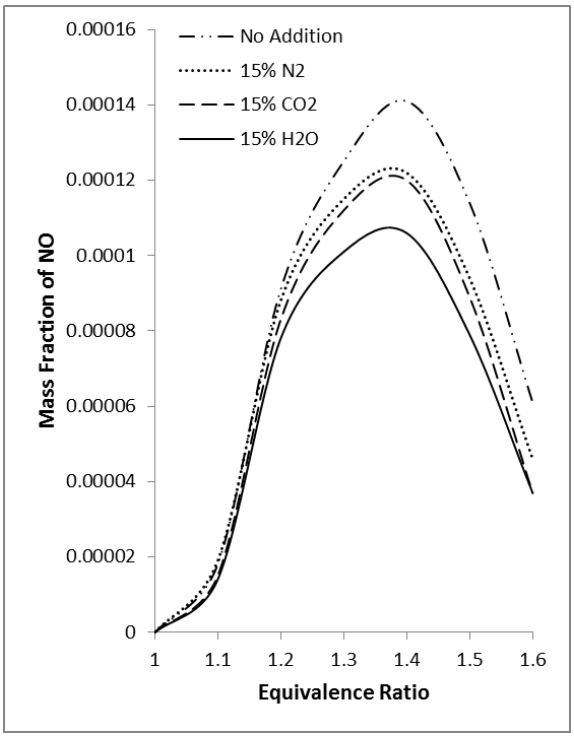

Figure 5. The mass fractions of NO at different equivalence ratios.

The mass fractions of NO with no dilution and the diluted combustions at ER=1.4 is given for different dilution rates in Figure 6. The increase of addition rates for N_2, CO_2, and H_2O in the upstream burning air gradationally decreases NO emissions. The best effect for NO attenuation is provided at H_2O dilution following by CO_2 and N_2. At 10% of addition rate, the reduction rates of NO for N_2, CO_2, and H_2O additions are 8.5%, 9.2%, and 17.7% respectively.

N_2 dilution reduces flame temperature, flame speed, thermal diffusivity and high temperature regions in the combustion chamber. It lowers NO emissions. CO_2 addition indicates more chemical effects than H_2O [11, 18]. The addition of CO_2 in the upstream air raises heat capacity of mixture and decreases combustion rate, reaction kinetics, flame speed, and flame temperature by causing a reductive effect on mixture concentration [14]. H_2O has the high heat holding capacity and drop the reaction temperature, burning velocity, and NO [5].

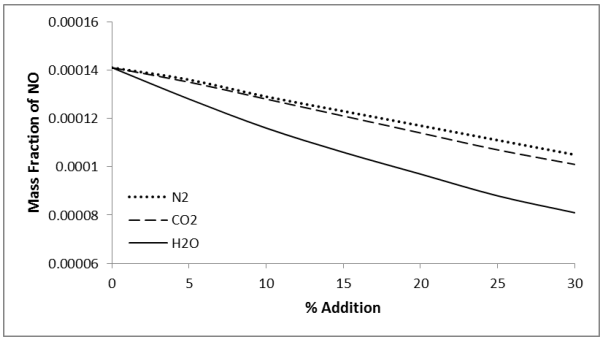

Figure 6. The mass fractions of NO at different N_2, CO_2, and H_2O addition rates.

The pressure effect on NO mass fractions for 15% dilution rate at ER=1.4 is indicated in Figure 7. The pressure gauge is absolute. The pressure has an ascender effect on NO. NO emissions especially become crucial in the combustion chambers of vehicle's engines and combustion systems running at high pressures. NO for non-addition, 15% N_2, 15% CO_2, and 15% H_2O dilution rates between 0 and 10 Atm increase 68.7%, 56.9%, 44.6%, and 56.6%. NO with 15% N_2, CO_2, and H_2O additions diminish 18.9%, 26.4%, and 30.2% in turn at 10 Atm pressure.

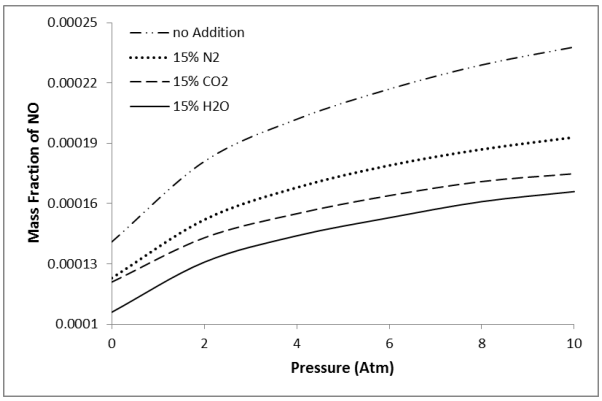

Figure 7. The mass fractions of NO at different pressures.

The effect of air inlet temperature at upstream on NO is given in Figure 8. The increase of air inlet temperature raises the reaction temperature and rates in the combustion chamber and the rising temperature causes NO to rise as well. NO increment between 500 and 800 K is 97.6%, 120.5%, 123.3%, and 110.6% for no addition, 15% N_2, 15% CO_2, and 15% H_2O addition rates. The decrease rates for NO at 800 K temperature for 15% N_2, CO_2, and H_2O additions is 6.7%, 9.1%, and 21.7% respectively.

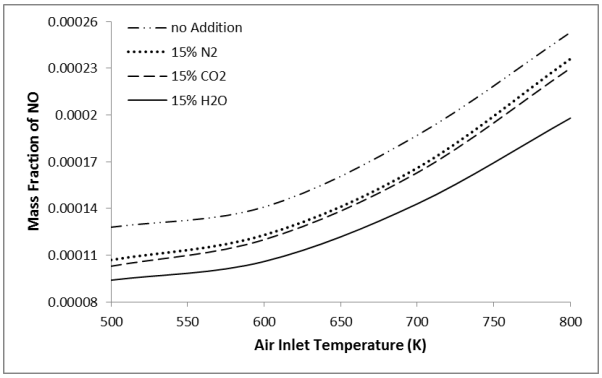

Figure 8. The mass fractions of NO at different air inlet temperatures.

The effect of inlet temperature of premixed synthesis gas/air mixture on NO emissions is presented in Figure 9. The rising inlet temperature of premixed mixture enhances the reaction temperature and implicitly NO emission as the upstream air inlet temperature does. NO increment between 250 and 325 K is 15.5%, 18.1%, 19.2%, and 17.7% for no addition, 15% N_2, 15% CO_2, and 15% H_2O dilution rates. NO decrement with 15% dilutions at 325 K is 24.1% for H_2O and approximately 12.7% for N_2 and CO_2.

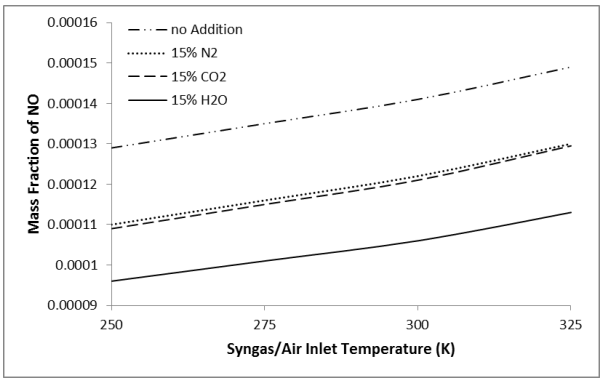

Figure 9. The mass fractions of NO at different synthesis gas/air inlet temperatures.

4. CONCLUSION

The hazardous NO emissions of adiabatic, turbulent, partially premixed combustion of humid air and synthesis gases are computationally investigated at different equivalence ratios, pressures, and inlet temperatures of upstream air and premixed gas/air under the dilutive effects of N_2, CO_2, and H_2O added into the upstream burning air. The following results are obtained:

- NO emission is the maximum at ER=1.39. To decrease NO formation, equivalence ratio needs to be diminished to 1 or lower values. The best reductive effect on NO emission is realized by H_2O addition followed by CO_2 and N_2. H_2O and CO_2 can be given to the combustion chamber by dissociating from the exhaust gases. The difference between NO of the combustion without dilution and 15% N_2, CO_2, and H_2O diluted ones is 13.4%, 14.8%, and 24.8% at ER=1.39.
- The increase in dilution rates of N_2, CO_2, and H_2O in the upstream air reduces NO. NO emission with 10% N_2, CO_2, and H_2O additions decreases 8.5%, 9.2%, and 17.7% in turn. The appropriate dilution ratios must be adjusted by taking consideration the reaction temperatures and system efficiency.
- The pressure increases NO emissions under all the combustion conditions with/without dilution. NO amount at the end of combustion with 15% N_2, CO_2, and H_2O addition into the upstream air decreases 18.9%, 26.4%, and 30.2% respectively at 10 Atm pressure.
- The rising air inlet temperature enhances NO emissions. The increment tendency in NO formation with the air inlet temperatures above 600 K is higher than that of previous temperature values. The inlet air can be heated by exhaust gases for providing the better combustion and ignition. NO decreases 6.7%, 9.1%, and 21.7% with 15% N_2, CO_2, and H_2O additions at 800 K.
- The increasing inlet premixed synthesis gas/air temperature uplifts NO amount. NO increases 15.5%, 18.1%, 19.2%, and 17.7% for the combustion without addition and with 15% N_2, CO_2, and H_2O additions between 250 and 325 K of the inlet temperature. The inlet temperature of premixed synthesis gas/air can be hold at 300 K.

REFERENCES

[1] Zhang Y., Shen W., Zhang H., Wu Y. and Lu J., Effects of Inert Dilution on The Propagation and Extinction of Lean Premixed Syngas/air Flames, Fuel, 157 (2015) 115–121.

[2] Singh D., Nishiie T., Tanvir S. and Qiao L., An Experimental and Kinetic Study of Syngas/air Combustion at Elevated Temperatures and The Effect of Water Addition, Fuel, 94 (2012) 448–456.

[3] Erik N. Y., Shale Gas and Environmental Effects, Cumhuriyet University Faculty of Science, Science Journal (CSJ), 37 (2016) 426–438.

[4] Ozturk S. and Eyriboyun M., NOx Formation in Combustion of Natural Gases Used in Turkey under Different Conditions, J. of Thermal Science and Technology, 30-2 (2010) 95–102.

[5] Li S., Li S., Mira D., Zhu M. and Jiang X., Investigation of Dilution Effects on Partially Premixed Swirling Syngas Flames Using a LES-LEM Approach, Journal of the Energy Institute, 91 (2018) 902–915.

[6] Xie Y., Wang J., Xu N., Yu S. and Huang Z., Comparative Study on The Effect of CO2 and H2O Dilution on Laminar Burning Characteristics of CO/H2/Air Mixtures, International Journal of Hydrogen Energy, 39 (2014) 3450–3458.

[7] Park S. and Kim Y., Effects of Nitrogen Dilution on The NOx Formation Characteristics of CH4/CO/H2 Syngas Counterflow Non-premixed Flames, International Journal of Hydrogen Energy,

42 (2017) 11945–11961.

[8] Parka S., Choib G. M. and Tanahashi M., Combustion Characteristics of Syngas on Scaled Gas Turbine Combustor in Pressurized Condition: Pressure, H2/CO Ratio, and N2 Dilution of Fuel, Fuel Processing Technology, 175 (2018) 104–112.

[9] Williams T. C., Shaddix C. R. and Schefer R. W., Effect of Syngas Composition and CO2-Diluted Oxygen on Performance of A Premixed Swirl-stabilized Combustor, Combust. Sci. and Tech., 180 (2008) 64–88.

[10] Huang M., Zhang Z., Shao W., Xiong Y., Liu Y., Lei F. and Xiao Y., Effect of Air Preheat Temperature on The MILD Combustion of Syngas, Energy Conversion and Management, 86 (2014) 356–364.

[11] Tian Y. Zang S. and Ge B., Experimental Investigation on The Combustion Performance of N2 Dilution in Syngas Non-premix Combustion in Humid Air Conditions, Applied Thermal Engineering, 107 (2016) 560–564.

[12] Tran M. V., Scribano G., Chong C. T., Ng J. H. and Ho T. X., Numerical and Experimental Study of The Influence of CO2 Dilution on Burning Characteristics of Syngas/air Flame, Journal of the Energy Institute, (2018) 1–9, in press.

[13] Giles D. E., Som S. and Aggarwal S. K., NOx Emission Characteristics of Counterflow Syngas Diffusion Flames with Airstream Dilution, Fuel, 85 (2006) 1729–1742.

[14] Chan Y. L., Zhu M. M., Zhang Z. Z., Liu P. F. and Zhang D. K., The Effect of CO2 Dilution on The Laminar Burning Velocity of Premixed Methane/air Flames, Energy Procedia 75 (2015) 3048–3053.

[15] Zhang Y., Yang T., Liu X., Tian L., Fu Z. and Zhang K., Reduction of Emissions from A Syngas Flame Using Micromixing and Dilution with CO2, Energy&Fuels, 26 (2012) 6595−6601.

[16] Donatelli A., Iovane P. and Molino A., High Energy Syngas Production by Waste Tyres Steam Gasification in A Rotary Kiln Pilot Plant, experimental and numerical investigations, Fuel, 89 (2010) 2721–2728.

[17] ANSYS Fluent Release 14.5. Tutorial 13. Partially Premixed Combustion in A Co-axial Combustor. 1-17, ANSYS, Inc., 2013.

[18] Prathap C., Ray A. and Ravi M. R., Investigation of Nitrogen Dilution Effects on The Laminar Burning Velocity and Flame Stability of Syngas Fuel at Atmospheric Condition, Combustion and Flame, 155 (2008) 145–160.

Cumhuriyet Science Journal
CSJ

e-ISSN: 2587-246X
ISSN: 2587-2680

Cumhuriyet Sci. J., Vol.40-4 (2019) 819-829

Companions Of Perturbed Type Inequalities For Higher-Order Differentiable Functions

Samet ERDEN [1]

[1] *Department of Mathematics, Faculty of Science, Bartın University, Bartın-TURKEY*

Received: 13.06.2019; Accepted: 24.10.2019 *http://dx.doi.org/10.17776/csj.577459*

Abstract. First of all, a novel inequality of Hadamard's type for functions higher order derivatives of which are convex is developed. It is also presented midpoint type results. Afterward, Ostrowski type inequalities for mappings whose derivatives are either Lipschitzian or Hölder continuous with are established. Furthermore, links between results given in the earlier paper and our outcomes are examined.

Keywords**:** Convex Functions, Lipschitz Continuity, Ostrowski's Inequality, Hermite-Hadamard inequality.

Yüksek Mertebeden Diferensiyellenebilir Fonksiyonlar için Perturbe Tipli Eşitsizliklerin Geliştirilmiş Durumları

Özet. Bu çalışmada, ilk olarak yüksek mertebeden türevleri konveks olan fonksiyonlar için Hadamard tipli yeni bir eşitsizlik geliştirilmiş ve aynı zamanda bu eşitsizliğin orta nokta tarzındaki sonuçları sunulmuştur. Daha sonra, *n*. mertebeden türevleri ya Lipschitzyan ya da $\sigma \in (0,1]$ olmak üzere $\sigma -$Hölder sürekli olan fonksiyonlar için Ostrowski tipli eşitsizlikler kurulmuştur. Bulunanlara ek olarak, bizim sonuçlarımız ile önceki makalelerde sunulmuş eşitsizlikler arasındaki bağlantılar incelenmiştir.

Anahtar Kelimeler**:** Konveks Fonksiyonlar, Lipschitzyan Süreklilik, Ostrowski Eşitsizliği, Hermite-Hadamard Eşitsizliği.

1. INTRODUCTION

The main purpose of the mathematical inequalities is to determine lower and upper bounds to mathematical expressions whose values are unknown exactly. So, inequality theory plays an important role in many areas of modern mathematics. Hermite-Hadamard inequality, introduced by C. Hermite and J. Hadamard but first published by Hadamard [1] in 1893, is one of the most significant inequalities in the literature because it gives an estimate of the mean value of a convex function. This inequality expresses that if $f : I \to \mathbb{R}$ is a convex function on the interval of real numbers and a, b are elements of I with $a < b$, then we have the chain of inequalities.

$$f\left(\frac{a+b}{2}\right) \leq \frac{1}{b-a}\int_a^b f(x)dx \leq \frac{f(a)+f(b)}{2}. \tag{1}$$

Another important inequality, published by Ostrowski [2] in 1938, is Ostrowski inequality obtained by using functions first derivatives of which are bound. This inequality is stated as follows:

* Corresponding author. *Email address:* *erdensmt@gmail.com*

Let $f:[a,b]\to \mathrm{R}$ be a differentiable mapping on (a,b) whose derivative $f':(a,b)\to \mathrm{R}$ is bounded on (a,b), i.e. $\|f'\|_\infty := \sup_{t\in(a,b)}|f'(t)|<\infty$. Then, we have the inequality

$$\left|f(x)-\frac{1}{b-a}\int_a^b f(t)dt\right|\le\left[\frac{1}{4}+\frac{\left(x-\frac{a+b}{2}\right)^2}{(b-a)^2}\right](b-a)\|f'\|_\infty, \tag{2}$$

for all $x\in[a,b]$. The constant $\frac{1}{4}$ is the best possible.

These two inequalities have attracted many researchers due to its wide application areas. A large number of authors have devoted their effort to observed different generalizations, refined, counterparts and extensions of (1) and (2) for various classes of mappings. In particular, some generalizations of the inequalities (1) and (2) for differentiable, twice differentiable and higher-order differentiable mappings are studied. For instance, Sarikaya and Set derived some novel Ostrowski type results for twice differentiable functions by using a new Montgomery type identity in [3]. Moreover, results similar to Ostrowski's inequality are provided for functions second derivatives of which are bounded in [4] and [5]. On the other side, an extension of the inequality (1) for twice differentiable functions is presented by Farissi et al. in reference [6].

The interested mathematicians focused on perturbed type inequalities which give more general and more extensive outcomes of (1) and (2). In [7], the author developed an identity to establish some inequalities of perturbed Ostrowski type for absolutely continuous as follows.

Theorem 1. Let $f:[a,b]\to \mathrm{C}$ be an absolutely continuous on $[a,b]$ and $x\in[a,b]$. Then, for any $\lambda_1(x)$ and $\lambda_2(x)$ complex numbers, we have

$$\frac{1}{b-a}\int_a^x (t-a)[f'(t)-\lambda_1(x)]dt+\frac{1}{b-a}\int_x^b (t-b)[f'(t)-\lambda_2(x)]dt$$
$$=f(x)+\frac{1}{2(b-a)}\left[(b-x)^2\lambda_2(x)-(x-a)^2\lambda_1(x)\right]-\frac{1}{b-a}\int_a^b f(t)dt$$

where the integrals in the left hand side are taken in the Lebesgue sense.

Afterward, researchers worked on perturbed inequalities for twice differentiable functions in [8] and [9].

We note that there are cases when first and second-order derivatives are not enough to solve certain mathematical issues. Hence, some researchers observed integral inequalities for higher-order differentiable mappings. As an illustration, authors provided some generalizations of Ostrowski type results for mappings higher-order derivatives are elements of L_1, L_p or L_∞ in [10], [11] and [12]. What is more, results that are higher order generalizations of Hermite-Hadamard inequality are deduced in [13] and [14]. In [15], Ozdemir and Yildiz examined midpoint formula related to (1) for higher order differentiable functions. In [16], Erden gave perturbed inequalities for mappings n.th derivatives of which are of bounded variation. In addition, it is presented some perturbed type integral inequalities for functions whose higher-order derivatives are either convex or Lipschitzian in [17].

In [18] and [19], Dragomir observed companions of Perturbed Ostrowski type inequalities for absolutely continuous functions. In [20], Erden established the following equality for $n-$times differentiable functions so as to refined Ostrowski type inequalities. He also investigated new quadrature rules to capture more effective results than the previous.

Lemma 1. Let $f : [a,b] \to \mathrm{R}$ be a $n-$ time differentiable function on (a,b). Then, for any $\lambda_i(x),\ i=1,2,3$ complex numbers and all $x \in \left[a, \frac{a+b}{2}\right]$, we have the identity

$$\begin{aligned}
&\int_a^x \frac{(t-a)^n}{n!}\left[f^{(n)}(t)-\lambda_1(x)\right]dt+\int_x^{a+b-x}\frac{1}{n!}\left(t-\frac{a+b}{2}\right)^n\left[f^{(n)}(t)-\lambda_2(x)\right]dt\\
&+\int_{a+b-x}^b \frac{(t-b)^n}{n!}\left[f^{(n)}(t)-\lambda_3(x)\right]dt\\
&=S(f\ :\ n,x)-\left[\lambda_1(x)+(-1)^n\lambda_3(x)\right]\frac{(x-a)^{n+1}}{(n+1)!}\\
&-\left[1+(-1)^n\right]\frac{\lambda_2(x)}{(n+1)!}\left(\frac{a+b}{2}-x\right)^{n+1}+(-1)^n\int_a^b f(t)dt,
\end{aligned} \tag{3}$$

where $S(f\ :\ n,x)$ is defined by

$$\begin{aligned}
&S(f\ :\ n,x)\\
&=\sum_{k=0}^{n-1}\frac{(-1)^{n+1}\left[f^{(k)}(a+b-x)+(-1)^k f^{(k)}(x)\right]}{(k+1)!}\left[(x-a)^{k+1}+(-1)^k\left(\tfrac{a+b}{2}-x\right)^{k+1}\right]
\end{aligned} \tag{4}$$

In [21], Kashif et al. developed new results of Ostrowski type for functions $n.th$ derivatives of which are element of either $L_1[a,b]$ or $L_2[a,b]$ by means of three-step kernel. Moreover, Qayyum et al. improved more comprehensive Ostrowski type results whose special cases give inequalities presented in the previous studies for functions having a five-step kernel in [22]. Both works also presented new efficient quadrature rules which can use to find the approximate value of expressions values of which cannot be calculated exactly.

In this study, our purpose is to establish new inequalities for mappings higher order derivatives of which are absolutely continuous. By utilizing the above equality, some companions of perturbed inequality for mappings higher order derivatives of which are either convex or Lipschitzian are examined. Results given in previous articles were recaptured when we gave specific values to the inequalities obtained in this work.

2. INEQUALITIES FOR CONVEX FUNCTIONS

Convex functions have become a cornerstone in many fields of Mathematics. Specifically, these type functions are a lot used in the inequality theory and optimization problems. The most famous of the inequalities obtained by using convex functions is Hermite-Hadamard inequality. Furthermore, midpoint and trapezoidal type results which are related to Hermite-Hadamard inequality plays an important role in a large number of areas of Mathematics. Now, we recall some definitions and properties concerning the convex functions which will use to establish our new results.

Supposing that I is an interval of real number with interior I°. Also, $\varphi^{(n-1)} : I \to \mathrm{R}$ be a convex function on I. In this case, $\varphi^{(n-1)}$ is continuous on I° and possess finite left and right derivatives at each point of I°. Furthermore, if i and j are element of I° and $i < j$, then $\varphi_{-}^{(n)}(i) \le \varphi_{+}^{(n)}(i) \le \varphi_{-}^{(n)}(j) \le \varphi_{+}^{(n)}(j)$, and this situation shows that both $\varphi_{-}^{(n)}$ and $\varphi_{+}^{(n)}$ are non-decreasing functions on I°. A convex function is well known to must be differentiable apart from at most countably many points.

We note that the sub differential of convex function $\varphi^{(n-1)}$ indicated by $\partial\varphi^{(n-1)}$ is the set of all functions $\omega : I \to [-\infty, \infty]$ such that $\omega(I^{\circ}) \subset \mathrm{R}$ satisfied the condition

$$\varphi^{(n-1)}(i) \ge \varphi^{(n-1)}(m) + (i-m)\omega(m)$$

for any $i, m \in I$. In this circumstance, if $\varphi^{(n-1)}$ is convex on I, then $\partial\varphi^{(n-1)}$ isn't empty, $\varphi_{-}^{(n)}$, $\varphi_{+}^{(n)} \in \partial\varphi^{(n-1)}$ and if ω is element of $\partial\varphi^{(n-1)}$, then

$$\varphi_{-}^{(n)}(i) \ge \omega(i) \ge \varphi_{+}^{(n)}(i)$$

for any $i \in I^{\circ}$. Specifically, ω is a nondecreasing mapping. Also, we must state that $\partial\varphi^{(n-1)} = \{\varphi^{(n)}\}$ if f is differentiable and convex on I°.

Theorem 2. Let $f : [a,b] \to \mathrm{R}$ be n times differentiable function on (a,b), and let n be odd number. If $f^{(n-1)}$ is a convex function with the lateral derivatives $f_{+}^{(n)}(a)$ and $f_{-}^{(n)}(b)$, then one has the inequality

$$\begin{aligned}
&\int_a^b f(t)dt \\
&\le \sum_{k=0}^{n-1} \frac{\left[f^{(k)}(a+b-x) + (-1)^k f^{(k)}(x)\right]}{(k+1)!} \left[(x-a)^{k+1} + (-1)^k \left(\frac{a+b}{2} - x\right)^{k+1}\right] \\
&+ \left[\frac{f_{-}^{(n)}(b) - f_{+}^{(n)}(a)}{(n+1)!}\right](x-a)^{n+1}
\end{aligned}$$

for any $x \in \left[a, \frac{a+b}{2}\right]$.

Proof. If we take $\lambda_1(x) = f_{+}^{(n)}(a)$, $\lambda_2(x) = f_{+}^{(n)}\left(\frac{a+b}{2}\right)$, $\lambda_3(x) = f_{-}^{(n)}(b)$ in the equality (3), since n is odd number, then, for any $x \in \left[a, \frac{a+b}{2}\right]$, we possess the identity

$$\begin{aligned}
&\sum_{k=0}^{n-1} \frac{\left[f^{(k)}(a+b-x) + (-1)^k f^{(k)}(x)\right]}{(k+1)!} \left[(x-a)^{k+1} + (-1)^k \left(\frac{a+b}{2} - x\right)^{k+1}\right] \\
&- \frac{f_{+}^{(n)}(a) - f_{-}^{(n)}(b)}{(n+1)!}(x-a)^{n+1} - \int_a^b f(t)dt
\end{aligned}$$

$$= \int_a^x \frac{(t-a)^n}{n!}\left[\omega(t) - f_+^{(n)}(a)\right]dt + \int_{a+b-x}^{b} \frac{(t-b)^n}{n!}\left[\omega(t) - f_-^{(n)}(b)\right]dt$$
$$+ \int_x^{a+b-x} \frac{1}{n!}\left(t - \frac{a+b}{2}\right)^n \left[\omega(t) - f_+^{(n)}\left(\frac{a+b}{2}\right)\right]dt$$

where $\omega \in \partial f^{(n-1)}$, because ω is equal to $f^{(n)}$ almost everywhere on $[a,b]$.

Let x be an element of $\left(a, \frac{a+b}{2}\right)$. One has

$$(t-a)^n\left[\omega(t) - f_+^{(n)}(a)\right] \geq 0$$

for any $t \in [a,x]$ and

$$\left(t - \frac{a+b}{2}\right)^n \left[\omega(t) - f_+^{(n)}\left(\frac{a+b}{2}\right)\right] \geq 0$$

for any $t \in [a, a+b-x]$. Also, as n is odd number, we have

$$(b-t)^n\left[f_-^{(n)}(b) - \omega(t)\right] \geq 0$$

for any $t \in [a+b-x, b]$. Hence, the desired inequality is proved.

Corollary 1. Under the sane assumptions of Theorem 2 with $x = \frac{a+b}{2}$, then the following inequality hold:

$$\int_a^b f(t)dt \leq \sum_{k=0}^{n-1} \frac{\left[1+(-1)^k\right]}{2^{k+1}(k+1)!} f^{(k)}\left(\frac{a+b}{2}\right)(b-a)^{k+1}$$
$$+\left[\frac{f_-^{(n)}(b) - f_+^{(n)}(a)}{(n+1)!}\right]\left(\frac{b-a}{2}\right)^{n+1}$$

which is a midpoint type inequality for mappings whose higher order derivatives are convex.

Corollary 2. Under all the all conditions of the Theorem 2, if we choose $x = \frac{3a+b}{4}$, one has the result

$$\int_a^b f(t)dt$$
$$\leq \sum_{k=0}^{n-1} \frac{\left[f^{(k)}\left(\frac{a+3b}{4}\right) + (-1)^k f^{(k)}\left(\frac{3a+b}{4}\right)\right]}{4^{k+1}(k+1)!}\left[1+(-1)^k\right](b-a)^{k+1}$$
$$+\left[\frac{f_-^{(n)}(b) - f_+^{(n)}(a)}{(n+1)!}\right]\left(\frac{b-a}{4}\right)^{n+1}.$$

Remark 1. If we take $n=1$ in the inequality presented in the theorem 2, we have

$$\frac{1}{b-a}\int_a^b f(t)dt \le \frac{1}{2}\left[f(a+b-x)+f(x)\right] + \frac{1}{2}\left[\frac{f'_-(b)-f'_+(a)}{b-a}\right](x-a)^2$$

which was proved by Dragomir in [19].

3. SOME RESULTS FOR LIPSCHITZIAN DERIVATIVES

Lipschitz continuity, which was called after Rudolf Lipschitz, is a more consistent form of uniform continuity. We began with the definition of Lipschitz continuity to this section.

$\phi : [a,b] \to \mathrm{R}$ is said to be *Lipschitzian*, if there exists a real constant $M > 0$ such that

$$|\phi(r)-\phi(s)| \le M|r-s|$$

for any $r,s \in [a,b]$.

A recent companion inequality for mappings whose higher order derivatives are Lipschitzian is provided in the following theorem.

Theorem 3. Let $f : I \to \mathrm{R}$ be a n times differentiable function on I° and $[a,b] \subset I^\circ$. If the nth derivative $f^{(n)} : I^\circ \to \mathrm{R}$ is Lipschitzian with the constants M_1, M_2 and M_3 on $[a,x]$, $[x,a+b-x]$ and $[a+b-x,b]$ respectively, then, for all x in $[a,\frac{a+b}{2}]$, we have

$$\left| S(f:n,x) - \left[f^{(n)}(x)+(-1)^n f^{(n)}(a+b-x)\right]\frac{(x-a)^{n+1}}{(n+1)!} - \frac{\left[1+(-1)^n\right]}{(n+1)!} f^{(n)}\left(\frac{a+b}{2}\right)\left(\frac{a+b}{2}-x\right)^{n+1} + (-1)^n \int_a^b f(t)dt \right|$$
$$\le \left[M_1+M_3\right]\frac{(x-a)^{n+2}}{(n+2)!} + M_2\frac{2}{n!(n+2)}\left(\frac{a+b}{2}-x\right)^{n+2}$$

where $S(f:n,x)$ is defined as in (4).

Proof. Should we write $f^{(n)}(x)$, $f^{(n)}\left(\frac{a+b}{2}\right)$ and $f^{(n)}(a+b-x)$ in place of $\lambda_1(x)$, $\lambda_2(x)$ and $\lambda_3(x)$ in the equality (3) respectively, because of the triangle inequality, then we possess the outcome

$$\left| S(f:n,x) - \left[f^{(n)}(x)+(-1)^n f^{(n)}(a+b-x)\right]\frac{(x-a)^{n+1}}{(n+1)!} - \frac{\left[1+(-1)^n\right]}{(n+1)!} f^{(n)}\left(\frac{a+b}{2}\right)\left(\frac{a+b}{2}-x\right)^{n+1} + (-1)^n \int_a^b f(t)dt \right| \tag{5}$$

$$\leq \int_a^x \frac{(t-a)^n}{n!}\left|f^{(n)}(t)-f^{(n)}(x)\right|dt+\int_{a+b-x}^b \frac{(b-t)^n}{n!}\left|f^{(n)}(t)-f^{(n)}(a+b-x)\right|dt$$
$$+\int_x^{a+b-x}\frac{1}{n!}\left|t-\frac{a+b}{2}\right|^n\left|f^{(n)}(t)-f^{(n)}\left(\frac{a+b}{2}\right)\right|dt.$$

Seeing that $f^{(n)} : I^\circ \to \mathrm{C}$ is Lipschitzian with the constant M_1 on $[a,x]$, we get

$$\int_a^x \frac{(t-a)^n}{n!}\left|f^{(n)}(t)-f^{(n)}(x)\right|dt$$
$$\leq M_1\int_a^x \frac{(t-a)^n}{n!}(x-t)dt = M_1\frac{(x-a)^{n+2}}{(n+2)!}.$$

Similarly, if the other two integrals in the right-hand side of (5) are observed, then the desired result can easily be obtained.

Corollary 3. Let $f : I \to \mathrm{R}$ be a n times differentiable function on I° and $[a,b]\subset I^\circ$. Also, let $x\in(a,b)$. If the nth derivative $f^{(n)} : I^\circ \to \mathrm{R}$ is Lipschitzian with the constant M on $[a,b]$, then one has

$$\left|S(f : n,x)-\left[f^{(n)}(x)+(-1)^n f^{(n)}(a+b-x)\right]\frac{(x-a)^{n+1}}{(n+1)!}\right.$$
$$\left.-\frac{\left[1+(-1)^n\right]}{(n+1)!}f^{(n)}\left(\frac{a+b}{2}\right)\left(\frac{a+b}{2}-x\right)^{n+1}+(-1)^n\int_a^b f(t)dt\right| \qquad (6)$$
$$\leq \frac{2M}{(n+2)!}\left[(x-a)^{n+2}+(n+1)\left(\frac{a+b}{2}-x\right)^{n+2}\right]$$

for any $x\in\left[a,\frac{a+b}{2}\right]$.

Remark 2. If we take $n=1$ in (6), the inequality (6) becomes

$$\left|\frac{1}{2}\left[f(x)+f(a+b-x)\right]\right.$$
$$\left.-\frac{1}{2}\left[f^{(n)}(x)-f^{(n)}(a+b-x)\right](x-a)^2-\int_a^b f(t)dt\right|$$
$$\leq \frac{M}{3}\left[(x-a)^3+2\left(\frac{a+b}{2}-x\right)^3\right],$$

which is provided by Dragomir in [19].

Furthermore, it can be derived trapezoidal and midpoint type inequalities by choosing $x=a$ and $x=\frac{a+b}{2}$ in the above results.

Now, we deal with another result acquired by using a more comprehensive condition than Lipschitz continuity in the next theorem.

Theorem 4. Let $f : I \to \mathrm{R}$ be a n time differentiable function on I° and $[a,b] \subset I^{\circ}$. If the conditions

$$\left|f^{(n)}(t) - f^{(n)}(a)\right| \le L_1 (t-a)^{\alpha} \quad \text{for any } t \in [a,x), \tag{7}$$

$$\left|f^{(n)}(t) - f^{(n)}\left(\frac{a+b}{2}\right)\right| \le L_2 \left|t - \frac{a+b}{2}\right|^{\beta} \quad \text{for any } t \in (x, a+b-x) \tag{8}$$

and

$$\left|f^{(n)}(t) - f^{(n)}(b)\right| \le L_3 (b-t)^{\gamma} \quad \text{for any } t \in [a,x) \tag{9}$$

are satisfied for $\alpha, \beta, \gamma > -1$ and $L_1, L_2, L_3 > 0$, then, for any $x \in \left[a, \frac{a+b}{2}\right]$, we have the inequality

$$\begin{aligned} &\left| S(f : n,x) - \left[f^{(n)}(a) + (-1)^n f^{(n)}(b)\right]\frac{(x-a)^{n+1}}{(n+1)!} \right. \\ &\left. - \frac{\left[1+(-1)^n\right]}{(n+1)!} f^{(n)}\left(\frac{a+b}{2}\right)\left(\frac{a+b}{2} - x\right)^{n+1} + (-1)^n \int_a^b f(t)dt \right| \\ &\le \frac{L_1}{n!}\frac{(x-a)^{n+\alpha+1}}{(n+\alpha+1)} + \frac{L_3}{n!}\frac{(x-a)^{n+\gamma+1}}{(n+\gamma+1)} \\ &+ \frac{L_2}{n!}\frac{2}{(n+\beta+1)}\left(\frac{a+b}{2} - x\right)^{n+\beta+1} \end{aligned} \tag{10}$$

where $S(f : n,x)$ is as shown in (4).

Proof. We take absolute value of both sides of the equality (3) for $\lambda_1(x) = f^{(n)}(a)$, $\lambda_2(x) = f^{(n)}\left(\frac{a+b}{2}\right)$, $\lambda_3(x) = f^{(n)}(b)$, due to the well-known triangle inequality, we get the inequality

$$\begin{aligned} &\left| S(f : n,x) - \left[f^{(n)}(a) + (-1)^n f^{(n)}(b)\right]\frac{(x-a)^{n+1}}{(n+1)!} \right. \\ &\left. - \frac{\left[1+(-1)^n\right]}{(n+1)!} f^{(n)}\left(\frac{a+b}{2}\right)\left(\frac{a+b}{2} - x\right)^{n+1} + (-1)^n \int_a^b f(t) \right| \\ &\le \int_a^x \frac{(t-a)^n}{n!}\left|f^{(n)}(t) - f^{(n)}(a)\right|dt + \int_{a+b-x}^b \frac{(b-t)^n}{n!}\left|f^{(n)}(t) - f^{(n)}(b)\right|dt \\ &+ \int_x^{a+b-x} \frac{1}{n!}\left|t - \frac{a+b}{2}\right|^n \left|f^{(n)}(t) - f^{(n)}\left(\frac{a+b}{2}\right)\right|dt. \end{aligned} \tag{11}$$

Now, should we calculate the first integral given in right hand side of the above inequality by

utilizing the property (7), we possess

$$\int_a^x \frac{(t-a)^n}{n!}\left|f^{(n)}(t)-f^{(n)}(a)\right|dt \le L_1\int_a^x \frac{(t-a)^n}{n!}(t-a)^{\alpha}\,dt$$
$$= L_1\frac{(x-a)^{n+\alpha+1}}{(n+\alpha+1)n!}.$$

If we substitute the resulting inequalities in (11) after having estimated the other two integrals by using the properties (8) and (9), we can easily find the desired inequality (10) which finishes the proof.

In particular, if we take in consideration Hölder condition that is a generalization of the Lipschitzian, then we can express a new result as follows.

Corollary 4. Let $f : I \to \mathrm{R}$ be a n time differentiable function on I° and $[a,b]\subset I^{\circ}$. If the nth derivative $f^{(n)}$ is $\sigma-$Hölder type on $[a,b]$, then we have the inequality

$$\left|f^{(n)}(r)-f^{(n)}(s)\right| \le K|r-s|^{\sigma}$$

for any $r,s\in[a,b]$, where $r\in(0,1]$ and $H>0$. In this case, the following inequality holds:

$$\left|S(f:n,x)-\left[f^{(n)}(a)+(-1)^n f^{(n)}(b)\right]\frac{(x-a)^{n+1}}{(n+1)!}\right.$$
$$\left.-\frac{\left[1+(-1)^n\right]}{(n+1)!}f^{(n)}\left(\frac{a+b}{2}\right)\left(\frac{a+b}{2}-x\right)^{n+1}+(-1)^n\int_a^b f(t)dt\right|$$
$$\le \frac{2}{(n+\sigma+1)}\frac{K}{n!}\left[(x-a)^{n+\sigma+1}+\left(\frac{a+b}{2}-x\right)^{n+\sigma+1}\right]$$

for any $x\in\left[a,\frac{a+b}{2}\right]$. Specifically, if we suppose that $f^{(n)}$ is Lipschitzian with the constant $K>0$ or if we take $\sigma=1$ in the above result, then, for any $x\in\left[a,\frac{a+b}{2}\right]$, we get

$$\left|S(f:n,x)-\left[f^{(n)}(a)+(-1)^n f^{(n)}(b)\right]\frac{(x-a)^{n+1}}{(n+1)!}\right.$$
$$\left.-\frac{\left[1+(-1)^n\right]}{(n+1)!}f^{(n)}\left(\frac{a+b}{2}\right)\left(\frac{a+b}{2}-x\right)^{n+1}+(-1)^n\int_a^b f(t)dt\right| \qquad (12)$$
$$\le \frac{2}{(n+2)}\frac{L}{n!}\left[(x-a)^{n+2}+\left(\frac{a+b}{2}-x\right)^{n+2}\right],$$

where $S(f:n,x)$ is as given in (4).

Remark 3. If we choose $n=1$ in (12), the inequality (12) reduce to the result

$$\left|\left[f(a+b-x)+f(x)\right]\frac{b-a}{2}-\left[f'(a)-f'(b)\right]\frac{(x-a)^2}{2}-\int_a^b f(t)dt\right|$$
$$\leq \frac{2K}{3}\left[(x-a)^3+\left(\frac{a+b}{2}-x\right)^3\right]$$

that was presented by Dragomir in the reference [19].

In addition to all these result, the inequalities given in this section can be examined the cases when $x=\frac{a+b}{2}$ and $x=\frac{3a+b}{4}$. What is more, it is clear that the cases when $n=1$ and $n=2$ of the results provided throughout this section relate to inequalities developed in some works listed in the references.

REFERENCES

[1] Hadamard J., Etude sur les proprietes des fonctions entieres et en particulier d'une fonction consideree par Riemann, J. Math. Pures Appl., 58 (1893), 171-215.

[2] Ostrowski A. M., Über die absolutabweichung einer differentiebaren funktion von ihrem integralmitelwert, Comment. Math. Helv. 10 (1938), 226-227.

[3] Sarikaya M. Z. and Set E., On new Ostrowski type Integral inequalities, Thai Journal of Mathematics, 12-1 (2014), 145-154.

[4] Dragomir S. S. and Barnett N. S., An Ostrowski type inequality for mappings whose second derivatives are bounded and applications, RGMIA Research Report Collection, 1-2 (1998).

[5] Dragomir S. S. and Sofo A., An integral inequality for twice differentiable mappings and application, Tamkang J. Math., 31-4 (2000).

[6] El Farissi A., Latreuch Z. and Belaidi B., Hadamard-Type inequalities for twice diffrentiable functions, RGMIA Reseaech Report collection, 12-1 (2009), art. 6.

[7] Dragomir S. S., Some perturbed Ostrowski type inequalities for absolutely continuous functions (I), Acta Universitatis Matthiae Belii, series Mathematics 23 (2015), 71-86.

[8] Budak H., Sarikaya M. Z. and Dragomir S. S., Some perturbed Ostrowski type inequality for twice differentiable functions, RGMIA Research Report Collection, 19, Article 47 (2016), 14 pp.

[9] Erden S., Budak H. and Sarikaya M. Z., Some perturbed inequalities of Ostrowski type for twice differentiable functions, RGMIA Research Report Collection, 19, Article 70 (2016), 11 pp.

[10] Cerone P., Dragomir S. S. and Roumeliotis J., Some Ostrowski type inequalities for n-time differentiable mappings and applications, Demonstratio Math., 32-4 (1999), 697-712.

[11] Sofo A., Integral inequalities for n- times differentiable mappings, with multiple branches, on the L_p norm, Soochow Journal of Mathematics, 28-2 (2002), 179-221.

[12] Wang M. and Zhao X., Ostrowski type inequalities for higher-order derivatives, J. of

Inequalities and App., Vol. 2009, Article ID 162689 (2009), 8 p.

[13] Latif M. A. and Dragomir S.S., On Hermite-Hadamard type integral inequalities for n-times differentiable Log-Preinvex functions, Filomat, 29-7 (2015), 1651--1661.

[14] Latif M. A.,, and Dragomir S.S., Generalization of Hermite-Hadamard type inequalities for n-times differentiable functions which are s-preinvex in the second sense with applications, Hacettepe J. of Math. and Stat., 44-4 (2015), 389-853.

[15] Özdemir M. E. and Yıldız Ç., A new generalization of the midpoint formula for n-time differentiable mappings which are convex, arXiv:1404.5128v1, (2014).

[16] Erden S., Some perturbed inequalities of Ostrowski type for funtions whose nth derivatives are of bounded, Iranian Journal of Mathematical Sciences and Informatics, in press, (2019).

[17] Erden S., New perturbed inequalities for functions whose higher degree derivatives are absolutely continuous, Konuralp Journal of Mathematics, 7-2, (2019), 371-379.

[18] Dragomir S. S., Perturbed Companions of Ostrowski's Inequality for Absolutely Continuous Functions (I), Analele Universitatii de Vest, Timisoara Seria Matematica - Informatica, LIV (1) (2016), 119- 138.

[19] Dragomir S. S., Perturbed Companions of Ostrowski's Inequality for Absolutely Continuous Functions (II), RGMIA Research Report Collection, 17, Article 19 (2014) 11 pp.

[20] Erden S., Refined Inequalities of Perturbed Ostrowski type for higher order absolutely continuous functions and applications, Submitted, (2019).

[21] Kashif A. R., Shoib M. and Latif M. A., Improved version of perturbed Ostrowski type inequalities for n-times di erentiable mappings with three-step kernel and its application, J. Nonlinear Sci. Appl. 9 (2016), 3319-3332.

[22] Qayyum A., Shoaib M. and Faye I., On new refinements and applications of efficient quadrature rules using n-times differentiable mappings, J. Computational Analysis abd Applicaions, 23-4 (2017), 723-739.

Cumhuriyet Science Journal
CSJ

e-ISSN: 2587-246X
ISSN: 2587-2680

Cumhuriyet Sci. J., Vol.40-4 (2019) 830-837

On fluorescent sensing of metal ions using water extracts of *Salvia officinalis*

***Idris SARGIN*[1,*]**

[1] *Department of Biochemistry, Faculty of Science, Selcuk University, 42075 Konya, Turkey*

Received: 02.07.2019; Accepted: 14.11.2019 *http://dx.doi.org/10.17776/csj.585503*

Abstract. Sensing of metal ions using fluorometric tools has wide applications in chemical, biological and environmental analysis. Plant phytochemicals, like flavonoids, exhibit intense fluorescence upon excitation by UV light. Leaves sage (*Salvia officinalis*), which is rich in polyphenolic and flavonoids compounds, were extracted using Soxhlet and microwave-assisted extractors. The extraction methods led to variations in the phytochemical composition of the extracts, which in turn affected their interaction with metal ions. Despite the variations in the composition, both of the extracts gave high fluorescence emissions when excited at 365 nm. Variations in fluorescence emissions of the extracts were studied in upon addition of each metal ion; i.e., Li^{+}, Na^{+}, K^{+}, Cs^{+}, Be^{2+}, Mg^{2+}, Sr^{2+}, Ba^{2+}, Al^{3+}, Tl^{3+}, Ge^{4+}, Sn^{4+}, Pb^{2+}, Sb^{3+}, Bi^{3+}, Se^{4+}, Cu^{2+}, Ag^{+}, Zn^{2+}, Cd^{2+}, Ti^{4+}, Cr^{3+}, Cr^{6+}, Mo^{6+}, W^{6+}, Mn^{2+}, Fe^{3+}, Ni^{2+}, Co^{2+} and Pd^{2+}. When they were added into the Soxhlet extract, some ions (Cr^{3+}, Pb^{2+}, Co^{2+}) induced intense fluorescence and some (Ge^{4+}, Mg^{2+}, K^{+}, Na^{+}) ions quenched the fluorescence emission. As for microwave-assisted extract, the addition of Sr^{2+}, Mg^{2+} and Co^{2+} ions enhanced the fluorescence emission of the extract, but Fe^{3+}, Be^{2+} and Cs^{+} lowered the fluorescence intensity. However, the results of the study should be considered as introductory and further selectivity and sensitivity studies should be done for each extract if they are used for sensing of metal ions. Yet, this study demonstrated that sage extracts has a potential for fluorescent sensing of certain metal ions.

***Keywords*:** Sage; Flavonoid; Metal ion sensing; Soxhlet extraction; Microwave irradiation.

Salvia officinalis'in su özütlerini kullanarak metal iyonlarının floresanla algılanması

Özet. Metal iyonlarının florometrik araçlar kullanarak algılanması kimyasal, biyolojik ve çevresel analizlerde geniş uygulamalara sahiptir. Flavonoidler gibi bitki fitokimyasalları, UV ışığı ile uyarıldıklarında yoğun floresans ışıma yaparlar. Polifenolik bileşikler ve flavonoidler bakımından zengin olan adaçayı (*Salvia officinalis*) yaprakları Soxhlet ve mikrodalga ekstraktörler kullanılarak özütlendi. Ekstraksiyon yöntemleri, özütlerin fitokimyasal kompozisyonunda değişikliklere neden olmuştur, bu da metal iyonlarıyla etkileşimlerini etkilemiştir. Kompozisyondaki değişikliklere rağmen, özütlerin her ikisi de 365 nm'de uyarıldığında yüksek floresans emisyonu vermiştir. Özütlerin floresans emisyonundaki değişmeler her bir iyonun ilave edilmesiyle çalışıldı; Li^{+}, Na^{+}, K^{+}, Cs^{+}, Be^{2+}, Mg^{2+}, Sr^{2+}, Ba^{2+}, Al^{3+}, Tl^{3+}, Ge^{4+}, Sn^{4+}, Pb^{2+}, Sb^{3+}, Bi^{3+}, Se^{4+}, Cu^{2+}, Ag^{+}, Zn^{2+}, Cd^{2+}, Ti^{4+}, Cr^{3+}, Cr^{6+}, Mo^{6+}, W^{6+}, Mn^{2+}, Fe^{3+}, Ni^{2+}, Co^{2+} ve Pd^{2+}. Soxhlet özütüne ilave edildiğinde, bazı iyonlar (Cr^{3+}, Pb^{2+}, Co^{2+}) yoğun floresansa neden olmuş, bazı (Ge^{4+}, Mg^{2+}, K^{+}, Na^{+}) iyonlar ise floresans emisyonunu söndürmüştür. Mikrodalga destekli özütte, Sr^{2+}, Mg^{2+} ve Co^{2+}'nın ilavesi, özütün floresans emisyonunu arttırdı, ancak Fe^{3+}, Be^{2+} ve Cs^{+} floresan şiddetini düşürdü. Bununla birlikte, çalışmanın sonuçları giriş niteliğinde olarak değerlendirilmeli ve metal iyonlarını algılamak için kullanılacaksa her özüt için seçicilik ve duyarlılık çalışmaları yapılmalıdır. Yine de, bu çalışma adaçayı özütlerinin belirli metal iyonlarının floresan algılama potansiyelinin olduğunu göstermiştir.

***Anahtar Kelimeler*:** Adaçayı; Flavonoid; Metal iyonu algılama; Soxhlet ekstraksiyonu; Mikrodalga ışınlaması.

* Corresponding author. *Email address:* *idris.sargin@selcuk.edu.tr*

1. INTRODUCTION

Extracts from plants have been subject of intensive studies because of their wide range of pharmacological activities. Sage (*Salvia officinalis*) is a medicinal and herbal plant [1]. Its biological activities are attributed to its phenolic compounds including carnosic acid, carnosol, rosmarinic acid, diterpenes, triterpenes and flavonoids [2, 3].

Apart from therapeutic activities and physiological importance [4], flavonoids, one group of the active ingredients in *S. officinalis* extracts, also display important characteristics [5]. These polyphenolic phytochemicals emit brilliant fluorescence when excited by UV light [6].

Detection of metal ions using fluorescence spectrometry is a simple and powerful technique in analytical chemistry. Designing fluorescent and water-soluble chemosensors for sensing metal ions in aqueous environments is of importance. Water-soluble and natural fluorescent chemosensors are needed for detection of metal ions by fluorescence spectrometry [7, 8].

Natural compounds as fluorescent probes for metal ions have attracted considerable attention in the past few years. For example, a plant alkaloid berberine was isolated from the stems of *Mahonia leschenaultti* and then used for detection of Ag^{+} ion [9]. In one study natural Isorhamnetin from Ginkgo leaves was applied for determination of Cu^{2+} in samples from rivers, lakes, vegetables and fruits [10]. In another study, a simple and green analytical procedure based on chlorophyll *a* was developed by Gao and et al., (2006) [11]. The authors reported the extraction and purification of chlorophyll *a* from the leaves of pea and use of chlorophyll *a* fluorometric detection of Hg^{2+} ion. A more recent study by Ahmad et al., (2018) reported that flavonoid containing methanolic extract of *Corchorus depressus* could be used as a spectrofluorometric assay for the detection of Benzo[a]pyrene [12]. Flavonoids also display affinity for metal ions by forming metal–flavonoids complexes. Flavonoids are able to form fluorescent chelates with a variety of metal ions [13].

This study aimed to test whether it is possible to develop a simple, cheap and fast spectrofluorometric chemosensor based on the water extract of common sage (*S. officinalis*) for detection of metal ions. In the study, two extraction procedures were used to see the effect of the extraction method on the composition of the *S. officinalis* extracts; the Soxhlet extraction and microwave-assisted extraction. Both extracts exhibited high fluorescence emission when excited by UV light despite the variations in their compositions. The change in the fluorescence intensity of the extracts was tested for 30 metal ions; Li^{+}, Na^{+}, K^{+}, Cs^{+}, Be^{2+}, Mg^{2+}, Sr^{2+}, Ba^{2+}, Al^{3+}, Tl^{3+}, Ge^{4+}, Sn^{4+}, Pb^{2+}, Sb^{3+}, Bi^{3+}, Se^{4+}, Cu^{2+}, Ag^{+}, Zn^{2+}, Cd^{2+}, Ti^{4+}, Cr^{3+}, Cr^{6+}, Mo^{6+}, W^{6+}, Mn^{2+}, Fe^{3+}, Ni^{2+}, Co^{2+}, Pd^{2+}.

2. MATERIALS AND METHODS

2.1. Preparation of *S. officinalis* extracts

Commercially available, dry sage (*Salvia officinalis*) was obtained from a local supplier. Dry aerial parts of *S. officinalis* were ground to powder using a commercial blender. Two extraction procedures were followed; Soxhlet extraction [14] and microwave-assisted extraction [15]. In Soxhlet extraction, 5.0 g of *S. officinalis* in a cellulose thimble was placed in the extractor and a flaks with 300 mL of ultrapure water (ELGA, PURELAB Option-Q) was fitted to the assembly. The extraction bed was heated at 80°C for 24 h. In microwave-assisted extraction, 5.0 g of *S. officinalis* powder in 300 mL of ultrapure water was microwave-irradiated at 400 W for 30 min in a MARS CEM microwave oven. The Soxhlet and microwave extracts were filtered using a filter paper (Whatman, No: 42), transferred into the glass flasks sealed with aluminium foil and stored at 4°C in dark (To protect from direct sunlight, the vessels were covered with aluminium foil). The pH of the Soxhlet and microwave extracts was measured as 5.13 and 5.67.

2.2. Flavonoid and phenolic content of the Soxhlet and microwave-assisted extracts of *S. officinalis*

Analysis of the flavonoid and phenolic content of the Soxhlet and the microwave extracts was done using high-performance liquid chromatography (Shimadzu HPLC-DAD) [5, 16]. The HPLC working conditions were as follows: Detector: DAD detector, max = 278 nm; auto sampler: SIL–10AD vp; system controller: SCL-10Avp; pump: LC-10ADvp; degasser: DGU-14A; column oven: CTO-10Avp; column: Agilent Eclipse XDB-C18, 250x4.60 mm, 5 µ; mobile phase: A: 3% acetic acid, B: methanol; flow rate: 0.8 mL min^{-1}; column temperature: 300 °C; injection volume: 20 µL.

Prior to the HPLC analysis, 10.0 mL of the extracts from the stock solutions were heated at 60 °C to dryness, and then the dried residue was dissolved in ultrapure water (ELGA, PURELAB Option-Q) to give a final concentration of 20 mg mL^{-1}.

2.3. Fluorescence properties of the *S. officinalis* extracts

The extracts were excited at 365 nm wavelength and the corresponding fluorescence intensity was recoded on Perkin Elmer LS 55 Fluorescence Spectrometer. Fluorescence intensity of the extracts in relation to excitation wavelength (λ_{ex}) was measured in range of 315–395 nm. Fluorescence emission (λ_{em}) of the extracts as function of dilution was also studied at λ_{ex} = 365 nm. Consecutive dilutions from the extracts were done with ultrapure water from 100 to 0.2 %.

2.4. Preparation of metal ion solutions

Thirty metal ion solutions were prepared from the solutions of metal ions for Merck AAS standard. Standard metal solution (1000 mg L^{-1}) was diluted to 1 mg L^{-1} with ultrapure water. The metal ions that were studied are as follows; Li^{+}, Na^{+}, K^{+}, Cs^{+}, Be^{2+}, Mg^{2+}, Sr^{2+}, Ba^{2+}, Al^{3+}, Tl^{3+}, Ge^{4+}, Sn^{4+}, Pb^{2+}, Sb^{3+}, Bi^{3+}, Se^{4+}, Cu^{2+}, Ag^{+}, Zn^{2+}, Cd^{2+}, Ti^{4+}, Cr^{3+}, Cr^{6+}, Mo^{6+}, W^{6+}, Mn^{2+}, Fe^{3+}, Ni^{2+}, Co^{2+}, Pd^{2+}.

2.5. Fluorescence emission of *S. officinalis* extracts in the presence of metal ions

Metal ion solution (2.0 mL, 1 mg L^{-1}) was added into 2.0 mL of the Soxhlet extract or the microwave-assisted extract, and the final solution was shaken for one minute and rested for 10 min. Then, the fluorescence emission spectrum of the final solution was recorded at λ_{ex} = 365 nm. The same procedure was applied to each metal solution.

3. RESULTS AND DISCUSSION

3.1. Variation in the flavonoid and phenolic content of *S. officinalis* extracts

The standard chromatogram and the chromatograms of the Soxhlet and microwave extracts are presented in Fig. 1. Table 1 lists the results of the HPLC analysis. The analysis revealed that both extracts had high content of catechin and rosmarinic acid. However, microwave irradiation led to higher results with regard to these compounds. But there were variations in phenolic and flavonoid contents of the extracts. For example, two phenolic compounds (benzoic acid and o-coum acid) were not detected in the microwave extract. Cinnamic acid was detected in the microwave extract but not in the Soxhlet extract. As for flavonoids, two flavones (apigenin and luteolin) and one flavanone (hesperidin) were detected in the extracts. Apigenin and luteolin contents of both extracts were very close to one another but hesperidin content of the extract from the microwave irradiation was higher by two folds than that of the Soxhlet extract. The chemical structure of apigenin, luteolin and hesperidin are presented in Fig. 2.

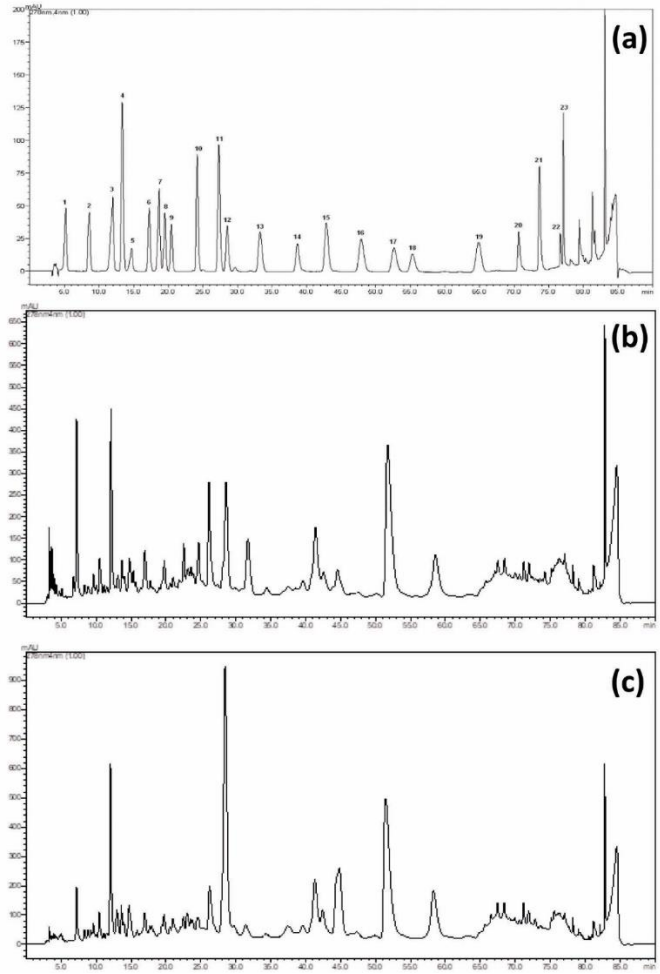

Fig. 1. The chromatogram of the standards **(a)** and the chromatograms of the Soxhlet **(b)** and microwave **(c)** extracts (1: gallic acid, 2: protocatechuic acid, 3: catechin, 4: p-hydroxy benzoic acid, 5: chlorogenic acid, 6: caffeic acid, 7: epicatechin, 8: syringic acid, 9: vanillin, 10: p-coum acid, 11: ferulic acid, 12: sinapinic acid, 13: benzoic acid, 14: o-coum acid, 15: rutin 16: hesperidin, 17: rosmarinic acid, 18: eriodictiol, 19: cinnamic acid, 20: quercetin, 21: luteolin, 22: kaempferol, 23:apigenin).

Table 1. The flavonoid and phenolic content of the Soxhlet and microwave-assisted *S. officinalis* extracts. (*nd: Not detected. (±) refers to standard deviations. Three repetitions were done.).

	Soxhlet extract	**Microwave extract**
	µg mL^{-1}	**µg mL^{-1}**
gallic acid	3.2 ± 0.04	3.5 ± 0.05
protocatechuic acid	12.5 ± 0.4	14.2 ± 0.4
catechin	402.4 ± 10.6	550.4 ± 12.2
p-hydroxy benzoic acid	nd*	nd
chlorogenic acid	70.2 ± 0.8	108.3 ± 0.8
caffeic acid	35.8 ± 1.9	28.6 ± 1.9
epicatechin	nd	nd
syringic acid	4.9 ± 0.2	3.9 ± 0.2
vanilin	nd	nd
p-coum acid	5.8 ± 0.1	5.1 ± 0.1
ferulic acid	20.8 ± 1.4	28.9 ± 1.3
sinapinic acid	40.3 ± 0.3	58.8 ± 0.3
benzoic acid	40.1 ± 1.2	nd
o-coum acid	2.1 ± 0.1	nd
rutin	nd	nd
hesperidin	14.7 ± 0.2	35.5 ± 0.2
rosmarinic acid	499.9 ± 8.2	693.7 ± 10.8
eriodictiol	nd	nd
cinnamic acid	nd	1.5 ± 0.1
quercetin	nd	nd
luteolin	19.2 ± 1.4	19.1 ± 1.4
kaempferol	nd	nd
apigenin	12.9 ± 0.4	11.8 ± 0.4

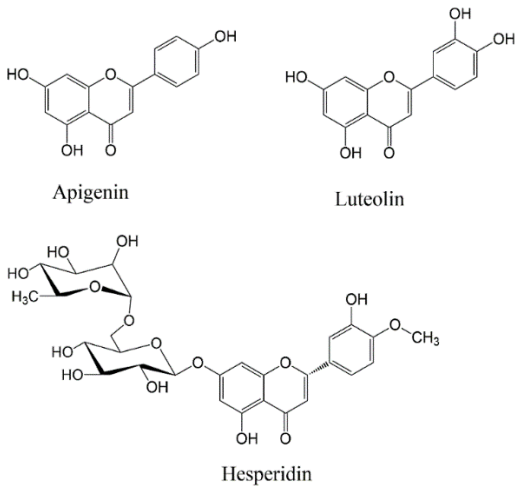

Fig. 2. Chemical structures of flavonoids identified in the Soxhlet and microwave-assisted extracts of common sage *S. officinalis*.

Previous literature studies have clearly demonstrated that flavonoids and phenolic compounds can coordinate metal ions and form stable complexes with metal cations. Biological activity of metal–flavonoids complexes, therefore, has been widely studied for their free radical scavenging activity [13]. In one study it was demonstrated that flavonoids (kaempferol, quercetin, myricetin, luteolin, catechin and naringenin) are capable of interacting of metal ions such as Cu^{2+} and Fe^{3+} ions through chelation [17]. Electron donating moieties (usually carbonyl and hydroxyl) of flavonoids are involved in formation of complexes with metal species. However, their interaction with metal ions are affected by the number and location of coordinating or chelating sites in flavonoid molecule [18]. Thus, due to this property, formation of flavonoid metal complexes has been widely utilized in spectrophotometric and spectrofluorometric studies [19, 20]. As depicted in Fig. 2, apigenin, luteolin and hesperidin have different number of hydroxyl functionalities in their structures, which may affect their interaction with metal ions.

3.2. Dependency of fluorescence emission of *S. officinalis* extracts on the extract concentration and excitation wavelength

The measurements revealed that dilution of the extract solutions led to enhancement in fluorescence emission intensity to a certain point. Further dilution, on the other hand, decreased the fluorescence intensity (Fig. 3). This behaviour was observed for both Soxhlet extract and the microwave-assisted extract. Dilution of the extracts led to blue shift in the spectra. Emitted fluorescence of the extracts was also affected by change in the excitation wavelength (Fig. 4). At higher wavelength a red shift was recorded for both of the extracts. Excitation of *S. officinalis* extracts at 395 nm led to the highest emission peak at 480 nm for the Soxhlet extract and 472 nm for microwave-assisted extract.

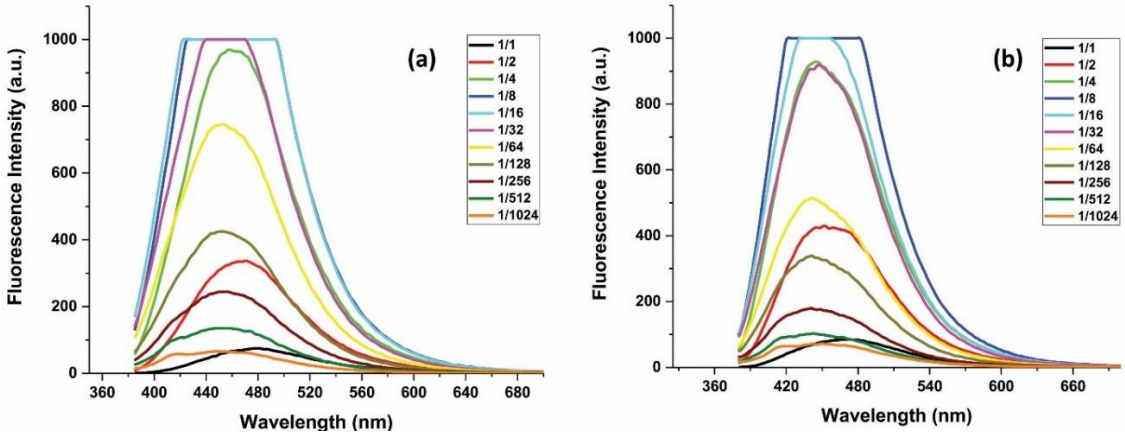

Fig. 3. Fluorescence intensity changes in the Soxhlet (a) and the microwave-assisted (b) extracts of common sage *S. officinalis* upon consecutive dilutions (λ_{ex} = 365 nm).

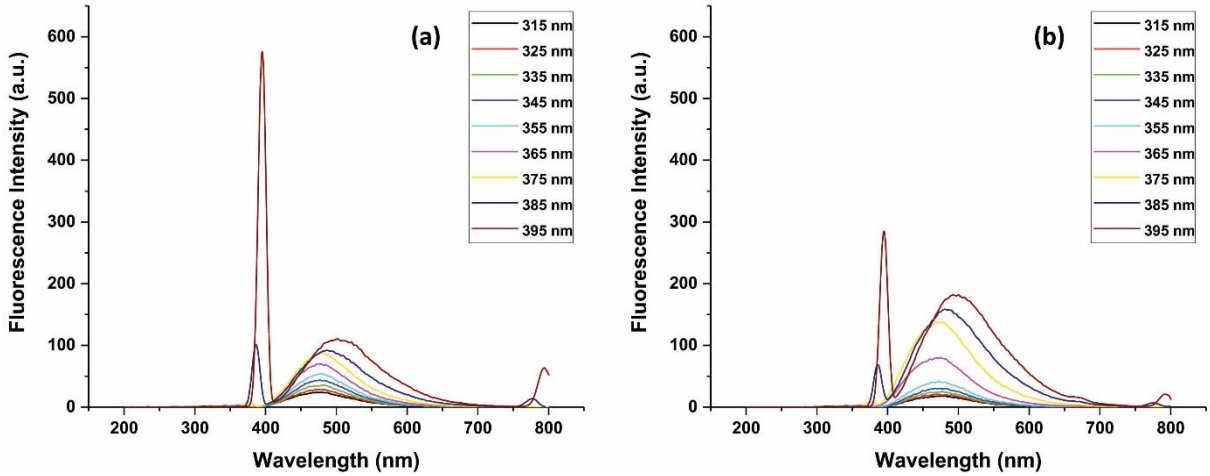

Fig. 4. Fluorescence emission spectra of the Soxhlet (a) and microwave-assisted (b) extracts of common sage *S. officinalis* as a function of excitation wavelength.

3.3. Fluorescence emission response of *S. officinalis* extracts to various metal ions

Fluorescence emission spectra of the Soxhlet and the microwave-assisted extracts in the presence of metal ions are presented in Fig. 5. A column graph according to maximum fluorescence emission peaks of the extracts upon addition of various metal ions is shown in Fig. 6. Co^{2+} ion led to increase in the fluorescence intensity of the Soxhlet extract. Ge^{4+} ions, on the other hand, had an opposite effect and lowered the fluorescence of the extract. A completely different fluorescence emission spectrum was obtained for the microwave-assisted extract. Addition of Sr^{2+} ions to the microwave-assisted extract enhanced the fluorescence emission of the extract. Fe^{3+} ions in the extract quenched the fluorescence.

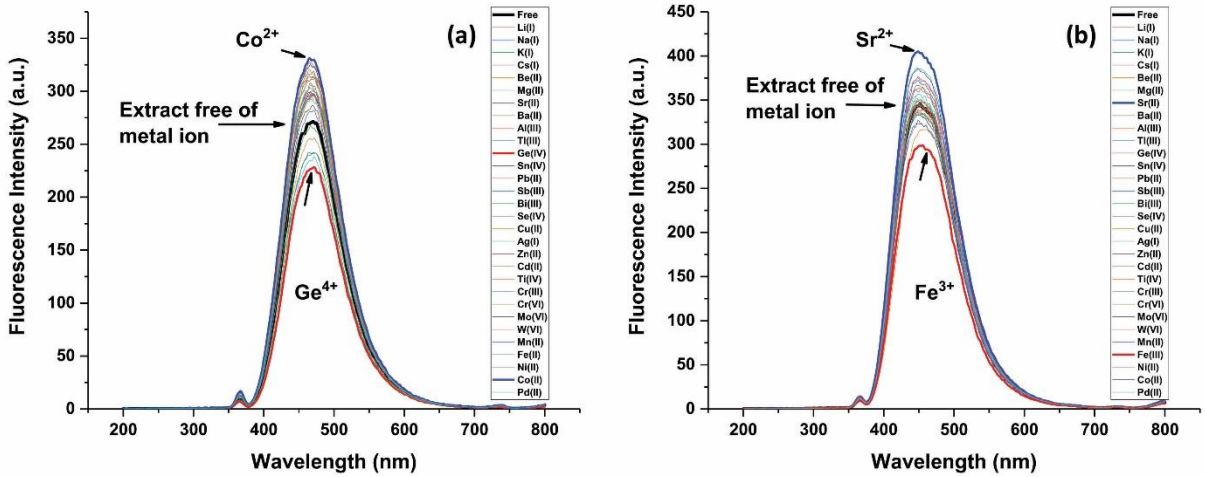

Fig. 5. Fluorescence emission changes in the Soxhlet (a) and microwave-assisted (b) extracts of common sage *S. officinalis* upon addition of different metal ions (final concentration: 0.5 mg L^{-1}). Equal volumes of the extracts and metal solutions were mixed, shaken and rested for 10 min (λ_{ex} = 365 nm).

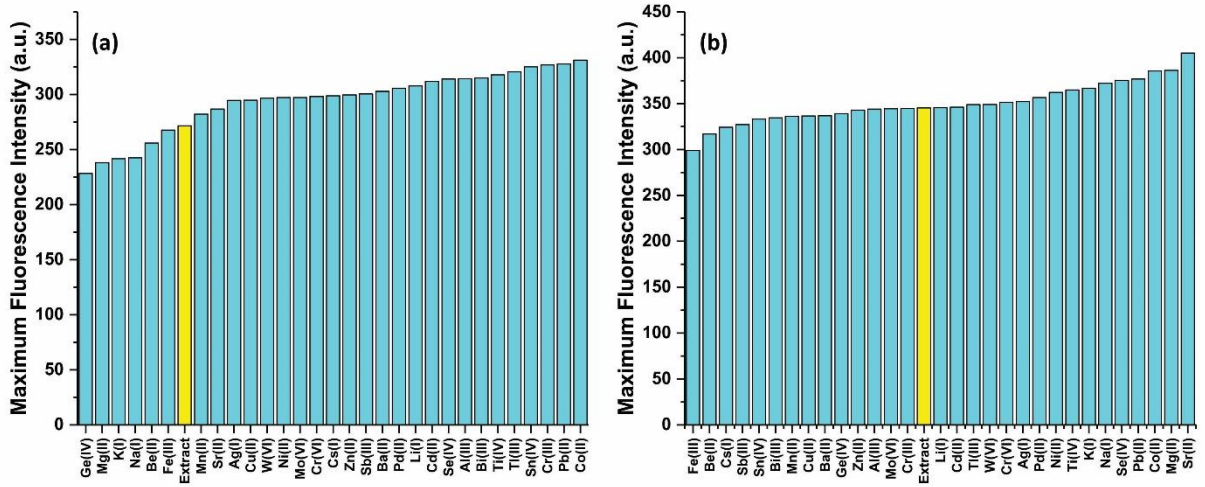

Fig. 6. Maximum fluorescence emission of the Soxhlet (a) and microwave-assisted (b) extracts of common sage *S. officinalis* upon addition of different metal ions (final concentration: 0.5 mg L^{-1}). Equal volumes of the extracts and metal solutions were mixed, shaken and rested for 10 min (λ_{ex} = 365 nm).

The variations observed in the fluorescence emission of the extracts upon addition of the metal ions can be attributed to the interaction of metal ions with apigenin, luteolin and hesperidin content of the extracts. These observations are in line with the earlier literature reports. In one study on apigenin and luteolin by Favora et al., (2007), it was demonstrated that chelation of apigenin and luteolin with Al^{3+} ions led to intense fluorescence emission [21]. The authors concluded that complexation with metal cations could transform poorly fluorescent molecular systems into efficient fluorophores. A study by Perez-Ruiz et al., (1999) reported that spectrofluorometric determination of hesperidin in the presence of Al^{3+} [22]. The authors based their method on the formation of a highly

fluorescent complex between hesperidin molecule and Al^{3+} ion. Yet, in some studies contradictory results were also reported. For example, in a recent study the authors concluded that presence of Fe^{3+}, Cu^{2+}, Mg^{2+}, Mn^{2+}, Zn^{2+} and Ca^{2+} ions did not have obvious effect on the interaction of apigenin with bovine serum albumin [23].

3.4. Turn-on fluorescence sensing of Co^{2+} using the Soxhlet extract of *S.* officinalis

The microwave extract exhibited the significant fluorescence intensity at presence of Co^{2+} ion. Therefore, the fluorescence response of the Soxhlet extract to Co^{2+} was studied further as a model ion (Fig. 7). In the experiments, the final concentration of the extract was adjusted to 50%, Co^{2+} ion solutions were added into the extract solutions, shaken for one minute and rested for 10 min. The lowest concentration of Co^{2+} ion that gave obvious fluorescence emission intensity was found to be 0.2 mg L^{-1}.

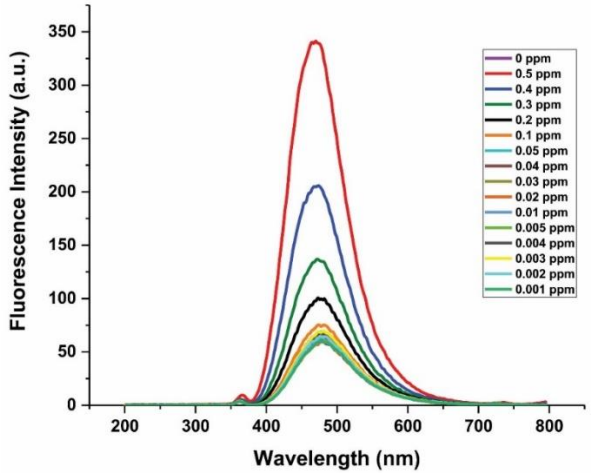

Fig. 7. Fluorescence emission spectra of the Soxhlet extract of *S. officinalis* as a function of Co^{2+} concentration.

4. CONCLUSION

This study revealed that the flavonoid and phenolic content of *S. officinalis* extract is highly dependent on the extraction method and parameters that are followed during an extraction procedure. Upon excitation by UV light, the Soxhlet and the microwave-assisted extracts emitted brilliant fluorescence, which can be attributed to the presence flavonoids (apigenin, luteolin and hesperidin). The extraction method greatly affected the content of the extracts by giving different HPLC profiles. Numerous previous studies have demonstrated clearly that flavonoid and phenolic molecules from plant extracts are capable of interacting with metal ions through chelation or complex formation. This study, however, aimed to find out whether it was possible to use plant extracts with high flavonoid contents for fluorescent sensing of metal ions. As the chemical contents of plant extracts are highly dependent on the solvent type and extraction procedure, in the study two different methods were followed for water extraction of *S. officinalis*. Due to the variation of their composition, the extracts showed different interaction with 30 metal ions including alkaline, alkaline earth and transition metal ions. The result of the study with Co^{2+} was encouraging; the Soxhlet extract was sensitive to Co^{2+} ion concentration of 0.2 mg L^{-1}. However, further studies are still needed to clarify the phenomena. The extracts can be used as simple, fast and low-cost turn-on fluorescence method for detection of, for example, Co^{2+} and Sr^{2+} ions; or for a turn-off fluorescence method for signalling of Ge^{4+} and Fe^{3+} ions; yet, this study should be considered as an introductory study. Therefore, preliminary studies were not done to optimize the conditions for each ion. Especially, in case of Co^{2+}, Sr^{2+}, Ge^{4+} and Fe^{3+} ions optimization conditions have to be investigated in a more detailed manner if sage extracts are used in any analytical metal sensing study. In future studies phytochemicals of sage plant can be extracted using different methods and the extracts can be tested in fluorescent sensing applications of metal ions.

REFERENCES

[1] Ghorbani A., Esmaeilizadeh M., Pharmacological properties of *Salvia officinalis* and its components, J. Tradit. Complem. Med., 7(2017) 433-440.

[2] Durling N.E., Catchpole O.J., Grey J.B., Webby R.F., Mitchell K.A., Foo L.Y., Perry N.B., Extraction of phenolics and essential oil from dried sage (*Salvia officinalis*) using ethanol–water mixtures, Food. Chem., 101(2007) 1417-1424.

[3] Ollanketo M., Peltoketo A., Hartonen K., Hiltunen R., Riekkola M.-L., Extraction of sage (*Salvia officinalis* L.) by pressurized hot water and conventional methods: Antioxidant activity of the extracts, Eur. Food. Res. Technol., 215(2002) 158-163.

[4] de Rijke E., Out P., Niessen W.M.A., Ariese F., Gooijer C., Brinkman U.A.T., Analytical

separation and detection methods for flavonoids, J. Chromatogr. A, 1112(2006) 31-63.

[5] Lu Y., Foo L.Y., Flavonoid and phenolic glycosides from *Salvia officinalis*, Phytochemistry, 55(2000) 263-267.

[6] Havsteen B.H., The biochemistry and medical significance of the flavonoids, Pharmacol. Therapeut., 96(2002) 67-202.

[7] Formica M., Fusi V., Giorgi L., Micheloni M., New fluorescent chemosensors for metal ions in solution, Coordin. Chem. Rev., 256(2012) 170-192.

[8] Jeong Y., Yoon J., Recent progress on fluorescent chemosensors for metal ions, Inorg. Chim. Acta, 381(2012) 2-14.

[9] Affrose A., Parveen S.D.S., Kumar B.S., Pitchumani K., Selective sensing of silver ion using berberine, a naturally occurring plant alkaloid, Sensor. Actuat. B-Chem., 206(2015) 170-175.

[10] Yang S., Jiang W., Zhao F., Xu L., Xu Y., Gao B., Sun H., Du L., Tang Y., Cao F., A highly sensitive and selective fluorescent sensor for detection of copper ions based on natural Isorhamnetin from ginkgo leaves, Sensor. Actuat. B-Chem., 236(2016) 386-391.

[11] Gao S., Tan G., Yuan H., Xiao D., Choi M.M.F., A Simple fluorometric method using Chlorophyll A for determination of Hg^{2+} ion, Microchim. Acta, 153(2006) 159-162.

[12] Ahmad W., Rana N.F., Riaz S., Ahmad N.M., Hameed M., Naeem A., Tahir R., Chemical sensing of Benzo [a] pyrene using *Corchorus depressu*s fluorescent flavonoids, Nat. Prod. Res., 32(2018) 968-971.

[13] Malešev D., Kuntić V., Investigation of metal-flavonoid chelates and the determination of flavonoids via metal-flavonoid complexing reactions, J. Serbian Chem. Soc., 72(2007) 921-939.

[14] Veličković D., Milenović D., Ristić M., Veljković V., Kinetics of ultrasonic extraction of extractive substances from garden (*Salvia officinalis* L.) and glutinous (*Salvia glutinosa* L.) sage. Ultrason. Sonochem., 13(2006) 150-156.

[15] Putnik P., Kovačević D.B., Penić M., Fegeš M., Dragović-Uzelac V., Microwave-assisted extraction (MAE) of dalmatian sage leaves for the optimal yield of polyphenols: HPLC-DAD identification and quantification, Food Anal. Method., 2016;9:2385-94.

[16] Kontogianni VG, Tomic G, Nikolic I, Nerantzaki AA, Sayyad N, Stosic-Grujicic S, Stojanovic I., Gerothanassis I.P., Tzakos A.G., Phytochemical profile of Rosmarinus officinalis and *Salvia officinalis* extracts and correlation to their antioxidant and anti-proliferative activity. Food Chem. 136(2013) 120-129.

[17] Fernandez M.T., Mira M.L., Florencio M.H., Jennings K.R., Iron and copper chelation by flavonoids: An electrospray mass spectrometry study, J. Inorg. Biochem., 92(2002) 105-111.

[18] Kasprzak M.M., Erxleben A., Ochocki J., Properties and applications of flavonoid metal complexes, RSC Adv., 5(2015) 45853-45877.

[19] Samsonowicz M., Regulska E., Spectroscopic study of molecular structure, antioxidant activity and biological effects of metal hydroxyflavonol complexes, Spectrochim. Acta A, 173(2017) 757-771.

[20] Özbek N., Alp H., Çelik G., Ak T., Çağılcı O.C., Yaylı N., Ocak U., Ocak M., A simple spectrofluorimetric method for iron determination with a chalcone-based Schiff base, J. Fluoresc. 27(2017) 635-641.

[21] Favaro G., Clementi C., Romani A., Vickackaite V., Acidichromism and ionochromism of luteolin and apigenin, the main components of the naturally occurring yellow weld: A spectrophotometric and fluorimetric study, J. Fluoresc., 17(2007) 707-714.

[22] Perez-Ruiz T., Martinez-Lozano C., Tomas V., Fenoll J., Spectrofluorometric determination of hesperidin by manual and flow-injection methods, Fresenius J. Anal. Chem., 364(1999) 279-283.

[23] Bi S., Yan L., Pang B., Wang Y., Investigation of three flavonoids binding to bovine serum albumin using molecular fluorescence technique, J. Lumin., 132(2012) 132-140.

Cumhuriyet Science Journal
CSJ

e-ISSN: 2587-246X
ISSN: 2587-2680

Cumhuriyet Sci. J., Vol.40-4 (2019) 838-845

Multiplicative Mappings of Gamma Rings

Bruno L. M. FERREİRA [1*], Ruth N. FERREİRA [1]

[1] *Federal Technological University of Paraná,Professora Laura Pacheco Bastos Avenue, 800, 85053-510, Guarapuava, Brazil.*

Received: 15.07.2019; Accepted: 04.11.2019 *http://dx.doi.org/10.17776/csj.592101*

Abstract. Let $\mathfrak{M}_i$ and Γ_i $(i = 1,2)$ be abelian groups such that $\mathfrak{M}_i$ is a Γ_i-ring. An ordered pair (φ, ϕ) of mappings is called a *multiplicative isomorphism* of $\mathfrak{M}_1$ onto $\mathfrak{M}_2$ if they satisfy the following properties: *(i)* φ is a bijective mapping from $\mathfrak{M}_1$ onto $\mathfrak{M}_2$, *(ii)* ϕ is a bijective mapping from Γ_1 onto Γ_2 and *(iii)* $\varphi(x\gamma y) = \varphi(x)\phi(\gamma)\varphi(y)$ for every $x, y \in \mathfrak{M}_1$ and $\gamma \in \Gamma_1$. We say that the ordered pair (φ, ϕ) of mappings is *additive* when $\varphi(x + y) = \varphi(x) + \varphi(y)$, for all $x, y \in \mathfrak{M}_1$. In this paper we establish conditions on $\mathfrak{M}_1$ that assures that (φ, ϕ) is additive.

***Keywords*:** Multiplicative mappings, Additivity, Gamma rings.

Gamma Halkalarında Çarpımsal Dönüşümler

Özet. $\mathfrak{M}_i$ ve Γ_i $(i = 1,2)$ değiştirmeli grup ve $\mathfrak{M}_i$ bir Γ_i-halka olsun. Aşağıdaki özellikler sağlanırsa dönüşümlerin (φ, ϕ) sıralı ikilisine $\mathfrak{M}_1$ den $\mathfrak{M}_2$ üzerine çarpımsal izomorfizm denir: *(i)* φ, $\mathfrak{M}_1$ den $\mathfrak{M}_2$, üzerine bijektif dönüşümdür. *(ii)* ϕ, Γ_1 den Γ_2 üzerine bijektif dönüşümdür. *(iii)* Her $x, y \in \mathfrak{M}_1$ ve $\gamma \in \Gamma_1$.için $\varphi(x\gamma y) = \varphi(x)\phi(\gamma)\varphi(y)$ dir ve Her $x, y \in \mathfrak{M}_1$ için $\varphi(x + y) = \varphi(x) + \varphi(y)$, olduğunda dönüşümlerin (φ, ϕ) sıralı ikilisine toplamsaldır denir. Bu makalede $\mathfrak{M}_1$ üzerinde (φ, ϕ) nin toplamsallığını garanti edecek koşulları vereceğiz.

***Anahtar Kelimeler*:** Çarpımsal dönüşümleri, Toplamsallık, Gamma halkaları.

2010 Mathematics Subject Classification. 16Y99

1. INTRODUCTION AND PRELIMINARIES

N. Nobusawa [1] introduced the concept of a Γ-ring which is called the Γ-ring in the sense of Nobusawa. He obtained an analogue of the Wedderburn's Theorem for Γ-rings with minimum condition on left ideals. W. E. Barnes [2] gave the definition of a Γ-ring as a generalization of a ring and he also developed some other concepts of Γ-rings such as Γ-homomorphism, prime and primary ideals, m-systems etc. Γ-rings are closely related to others ternary structures as ternary algebras, associative triple systems and associative pairs, which have been extensively studied see [3], [4] and [5].

Let $\mathfrak{M}$ and Γ be two abelian groups. If there exists a mapping $\mathfrak{M} \times \Gamma \times \mathfrak{M} \to \mathfrak{M}$ (the image of (x, α, y) is denoted by $x\alpha y$ where $x, y \in \mathfrak{M}$ and $\alpha \in \Gamma$). We call $\mathfrak{M}$ a *Γ-ring* if the following conditions are satisfied:

1. $x\alpha y \in \mathfrak{M}$,

* Corresponding author. *Email address:* *brunoferreira@utfpr.edu.br*

2. $(x+y)\alpha z = x\alpha z + y\alpha z, x\alpha(y+z) = x\alpha y + x\alpha z,$
3. $x(\alpha+\beta)y = x\alpha y + x\beta y,$
4. $(x\alpha y)\beta z = x\alpha(y\beta z),$

for all $x, y, z \in \mathfrak{M}$ and $\alpha, \beta \in \Gamma$.

A nonzero element $1 \in \mathfrak{M}$ is called a multiplicative γ-identity of $\mathfrak{M}$ or *γ-unity element* (for some $\gamma \in \Gamma$) if $1\gamma x = x\gamma 1 = x$ for all $x \in \mathfrak{M}$. A nonzero element $e_1 \in \mathfrak{M}$ is called a *γ_1-idempotent* (for some $\gamma_1 \in \Gamma$) if $e_1\gamma_1 e_1 = e_1$ and a *nontrivial γ_1-idempotent* if it is a γ_1-idempotent different from multiplicative γ_1-identity element of $\mathfrak{M}$.

Let Γ and $\mathfrak{M}$ be two abelian groups such that $\mathfrak{M}$ is a Γ-ring and $e_1 \in \mathfrak{M}$ a nontrivial γ_1-idempotent. Let us consider $e_2 : \Gamma \times \mathfrak{M} \to \mathfrak{M}$ and $e'_2 : \mathfrak{M} \times \Gamma \to \mathfrak{M}$ two $\mathfrak{M}$-additive maps verifying the conditions $e_2(\gamma_1, a) = a - e_1\gamma_1 a$ and $e_{2'}(a, \gamma_1) = a - a\gamma_1 e_1$. Let us denote $e_2 \alpha a = e_2(\alpha, a)$, $a\alpha e_2 = e_{2'}(a, \alpha)$, $1_1 \alpha a = e_1 \alpha a + e_2 \alpha a$, $a\alpha 1_1 = a\alpha e_1 + a\alpha e_2$ and suppose $(a\alpha e_2)\beta b = a\alpha(e_2 \beta b)$ for all $a, b \in \mathfrak{M}$ and $\alpha, \beta \in \Gamma$. Then $1_1\gamma_1 a = a\gamma_1 1_1 = a$ and $(a\alpha 1_1)\beta b = a\alpha(1_1 \beta b)$, for all $a, b \in \mathfrak{M}$ and $\alpha, \beta \in \Gamma$, allowing us to write $1_1 = e_1 + e_2$ and $\mathfrak{M}$ as a direct sum of subgroups $\mathfrak{M} = \mathfrak{M}_{11} \oplus \mathfrak{M}_{12} \oplus \mathfrak{M}_{21} \oplus \mathfrak{M}_{22}$, where $\mathfrak{M}_{ij} = e_i\gamma_1\mathfrak{M}\gamma_1 e_j \ (i, j = 1,2)$, called *Peirce decomposition* of $\mathfrak{M}$ relative to e_1, satisfying the multiplicative relations:

1. $\mathfrak{M}_{ij}\Gamma\mathfrak{M}_{kl} \subseteq \mathfrak{M}_{il} \ (i, j, k, l = 1,2)$;
2. $\mathfrak{M}_{ij}\gamma_1\mathfrak{M}_{kl} = 0$ if $j \neq k \ (i, j, k, l = 1,2)$.

For the reader interested in the Peirce decomposition of Γ-rings we indicate [6]. If $\mathfrak{A}$ and $\mathfrak{B}$ are subsets of a Γ-ring $\mathfrak{M}$ and $\Theta \subseteq \Gamma$, we denote $\mathfrak{A}\Theta\mathfrak{B}$ the subset of $\mathfrak{M}$ consisting of all finite sums of the form $\sum_i a_i\gamma_i b_i$ where $a_i \in \mathfrak{A}, \gamma_i \in \Theta$ and $b_i \in \mathfrak{B}$. A *right ideal (resp., left ideal)* of a Γ-ring $\mathfrak{M}$ is an additive subgroup $\mathfrak{I}$ of $\mathfrak{M}$ such that $\mathfrak{I}\Gamma\mathfrak{M} \subseteq \mathfrak{I}$ (resp., $\mathfrak{M}\Gamma\mathfrak{I} \subseteq \mathfrak{I}$). If $\mathfrak{I}$ is both a right and a left ideal of $\mathfrak{M}$, then we say that $\mathfrak{I}$ is an *ideal* or *two-side ideal* of $\mathfrak{M}$.

An ideal $\mathfrak{P}$ of a Γ-ring $\mathfrak{M}$ is called *prime* if for any ideals $\mathfrak{A}, \mathfrak{B} \subseteq \mathfrak{M}$, $\mathfrak{A}\Gamma\mathfrak{B} \subseteq \mathfrak{P}$ implies that $\mathfrak{A} \subseteq \mathfrak{P}$ or $\mathfrak{B} \subseteq \mathfrak{P}$. A Γ-ring $\mathfrak{M}$ is said to be *prime* if the zero ideal is prime.

Theorem 1.1 *[7, Theorem 4] If $\mathfrak{M}$ is a Γ-ring, the following conditions are equivalent:*

1. $\mathfrak{M}$ is a prime Γ-ring;
2. if $a, b \in \mathfrak{M}$ and $a\Gamma\mathfrak{M}\Gamma b = 0$, then $a = 0$ or $b = 0$.

Let $\mathfrak{M}_i$ and $\Gamma_i \ (i = 1,2)$ be abelian groups such that $\mathfrak{M}_i$ is a Γ_i-ring $(i = 1,2)$. An ordered pair (φ, ϕ) of mappings is called a *multiplicative isomorphism* of $\mathfrak{M}_1$ onto $\mathfrak{M}_2$ if they satisfy the following properties:

1. φ is a bijective mapping from $\mathfrak{M}_1$ onto $\mathfrak{M}_2$;
2. ϕ is a bijective mapping from Γ_1 onto Γ_2;
3. $\varphi(x\gamma y) = \varphi(x)\phi(\gamma)\varphi(y)$ for all $x, y \in \mathfrak{M}_1$ and $\gamma \in \Gamma_1$.

We say that a multiplicative isomorphism (φ, ϕ) of $\mathfrak{M}_1$ onto $\mathfrak{M}_2$ is *additive* when $\varphi(x+y) = \varphi(x) + \varphi(y)$ for all $x, y \in \mathfrak{M}_1$.

2. GAMMA RINGS AND THE MULTIPLICATIVE ISOMORPHISMS

The study of the question of when a multiplicative isomorphism is additive has become an active research area in associative ring theory. In this case, one often tries to establish conditions on the ring

which assures the additivity of every multiplicative isomorphism defined on it. The first result in this direction is due to Martindale III [8] who obtained a pioneer result in 1969, where in his condition requires that the ring possesses idempotents. In recent papers [9],[10] Ferreira has studied the additivity of elementary maps and multiplicative derivation on Gamma rings. This motivated us in the present paper we investigate the problem of when a multiplicative isomorphism is additive for the class of gamma rings.

Let us state our main theorem.

Theorem 2.1 *Let $\mathfrak{M}$ be a Γ-ring containing a family $\{e_\alpha|\alpha \in \Lambda\}$ of nontrivial γ_α-idempotents which satisfies:*

1. If $x \in \mathfrak{M}$ is such that $x\Gamma\mathfrak{M} = 0$, then $x = 0$;
2. If $x \in \mathfrak{M}$ is such that $e_\alpha\Gamma\mathfrak{M}\Gamma x = 0$ for all $\alpha \in \Lambda$, then $x = 0$ (and hence $\mathfrak{M}\Gamma x = 0$ implies $x = 0$);
3. For each $\alpha \in \Lambda$ and $x \in \mathfrak{M}$, if $(e_\alpha\gamma_\alpha x\gamma_\alpha e_\alpha)\Gamma\mathfrak{M}\Gamma(1_\alpha - e_\alpha) = 0$ then $e_\alpha\gamma_\alpha x\gamma_\alpha e_\alpha = 0$.

Then any multiplicative isomorphism (φ, ϕ) of $\mathfrak{M}$ onto an arbitrary gamma ring is additive.

The following lemmas have the same hypotheses of Theorem 2.1 and we need these lemmas for the proof of this theorem. Thus, let us consider $e_1 \in \{e_\alpha|\alpha \in \Lambda\}$ a nontrivial γ_1-idempotent of $\mathfrak{M}$ and .

Lemma 2.1 $\varphi(0) = 0$.

Proof. Since φ is onto, we can choose $x \in \mathfrak{M}$ such that $\varphi(x) = 0$. Thus $\varphi(0) = \varphi(0\gamma_1 x) = \varphi(0)\phi(\gamma_1)\varphi(x) = \varphi(0)\phi(\gamma_1)0 = 0$.

Lemma 2.2 $\varphi(x_{ii} + x_{jk}) = \varphi(x_{ii}) + \varphi(x_{jk}), j \neq k$.

Proof. First assume that $i = j = 1$ and $k = 2$. Since φ is onto, let z be an element of $\mathfrak{M}$ such that $\varphi(z) = \varphi(x_{11}) + \varphi(x_{12})$. For arbitrary $\gamma \in \Gamma$ and $a_{1l} \in \mathfrak{M}_{1l}$ $(l = 1,2)$ we have

$\varphi(z\gamma_1 e_1\gamma a_{1l}) = \varphi(z)\phi(\gamma_1)\varphi(e_1\gamma a_{1l}) = (\varphi(x_{11}) + \varphi(x_{12}))\phi(\gamma_1)\varphi(e_1\gamma a_{1l}) =$
$\varphi(x_{11}\gamma_1 e_1\gamma a_{1l}) + \varphi(x_{12}\gamma_1 e_1\gamma a_{1l}) = \varphi(x_{11}\gamma_1 e_1\gamma a_{1l}) + \varphi(0) = \varphi((x_{11} + x_{12})\gamma_1 e_1\gamma a_{1l})$.

Hence $(z - (x_{11} + x_{12}))\gamma_1 e_1\gamma a_{1l} = 0$. In a similar way, for $a_{2l} \in \mathfrak{M}_{2l}$ $(l = 1,2)$ we get that $(z - (x_{11} + x_{12}))\gamma_1 e_1\gamma a_{2l} = 0$. It follows that

$$(z - (x_{11} + x_{12}))\gamma_1 e_1\gamma a = 0, \tag{1}$$

where $a = a_{11} + a_{12} + a_{21} + a_{22}$. Next, for arbitraries $\gamma \in \Gamma$ and $a_{1l} \in \mathfrak{M}_{1l}$ $(l = 1,2)$ we have

$\varphi(z\gamma_1 e_2\gamma a_{1l}) = \varphi(z)\phi(\gamma_1)\varphi(e_2\gamma a_{1l}) = (\varphi(x_{11}) + \varphi(x_{12}))\phi(\gamma_1)\varphi(e_2\gamma a_{1l}) =$
$\varphi(x_{11}\gamma_1 e_2\gamma a_{1l}) + \varphi(x_{12}\gamma_1 e_2\gamma a_{1l}) = \varphi(0) + \varphi(x_{12}\gamma_1 e_2\gamma a_{1l}) = \varphi((x_{11} + x_{12})\gamma_1 e_2\gamma a_{1l})$

which implies $(z-(x_{11}+x_{12}))\gamma_1 e_2 \gamma a_{1l}=0$. In a similar way, we get that $(z-(x_{11}+x_{12}))\gamma_1 e_2 \gamma a_{2l}=0$. Hence

$$(z-(x_{11}+x_{12}))\gamma_1 e_2 \gamma a=0, \tag{2}$$

where $a=a_{11}+a_{12}+a_{21}+a_{22}$, by condition *(i)* of the Theorem. From (1) and (2), we have $(z-(x_{11}+x_{12}))\gamma_1 1_1 \gamma a=0$, where $a=a_{11}+a_{12}+a_{21}+a_{22}$, which implies $(z-(x_{11}+x_{12}))\Gamma\mathfrak{M}=0$ and resulting in $z=x_{11}+x_{12}$, by condition *(i)* of the Theorem.

Now assume that $i=k=1$ and $j=2$. Again, we may find an element z of $\mathfrak{M}$ such that $\varphi(z)=\varphi(x_{11})+\varphi(x_{21})$. For arbitraries $\gamma\in\Gamma$ and $a_{l1}\in\mathfrak{M}_{l1}$ $(l=1,2)$ we have
$\varphi(a_{l1}\gamma e_1\gamma_1 z)=\varphi(a_{l1}\gamma e_1)\phi(\gamma_1)\varphi(z)=\varphi(a_{l1}\gamma e_1)\phi(\gamma_1)(\varphi(x_{11})+\varphi(x_{21}))=$
$\varphi(a_{l1}\gamma e_1\gamma_1 x_{11})+\varphi(a_{l1}\gamma e_1\gamma_1 x_{21})=\varphi(a_{l1}\gamma e_1\gamma_1 x_{11})+\varphi(0)=\varphi(a_{l1}\gamma e_1\gamma_1(x_{11}+x_{21}))$.
It follows that $a_{l1}\gamma e_1\gamma_1(z-(x_{11}+x_{21}))=0$. In a similar way, for arbitraries $\gamma\in\Gamma$ and $a_{l2}\in\mathfrak{M}_{l2}$ $(l=1,2)$ we get that $a_{l2}\gamma e_1\gamma_1(z-(x_{11}+x_{21}))=0$. This implies

$$a\gamma e_1\gamma_1(z-(x_{11}+x_{21}))=0, \tag{3}$$

where $a=a_{11}+a_{12}+a_{21}+a_{22}$. Next, for arbitraries $\gamma\in\Gamma$ and $a_{l1}\in\mathfrak{M}_{l1}$ $(l=1,2)$ we have
$\varphi(a_{l1}\gamma e_2\gamma_1 z)=\varphi(a_{l1}\gamma e_2)\phi(\gamma_1)\varphi(z)=\varphi(a_{l1}\gamma e_2)\phi(\gamma_1)(\varphi(x_{11})+\varphi(x_{21}))=$
$\varphi(a_{l1}\gamma e_2\gamma_1 x_{11})+\varphi(a_{l1}\gamma e_2\gamma_1 x_{21})=\varphi(0)+\varphi(a_{l1}\gamma e_2\gamma_1 x_{11})=\varphi(a_{l1}\gamma e_2\gamma_1(x_{11}+x_{21}))$.
It follows that $a_{l1}\gamma e_2\gamma_1(z-(x_{11}+x_{21}))=0$. In a similar way, for arbitraries $\gamma\in\Gamma$ and $a_{l2}\in\mathfrak{M}_{l2}$ $(l=1,2)$ we get that $a_{l2}\gamma e_2\gamma_1(z-(x_{11}+x_{21}))=0$ which implies

$$a\gamma e_2\gamma_1(z-(x_{11}+x_{21}))=0, \tag{4}$$

where $a=a_{11}+a_{12}+a_{21}+a_{22}$, by condition *(i)* of the Theorem. From (3) and (4) we have $a\gamma 1_1\gamma_1(z-(x_{11}+x_{21}))=0$ which implies $\mathfrak{M}\Gamma(z-(x_{11}+x_{21}))=0$ resulting in $z=x_{11}+x_{21}$, by condition *(ii)* of the Theorem.

Similarly, we prove the remaining cases.

Lemma 2.3 $\varphi(a_{1j}+b_{12}\gamma c_{1l})=\varphi(a_{1j})+\varphi(b_{12}\gamma c_{1l})$ $(j,l=1,2)$

Proof. First, let us note that

$$a_{1j}+b_{12}\gamma c_{1l}=(e_1+b_{12})\gamma_1(a_{1j}+e_2\gamma c_{1l}).$$

Hence

$$\varphi(a_{1j}+b_{12}\gamma c_{1l})=\varphi((e_1+b_{12})\gamma_1(a_{1j}+e_2\gamma c_{1l}))=\varphi(e_1+b_{12})\phi(\gamma_1)\varphi(a_{1j}+e_2\gamma c_{1l})=(\varphi(e_1)+\varphi(b_{12}))\phi(\gamma_1)\varphi(a_{1j}+e_2\gamma c_{1l})=\varphi(e_1)\phi(\gamma_1)\varphi(a_{1j}+e_2\gamma c_{1l})+\varphi(b_{12})\phi(\gamma_1)\varphi(a_{1j}+e_2\gamma c_{1l})=\varphi(a_{1j})+\varphi(b_{12}\gamma a_{1j})$$

, by Lemma 2.2.

Lemma 2.4 *φ is additive on $\mathfrak{M}_{12}$.*

Proof. Let $x_{12}, y_{12}\in\mathfrak{M}_{12}$ and choose $z\in\mathfrak{M}$ such that $\varphi(z)=\varphi(x_{12})+\varphi(y_{12})$, where $z=z_{11}+z_{12}+z_{21}+z_{22}$. For an arbitrary $a_{1l}\in\mathfrak{M}_{1l}$ $(l=1,2)$ we have

$$\varphi(z\gamma_1 e_1\gamma a_{1l})=\varphi(z)\phi(\gamma_1)\varphi(e_1\gamma a_{1l})=(\varphi(x_{12})+\varphi(y_{12}))\phi(\gamma_1)\varphi(e_1\gamma a_{1l})=\varphi(x_{12}\gamma_1 e_1\gamma a_{1l})+\varphi(y_{12}\gamma_1 e_1\gamma a_{1l})=0$$

which implies $z\gamma_1 e_1\gamma a_{1l}=0$. It follows that $(z-(x_{12}+y_{12}))\gamma_1 e_1\gamma a_{1l}=0$. In a similar way, for an arbitrary $a_{2l}\in\mathfrak{M}_{2l}$ $(l=1,2)$ we get that $(z-(x_{12}+y_{12}))\gamma_1 e_1\gamma a_{2l}=0$. Hence

$$(z-(x_{12}+y_{12}))\gamma_1 e_1\gamma a=0, \tag{5}$$

where $a=a_{11}+a_{12}+a_{21}+a_{22}$. Now, for an arbitrary element $a_{1l}\in\mathfrak{M}_{1l}$ $(l=1,2)$ we have

$$\varphi(z\gamma_1 e_2\gamma a_{1l})=\varphi(z)\phi(\gamma_1)\varphi(e_2\gamma a_{1l})=(\varphi(x_{12})+\varphi(y_{12}))\phi(\gamma_1)\varphi(e_2\gamma a_{1l})=\varphi(x_{12}\gamma_1 e_2\gamma a_{1l})+\varphi(y_{12}\gamma_1 e_2\gamma a_{1l})=\varphi(x_{12}\gamma_1 e_2\gamma a_{1l}+y_{12}\gamma_1 e_2\gamma a_{1l})=\varphi((x_{12}+y_{12})\gamma_1 e_2\gamma a_{1l})$$

, by Lemma 2.3. It follows that $(z-(x_{12}+y_{12}))\gamma_1 e_2\gamma a_{1l}=0$. Next, for an arbitrary element $a_{2l}\in\mathfrak{M}_{2l}$ $(l=1,2)$ we have

$$\varphi(z\gamma_1 e_2\gamma a_{2l})=\varphi(z)\phi(\gamma_1)\varphi(e_2\gamma a_{2l})=(\varphi(x_{12})+\varphi(y_{12}))\phi(\gamma_1)\varphi(e_2\gamma a_{2l})=\varphi(x_{12})\phi(\gamma_1)\varphi(e_2\gamma a_{2l})+\varphi(y_{12}\phi(\gamma_1)\varphi(e_2\gamma a_{2l})=(\varphi(e_1)+\varphi(x_{12}))\phi(\gamma_1)(\varphi(e_2\gamma a_{2l})+\varphi(y_{12}\gamma_1 e_2\gamma a_{2l}))=\varphi(e_1+x_{12})\phi(\gamma_1)\varphi(e_2\gamma a_{2l}+y_{12}\gamma_1 e_2\gamma a_{2l})=\varphi(e_1+x_{12})\gamma_1(e_2\gamma a_{2l}+y_{12}\gamma_1 e_2\gamma a_{2l})=\varphi((x_{12}+y_{12})\gamma_1 e_2\gamma a_{2l})$$

, by Lemma 2.2. It follows that $(z-(x_{12}+y_{12}))\gamma_1 e_2\gamma a_{2l}=0$. Hence

$$(z-(x_{12}+y_{12}))\gamma_1 e_2\gamma a=0, \tag{6}$$

where $a=a_{11}+a_{12}+a_{21}+a_{22}$, by condition *(i)* of the Theorem. From (5) and (6) we have $(z-(x_{12}+y_{12}))\gamma_1 1_1\gamma a=0$ which implies $(z-(x_{12}+y_{12}))\Gamma\mathfrak{M}=0$ and resulting in $z=x_{12}+y_{12}$, by condition *(i)* of the Theorem.

Lemma 2.5 *φ is additive on $\mathfrak{M}_{11}$.*

Proof. Let $x_{11}, y_{11} \in \mathfrak{M}_{11}$ and choose $z \in \mathfrak{M}$ such that $\varphi(z) = \varphi(x_{11}) + \varphi(y_{11})$, where $z = z_{11} + z_{12} + z_{21} + z_{22}$. Firstly, let us note that $\varphi(z) = \varphi(x_{11}\gamma_1 e_1) + \varphi(y_{11}\gamma_1 e_1) = (\varphi(x_{11}) + \varphi(y_{11}))\phi(\gamma_1)\varphi(e_1) = \varphi(z)\phi(\gamma_1)\varphi(e_1) = \varphi(z_{11} + z_{21})$

It follows that $z = z_{11} + z_{21}$ which results in $z_{12} = z_{22} = 0$. Similarly, we prove that $z_{21} = 0$ .This implies $z \in M_{11}$ which leads to $z - (x_{11} + y_{11}) \in M_{11}$. Next, for an arbitrary element $a_{ij} \in \mathfrak{M}_{ij}$ $(i,j = 1,2)$, applying Lemma 2.4 we get that

$$\begin{aligned}
&\varphi(z\alpha e_k\gamma_1 a_{ij}\gamma_1 e_l\beta e_2)\\
&= \varphi(z)\phi(\alpha)\varphi(e_k\gamma_1 a_{ij}\gamma_1 e_l\beta e_2)\\
&= (\varphi(x_{11}) + \varphi(y_{11}))\phi(\alpha)\varphi(e_k\gamma_1 a_{ij}\gamma_1 e_l\beta e_2)\\
&= \varphi(x_{11})\phi(\alpha)\varphi(e_k\gamma_1 a_{ij}\gamma_1 e_l\beta e_2) + \varphi(y_{11})\phi(\alpha)\varphi(e_k\gamma_1 a_{ij}\gamma_1 e_l\beta e_2)\\
&= \varphi(x_{11}\alpha e_k\gamma_1 a_{ij}\gamma_1 e_l\beta e_2) + \varphi(y_{11}\alpha e_k\gamma_1 a_{ij}\gamma_1 e_l\beta e_2)\\
&= \varphi(x_{11}\alpha e_k\gamma_1 a_{ij}\gamma_1 e_l\beta e_2 + y_{11}\alpha e_k\gamma_1 a_{ij}\gamma_1 e_l\beta e_2)\\
&= \varphi((x_{11} + y_{11})\alpha e_k\gamma_1 a_{ij}\gamma_1 e_l\beta e_2)
\end{aligned}$$

$(k,l = 1,2)$ which implies $z\alpha e_k\gamma_1 a_{ij}\gamma_1 e_l\beta e_2 = (x_{11} + y_{11})\alpha e_k\gamma_1 a_{ij}\gamma_1 e_l\beta e_2$ and resulting in $(z - (x_{11} + y_{11}))\alpha e_k\gamma_1 a_{ij}\gamma_1 e_l\beta e_2 = 0$. It follows that

$$(z - (x_{11} + y_{11}))\alpha e_k\gamma_1 a\gamma_1 e_l\beta e_2 = 0(k,l = 1,2), \tag{7}$$

where $a = a_{11} + a_{12} + a_{21} + a_{22}$, by condition *(i)* of the Theorem.

From (7) we have $(z - (x_{11} + y_{11}))\alpha 1_1\gamma_1 a\gamma_1 1_1\beta e_2 = 0$ which implies $(z - (x_{11} + y_{11}))\alpha a\beta e_2 = 0$. It follows that $(z - (x_{11} + y_{11}))\Gamma\mathfrak{M}\Gamma(1_1 - e_1) = 0$, that is,

$$(e_1\gamma_1(z - (x_{11} + y_{11})\gamma_1 e_1)\Gamma\mathfrak{M}\Gamma(1_1 - e_1) = 0.$$

By condition *(iii)* of the Theorem we conclude that $z = x_{11} + y_{11}$.

Lemma 2.6 *φ is additive on $e_1\Gamma\mathfrak{M}$.*

Proof. Let $x, y \in \mathfrak{M}$ and $\lambda, \mu \in \Gamma$ be arbitrary elements and let us write $x = x_{11} + x_{12} + x_{21} + x_{22}$ and $y = y_{11} + y_{12} + y_{21} + y_{22}$. It follows that $e_1\lambda x = e_1\lambda x_{11} + e_1\lambda x_{12} + e_1\lambda x_{21} + e_1\lambda x_{22}$ and $e_1\mu y = e_1\mu y_{11} + e_1\mu y_{12} + e_1\mu y_{21} + e_1\mu y_{22}$. Hence, by Peirce decomposition properties of $\mathfrak{M}$ and making use of the Lemmas 2.2, 2.4 and 2.5, we can see that

$$\varphi(e_1\lambda x + e_1\mu y) = \varphi((e_1\lambda x_{11} + e_1\lambda x_{12} + e_1\lambda x_{21} + e_1\lambda x_{22})$$

$$+(e_1\mu y_{11} + e_1\mu y_{12} + e_1\mu y_{21} + e_1\mu y_{22}))$$

$$= \varphi((e_1\lambda x_{11} + e_1\mu y_{11}) + (e_1\lambda x_{21} + e_1\mu y_{21})$$

$$+(e_1\lambda x_{12} + e_1\mu y_{12}) + (e_1\lambda x_{22} + e_1\mu y_{22}))$$

$$= \varphi((e_1\lambda x_{11} + e_1\mu y_{11}) + (e_1\lambda x_{21} + e_1\mu y_{21}))$$

$$+\varphi((e_1\lambda x_{12} + e_1\mu y_{12}) + (e_1\lambda x_{22} + e_1\mu y_{22}))$$

$$= \varphi(e_1\lambda x_{11} + e_1\lambda x_{21}) + \varphi(e_1\mu y_{11} + e_1\mu y_{21})$$

$$+\varphi(e_1\lambda x_{12} + e_1\lambda x_{22}) + \varphi(e_1\mu y_{12} + e_1\mu y_{22})$$

$$= \varphi(e_1\lambda x_{11} + e_1\lambda x_{21} + e_1\lambda x_{12} + e_1\lambda x_{22})$$

$$+\varphi(e_1\mu y_{11} + e_1\mu y_{21} + e_1\mu y_{12} + e_1\mu y_{22})$$

$$= \varphi(e_1\lambda x) + \varphi(e_1\mu y)$$

holds true, as desired.

Proof of Theorem 2.1. Suppose that $x, y \in \mathfrak{M}$ and choose $z \in \mathfrak{M}$ such that $\varphi(z) = \varphi(x) + \varphi(y)$. Since φ is additive on $e_\alpha\Gamma\mathfrak{M}$ for all $\alpha \in \Lambda$, by Lemma 2.6, then for an arbitrary element $r \in \mathfrak{M}$ and elements $\lambda, \mu \in \Gamma$ we have

$$\varphi(e_\alpha\lambda r\mu z) = \varphi(e_\alpha)\phi(\lambda)\varphi(r)\phi(\mu)\varphi(z)$$

$$= \varphi(e_\alpha)\phi(\lambda)\varphi(r)\phi(\mu)(\varphi(x) + \varphi(y))$$

$$= \varphi(e_\alpha)\phi(\lambda)\varphi(r)\phi(\mu)\varphi(x) + \varphi(e_\alpha)\phi(\lambda)\varphi(r)\phi(\mu)\varphi(y)$$

$$= \varphi(e_\alpha \lambda r \mu x) + \varphi(e_\alpha \lambda r \mu y)$$

$$= \varphi(e_\alpha \lambda r \mu x + e_\alpha \lambda r \mu y)$$

$$= \varphi(e_\alpha \lambda r \mu (x + y)).$$

Hence $e_\alpha \lambda r \mu z = e_\alpha \lambda r \mu (x + y)$ which results in

$$e_\alpha \Gamma \mathfrak{M} \Gamma (z - (x + y)) = 0$$

for all $\alpha \in \Lambda$. From condition *(ii)* of the Theorem, we conclude that $z = x + y$. This shows that φ is additive on $\mathfrak{M}$.

Corollary 2.1 *Let $\mathfrak{M}$ be a prime Γ-ring containing a γ_1-idempotent e_1 ($\mathfrak{M}$ need not have a γ_1-identity element), where $\gamma_1 \in \Gamma$. Suppose $e_2 : \Gamma \times \mathfrak{M} \to \mathfrak{M}$, $e'_2 : \mathfrak{M} \times \Gamma \to \mathfrak{M}$ two $\mathfrak{M}$-additive maps such that $e_2(\gamma_1, a) = a - e_1 \gamma_1 a$, $e_{2'}(a, \gamma_1) = a - a\gamma_1 e_1$, for all $a \in \mathfrak{M}$, and if we denote $e_2 a a = e_2(a, a)$, $a a e_2 = e_{2'}(a, a)$, $1_1 a a = e_1 a a + e_2 a a$, $a a 1_1 = a a e_1 + a a e_2$, then $(a a e_2)\beta b = a\alpha(e_2 \beta b)$ for all $\alpha, \beta \in \Gamma$ and $a, b \in \mathfrak{M}$. Then any multiplicative isomorphism (φ, ϕ) of $\mathfrak{M}$ onto an arbitrary gamma ring is additive.*

Proof. The result follows directly from the Theorem 2.1.

Corollary 2.2 *Let $\mathfrak{M}$ be a prime Γ-ring containing a γ_1-idempotent and a γ_1-unity element, where $\gamma_1 \in \Gamma$. Then any multiplicative isomorphism (φ, ϕ) of $\mathfrak{M}$ onto an arbitrary gamma ring is additive.*

REFERENCES

[1] N. Nobusawa, On a generalization of the ring theory, Osaka J. Math., 1 (1964) 81-89.

[2] W. E. Barnes, On the gamma Nobusawa, Pacific J. Math., 18 (1966) 411-422.

[3] M.R. Hestenes, On a ternary algebra, Scripta Math., 29 (1973) 253-272.

[4] O. Loos, Assoziative Triplesysteme, Manuscripta Math., 7 (1972) 103-112.

[5] W.G. Lister, Ternary rings, Trans. Amer. Math. Soc., 154 (1971) 37-55.

[6] R. N. Mukherjee Some results on Γ-rings, Indian J. pure appl. Math., 34 (2003) 991-994.

[7] S. Kyuno, On prime gamma rings, Pacific J. Math., 75 (1978) 185-190.

[8] W. S. Martindale III, When are multiplicative mappings additive?, Proc. Amer. Math. Soc., 21 (1969) 695-698.

[9] B. L. M. Ferreira, Multiplicative derivation of gamma rings, Algebra, Groups and Geometries, 34 (2017) 401-406.

[10] B. L. M. Ferreira, Additivity of elementary maps on gamma ring, Extracta Mathematicae, 34 (2019) 61-76.

Cumhuriyet Science Journal
CSJ

e-ISSN: 2587-246X
ISSN: 2587-2680

Cumhuriyet Sci. J., Vol.40-4 (2019) 846-853

Investigation of Beta Radiation Absorption Properties of Tungstate and Molybdate Doped Wallpapers

Yusuf KAVUN [1*] ***Serkan URUŞ*** [2] ***, Ahmet TUTUŞ*** [3] ***, Selami EKEN*** [4] ***,***

Ruken ÖZBEK [2]

[1,*]*Kahramanmaras Sutcu Imam Univ, Vocational School of Health Services, Dept. of Medica Imaging Techniques, 46100, Kahramanmaras, Turkey*

[2] *Kahramanmaras Sutcu Imam Univ, Dept. Chemistry, 46100, Kahramanmaras, Turkey*

[3] *Kahramanmaras Sutcu Imam Univ, Fac Forestry, Dept Forest Ind. Engineering, Kahramanmaras, Turkey*

[4]*Kahramanmaras Sutcu Imam Univ, Fac Med, Dept Rad. Oncology, 46100, Kahramanmaras, Turkey*

Received: 03.08.2019; Accepted: 25.11.2019 *http://dx.doi.org/10.17776/csj.600967*

Abstract. It is very important that the shielding material used in radiation treatment and imaging centers can effectively protect against radiation and that this material is cost-effective. Therefore, studies are underway on the development of different types of shielding materials. In this study, radiation absorption properties of sodium tungstate (Na2WO4) and sodium molybdate (Na2MoO4) coated wall papers were investigated. The beta radiation absorption properties of these elements which are applied on wall papers in different densities (100% precipitated calcium carbonate (PCC), 2.5 g, 5 g, and 7.5 g amounts of Na2WO4 and Na2MoO4 and various thicknesses (0.172-0.258 mm) were investigated. The wallpapers were irradiated with 4 MeV-energized electrons and measurements were taken with the PTW brand electron detector. The linear absorption coefficients of the wallpapers were obtained and half value layer (HVL) and one-tenth value layer (TVL) were calculated from these results. According to the results, it is observed that the beta radiation absorption properties of these wallpapers increase as the density of Na2WO4 and Na2MoO4 increases and as the coating thickness increases in the coating materials used to cover the surface of the wallpapers.

Keywords**:** Wallpaper, Radiation shielding, Attenuation coefficient, Na2WO4, Na2MoO4.

Tungstat ve Molibdat Katkılı Duvar Kâğıtlarının Beta Radyasyon Absorbsiyon Özelliklerinin İncelenmesi

Özet. Radyasyonla tedavi ve görüntüleme merkezlerinde kullanılan zırhlama materyalinin etkin bir şekilde radyasyona karşı koruma sağlaması ve bu malzemenin düşük maliyetli olması çok önemlidir. Bu nedenle faklı zırhlama materyallerinin geliştirilmesi üzerinde çalışmalar devam etmektedir. Bu çalışmada, farklı yüzdelerde sodyum tungstat (Na2WO4) ve sodyum molibdat (Na2MoO4) ile kaplanmış duvar kâğıtlarının beta radyasyon soğurma özellikleri araştırılmıştır. Duvar kâğıtları üzerine farklı yoğunluklarda (% 100 çöktürülmüş kalsiyum karbonat (PCC), 2.5 gr, 5 gr, ve 7.5 gr.) Na2WO4 ve Na2MoO4 kaplanarak (0.172-0.258 mm aralığında) duvar kağıtlarının radyasyon soğurma özellikleri incelenmiştir. 4 MeV enerjili elektronlar ile kâğıtlar ışınlanmış ve PTW marka elektron detektörü ile ölçümler alınmıştır. Duvar kâğıtlarının lineer soğurma katsayıları elde edilerek bu sonuçlardan yarı değer kalınlığı (HVL) ve onda bir değer kalınlığı (TVL) hesaplanmıştır. Elde edilen sonuçlara göre duvar kâğıtlarının yüzeyini kaplamak için kullanılan kaplama materyallerinde Na2WO4 ve Na2MoO4 yoğunluğu arttıkça ve kaplama kalınlığı arttıkça bu kâğıtların beta radyasyonu soğurma özelliklerinin arttığı görülmektedir.

Anahtar Kelimeler: *D*uvar kâğıdı, Radyasyon zırhlama, Soğurma katsayısı, Na2WO4, Na2MoO4.

* Corresponding author. *Email address:* *yusufkavun@gmail.com*

1. INTRODUCTION

The use of radiation in the diagnosis and treatment of diseases and use in medical applications has been widely used. While technologically developed the diagnosis and imaging using radiation, it has some risks during application of radiation in treatment centers [1]. Therefore, radiation treatment centers have to take various precautions against any radiation leakage that may occur. Effective shielding during the various radiological applications is the first of these measures [2]. The various materials have been placed between a source and the target may affect the amount of radiation delivered from the source to the target [3]. The type of radiation-emitting substance, the released particle and energy level change the material to be used in shielding [4-6]. For example, Plexi glass is an effective way for the shielding against for Beta particles, X-ray and gamma ray. Radiation-protective materials are often used in hospitals, clinics, and dental practices to protect the patients and staffs from direct and secondary radiation during diagnostic imaging [7]. The radiation permeability depends on the structure of the protective materials [8].

In controlled and uncontrolled areas, the effective shielding can be designed to meet the recommended effective dose limits for staff and patients. These designs can be varied according to the characteristics of the devices to be used in the application and have certain standards [9]. Such as, while selecting the type of the material to form the shielding walls, it is assumed that the closest interaction must be the closest 0.3 m distance from the wall. In addition, the effective dose limits for the staff that are exposed to radiation are evaluated monthly in order to control the effectiveness of shielding [7]. In this study, as shown in figure 1, the beta radiation absorption properties of sodium tungstate (Na_2WO_4) and sodium molybdate (Na_2MoO_4) doped wallpaper samples were investigated. The beta radiation shielding properties of these doped wall paper samples in different densities and thicknesses were investigated.

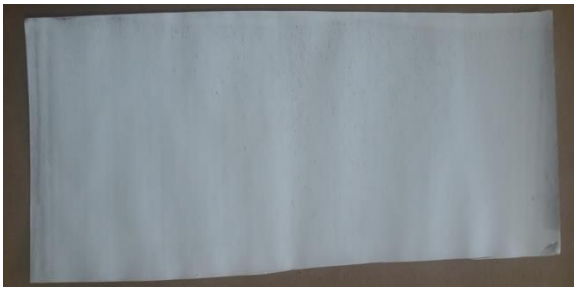

Figure 1. An example of Na_2WO_4 and Na_2MoO_4 doped wallpaper

2. MATERIALS AND METHODS

Within the scope of this research, 85 grams of wall papers were obtained from the market and used. Mixtures of sodium tungstate (Na_2WO_4) and sodium molybdate (Na_2MoO_4) salts (100% precipitated calcium carbonate (PCC), 2.5 gr., 5 gr., and 7.5 gr. of Na_2WO_4 and Na_2MoO_4) were applied on the surface of the wallpapers. The prepared wallpapers placed between solid phantoms using 4 MeV energy electrons were irradiated. VARIAN brand [9] linear accelerator was used for irradiation and PTW [10] brand electron detector was used for dose measurements. As can be seen in Figure 2, samples were placed at a distance of 100 cm from the gantry and the detector was placed just below the samples. Measurements were made in triplicate for each sample.

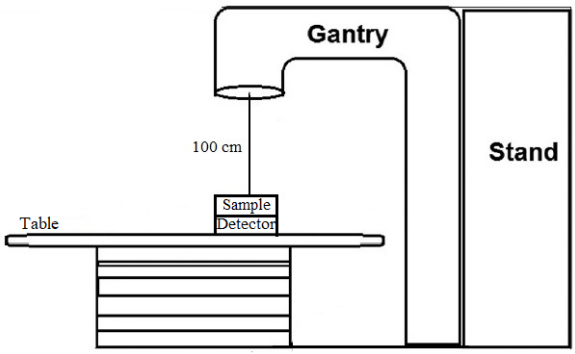

Figure 2. Experimental setup

The X-ray applied to the prepared wallpaper samples and solid phantom behave according to the properties of the absorber through which it passes. According to Beer-Lambert Law;

$$I = I_0 . e^{-\mu t} \quad (1)$$

I_0 is the sample-free counts, I sample counts, t (cm) is the thickness of the sample and μ (cm^{-1}) is the linear absorption coefficient. Equation (1) was used in the calculation of linear absorption coefficient and results were obtained according to the properties of the absorber material. The half value layer (HVL) [11, 12] is the material thickness required to reduce the intensity of the beam interacting with the material in half. One-tenth (1/10) value layer (TVL) is the material thickness required to reduce the intensity of the beam interacting with the material to 1/10 [12, 13].

$$HVL = \frac{\ln 2}{\mu} \quad (2)$$

$$TVL = \frac{\ln 10}{\mu} \quad (3)$$

High atomic and water soluble chemicals were selected for the study. According to these properties, sodium molybdate (Na_2MoO_4) with a density of 3.78 g / cm3 and sodium tungstate (Na_2WO_4) with 4.18 g / cm^3 were studied. The process of preparing the mortar and applying it on the wallpaper was done as follows: In order to develop different shielding materials that can be used in radiation application centers, mixtures containing sodium tungstate (Na_2WO_4) and sodium molybdate (Na_2MoO_4) salts were prepared separately by taking calcium carbonate (PCC) precipitated in 5%, 10% and 15% ratios, 15% starch and 85%, 80%, 75% and 70% ratios specified in the table below. Prepared mixtures and their ratios are shown in Tables 1 and 2.

Table 1. Preparation of Na_2MoO_4 doped coated mortar at different mixing ratios

Group	Na_2MoO_4 (%)	Starch (%)	PCC(%)
1	0	15	85
2	5	15	80
3	10	15	75
4	15	15	70

Table 2. Preparation of Na_2WO_4 doped coated mortar at different mixing ratios

Group	Na_2WO_4 (%)	Starch (%)	PCC (%)
1	0	15	85
2	5	15	80
3	10	15	75
4	15	15	70

3. RESULTS AND DISCUSSION

The main purpose of shielding in radiation treatment centers is to prevent the radiation released from the linear accelerator out of the treatment room as much as possible. This equivalent radiation dose is 0.02 mSv per week, except in public and uncontrolled areas [13]. The energy and amount of radiation interacting with the material determine the quality of material in shielding. HVL represents the material thickness required to reduce the amount of radiation to half and TVL to one tenth. The linear absorption coefficients, HVL and TVL values were calculated by applying 4 MeV energy electrons shown in Table 5. The HVL values of sodium molybdate (Na_2MoO_4) applied wallpaper samples having different densities ranged from the range of 16.91 to 115.52. The TVL values were between 9.36 and 383.76. The HVL values for sodium tungstate (Na_2WO_4) were between 14.44 and 63.01. The TVL values varied between 47.97 and 209.33. Figures 4 and 5 show the attenuation coefficient values applied 4 MeV energy electrons to the wallpaper samples doped with sodium molybdate (Na_2MoO_4) and sodium tungstate (Na_2WO_4). It was observed that the attenuation coefficient values increased depending on the thickness of the wallpapers doped with 3, 6 and 9 layers of material with different thicknesses. Accordingly, Figure 3 and 4 show the variation of HVL and TVL values. Figure 5 shows the comparison of HVL and TVL values obtained by using (2) and (3) equations. In Table 6, HVL and TVL values of concrete, steel and lead obtained at different energies used as radiation shielding materials in some radiotherapy centers are given. As shown in this table 6, lead has the lowest HVL and TVL values while concrete has the highest values. when in table 6 the HVL and TVL values of some materials values are compared with the Na_2MoO_4 and Na_2WO_4 in Table 5, it can be seen in table 5 that the values we obtained have higher HVL and TVL values. Accordingly, it is understood that these materials are not suitable for shielding use alone.

Table 3. Thickness and linear attenuation coefficient vales of wallpapers doped with sodium molybdate (Na_2MoO_4)

Layer	PCC Thick. (mm)	μ(cm^{-1})	2.5 gr Thick. (mm)	μ(cm^{-1})	5.0 gr Thick. (mm)	μ(cm^{-1})	7.5 gr Thick. (mm)	μ(cm^{-1})
3	0.172	0.021	0.199	0.006	0.197	0.013	0.183	0.009
6	0.181	0.029	0.225	0.011	0.213	0.020	0.213	0.023
9	0.184	0.041	0.246	0.017	0.235	0.023	0.241	0.028

Table 4. Thickness and linear attenuation coefficient vales of wallpapers coated with sodium tungstat (Na_2WO_4)

Layer	PCC Thick.(mm)	μ(cm^{-1})	2.5 gr Thick. (mm)	μ(cm^{-1})	5.0 gr Thick. (mm)	μ(cm^{-1})	7.5 gr Thick. (mm)	μ(cm^{-1})
3	0.186	0.044	0.212	0.017	0.208	0.014	0.209	0.011
6	0.192	0.046	0.223	0.024	0.236	0.018	0.226	0.021
9	0.197	0.048	0.230	0.027	0.258	0.026	0.243	0.025

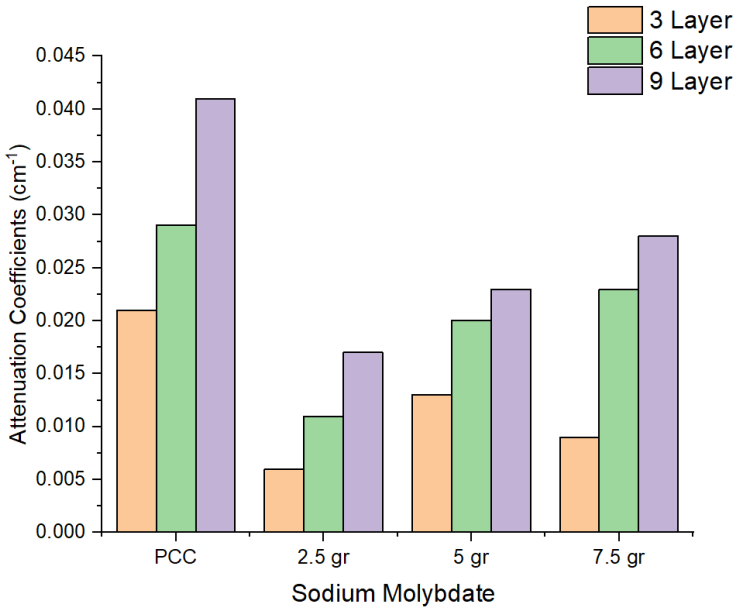

Figure 3. Linear attenuation coefficient values of wallpapers coated with sodium molybdate (Na_2MoO_4) obtained by applying 4 MeV energy electrons

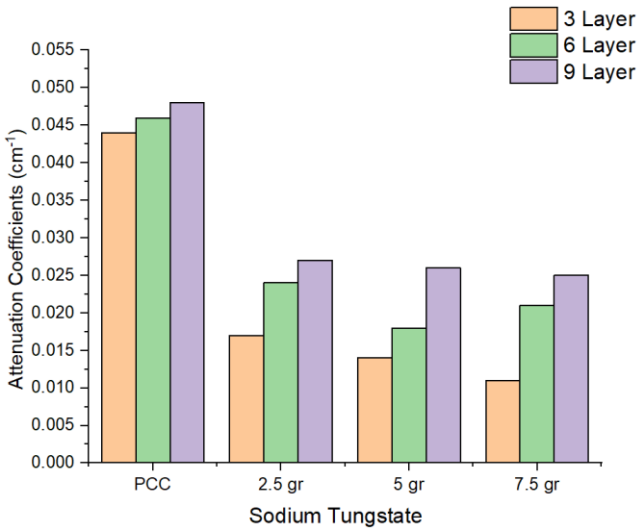

Figure 4. Linear attenuation coefficient values of wallpapers coated with sodium tungstate (Na_2WO_4) obtained by applying 4 MeV energy electrons

Table 5. Calculated HVL and TVL values

(Na_2MoO_4)				(Na_2WO_4)			
PCC Thickness	**μ(cm-1)**	**HVL**	**TVL**	**PCC Thickness**	**μ(cm-1)**	**HVL**	**TVL**
0.172	0.021	33.01	11.57	0.186	0.044	15.75	52.33
0.181	0.029	23.90	10.23	0.192	0.046	15.07	50.06
0.184	0.041	16.91	9.36	0.197	0.048	14.44	47.97
2.5 gr Thickness				**2.5 gr Thickness**			
0.199	0.006	115.52	383.76	0.212	0.017	40.77	135.45
0.225	0.011	63.01	209.33	0.223	0.024	28.88	95.94
0.246	0.017	40.77	135.45	0.23	0.027	25.67	85.28
5.0 gr Thickness				**5.0 gr Thickness**			
0.197	0.013	53.32	177.12	0.208	0.014	49.51	164.47
0.213	0.02	34.66	115.13	0.236	0.018	38.51	127.92
0.235	0.023	30.14	100.11	0.258	0.026	26.66	88.56
7.5 gr Thickness				**7.5 gr Thickness**			
0.183	0.009	77.02	255.84	0.209	0.011	63.01	209.33
0.213	0.023	30.14	100.11	0.226	0.021	33.01	109.65
0.241	0.028	24.76	82.24	0.243	0.025	27.73	92.10

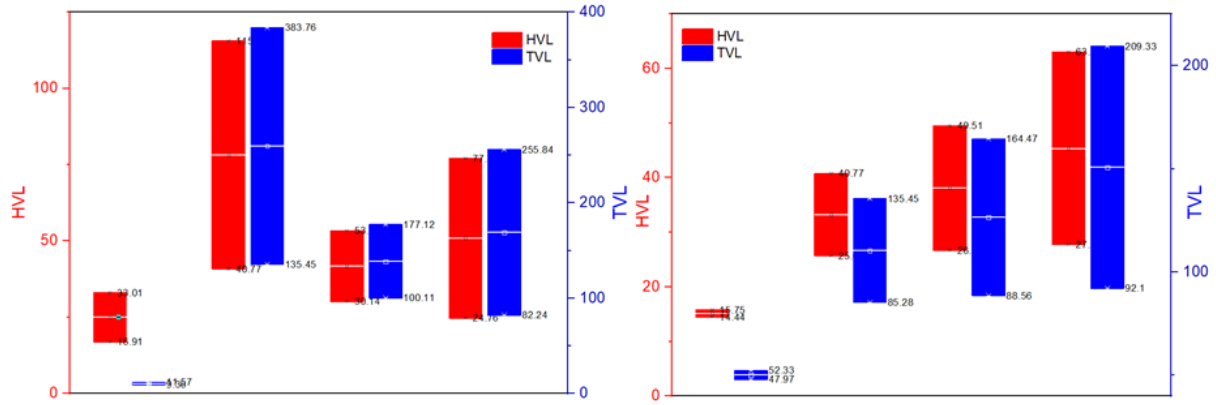

Figure 5. Calculated HVL and TVL values

Table 6. HVL and TVL values of some materials [14].

		HVL (cm)			TVL (cm)		
Isotope	**(MeV)**	**Concrete**	**Steel**	**Lead**	**Concrete**	**Steel**	**Lead**
^{137}Cs	0.66	4.8	1.6	0.65	15.7	5.3	2.1
^{60}Co	1.17, 1.33	6.2	2.1	1.2	20.6	6.9	4
^{198}Au	0.41	4.1		0.33	13.5		1.1
^{192}Ir	0.13 to 1.06	4.3	1.3	0.6	14.7	4.3	2
^{226}Ra	0.047 to 204	6.9	2.2	1.66	23.4	7.4	5.5

4. CONCLUSION

In this study, sodium tungstate (Na_2WO_4) and sodium molybdate (Na_2MoO_4) doped wallpaper samples prepared and used as the radiation shielding materials. The linear absorption coefficients were raised while the thickness of the doped material applied to the wallpapers and the amount of Na_2WO_4 and Na_2MoO_4 using 4 MeV energy electrons. Accordingly, HVL and TVL values of these materials were decreased. As

understood from these results, beta radiation permeability decreases with increasing amount of sodium tungstate and sodium molybdate. Therefore, sodium tungstate (Na_2WO_4) and sodium molybdate (Na_2MoO_4) salts can be used in radiation treatment by mixing together with other materials in the radiation treatment centers that require radiation shielding or in many areas where beta radiation is applied. These materials are not sufficient for use alone. Because, the obtained HVL-TVL values of sodium tungstate (Na_2WO_4) and sodium molybdate (Na_2MoO_4) were high when compared to the literature [14] (table 6). A successful shielding can be achieved when these materials are used in conjunction with low HVL and TVL materials in the future studies.

Na_2WO_4 and Na_2MoO_4 salts are used in different agent such as paints, textiles, plastics, crops, cleaning washings and pesticides [15]. As seen in the applications, it can be said that these compounds can be stable in the air having moisture. Nevertheless, to preserve the properties of these materials, it is suitable to coat the wallpaper surface with a coating material. Also, radiation treatment centers should be well ventilated and preserve against moisture. In addition, the chemical properties of the wallpaper surfaces can be preserved for a long time by coating them with materials such as gel or paint.

REFERENCES

[1] Köklü, N., Effects of Radiation on Human Health and Its Applıcatıon Fıelds in Medıcal, Master Thesis, Selçuk University, Institute of Science, 2006.

[2] Martin J. E., Physics for Radiation Protection: A Handbook", 2nd ed., Weinheim, WILEY-VCH Verlag GmbH & Co. KGaA, 2006.

[3] Aggrey-Smith S., Preko K., Owusu F. W., and Amoako J. K., Study of Radiation Shielding Properties of selected Tropical Wood Species for X-rays in the 50-150 keV Range, Journal of Science and Technology 4 (2016) 1-8.

[4] Abrath, F. G., Bello, J., and Purdy, J. A., Attenuation of Primary and Scatter Radiation in Concrete and Steel for 18 MeV X-Rays from a Clinac-20 Linear Accelerator., Health Physics, 45(5) (1983) 969-73.

[5] Barish, R. J., Evaluation of a New High-Density Shielding Material., Health Physics, 64(4) (1993) 412-6.

[6] Al-Affan, I. A. M., Estimation of the Dose at the Maze Entrance for X-Rays from Radiotherapy Linear Accelerators, Med. Phys., 27(1) (2000) 231-8.

[7] Çatak M.N., Shielding Linear Accelerator Devices According to NCRP–151 Report, Master Thesis, Ankara University, Institute of Science, 2012.

[8] Tel, E. Sarpun, İ. H., Şahan, M., Bulbul A. and Özgen, M., Analysis of Dose—Thickness Interaction with X-Rays Energy of 6 and 18 MeV for Beech Wooden Materials, Journal of Physical Science and Application, 7(2) (2017) 42-45.

[9] VARİAN, Varian Medical Systems, Clinac, On-Board Imager and Rapidarc, Are Registered Trademarks, And Exact and Laserguard Are Trademarks of Varian Medical Systems, Inc. 2012.

[10] PTW-Freiburg and Ptw-New York: Advanced Markus, Bragg Peak, Curıementor, Dıamentor, Farmer, Markus, Nomex, Octavıus, Pin Point, Roos, Trufix, 2017.

[11] Agar, O., et al., An extensive investigation on gamma ray shielding features of Pd/Ag-based alloys. Nuclear Engineering and Technology, 51(3) (2019) 853-859.

[12] Akkaş A., Determination of the Tenth and Half Value Layer Thickness of Concretes with Different Densities, Acta Physica Polonica A, 129 (2016) 770-772.

[13] Kavaz, E., et al., The Mass stopping power/projected range and nuclear shielding behaviors of barium bismuth borate glasses and influence of cerium oxide. Ceramics International, 45(12) (2019) 15348-15357.

[14] Safety Reports Series, Radiation Protection in the Design of Radiotherapy Facilities, IAEA, Vienna, No. 47, (2006), ISBN 92–0–100505–9.

[15] EPA Chemical and Products Database (CPDat), Adres:https://comptox.epa.gov/dashboard/dsstoxdb/results?search=DTXSID2052788#exposure. Retrieved November 18, 2019.

Cumhuriyet Science Journal
CSJ

e-ISSN: 2587-246X
ISSN: 2587-2680

Cumhuriyet Sci. J., Vol.40-4 (2019) 854-859

Application of Heterocyclic Compounds as Catalysts in Suzuki-Miyaura Cross-Coupling Reaction

Senem AKKOÇ[1,*]

[1] *Süleyman Demirel University, Faculty of Pharmacy, Department of Basic Pharmaceutical Sciences, 32260, Isparta, Turkey*

Received: ?; Accepted: ?

http://dx.doi.org/10.17776/csj.613060

Abstract. Four different benzimidazolium salts (**1-4**) were prepared in three steps at 80 ºC and their structures were elucidated using spectroscopic methods. The compounds (**1-4**) obtained were tested in *in situ* medium as catalyst in the carbon-carbon (C-C) bond formation reactions of two different boronic acid derivatives with various aryl halides in the presence of palladium acetate $(PdOAc)_2$ and sodium tertiarybutoxide ($NaOBu^t$) as a base. With this reaction, four coupling products (**5-8**) were synthesized in different yields ranging from 11 to 93%. Compound **2** from the carbene precursors tested in the Suzuki-Miyaura cross-coupling reaction was found to be a more effective catalyst candidate than others.

***Keywords*:** Suzuki-Miyaura coupling reaction, Benzimidazolium salt, Catalyst.

Suzuki-Miyaura Çapraz Eşleşme Reaksiyonunda Katalizör Olarak Heterosiklik Bileşiklerin Uygulanması

Özet. Dört farklı benzimidazolyum tuzu (**1-4**) üç basamakta 80 ºC de hazırlandı ve yapıları spektroskopik yöntemler kullanılarak aydınlatıldı. Elde edilen bileşikler (**1-4**), palladyum asetat $(PdOAc)_2$ ve bir baz olarak sodyum tersiyerbütoksitin ($NaOBu^t$) varlığında iki farklı boronik asit türevi ile farklı aril halojenürlerin karbon-karbon (C-C) bağ oluşum reaksiyonlarında katalizör olarak *in situ* ortamda test edildi. Bu reaksiyon ile dört eşleşme ürünü (**5-8**) %11 ile %93 arasında değişen farklı verimlerde sentezlendi. Suzuki-Miyaura çapraz eşleşme reaksiyonunda test edilen karben öncüllerinden bileşik **2** diğerlerinden daha etkili bir katalizör adayı olduğu bulundu.

***Anahtar Kelimeler*:** Suzuki-Miyaura eşleşme reaksiyonu, Benzimidazolyum tuzu, Katalizör.

1. INTRODUCTION

Compounds containing benzimidazole nucleus demonstrate a wide variety of biological activity properties such as anticancer, antitubercular antimicrobial, antifungal, antioxidant, antidiabetic and etc [1-13]. On the other hand, heterocyclic benzimidazole derivatives have different application area and can be used as catalysts [14-16] and sensors [17, 18]. Therefore, benzimidazoles and their derivatives are consumed in large quantities in the chemical, medical and biological industries. So, they are among the most frequently synthesized heterocyclic compounds in the research studies, too.

Many chemicals used in pharmaceutical and agricultural chemistry have C-C (carbon-carbon) and C-N (carbon-nitrogen) bonds. Therefore, the formation reactions of these bonds are used in the synthesis of many organic materials of industrial importance [19]. Suzuki-Miyaura, Mizoroki-Heck, Sonogashira-Hagihara, Stille, Negishi, Kumada-Tamao-Corriu and Hiyama cross-coupling reactions are important C-C bond formation reactions (Scheme 1).

* Corresponding author. *Email address:* *senemakkoc@sdu.edu.tr, sanem.akkoc44@gmail.com*

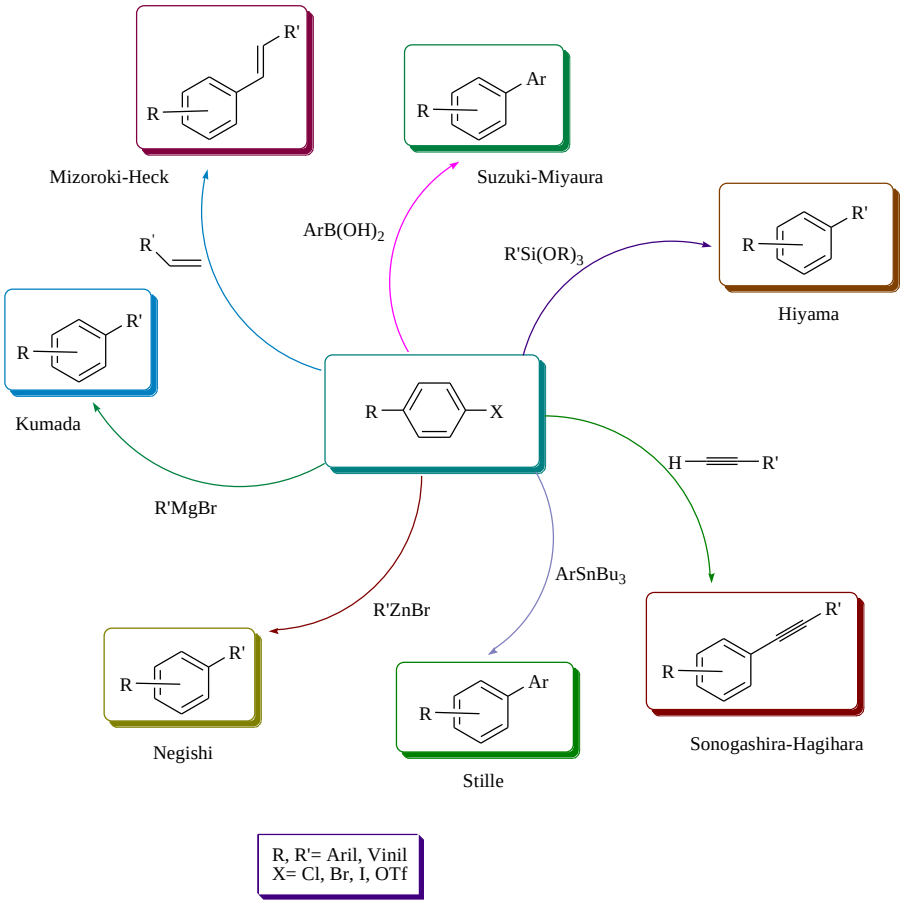

Scheme 1. Examples of C-C bond formation reactions.

Suzuki-Miyaura coupling reaction, which is the most studied species among the cross-coupling reactions, is the reaction to form biaryl derivatives with organoborane derivatives of aryl halides in the presence of palladium catalyst and a base. The fact that boronic acid compounds commonly used in these reactions are non-toxic, stable against to air and moisture, and are commercially easily find adds particular importance to Suzuki-Miyaura cross-coupling reactions.

Inspired by the wide application areas of benzimidazoles, in this study, four different benzimidazolium salts were synthesized in order to find effective catalyst candidates and their structures were characterized. The catalytic activity studies were done in the Suzuki-Miyaura reaction and catalysts generated from compounds **1-4** and $Pd(OAc)_2$ as *in situ* gave C-C coupling products in high yields for 2 h at 80 °C.

2. MATERIALS AND METHODS

2.1. Reagents

Necessary reagents for the synthesis of the targeted heterocyclic compounds (**1-4**) and their catalytic activity studies were commercially purchased from Sigma-Aldrich, Merck and Scharlau. These are 3-methylbenzyl chloride, 2-(bromomethyl) benzonitrile, 2-methylbenzyl chloride, 1-(chloromethyl)naphthalene, 3-methoxybenzyl chloride, thianaphthene-2-boronic acid, phenylboronic acid, 4-chloroacetophenone, 4-chlorotoluene, 4-chloroanisole, 4-chloronitrobenzene, potassium hydroxide (KOH), sodium tertiarybutoxide ($NaOBu^t$), *N*,*N*-dimethylformamide (DMF), dichloromethane, formic acid, hexane, ethyl acetate, ethyl alcohol and diethyl ether.

NMR and IR were used for characterize the structures of the compounds obtained. In Erciyes University Central Research Laboratory, both ^1H NMR and ^{13}C NMR spectra were taken with Bruker Ultra Shield 400 MHz NMR Spectroscopy using $CDCl_3$ or DMSO-d_6 solvents. FT-IR Spectra were recorded in the range of 400-4000 cm^{-1} by Pye Unicam spectroscopy.

Gas Chromatography (GC) was used to measure the catalytic activity of the generated compounds.

This was carried out by the SHIMADZU-2010 Plus (Kyoto, Japan) with a ROSTEK packed stainless steel column with a length and ID of 2.0 M, 2.0 mm respectively, was used with high purity nitrogen at a flow rate of 40 mL/min as a carrier gas and a flame ionization detector (FID) set at a temperature of 320 °C with an injection port temperature of 300 °C. Additionally, thermo Trace GC (Massachusetts, ABD) with Finnigan Polaris Q ion trap mass spectrometer in positive ion EI mode (GC-MS) was used to identify the catalytic activity results of some compounds in Suzuki-Miyaura coupling reaction. The instrument settings were used as injection port: 300 °C, injection type: split (1:20), injection volume: 1 µL (sample dissolved in 1 mL CH_2Cl_2 diluted 1:2), GC column: Zebron ZB5ms 30 m x 0.25 mm ID x 0.25 µm film thickness, carrier gas: helium (1.3 mL/min), oven program: 40 °C, hold 3 minutes, 12 °C/min ramp to 300 °C, hold 5 minutes, transfer line: 280 °C, MS temperature: 240 °C, EI electron energy: 70 eV, MS range: 46-650 m/z (3 minute solvent delay).

2.2. Synthesized benzimidazolium salts, 1-4

Four benzimidazolium salts (**1-4**) were prepared easily and economically according to the literature procedures [20] (Scheme 2) and their structures were characterized using different spectroscopic methods [20].

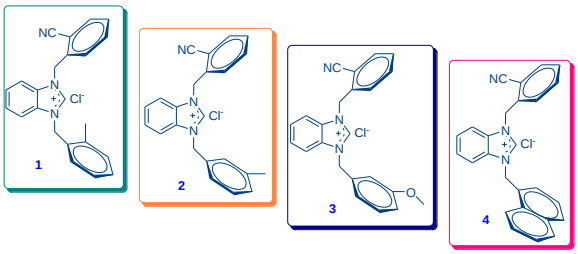

Scheme 2. The open structures of the synthesized benzimidazolium salts **1-4.**

2.3. Experimental protocol for the Suzuki-Miyaura coupling reaction

The catalytic activity studies were done according to the protocols in the literature [15, 16, 21]. Briefly, benzimidazolium salts (**2-5**), $Pd(OAc)_2$ (0.1 mmol), aryl chlorides (1 mmol), boronic acid derivatives (1.5 mmol) and $NaOBu^t$ (2 mmol) as base in DMF/H_2O (1:1) mixture as solvents were added to a 25 mL Schleng tube. The reaction was conducted at 80 °C for 2 h. After the specified period of time completed, the reaction temperature was dropped to room temperature. Ethyl acetate and hexane (1:5) were added on this reaction mixture and it mixed at rapidly. The two phases formed were separated and $MgSO_4$ was added to the organic phase for removing water. The products were purified with flash column chromatography using 5 mL of hexane and 1 mL of ethyl acetate as solvents. Final products were analyzed using GC.

3. RESULTS AND DISCUSSION

Catalytic activities of the compounds (**1-4**) were tested in Suzuki-Miyaura reaction. For this, benzimidazolium salt (**1-4**), $Pd(OAc)_2$, aryl chloride, phenylboronic acid/tianaphthene-2-boronic acid and $NaOBu^t$ were used. The reaction was carried out in DMF/H_2O mixture at 80 °C with heating for two hours. At the end of the this time (2 h), the waited product (**5-8**) was purified by column chromatography and analyzed using GC. The results obtained are presented in Table 1.

In the presence of catalysts synthesized from **1-4**/$Pd(OAc)_2$, various Suzuki-Miyaura coupling products (**5-8**) were obtained from the reaction of 4-chloronitrobenzene, 4-chloroanisole or 4-chlorotoluene with phenylboronic acid and 4-chloroacetophenone with tianaften-2-boronic acid. These are 1-phenyl-4-nitrobenzene (**5**), 1-phenyl-4-methoxybenzene (**6**), 1-phenyl-4-methylbenzene (**7**) and 1-(4-(benzo[*b*]thiophen-2-yl)phenyl ethanone (**8**). It is seen that from Table 1 the reaction yields of the Suzuki-Miyaura coupling products are between 11 and 93% and their conversions are among 11 and 98%.

The product 1-phenyl-4-nitrobenzene (**5**), formed from the coupling of phenylboronic acid with 4-chloronitrobenzene, was obtained in 27% yield using ligand **1** (Table 1, Entry 1) (Figure 1).

Table 1. Application of synthesized compounds as catalysts in the Suzuki-Miyaura cross-coupling reaction. [a]

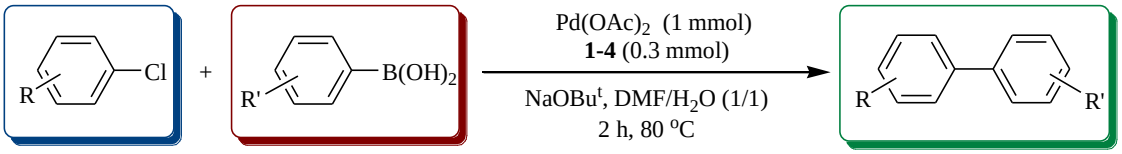

Entry	Aryl chloride	Boronic acid derivative	LHX	Product	Yield (%)	Conversion (%)
1	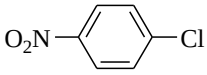	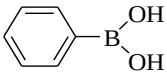	1	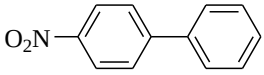 5	27	29
2			2		61	93
3			3		31	41
4			4		31	56
5	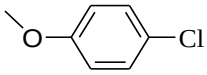		1	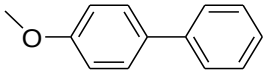 6	65	85
6			2		91	96
7			3		21	22
8			4		19	52
9	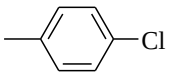		1	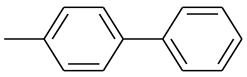 7	74	89
10			2		48	85
11			3		93	98
12			4		13	68
13	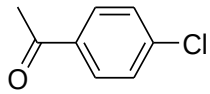	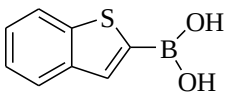	1	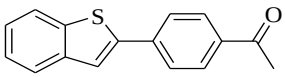 8	11	11
14			2		82	94
15			3		58	74
16			4		44	61

[a] Reaction conditions: *p*-R-C_6H_4Cl (1 mmol), $Pd(OAc)_2$, boronic acid derivative (1.5 mmol), $NaOBu^t$ (2 mmol), LHX (**1-4**), DMF-H_2O (2-2 mL), 80 °C, 2 h.

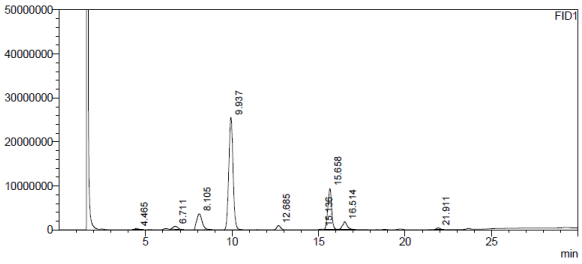

Figure 1. Carbon-Carbon coupling of 4-chloronitrobenzene with phenylboronic acid in the presence of $Pd(OAc)_2$ and compound **1**.

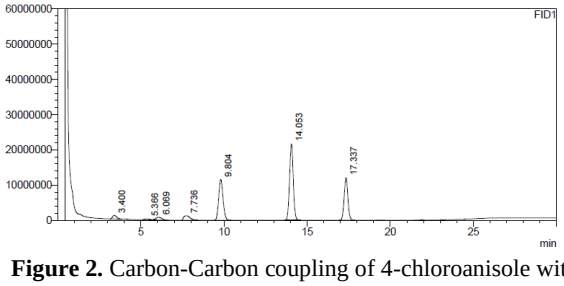

Figure 2. Carbon-Carbon coupling of 4-chloroanisole with phenylboronic acid in the presence of $Pd(OAc)_2$ and compound **1**.

The 1-phenyl-4-nitrobenzene (**5**) product was obtained in a higher yield in the presence of ligand **2** containing 3-methylbenzyl substituent (Table 1, entry 2). Furthermore, the highest yield was obtained when compound **2** was used in the coupling of 4-chloroanisole with phenyl boronic acid (Table 1, entry 6) (Figure 3).

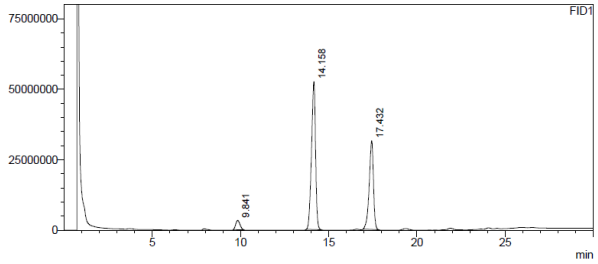

Figure 3. Carbon-Carbon coupling of phenylboronic acid with 4-chloroanisole in the presence of $Pd(OAc)_2$ and compound **2**.

Using compounds **1**, **2** and **4**, the images of results of C-C coupling of 4-chloroacetophenone with thianaphthene-2-boronic acid in the presence of $Pd(OAc)_2$ were given in the figures 4-6, respectively.

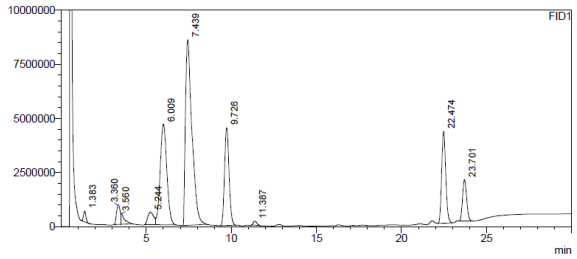

Figure 4. Carbon-Carbon coupling of 4-chloroacetophenone with thianaphthene-2-boronic acid in the presence of $Pd(OAc)_2$ and compound **1**.

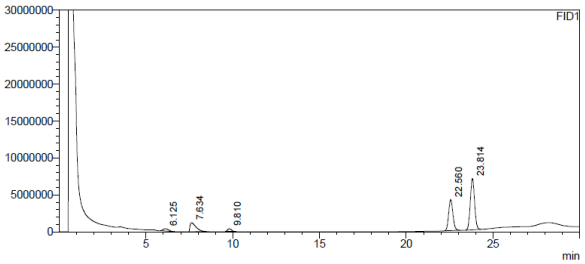

Figure 5. Carbon-Carbon coupling of 4-chloroacetophenone with thianaphthene-2-boronic acid in the presence of $Pd(OAc)_2$ and compound **2**.

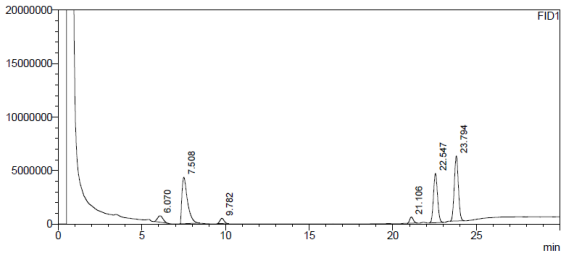

Figure 6. Carbon-Carbon coupling of 4-chloroacetophenone with thianaphthene-2-boronic acid in the presence of $Pd(OAc)_2$ and compound **4**.

The highest yield and conversion were obtained when ligand **3** was used to obtain 1-phenyl-4-methylbenzene (**7**) product (Table 1, entry 11). The lowest activity in the coupling of thianapheten-2-boronic acid with 4-chloroacetophenone was obtained when ligand **1** with 2-methylbenzyl substituent was used (Table 1, entry 13). On the other hand, the highest yield was obtained when ligand **2** was used in the same coupling reaction (Table 1, entry 14). This result attaches extreme importance to ligand **2**.

4. CONCLUSION

In this study, four different organic compounds were prepared according to the methods in the literature and their structures were characterized by various spectroscopic methods. These compounds were used as catalysts for the C-C coupling of various aryl halides with two different phenylboronic acids by interacting with $Pd(OAc)_2$ in *in situ* medium. Although the activities of the tested catalysts were generally obtained very close to each other, it was seen that the catalyst formed as *in situ* by using compound **2** was observed more active than the others.

REFERENCES

[1] Akkoç S., Derivatives of 1-(2-(Ppiperidin-1-yl)ethyl)-1H-benzo[d]imidazole: Synthesis, Ccharacterization, Ddetermining of Eelectronic Pproperties and Ccytotoxicity Sstudies, ChemistrySelect, 4 (2019) 4938-4943.

[2] Akkoç S., Kayser V. and İlhan İ.Ö., Synthesis and in vitro Aanticancer Eevaluation of Ssome Bbenzimidazolium Ssalts, J. Heterocycl. Chem. 56 (2019) 2934-2944in press.

[3] Popov A.B., Stolić I., Krstulović L., Taylor M.C., Kelly J.M., Tomić S., et al., Novel symmetric bis-benzimidazoles: Synthesis, DNA/RNA binding and antitrypanosomal activity, Eur. J. Med. Chem., 173 (2019) 63-

75.
[4] Zaman K., Rahim F., Taha M., Ullah H., Wadood A., Nawaz M., et al., Synthesis, in vitro urease inhibitory potential and molecular docking study of Benzimidazole analogues, Bioorg. Chem. 89 (2019) 103024.
[5] Sadaf H., Imtiaz ud D., Fettouhi M., Fazal A., Ahmad S., Farooqi B.A., et al., Synthesis, crystal structures and biological activities of palladium(II) complexes of benzimidazole and 2-methylbenzimidazole. Polyhedron, (2019).
[6] Fang Y., Zhou H., Gu Q. and Xu J., Synthesis and evaluation of tetrahydroisoquinoline-benzimidazole hybrids as multifunctional agents for the treatment of Alzheimer's disease, Eur. J. Med. Chem., 167 (2019) 133-145.
[7] Keri R.S., Rajappa C.K., Patil S.A. and Nagaraja B.M., Benzimidazole-core as an antimycobacterial agent, Pharmacol. Rep., 68 (2016)1254-1265.
[8] Akkoç S., Antiproliferative activities of 2-hydroxyethyl substituted benzimidazolium salts and their palladium complexes against human cancerous cell lines, Synth. Commun., 49 (2019) 2903-2914.
[9] Gök Y., Akkoç S., Çelikal Ö.Ö., Özdemir İ. and Günal S., In vitro antimicrobial studies of naphthalen-1-ylmethyl substituted silver N-heterocyclic carbene complexes, Arabian J. Chem., (2015).
[10] Singh I., Luxami V. and Paul K., Effective synthesis of benzimidazoles-imidazo[1,2-a]pyrazine conjugates: A comparative study of mono-and bis-benzimidazoles for antitumor activity, Eur. J. Med. Chem. 180 (2019) 546-561.
[11] Menteşe E., Emirik M. and Sökmen B.B., Design, molecular docking and synthesis of novel 5,6-dichloro-2-methyl-1H-benzimidazole derivatives as potential urease enzyme inhibitors, Bioorg. Chem., 86 (2019)151-158.
[12] Babkov D.A., Zhukowskaya O.N., Borisov A.V., Babkova V.A., Sokolova E.V., Brigadirova A.A., et al., Towards multi-target antidiabetic agents: Discovery of biphenyl-benzimidazole conjugates as AMPK activators, Bioorg. Med. Chem. Lett. 29 (2019) 2443-2447.
[13] Mohanty S.K., Khuntia A., Yellasubbaiah N., Ayyanna C., Naga Sudha B. and Harika M.S., Design, synthesis of novel azo derivatives of benzimidazole as potent antibacterial and anti tubercular agents, Beni-Suef Uni. J. Bas. Appl. Sci. 7 (2018) 646-651.
[14] Fukutake T., Wada K., Yu H., Hosokawa S. and Feng Q., Development of titania-supported iridium catalysts with excellent low-temperature activities for the synthesis of benzimidazoles via hydrogen transfer, Mol. Catal. 477 (2019) 110550.
[15] Akkoç S., Gök Y., lhan l.Ö. and Kayser V., In situ Ggeneration of Eefficient Ppalladium N-heterocyclic Ccarbene Ccatalysts Uusing Bbenzimidazolium Ssalts for the Suzuki-Miyaura Ccross-coupling Rreaction, Curr. Org. Synth., 13 (2016) 761-766.
[16] Akkoç S., Özer İlhan İ., Gök Y. and Kayser V., Carbon-carbon bond formation catalyzed by PEPPSI Pd-NHC, Inorg. Chim. Acta, 461 (2017) 52-56.
[17] Suman G.R., Bubbly S.G., Gudennavar S.B. and Gayathri V., Benzimidazole and benzothiazole conjugated Schiff base as fluorescent sensors for Al3+ and Zn2+, J. Photochem. Photobiol., A, 382 (2019) 111947.
[18] Suman G.R., Bubbly S.G. and Gudennavar S.B., Benzimidazole and benzothiazole fluorophores with large Stokes shift and intense sky-blue emission in aggregation as Al3+ and Pb2+ sensors, J. Lumin. 215 (2019) 116688.
[19] Weissermel K. and Arpe H-J., Industrial Organic Chemistry, Weinheim. 2008.
[20] Akkoç S., Kayser V., İlhan İ.Ö., Hibbs D.E., Gök Y., Williams P.A., et al., New compounds based on a benzimidazole nucleus: synthesis, characterization and cytotoxic activity against breast and colon cancer cell lines, J. Organomet. Chem. 839 (2017) 98-107.
[21] Aslan H.G., Akkoç S., Kökbudak Z. and Aydın L., Synthesis, characterization, and antimicrobial and catalytic activity of a new Schiff base and its metal(II) complexes, J. Iran. Chem. Soc. 14 (2017) 2263-2273.

Cumhuriyet Science Journal
CSJ

e-ISSN: 2587-246X
ISSN: 2587-2680

Cumhuriyet Sci. J., Vol.40-4 (2019) 860-866

Construction of Continuous Bivariate Distribution by Transmuting Dependent Distribution

Hüseyin ÜNÖZKAN [1], *Mehmet YILMAZ* [2*]

[1] *Ankara University, Graduate School of Natural and Applied Science, Department of Statistics, Turkey*

[2] *Ankara University, Faculty of Science, Department of Statistics, 06100, Ankara, Turkey*

Received: 10.09.2019; Accepted: 02.10.2019 *http://dx.doi.org/10.17776/csj.618236*

Abstract. In this study, a new bivariate distribution family is introduced by adding an appropriate term to independent class. By choosing a base distribution which is negatively dependent from the same marginals we derive a new distribution around the product of marginals, i.e. independent class of distribution. We note that the new distribution has additional parameter which would provide additional flexibility in applications. The joint probability density, joint reliability and reversed hazard rate functions of the new bivariate distribution are obtained. Furthermore, we obtain lower and upper bounds of Spearman's correlation coefficient. Two example are given to illustrate this family. This new bivariate continuous distribution can make more appropriate modeling of some data sets in terms of the Spearman rank coefficient.

***Keywords*:** Transmuted bivariate distribution, Dependence, Bivariate distribution, Spearman's Rho correlation coefficient, Fréchet bounds.

Bağımlı Dağılım Fonksiyonunun Dönüştürülmesi ile İki Boyutlu Sürekli Dağılım Fonksiyonu Oluşturulması

Özet. Bu çalışmada, bağımsız dağılım fonksiyonuna uygun bir terim eklenerek yeni bir iki boyutlu dağılım fonksiyonu tanıtılmıştır. Bu yeni dağılım karmaşık bir yapıda değildir. Aynı marjinallere sahip dağılım fonksiyonları sınıfından bir temel dağılım seçilerek, bağımsız dağılım fonksiyonu etrafında yeni dağılım türetilmiştir. Bu yeni dağılımın fazladan bir parametresi olup, uygulama alanlarında modelleme esnasında esneklik sağlayacağı düşünülmektedir. Bu yeni iki boyutlu dağılımın ortak olasılık yoğunluk fonksiyonu, ortak güvenirlilik fonksiyonu ve ters bozulma oranı fonksiyonu elde edilmiştir. Bunun yanı sıra, bu metot ile elde edilen yeni dağılım fonksiyonunun Spearman Sıra Korelasyonu katsayısı bakımından biraz daha esneklik kazandırabileceği söylenebilir.

Anahtar Kelimeler: *Dönüştürülmüş iki boyutlu dağılım, Bağımlılık, İki boyutlu dağılım, Spearman sıra korelasyonu, Fréchet sınırları.*

1. INTRODUCTION

In both statistical theory and practice, univariate models are sometimes insufficient to explain random phenomena. Bivariate distributions are very important in modeling dependent random quantities in many different areas. We need to construct a joint distribution with specific marginals and higher or lower correlations. Dolati and Ubeda-Flores [1] introduced a method based on the choice of pairs of order statistics of the marginal distributions. Lai and Xie [2] studied on construction of continuous bivariate distributions that possesses the Positive Quadrant Dependence property. According to similar work of [2], [3] introduces some conditions for negatively dependent families. Inspired by these studies, we desire to propose a simpler but useful model. After giving the necessary conditions to construct a new distribution,

* Corresponding author. *Email address:* *mehmetyilmaz@ankara.edu.tr*

Spearman's rank correlation coefficient is calculated on two illustrative examples and the usefulness of this family is discussed. Furthermore, some reliability properties are studied for this family.

Let (X_1, Y_1) and (X_2, Y_2) be two independent vectors of random variables with common distribution function $H(x,y)$. Note that, $H(x,y)$ belongs to the distribution family $\mathcal{F}(F,G)$ where F and G denote respectively marginals of X and Y. Let $X_{(1)}$, $X_{(2)}$ and $Y_{(1)}$, $Y_{(2)}$ be their corresponding order statistics. According to [4], consider the random vector

$$(Z_1, Z_2) = \begin{cases} (X_{(1)}, Y_{(2)}), \text{with probability } 1/2 \\ (X_{(2)}, Y_{(1)}), \text{ with probability } 1/2. \end{cases}$$

Then the distribution of (Z_1, Z_2) is given by

$$H_1(x,y) = H(x,y)[1 - \bar{H}(x,y)], \tag{1}$$

where $\bar{H}(x,y)$ denotes survival function of (X,Y) *i.e.*, $Pr(X > x, Y > y)$. If we consider the random vector

$$(T_1, T_2) = \begin{cases} (X_{(1)}, Y_{(1)}), \text{with probability } 1/2 \\ (X_{(2)}, Y_{(2)}), \text{ with probability } 1/2. \end{cases}$$

Then the distribution function of (T_1, T_2) is given by

$$H_2(x,y) = F(x)G(y) + H(x,y)\bar{H}(x,y). \tag{2}$$

If we look at the equations (1) and (2) immediately, it is possible to say that the model formed by obtaining a mixture of H_1 and H_2 is not a simple structure. With this in mind, our contribution is to propose a simpler model. According to eq. (2.1) and and the conditions (2.2)-(2.4) of Han (2011) [3], the following assumption is sufficient for our purpose: Suppose that $\psi(x,y) = -H(x,y)\bar{H}(x,y)$. Then we have a function defined as $H_1^*(x,y) = F(x)G(y) + \psi(x,y)$. For subsequent discussions, following theorem explains the necessity of having negative dependence (or independence) condition on $H(x,y)$.

Theorem1. Let $H(x,y)$ be a distribution function belongs to the distribution family $\mathcal{F}(F,G)$ which is differentiable on $\mathbb{R}^2$ and $h(x,y) = \frac{\partial^2 H(x,y)}{\partial x \partial y}$ denote the joint probability density function. Then $H_1^*(x,y) = F(x)G(y) - H(x,y)\bar{H}(x,y)$ is a distribution function if $H(x,y) \leq F(x)G(y)$, for all $(x,y) \in \mathbb{R}^2$ (or $H(x,y) = F(x)G(y)$, for all $(x,y) \in \mathbb{R}^2$).

Proof. Multivariate distribution function must satisfy following properties (see, Barlow and Proschan, 1975, Chapter 5), [4]:

(P1)

$$\lim_{x\to\infty} F(x)G(y) - H(x,y)\bar{H}(x,y) = G(y),$$

$$\lim_{y\to\infty} F(x)G(y) - H(x,y)\bar{H}(x,y) = F(x),$$

$$\lim_{x\wedge y\to\infty} F(x)G(y) - H(x,y)\bar{H}(x,y) = 1.$$

(P2) $\frac{\partial H_1^*(x,y)}{\partial x} \geq 0$ and $\frac{\partial H_1^*(x,y)}{\partial y} \geq 0$. For the simplicity $f_x = \frac{dF(x)}{dx}$ and $g_y = \frac{dG(y)}{dy}$. Then

$$\frac{\partial H_1^*(x,y)}{\partial x} = f_x G(y) - \frac{\partial H(x,y)}{\partial x}\bar{H}(x,y) - H(x,y)\frac{\partial \bar{H}(x,y)}{\partial x}$$
$$= f_x\big(G(y) - Pr(Y \le y|X = x)\bar{H}(x,y) + H(x,y)Pr(Y > y|X = x)\big)$$

Now, by noting that negatively dependence implies $Pr(Y \le y|X = x) \le G(y)$, then we have

$$\frac{\partial H_1^*(x,y)}{\partial x} \ge f_x\big(Pr(Y \le y|X = x)[1 - \bar{H}(x,y)] + H(x,y)Pr(Y > y|X = x)\big)$$
$$\ge 0.$$

Obviously, $\frac{\partial H_1^*(x,y)}{\partial y} \ge 0$.

(P3) $\frac{\partial^2 H_1^*(x,y)}{\partial x \partial y} \ge 0$. For the simplicity, let $h_0 = f(x)g(y)$, $H_0 = F(x)G(y)$ and $h_{xy} = \frac{\partial^2 H(x,y)}{\partial x \partial y}$. Then

$$\frac{\partial^2 H_1^*(x,y)}{\partial x \partial y} = h_0 - h_{xy}[H(x,y) + \bar{H}(x,y)] - \frac{\partial H(x,y)}{\partial x}\frac{\partial \bar{H}(x,y)}{\partial y} - \frac{\partial H(x,y)}{\partial y}\frac{\partial \bar{H}(x,y)}{\partial x}.$$

Now, according to Domma (2011) [5], by noting that negative dependence implies both $h_{xy}H(x,y) \le \frac{\partial H(x,y)}{\partial x}\frac{\partial H(x,y)}{\partial y}$ and $h_{xy}\bar{H}(x,y) \le \frac{\partial \bar{H}(x,y)}{\partial x}\frac{\partial \bar{H}(x,y)}{\partial y}$. Hence, we have

$$\frac{\partial^2 H_1^*(x,y)}{\partial x \partial y} \ge h_0 - \left[\frac{\partial H(x,y)}{\partial x} + \frac{\partial \bar{H}(x,y)}{\partial x}\right]\left[\frac{\partial H(x,y)}{\partial y} + \frac{\partial \bar{H}(x,y)}{\partial y}\right].$$

By considering $\frac{\partial \bar{H}(x,y)}{\partial x} = -f_x + \frac{\partial H(x,y)}{\partial x}$ and $\frac{\partial \bar{H}(x,y)}{\partial y} = -f_y + \frac{\partial H(x,y)}{\partial y}$, the expressions in square brackets are rewritten as $h_0 - 2f_y\frac{\partial H(x,y)}{\partial x} - 2f_x\frac{\partial H(x,y)}{\partial y} + 4\frac{\partial H(x,y)}{\partial x}\frac{\partial H(x,y)}{\partial y}$. After some simplification, the above inequality becomes:

$$\frac{\partial^2 H_1^*(x,y)}{\partial x \partial y} \ge 2\frac{\partial H(x,y)}{\partial x}\left(f_y - \frac{\partial H(x,y)}{\partial y}\right) + 2\frac{\partial H(x,y)}{\partial y}\left(f_x - \frac{\partial H(x,y)}{\partial x}\right)$$
$$\ge 0.$$

This completes the proof.

According to Therorem1, by assuming $H(x,y)$ be negatively dependent or independent, we can define a new pairs of random variables U and V as below:

$$(U,V) = \begin{cases} (T_1, T_2), & \text{with probability} \quad \alpha \\ (Z_1^*, Z_2^*), & \text{with probability} \quad 1-\alpha, \end{cases}$$

where (Z_1^*, Z_2^*) is distributed as H_1^*. Hence, the distribution of (U,V) is given by

$$F(x,y) = Pr(U \le x, V \le y) = \alpha H_2(x,y) + (1-\alpha)H_1^*(x,y)$$
$$= F(x)G(y) + (2\alpha - 1)H(x,y)\bar{H}(x,y). \quad (3)$$

By letting $\lambda = 2\alpha - 1$, where $\lambda \in [-1,1]$, eq. (3) can be rewritten as

$$F(x,y) = F(x)G(y) + \lambda H(x,y)\bar{H}(x,y). \quad (4)$$

$\lambda = 0$ indicates $F = F(x)G(y)$, $\lambda = -1$ indicates that F is negatively dependent and $\lambda = 1$ indicates that F is positively dependent. Note that, if $H(x,y) = F(x)G(y)$, F indicates well-known bivariate distribution which is called as Farlie-Gumbel-Morgenstern distribution (see, [6] and [7]).

We need the survival and probability density function for subsequent discussions. These functions are respectively given by

$$\bar{F}(x,y) = \bar{F}(x)\bar{G}(y) + \lambda H(x,y)\bar{H}(x,y)$$

and

$$f(x,y) = f(x)g(y) + \lambda h(x,y)[\bar{H}(x,y) + H(x,y)] - \lambda k(x,y),$$

where $k(x,y) = Pr(X \leq x|Y = y)Pr(Y > y|X = x) + Pr(X > x|Y = y)Pr(Y \leq y|X = x)$.

2. REVERSED HAZARD RATE OF THE NEW FAMILY OF BIVARIATE DISTRIBUTION

The bivariate reversed hazard is defined by Bismi [8] as $rv(x,y) = f(x,y)/F(x,y)$. Furthermore, the bivariate hazard rate function defined by Basu [9] as $r(x,y) = f(x,y)/\bar{F}(x,y)$. Analogously to the hazard gradient by Johnson and Kotz [10], Roy [11] defined the bivariate reversed hazard rate and the bivariate hazard rate as follows: $\boldsymbol{rv}_{1,2}(x,y) = (rv_1(x,y), rv_2(x,y))$, where

$$rv_1(x,y) = \frac{\partial log F(x,y)}{\partial x}, rv_2(x,y) = \frac{\partial log F(x,y)}{\partial y},$$

and $\boldsymbol{r}_{1,2}(x,y) = (r_1(x,y), r_2(x,y))$, where

$$r_1(x,y) = \frac{-\partial log \bar{F}(x,y)}{\partial x}, r_2(x,y) = \frac{-\partial log \bar{F}(x,y)}{\partial y}.$$

Reversed hazard rate gradients of $F(x,y)$ given by eq. (4) are as follows:

$$rv_1(x,y) = w(x,y,\lambda)rv_1(x,\infty) + (1 - w(x,y,\lambda))\left(rv_{1_H}(x,y) - r_{1_H}(x,y)\right),$$
$$rv_2(x,y) = w(x,y,\lambda)rv_2(\infty,y) + (1 - w(x,y,\lambda))\left(rv_{2_H}(x,y) - r_{2_H}(x,y)\right).$$

Accordingly, after some simplifications, bivariate reversed hazard rate can be given by

$$rv(x,y) = w(x,y,\lambda)rv_1(x,\infty)rv_2(\infty,y) + \big(1 - w(x,y,\lambda)\big)\big(rv_H(x,y) + r_H(x,y)\big)$$
$$-(1 - w(x,y,\lambda))\big[rv_{1_H}(x,y)r_{2_H}(x,y) + rv_{2_H}(x,y)r_{1_H}(x,y)\big],$$

where $w(x,y,\lambda) = \frac{F(x)G(y)}{F(x)G(y)+\lambda H(x,y)\bar{H}(x,y)}$.

3. LOWER AND UPPER BOUNDS ON SPEARMAN'S RHO MEASURE FOR THE NEW FAMILY OF BIVARIATE DISTRIBUTION

This section deals with obtaining bounds for the bivariate distribution family given by the eq. (4). According to Hoeffding [12] and Fréchet [13], for any bivariate distribution belonging to $\mathcal{F}(F,G)$ contains Fréchet a lower bound and an upper bound. These bounds are respectively defined as

$$F^-(x,y) = \max\{F(x) + G(y) - 1, 0\} \quad (5)$$
$$F^+(x,y) = \min\{F(x), G(y)\}. \quad (6)$$

For $F \in \mathcal{F}(F,G)$, Spearman's rho can be expressed as

$$\rho_S(X,Y) = 12 \int_{\mathbb{R}} \int_{\mathbb{R}} \{F(x,y) - F(x)G(y)\} dG(y) dF(x) \quad (7)$$

(see, Schweizer and Wolff [14]). The coefficient of Spearman's rho for the new family can be obtained by

$$\rho_s = 12\lambda \int_{\mathbb{R}} \int_{\mathbb{R}} H(x,y)\bar{H}(x,y)dG(y)dF(x)\,. \tag{8}$$

Hence, by using the fact that $H(x,y) \le F(x)G(y)$, for $\lambda > 0$, we have the upper bound as $\rho_s \le \frac{\lambda}{3}$. To obtain the lower bound for $\lambda > 0$, we use the eq. (5), then the lower bound is $\rho_s \ge 0$. According to sign of λ, we achieve the bounds as below:

$$\rho_s \in \begin{cases} \left[\frac{-\lambda}{3}, 0\right], for\ \lambda < 0 \\ 0 \qquad\quad , for\ \lambda = 0 \\ \left[0, \frac{\lambda}{3}\right] \quad , for\ \lambda > 0. \end{cases}$$

We have two example to illustrate this family.

Example1. The Farlie-Gumbel –Morgenstern (FGM) family of bivariate distributions are given by $H(x,y) = F(x)G(y)[1 + \theta\,\bar{F}(x)\bar{G}(y)]$, for $\theta \in [-1,1]$. By taking $\theta \in [-1,0]$, the distribution $F(x,y)$ is given by

$$F(x,y) = F(x)G(y) + \lambda F(x)G(y)\bar{F}(x)\bar{G}(y)[1 + \theta\bar{F}(x)\bar{G}(y)][1 + \theta\,F(x)G(y)],$$

where $\lambda \in [-1,1]$ and $\theta \in [-1,0]$. Hence, $\rho_s = \lambda\left(\frac{1}{3} + \frac{\theta}{6} + \frac{\theta^2}{75}\right)$. Since $\theta \in [-1,0]$, $\frac{9\lambda}{50} \le \rho_s \le \frac{\lambda}{3}$ for $\lambda > 0$, and $\frac{\lambda}{3} \le \rho_s \le \frac{9\lambda}{50}$ for $\lambda < 0$.

We conclude that this family model weak dependence as FGM does.

Example2. The bivariate Gumbel- Exponential (BGE) distribution is given by $H(x,y) = 1 - e^{-x} - e^{-y} + e^{-x-y-\theta xy}$, for $\theta \in [0,1]$. The distribution $F(x,y)$ is given by

$$F(x,y) = 1 - e^{-x} - e^{-y} + e^{-x-y} + \lambda\begin{pmatrix} e^{-x-y-\theta xy} - e^{-2x-y-\theta xy} - e^{-x-2y-\theta xy} \\ +e^{-2x-2y-2\theta xy} \end{pmatrix},$$

where $\lambda \in [-1,1]$ and $\theta \in [0,1]$. According to Yela and Cuevas [15], the Spearman's rho coefficient of BGE distribution is $\rho_s^{BGE} = 12\left[-\frac{e^{\frac{4}{\theta}}}{\theta}Ei\left(-\frac{4}{\theta}\right) - \frac{1}{4}\right]$, where $Ei(\cdot)$ is the exponential integral function. Then, ρ_s can be obtained as

$$\rho_s = 12\lambda\frac{e^{\frac{4}{\theta}}}{\theta}\left[-Ei\left(-\frac{4}{\theta}\right) + 2e^{\frac{2}{\theta}}Ei\left(-\frac{6}{\theta}\right) - \frac{e^{\frac{1}{2\theta}}Ei\left(-\frac{9}{2\theta}\right)}{2}\right].$$

The following plot shows the shape of ρ_s^{BGE} for different values of θ. Here, the approximate values obtained by Matlab package program are used in Ei evaluations.

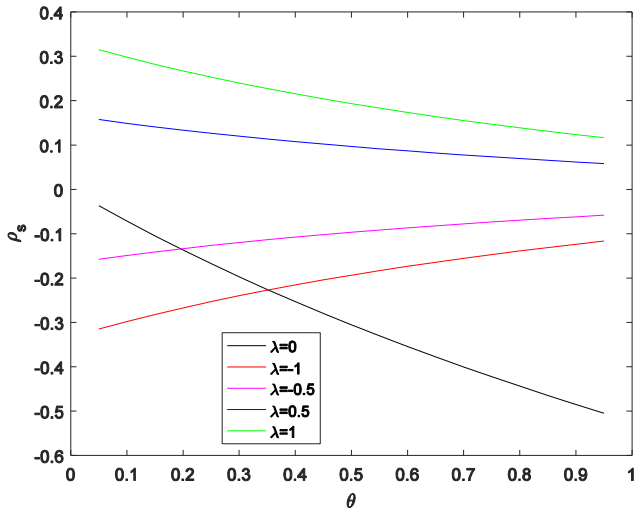

Figure 1. Plots of the ρ_s for some parameter values.

As can be seen from the Figure1, for the negative values of λ, it can be said that F can model negative dependence slightly better than BGE in small theta values. Moreover, for the positive values of λ, F can be used to model weak positive dependence.

4. CONCLUSION

In this study, we proposed a new bivariate distribution using a base distribution from the negative dependency class which is in $\mathcal{F}(F, G)$. Thus, this new distribution can reveal both negative dependence, positive dependence and independence between the random variables X and Y. As a result of illustrative examples, it can be said that distributions can be derived for pairs of random variables with higher correlations considering some base distributions.

If we pay attention to Example 2 again, we can explain a structure by illustrating a random phenomenon which looks essentially negatively dependent but may also be positively dependent as follows:

As the temperatures usually begin to increase in spring, snow starts to melt into the stream. This leads to a rapid increase in the water level of the river. Thereby, it can be thought that there is a positive dependence between temperature and the amount of water level of the river. On the other hand, during the summer season, as the temperatures rise, the water level in the river will decrease due to evaporation. In this case, there is a negative dependence between these two random variables.

The proposed distribution may be useful to model the relationship between river water level and temperature all year round.

REFERENCES

[1] Dolati A. and Ubeda-Flores M., Constructing Copulas by Means of Pairs of Order Statistics, Kybernetika, 45-6 (2009) 992-1002.
[2] Lai C. D. and Xie M., A New Family of Positive Quadrant Dependent Bivariate Distributions, Statistics and Probability Letters, 46-4 (2000) 359-364.
[3] Han Kwang-Hee., A New Family of Negative Quadrant Dependent Bivariate Distributions with Continuous Marginal, Journal of the Chungcheong Mathematical Society, 24-4 (2011) 795-805.
[4] Technical Report, Holt, Rinehart and Winston, New York, 1975.

[5] Domma F., Bivariate Reversed Hazard Rate, Notions, and Measures of Dependence and their Relationships, Communications in Statistics - Theory and Methods, 40-6 (2011) 989-999, DOI: 10.1080/03610920903511777.
[6] Farlie D., The Performance of Some Correlation Coefficients for a General Bivariate Distribution, Biometrika, 47-3/4 (1960) 307-323.
[7] Gumbel E. J., Bivariate Exponential Distributions, Journal of the American Statistical Association, 55-292 (1960) 698-707.
[8] Bismi G., Bivariate Burr Distributions, unpublished PhD Thesis, Cochin University of Science and Technology, 2005.
[9] Basu A.P., Bivariate Failure Rate, Journal of the American Statistical Association, 66 (1971) 103–104.
[10] Johnson N. L. and Kotz S., A Vector Multivariate Hazard Rate, Journal of Multivariate Analysis, 5-1 (1975) 53-66.
[11] Roy D., A Characterization of Model Approach for Generating Bivariate Life Distributions Using Reversed Hazard Rates, Journal of Japan Statistical Society, 32-2 (2002) 239–245.
[12] Hoeffding W., Masstabinvariante Korrelationstheorie, Schriften des Mathematischen Instituts und Instituts fur Angewandte Mathematik der Universitat Berlin, 5 (1940) 181-233.
[13] Fréchet M., Sur Les Tableaux de Corrélation Dont Les marges Sont Donnees, Annales de l'Université de Lyon, Sciences, 4 (1951) 13–84.
[14] Schweizer B. and Wolff E., On Nonparametric Measures of Dependence for Random Variables, The Annals of Statistics, 9-4 (1981) 879-885.
[15] Yela P.J. and Cuevas T.J.R., Estimating the Gumbel-Barnett Copula Parameter of Dependence, Revista Colombiana de Estadística, 41-1 (2018) 53-73.

Cumhuriyet Science Journal
CSJ

e-ISSN: 2587-246X
ISSN: 2587-2680

Cumhuriyet Sci. J., Vol.40-4 (2019) 867-874

An Extension Theorem for Weighted Ricci Curvature on Finsler Manifolds

Yasemin SOYLU [1]

[1] *University of Giresun, Department of Mathematics, Giresun, Turkey*

Received: 11.09.2019; Accepted: 19.12.2019 *http://dx.doi.org/10.17776/csj.618537*

Abstract. Let (M, F) be a forward complete and connected Finsler manifold of dimensional $n \geq 2$. In this study, we extend Wan's extension theorem in Riemannian manifolds to Finsler manifolds by using the weighted Ricci curvature Ric_N bounded below. The proof of theorem is obtained by the Laplacian comparison theorem on Finsler manifolds and the excess function.

Keywords**:** Distance function, Finsler manifold, Weighted Ricci curvature.

Finsler Manifoldlar Üzerinde Ağırlıklı Ricci Eğriliği İçin Bir Genişleme Teoremi

Özet. (M,F) tam ve bağlantılı n≥2 boyutlu bir Finsler manifold olsun. Bu çalışmada aşağıdan sınırlı Ric_N ağırlıklı Ricci eğriliği yardımıyla Wan'ın Riemann manifoldlarında elde ettiği genişleme teoremi Finsler manifoldlara genişletilmiştir. Teoremin ispatı Finsler manifoldlar üzerindeki Laplasyan karşılaştırma teoremi ve excess fonksiyonu kullanılarak elde edilmiştir.

Anahtar Kelimeler: Uzaklık fonksiyonu, Finsler manifold, Ağırlıklı Ricci eğriliği.

1. INTRODUCTION

Finsler geometry includes analogues for many of the natural objects in Riemannian geometry. It is just Riemannian geometry without quadratic restriction. The recent works have shown that some results in Riemannian geometry have been extended to the Finsler setting. For example in this scope, the reader is referred to [1, 2, 3] and references therein.

In the Riemannian case, in [4], Myers obtained a compactness theorem. The theorem of Myers concludes that if $Ric \geq (n-1)K > 0$, then $diam(M) \leq \pi/\sqrt{K}$. Later, Calabi [5] extended this theorem as follows:

Theorem 1. Let M be a complete and connected n-dimensional Riemannian manifold with non-negative Ricci curvature. Suppose there exists a point $p_o \in M$ such that every geodesic ray $\gamma(t)$ issuing from p_o satisfies

$$\limsup_{k\to\infty} \left(\int_0^k Ric(s)^{1/2} ds - 1/2 \ln(k) \right) = \infty, \tag{1}$$

then manifold is compact.

In [6] Cheeger-Gromov-Taylor have proved the following result:

* Corresponding author. *Email address:* *yasemin.soylu@giresun.edu.tr*

Theorem 2. Let M^n be a complete and connected Riemannian manifold. If there exist $o \in M$ and $r_0, \nu > 0$ such that

$$Ric(x) \geq \frac{(n-1)(\frac{1}{4}+\nu^2)}{r^2} \tag{2}$$

holds for all $r(x) \geq r_0 > 0$, then M is compact and the diameter is bounded from above by $diam_o(M) < r_0 e^{\pi/\nu}$, where r is distance function defined with respect to fixed point $o \in M$.

The idea of their proof relies on studying carefully the index form or the second variation.

Recently, Wan [7] gave a complementary extension of Calabi and Cheeger-Gromov-Taylor's theorems by showing that the manifold has no ray issuing from some point.

Theorem 3. Let (M, g) be a complete n-dimensional Riemannian manifold and satisfy

$$Ric \geq \frac{H(n,\ell,\omega)}{(r+\omega)^\ell} \tag{3}$$

for all $r \geq 0$, $\omega > 0$ and $\ell \geq 2$, where r is a distance function $r(x) = d(x, o)$ with respect to a fixed point $o \in M$ and H is a constant depending on n, ℓ and ω. Then manifold is compact. Here H can be chosen to equal to $(n-1).\omega^{\ell-2}.\frac{(\ell-1)^\ell}{(\ell-2)^{\ell-2}}$ for $\ell > 2$ and $(n-1).(1+\frac{\omega}{\varepsilon})$, $\varepsilon > 0$ for $\ell = 2$.

Qui [8] used the idea of Wan, by using the excess function and V-Laplacian comparison theorem, he derived an extension of Bonnet– Myers type theorem with the Bakry–Emery Ricci curvature $Ric_V := Ric - \frac{1}{2}L_V g$. Also, he showed that when the vector field V is the gradient of some smooth function f on M, i.e., $V = \nabla f$, if Ric_V has a positive lower bound and $|f|$ is bounded, then manifold is compact. Moreover, for the m-Bakry-Emery Ricci curvature $Ric_V^m := Ric - \frac{1}{2}L_V g - \frac{1}{m-n}V^* \otimes V^*$, he obtained a compactness theorem by using a similar method as in the proof of Wan.

Also, these type theorems and other calculations in Riemannian geometry has been generalized in various direction by a lot of authors [9, 10, 11, 12] and references therein.

Motivated by the above studies, in this paper we will prove the corresponding Wan's above theorem, for the weighted Ricci curvature Ric_N on Finsler manifolds. In particular, we will use the Laplacian comparison theorem on Finsler manifolds and the excess function. Our main result is as follows:

Theorem 4. Let $(M, F, d\mu)$ be a forward complete and connected Finsler manifold of dimension n with arbitrary volume form and let r be the distance function $r(x) = d(x, o)$ with respect to a fixed point $o \in M$. Suppose that the weighted Ricci curvature

$$Ric_N := Ric_\infty - \frac{S^2}{N-n} \geq A\psi(r) \tag{4}$$

for all $N \in (n, \infty)$ and A is a constant depending on ψ and N. Then

- Manifold is compact,
- Let ϵ and δ be positive arbitrary constants. Then A can be chosen as $(\frac{N-1}{\epsilon})(\int_\epsilon^\infty \psi(s)ds)^{-1} + \delta$.

Remark 5. If we choose $\psi = \frac{1}{r^2}$ and $\psi = \frac{1}{(r+1)^2}$, then Theorem 4 becomes Theorem 2 and Theorem 3 in [13], respectively.

Remark 6. If ψ satisfies $\int_{\epsilon}^{\infty} \psi(s)ds = \infty$, then A can be chosen as an arbitrary positive real number.

Choose $\psi = \frac{1}{(r+\omega)^{\ell}}$ such that $\ell \in \mathbb{R}$ and $\omega > 0$. So we can obtain the following result:

Corollary 7. Let $(M, F, d\mu)$ be a forward complete and connected Finsler manifold of dimension n with arbitrary volume form and let r be the distance function $r(x) = d(x, o)$ with respect to a fixed point $o \in M$. Suppose that the weighted Ricci curvature

$$Ric_N \geq \frac{B(n,\ell,\omega)}{(r+\omega)^{\ell}} \tag{5}$$

for all $r \geq 0$ and $\omega > 0$, where r is a distance function $r(x) = d(x, o)$ with respect to a fixed point $o \in M$ and B is a positive constant depending on N, ℓ and ω. Then manifold is compact. Here B can be chosen to equal to

- $(N-1).\omega^{\ell-2}.\frac{(\ell-1)^{\ell}}{(\ell-2)^{\ell-2}} + \delta$ *for* $\ell > 2$,
- $\frac{(N-1)(\ell-1)}{\epsilon}.(\omega+\epsilon)^{\ell-1} + \delta$ *for* $1 < \ell \leq 2$,
- *an arbitrary positive real number for* $\ell \leq 1$

(ϵ, δ are positive constants).

Additionally, if $Ric_N \geq \delta > 0$, we can rescale the metric such that δ is bigger than the right hand of (5). So manifold is compact (see [13]). By taking $\psi \equiv constant$ in Theorem 4 we have

Corollary 8. Let $(M, F, d\mu)$ be a forward complete and connected Finsler manifold of dimension n with arbitrary volume form. Assume that $Ric_N \geq (N-1)C$, $C > 0$, then manifold is compact and the diameter has an upper bound.

The proof of Corollary 8 is almost the same steps of Theorem 2 in [13]. So, it may be omitted here.

Now, we review below a summary of the basic concepts associated with the Finsler geometry.

2. FINSLER GEOMETRY

Let M be a differentiable n-manifold and TM be the tangent bundle on M, where T_xM is tangent space at $x \in M$. Set $T_0M = TM\backslash\{0\}$. Let $\pi: TM \to M$ be the natural projection and (x, y) be a point of TM such that $x \in M$ and $y \in T_xM$.

Definition 9. A Finsler metric $F: TM \to [0, \infty)$ is a $\mathcal{C}^{\infty}$-Finsler structure of M with the following conditions:

1. F is $\mathcal{C}^{\infty}$ on T_0M (Regularity),
2. $F(x, \lambda y) = \lambda F(x, y)$ for all $\lambda > 0$ (Positive homogeneity),
3. The $n \times n$ Hessian matrix

$$g_{ij} := \frac{1}{2}[F^2]_{y^i y^j} \tag{6}$$

is positive-definite at every point of T_0M (Strong convexity).

The pair (M, F) is called a Finsler manifold.

The Chern curvature R^V for vectors fields $X, Y, Z \in T_xM\backslash\{0\}$ is defined by

$$R^V(X,Y)Z := \nabla^V_X \nabla^V_Y Z - \nabla^V_Y \nabla^V_X Z - \nabla^V_{[X,Y]} Z. \tag{7}$$

In the Riemannian case this curvature does not depend on V and coincides with the Riemannian curvature tensor. The flag curvature is defined as follows:

$$K(V,W) := \frac{g_V(R^V(V,W)W,V)}{g_V(V,V)g_V(W,W) - g_V(V,W)^2}, \tag{8}$$

where $V, W \in T_xM\backslash\{0\}$ are linearly independent vectors. Then the Ricci curvature of V (as the trace of the flag curvature) is given as

$$Ric(V) := \sum_{i=1}^{n-1} K(V, E_i), \tag{9}$$

where $\{E_1, E_2, \ldots, E_{n-1}, V/F(V)\}$ is an orthonormal basis of T_xM with respect to g_V, namely $g_V(E_i, E_j) = \delta_{ij}$ and $g_V(V, E_i) = 0$ for all $i, j = 1, \ldots, n-1$.

Let $d\mu = \sigma_F(x)dx^1dx^2 \ldots dx^n$ be the volume form on M. For a vector $V \in T_xM\backslash\{0\}$,

$$\tau(x,V) := \ln \frac{\sqrt{\det(g_{ij}(x,V))}}{\sigma_F(x)} \tag{10}$$

is a scalar function on $T_xM\backslash\{0\}$ which is called the distortion of $(M, F, d\mu)$. We say that the distortion τ is a $\mathcal{C}^\infty$-function, if M is a Riemannian manifold. Setting

$$S(x,V) := \frac{d}{dt}(\tau(\gamma(t), \dot{\gamma}(t)))|_{t=0}, \tag{11}$$

where γ is the geodesic with $\gamma(0) = x$, $\dot{\gamma}(0) = V$. $S(x, \lambda V) = \lambda S(x, V)$ for all $\lambda > 0$. S is a scalar function on $T_xM\backslash\{0\}$ which is called the S-curvature. From the definition, it seems that the S-curvature measures the rate of change in the distortion along geodesics in the direction $V \in T_xM$.

For all $N \in (n, \infty)$, we define the weighted Ricci curvature of $(M, F, d\mu)$ as follows (see [1]):

$$\begin{cases} Ric_N(W) := Ric(W) + \dot{S}(W) - \dfrac{S(W)^2}{N-n}, \\ Ric_\infty(W) := Ric(W) + \dot{S}(W), \\ Ric_n(W) := \begin{cases} Ric + \dot{S}(W), & \text{if } S(W) = 0 \\ -\infty & \text{otherwise.} \end{cases} \end{cases}$$

Also $Ric_N(\beta W) := \beta^2 Ric_N(W)$ for $\beta > 0$.

We say that (M, F) is forward complete if each geodesic $\gamma: [0, \ell] \to M$ is extended to a geodesic on $[0, \infty)$, in other words, if exponential map is defined on whole TM. Then the Hopf-Rinow theorem gives that every pair of points in M can be joined by a minimal geodesic.

The Legendre transformation $\mathcal{L}: TM \to T^*M$ is defined as

$$\mathcal{L}(Z) := \begin{cases} g_Z(Z, .), & Z \in T_0M, \\ 0 & Z = 0. \end{cases}$$

For a smooth function $h: M \to \mathbb{R}$, the gradient vector of h at $x \in M$ is defined as $\nabla h(x) := \mathcal{L}^{-1}(dh)$.

Given a smooth vector field $Z = Z^i \, \partial / \partial x^i$ on M, the divergence of Z with respect to an arbitrary volume form $d\mu = e^{\varphi} dx^1 dx^2 \dots dx^n$ is defined by

$$divZ := \sum_{i=1}^{n} \left(\frac{\partial Z^i}{\partial x^i} + Z^i \frac{\partial \varphi}{\partial x^i} \right). \tag{12}$$

Then we define the Finsler-Laplacian of h by $\Delta h := div(\nabla h) = div(\mathcal{L}^{-1}(dh))$.

Let $U = \{x \in M: \nabla u|_x \neq 0\}$. The Hessian of u on U is defined by follows:

$$H(u)(V, W) := VW(u) - \nabla_V^{\nabla u} W(u), \quad \forall \, V, W \in TM|_U.$$

We know that $H(u)$ is symmetric, and it can be rewritten as

$$H(u)(V, W) = g_{\nabla u}(\nabla_V^{\nabla u} \nabla u, W).$$

The following lemma will be very useful in the proofs of our main results (see [14]).

Lemma 10. Let $(M, F, d\mu)$ be a Finsler n-manifold, and $u: M \to R$ a smooth function on M. Then on $U = \{x \in M: \nabla u|_x \neq 0\}$ we have

$$\Delta u = \sum_i H(u)(E_i, E_i) - S(\nabla u) := tr_{\nabla u} H(u) - S(\nabla u), \tag{13}$$

where $E_1, E_2, \dots, E_n$ is a local $g_{\nabla u}$-orthonormal frame on U.

Finally, define revesibility $\lambda := \lambda(M, F)$ as follows:

$$\lambda := \sup_{x \in M, y \in TM \setminus 0} \frac{F(x, -y)}{F(x, y)}. \tag{14}$$

It is clear that $\lambda \in [1, \infty]$, and $\lambda = 1$ if and only if (M, F) is called reversible.

3. THE PROOF OF THE MAIN RESULT

Let $(M, F, d\mu)$ be a Finsler manifold of dimensional n and $r(x) = d(o, x)$ be a distance function with respect to a fixed point $o \in M$. It is well known that r is only smooth on $M - (C_o \cup \{o\})$ where C_o is the cut locus of the point $o \in M$. We assume that σ is a minimal unit speed geodesic segment. We have $\nabla r = \sigma'(t)$ in the adapted coordinates with respect to the r, and the distance function r satisfies $F(\nabla r) = 1$ for all $p \in M - (C_o \cup \{o\})$ (see [15]). On the other hand, using the Finsler metric we obtain a weighted Riemannian metric $g_{\nabla r}$. Thus we apply the Riemannian calculation for $g_{\nabla r}$ (on $M - (C_o \cup \{o\})$).

In order to prove the Theorem 4 we first give an upper estimate for the Laplacian of the distance function $r(x) = d(o, x)$.

Lemma 11. [16] If $\mathrm{Ric}_N \geq 0$ for $N \in (n, \infty)$, then the Laplacian of the distance function $r(x) = d(o, x)$ from any given point $o \in M$ can be estimated as follows:

$$\Delta r \leq \frac{N-1}{r} \tag{15}$$

in the sense of distributions on $M\backslash\{o\}$.

Now, we can prove our main theorem using the above notations.

Proof of Theorem 4. Let $\sigma(t)$ be a unit speed ray starting from a fixed point $o \in M$ with $\sigma(0) = o$. For every $t > 0$, $\Delta r(\gamma(t))$ denotes the Finsler-Laplacian of distance function r from a fixed point $o \in M$. It satisfies $F(\nabla r) = 1$. In the Finsler case, recall that the Bochner-Weitzenböck formula [17] for a smooth function $u \in \mathcal{C}^\infty(M)$

$$0 = \Delta^{\nabla u}\left(\frac{F(\nabla u)^2}{2}\right) = \mathrm{Ric}_\infty(\nabla u) + D(\Delta u)(\nabla u) + \| \nabla^2 u \|^2_{HS(\nabla u)}. \tag{16}$$

From the Bochner formula applied to distance function r and by Lemma 10, we have, on $M - (C_p \cup \{p\})$,

$$\begin{aligned} 0 &= \mathrm{Ric}_\infty(\nabla r) + D(\Delta r)(\nabla r) + \| \nabla^2 r \|^2_{HS(\nabla r)} \\ &\geq \mathrm{Ric}_\infty(\nabla r) + g_{\nabla r}(\nabla^{\nabla r}\Delta r, \nabla r) + \frac{1}{n-1}(tr_{\nabla r}\mathrm{Hess} r)^2 \\ &= \mathrm{Ric}_\infty(\nabla r) + g_{\nabla r}(\nabla^{\nabla r}\Delta r, \nabla r) + \frac{(\Delta r + S(\nabla r))^2}{n-1}. \end{aligned} \tag{17}$$

Using the basic inequality

$$(x+z)^2 \geq \frac{1}{\nu+1}x^2 - \frac{1}{\nu}z^2$$

holding for all real numbers x, z and positive real number ν, we have

$$\frac{(\Delta r + S(\nabla r))^2}{n-1} \geq \frac{(\Delta r)^2}{(n-1)(\nu+1)} - \frac{(S(\nabla r))^2}{(n-1)\nu}. \tag{18}$$

In the case where $N > n$, taking $\nu = \frac{N-n}{n-1} > 0$, (17) yields

$$\begin{aligned} 0 &\geq \mathrm{Ric}_\infty(\nabla r) + g_{\nabla r}(\nabla^{\nabla r}\Delta r, \nabla r) + \frac{(\Delta r)^2}{N-1} - \frac{(S(\nabla r))^2}{N-n} \\ &= \mathrm{Ric}_N(\nabla r) + \frac{\partial}{\partial r}(\Delta r) + \frac{(\Delta r)^2}{N-1}. \end{aligned} \tag{19}$$

Integrating the inequality (19) over the interval $[\epsilon, t]$, we get

$$0 \geq \int_\epsilon^t \mathrm{Ric}_N(\nabla r)ds + \Delta r(t) - \Delta r(\epsilon) + \frac{1}{N-1}\int_\epsilon^t (\Delta r)^2 ds \tag{20}$$

for any $\epsilon > 0$. Because $\mathrm{Ric}_N \geq A\psi(r) > 0$, by Lemma 11, we have $\Delta r(\sigma(t)) \leq \frac{N-1}{t}$.

Now, let $r_1(x) = d(o, x)$ and $r_2(x) = d(\sigma(j), x)$. We can think of the excess function e as

$$e(x) := d(o, x) + d(\sigma(j), x) - j, \tag{21}$$

which measures how much the triangle inequality fails to be an equality. By the triangle inequality, we have $e(x) \geq 0$ and $e(\sigma(t)) = 0$ for $0 \leq t \leq j$. Thus

$$\Delta e(\sigma(t)) = \Delta d(o, \sigma(t)) + \Delta d(\sigma(j), \sigma(t)) \geq 0. \tag{22}$$

From here, we have

$$\Delta r(\sigma(t)) = \Delta d(\sigma(0), \sigma(t)) \geq -\Delta d(\sigma(j), \sigma(t)) \geq -\frac{n-1}{j-t}. \tag{23}$$

By taking $j \to \infty$ in the above inequality, we obtain $\Delta r(\sigma(t)) \geq 0$ and therefore we have

$$0 \leq \Delta r(\sigma(t)) \leq \frac{N-1}{t}. \tag{24}$$

From (20), (24) and the assumption of Theorem 4, we have

$$0 \leq \frac{1}{N-1}\int_{\epsilon}^{t} (\Delta r)^2 ds \leq \frac{N-1}{\epsilon} - \int_{\epsilon}^{t} A\psi(s) ds \tag{25}$$

We observe that this is a contradiction if A is very large (see [7]). So manifold must be compact. Now we calculate the A constant we need. By taking $t \to \infty$ and solving . The term

$$\frac{N-1}{\epsilon} - A\int_{\epsilon}^{\infty} \psi(s) ds \leq 0, \tag{26}$$

we get

$$A \geq \left(\frac{N-1}{\epsilon}\right)\left(\int_{\epsilon}^{\infty} \psi(s) ds\right)^{-1}. \tag{27}$$

This allows to choose $A = \left(\frac{N-1}{\epsilon}\right)\left(\int_{\epsilon}^{\infty} \psi(s) ds\right)^{-1} + \delta$ for any $\delta > 0$. Therefore theorem holds.

Proof of the Corollary 7. If we take $A = B(n, \ell, \omega)$ and $\psi(s) = \frac{1}{(r+\omega)^{\ell}}$ in the proof of the Theorem 4, then we have

$$0 \leq \frac{1}{N-1}\int_{\epsilon}^{t} (\Delta r)^2 ds \leq \frac{N-1}{\epsilon} - \int_{\epsilon}^{t} \frac{B(n,\ell,\omega)}{(s+\omega)^{\ell}} ds$$

$$= \frac{N-1}{\epsilon} - \frac{B}{\ell-1}\left[\frac{1}{(\epsilon+\omega)^{\ell-1}} - \frac{1}{(t+\omega)^{\ell-1}}\right] \tag{28}$$

from the inequality (25). Let $t \to \infty$. So we get

$$B \geq (N-1)(\ell-1)\frac{(\epsilon+\omega)^{\ell-1}}{\epsilon}. \tag{29}$$

The term $\frac{(\epsilon+\omega)^{\ell-1}}{\epsilon}$ attains its minimal value when $\epsilon = \frac{\omega}{\ell-2}$ for $\ell > 2$. Inserting $\epsilon = \frac{\omega}{\ell-2}$ into the above inequality, we have $(N-1).\omega^{\ell-2}.\frac{(\ell-1)^{\ell}}{(\ell-2)^{\ell-2}} + \delta$, $\delta > 0$. It is easy to see that (ii) for $1 < \ell \leq 2$ and (iii) for $\ell \leq 1$.

REFERENCES

[1] Ohta S., Finsler interpolation inequalities, Calc. Var. Partial Differ. Equ., 36 (2009) 211-249.

[2] Wu B., A note on the generalized Myers theorem for Finsler manifolds, Bull. Korean Math. Soc., 50 (2013) 833–837.

[3] Yin S., Two compactness theorems on Finsler manifolds with positive weighted Ricci curvature, Results Math., 72 (2017) 319–327.

[4] Myers S.B., Riemannian manifolds with positive mean curvature, Duke Math. J., 8-2 (1941) 401-404.

[5] Calabi E., On Ricci curvature and geodesics, Duke Math. J., 34 (1967) 667–676.

[6] Cheeger J., Gromov M. and Taylor M., Finite propagation speed, kernel estimates for functions of the Laplace operator, and the geometry of complete Riemannian manifolds, J. Differ. Geom., 17-1 (1982) 15-53.

[7] Wan J., An extension of Bonnet–Myers theorem, Math. Z., 291 (2019) 195–197.

[8] Qui H., Extensions of Bonnet-Myers' type theorems with the Bakry-Emery Ricci curvature, https://arxiv.org/abs/1905.01452, (2019).

[9] Lott J., Some geometric properties of the Bakry-Emery-Ricci Tensor, Comment. Math. Helv., 78 (2003) 865-883.

[10] Wei G. and Wylie W., Comparison geometry for the Bakry-Emery-Ricci tensor, J. Differential Geom., 83 (2009) 337-405.

[11] Deshmukh S. and Al-Solamy F.R., Conformal vector fields on a Riemannian manifold, Balkan J. Geom. Appl., 19 (2014) 86-93.

[12] Eker S., The Bochner Vanishing Theorems on the Conformal Killing Vector Fields, TWMS J. App. Eng. Math., 9-1 Special Issue (2019) 114-120.

[13] Soylu Y., Upper Bounds on the Diameter for Finsler Manifolds with Weighted Ricci Curvature, Miskolc Math. Notes, 19-2 (2018) 1173-1184.

[14] Wu B. and Xin Y., Comparison theorems in Finsler geometry and their applications, Math. Ann., 337 (2007) 177–196.

[15] Shen Z., Lectures on Finsler Geometry, World Scientific, Singapore, 2001.

[16] Ohta S. and Sturm K.T., Heat flow on Finsler manifolds, Commun. Pure Appl. Math., 62 (2009) 1386-1433.

[17] Ohta S. and Sturm K.T., Bochner-Weitzenböck formula and Li-Yau estimates on Finsler manifolds, Adv. Math., 252 (2014) 429-448.

Cumhuriyet ScienceJournal
CSJ

e-ISSN: 2587-246X
ISSN: 2587-2680

Cumhuriyet Sci. J.,Vol.40-4(2019) 875-885

Inverse Nodal Problems for Dirac-Type Integro-Differential System with Boundary Conditions Polynomially Dependent on the Spectral Parameter

Baki KESKİN [1]* ***H. Dilara TEL***[2]

1,2 Sivas Cumhuriyet University Faculty of Science Department of Mathematics, Sivas, TURKEY

Received:16.09.2019; Accepted: 30.12.2019 *http://dx.doi.org/10.17776/csj.620668*

Abstract. In this work, we study t*he inverse nodal problem for Dirac type integro-differential operator with the boundary conditions dependent spectral parameter polynomially. We prove that dense subset of the nodal points determines the coefficients of differential part of operator and gives partial information for integral part of it.*

***Keywords*:** Dirac operator, integro-differential operators, inverse nodal problem, parameter dependent boundary conditions.

Sınır Koşulları Spektral Parametreye Polinom Şeklinde Bağlı Olan Dirac Tipli İntegro-Diferansiyel Sistemi İçin Ters Nodal Problemler

Özet. Bu çalışmada sınır koşulunun spektral parametreye polinom şeklinde bağlı olduğu Dirac tipli integro diferansiyel operatörü ele aldık ve nodal noktaların yoğun bir alt kümesinin operatörün diferansiyel kısmının katsayılarını belirlediğini, integral parçası için de kısmi bilgi verdiğini gösterdik.

***Anahtar Kelimeler*:** Dirac operatörü, integro diferansiyel operator, ters nodal problem, parametreye bağlı sınır koşulu.

1. INTRODUCTION

We consider the following boundary value problem $L(\Omega, M, a_1, a_2, b_1, b_2)$, generated by the Dirac-type integro-differential system

$$BY'(x) + \Omega(x)Y(x) + \int_0^x M(x,t)Y(t)dt = \lambda Y(x), \qquad x \in (0,\pi) \qquad (1)$$

with the spectral parameter dependent boundary conditions

$$\begin{cases} a_1(\lambda)y_1(0) + a_2(\lambda)y_2(0) = 0 \\ b_1(\lambda)y_1(\pi) + b_2(\lambda)y_2(\pi) = 0 \end{cases} \qquad (2)$$

* Corresponding author. *Email address:* *bkeskin@cumhuriyet.edu.tr*

where $a_v(\lambda)=\sum_{k=0}^{s_v} a_{vk}\lambda^k$ and $b_v(\lambda)=\sum_{k=0}^{r_v} b_{vk}\lambda^k$, $(v=1,2)$ are monic polynomial with real cofficients; $a_1(\lambda)$ and $a_2(\lambda)$ have no common zeros and same for $b_1(\lambda)$ and $b_2(\lambda)$, λ is the spectral parameter, $B=\begin{pmatrix}0 & 1\\ -1 & 0\end{pmatrix}$, $\Omega(x)=\begin{pmatrix}V(x)+m & 0\\ 0 & V(x)-m\end{pmatrix}$, $M(x,t)=\begin{pmatrix}\chi_{11}(x,t) & \chi_{12}(x,t)\\ \chi_{21}(x,t) & \chi_{22}(x,t)\end{pmatrix}$, $Y(x)=\begin{pmatrix}y_1(x)\\ y_2(x)\end{pmatrix}$, $\Omega(x)$ and $M(x,t)$ are real-valued functions in the class of $W_2^1(0,\pi)$ where m is a real constant. Throughout this paper, we denote $p(x)=V(x)+m$, $r(x)=V(x)-m$.

Inverse nodal problems were first proposed and solved for Sturm-Liouville operator by McLaughlin in 1988 [1]. In this study, it has been shown that a dense subset of zeros of eigenfunctions, called nodal points, uniquelly determines the potential of the Sturm Liouville operator. In 1989, Hald and McLaughlin gave some numerical schemes for reconstructing potential from nodal points for more general boundary conditions [2]. In 1997 Yang gave an algorithm to determine the coefficients of operator for the inverse nodal Sturm-Liouville problem [3]. Inverse nodal problems have been addressed by various researchers in several papers for different operators [4], [5], [6], [7], [8], [9], [10], [11] and [12]. The inverse nodal problems for Dirac operators with various boundary conditions have been studied and shown that the dense subsets of nodal points which are the first components of the eigenfunctions determines the coefficients of discussed operator by Yang C-F, Huang Z-Y [13]; Yang C-F, Pivovarchik VN [14] and Guo Y, Wei Y [15].

In recent years, perturbation of a differential operator by a Volterra type integral operator, namely the integro-differential operator has acquired significant popularity and major attention from several authors and take significant place in the literature [16], [17], [18], [19] *and* [20]. Integro-differential operators are nonlocal, and therefore they are more difficult for investigation, than local ones. New methods for solution of these problems are being developed. For Sturm-Liouville type integro-differential operators, there exist some studies about inverse problems but there is very little study for Dirac type integro-differential operators. The inverse nodal problem for Dirac type integro-differential operators was first studied by [21]. In their study, it is shown that the coefficients of the differential part of the operator can be determined by using nodal points and nodal points also gives the partial information about integral part. In [22] the authors considered boundary conditions depend on the spectral parameter linearly. In our study, we deal with an inverse nodal problem of reconstructing the Dirac type integro-differential operators with the spectral parameter in the boundary conditions polynomially. We have obtained asymptotic estimates of the solutions, eigenvalues and nodal points of considered problem. We have proved that the operator can be reconstructed by given dense subset of the nodal points.

2. MAIN RESULTS

Let $\varphi(x,\lambda)=\begin{pmatrix}\varphi_1(x,\lambda)\\ \varphi_2(x,\lambda)\end{pmatrix}$ be the solution of (1) under the the initial condition $\varphi(0,\lambda)=\begin{pmatrix}a_2(\lambda)\\ -a_1(\lambda)\end{pmatrix}$. It is easy to see that this solution is an entire function of λ for each fixed x and t. One can easily verify that the function $\varphi(x,\lambda)$ satisfies

$$\varphi_1(x,\lambda)=a_1(\lambda)sin\lambda x+a_2(\lambda)cos\lambda x$$

$$+\int_0^x p(t)\varphi_1(t)sin\lambda(x-t)dt+\int_0^x r(t)\varphi_2(t)cos\lambda(x-t)dt$$

$$+\int_0^x\int_0^t\{M_{11}(t,\xi)\varphi_1(\xi)+M_{12}(t,\xi)\varphi_2(\xi)\}sin\lambda(x-t)d\xi dt$$

$$+\int_0^x\int_0^t\{M_{21}(t,\xi)\varphi_1(\xi)+M_{12}t,\xi)\varphi_2(\xi)\}cos\lambda(x-t)\}d\xi dt$$

$$\varphi_2(x,\lambda)=-a_1(\lambda)cos\lambda x+a_2(\lambda)(\lambda)sin\lambda x$$

$$-\int_0^x p(t)\varphi_1(t)cos\lambda(x-t)dt+\int_0^x r(t)\varphi_2(t)sin\lambda(t-x)dt$$

$$-\int_0^x\int_0^t\{M_{11}(t,\xi)\varphi_1(\xi)+M_{12}(t,\xi)\varphi_2(\xi)\}cos\lambda(x-t)d\xi dt$$

$$+\int_0^x\int_0^t\{M_{21}(t,\xi)\varphi_1(\xi)+M_{12}t,\xi)\varphi_2(\xi)\}sin\lambda(x-t)d\xi dt$$

Theorem1. The functions $\varphi_1(x,\lambda)$ and $\varphi_2(x,\lambda)$ have the following asymptotic expansions:

$$\varphi_1(x,\lambda)=a_1(\lambda)sin[\lambda x-w(x)]+a_2(\lambda)cos[\lambda x-w(x)] \tag{3}$$

$$+\frac{a_1(\lambda)m}{\lambda}sin[\lambda x-w(x)]-\frac{a_1(\lambda)m^2x}{2\lambda}cos[\lambda x-w(x)]$$

$$+\frac{a_2(\lambda)m^2x}{2\lambda}sin[\lambda x-w(x)]-\frac{a_1(\lambda)}{2\lambda}K(x)sin[\lambda x-w(x)]$$

$$-\frac{a_2(\lambda)}{2\lambda}K(x)cos[\lambda x-w(x)]+\frac{a_1(\lambda)}{2\lambda}L(x)cos[\lambda x-w(x)]$$

$$-\frac{a_2(\lambda)}{2\lambda}L(x)sin[\lambda x-w(x)]+o\left(\frac{e^{|\tau|x}}{\lambda^{1-s}}\right)$$

$$\varphi_2(x,\lambda)=-a_1(\lambda)cos[\lambda x-w(x)]+a_2(\lambda)sin[\lambda x-w(x)] \tag{4}$$

$$-\frac{a_2(\lambda)m}{\lambda}sin[\lambda x-w(x)]-\frac{a_1(\lambda)m^2x}{2\lambda}sin[\lambda x-w(x)]$$

$$-\frac{a_2(\lambda)m^2x}{2\lambda}cos[\lambda x-w(x)]+\frac{a_1(\lambda)}{2\lambda}K(x)cos[\lambda x-w(x)]$$

$$-\frac{a_2(\lambda)}{2\lambda}K(x)sin[\lambda x - w(x)] + \frac{a_1(\lambda)}{2\lambda}L(x)sin[\lambda x - w(x)]$$

$$+\frac{a_2(\lambda)}{2\lambda}L(x)cos[\lambda x - w(x)] + o\left(\frac{e^{|\tau|x}}{\lambda^{1-s}}\right)$$

for sufficiently large $|\lambda|$, uniformly in x, where, $w(x) = \frac{1}{2}\int_0^x (p(t) + r(t))dt$,
$K(x) = \int_0^x (M_{11}(t,t) + M_{22}(t,t))dt$, $L(x) = \int_0^x (M_{12}(t,t) - M_{21}(t,t))dt$ and $\tau = Im\lambda$

Proof To apply the method of successive approximations to (4) and (5), put

$$\varphi_{1,0}(x,\lambda) = a_1(\lambda)sin\lambda x + a_2(\lambda)cos\lambda x$$

$$\varphi_{2,0}(x,\lambda) = -a_1(\lambda)cos\lambda x + a_2(\lambda)sin\lambda x$$

$$\varphi_{1,n+1}(x,\lambda) = \int_0^x p(t)\varphi_{1,n}(t)sin\lambda(x-t)dt + \int_0^x r(t)\varphi_{2,n}(t)cos\lambda(x-t)dt$$

$$+\int_0^x\int_0^t \{M_{11}(t,\xi)\varphi_{1,n}(\xi) + M_{12}(t,\xi)\varphi_{2,n}(\xi)\}sin\lambda(x-t)d\xi dt$$

$$+\int_0^x\int_0^t \{M_{21}(t,\xi)\varphi_{1,n}(\xi) + M_{22}(t,\xi)\varphi_{2,n}(\xi)\}cos\lambda(x-t)d\xi dt$$

$$\varphi_{2,n+1}(x,\lambda) = -\int_0^x p(t)\varphi_{1,n}(t)cos\lambda(x-t)dt + \int_0^x r(t)\varphi_{2,n}(t)sin\lambda(t-x)dt$$

$$-\int_0^x\int_0^t \{M_{11}(t,\xi)\varphi_{1,n}(\xi) + M_{12}(t,\xi)\varphi_{2,n}(\xi)\}cos\lambda(x-t)d\xi dt$$

$$+\int_0^x\int_0^t \{M_{21}(t,\xi)\varphi_{1,n}(\xi) + M_{22}t,\xi)\varphi_{2,n}(\xi)\}sin\lambda(x-t)d\xi dt$$

Then we have

$$\varphi_{1,1}(x,\lambda) = -a_1(\lambda)w(x)cos\lambda x + a_2(\lambda)w(x)sin\lambda x$$

$$+\frac{a_1(\lambda)m}{\lambda}sin\lambda x - \frac{a_1(\lambda)}{2\lambda}K(x)sin\lambda x$$

$$+\frac{a_1(\lambda)}{2\lambda}L(x)cos\lambda x - \frac{a_2(\lambda)}{2\lambda}K(x)cos\lambda x$$

$$-\frac{a_2(\lambda)}{2\lambda}L(x)sin\lambda x+o\left(\frac{e^{|\tau|x}}{\lambda^{1-s}}\right)$$

$$\varphi_{2,1}(x,\lambda)=-a_1(\lambda)w(x)sin\lambda x-a_2(\lambda)w(x)cos\lambda x$$

$$-\frac{a_2(\lambda)m}{\lambda}sin\lambda x+\frac{a_1(\lambda)}{2\lambda}K(x)cos\lambda x$$

$$+\frac{a_1(\lambda)}{2\lambda}L(x)sin\lambda x-\frac{a_2(\lambda)}{2\lambda}K(x)sin\lambda x$$

$$+\frac{a_2(\lambda)}{2\lambda}L(x)cos\lambda x+o\left(\frac{e^{|\tau|x}}{\lambda^{1-s}}\right)$$

and for n ∈ $\mathbb{Z}^+$

$$\varphi_{1,2n+1}(x,\lambda)=(-1)^{n+1}a_1(\lambda)\frac{w^{2n+1}(x)}{(2n+1)!}cos\lambda x+(-1)^n a_2(\lambda)\frac{w^{2n+1}(x)}{(2n+1)!}sin\lambda x$$

$$+(-1)^n\frac{a_1(\lambda)m}{\lambda}\frac{w^{2n}(x)}{(2n)!}sin\lambda x+(-1)^n\frac{a_1(\lambda)m^2x}{2\lambda}\frac{w^{2n-1}(x)}{(2n-1)!}sin\lambda x$$

$$+(-1)^n\frac{a_2(\lambda)m^2x}{2\lambda}\frac{w^{2n-1}(x)}{(2n-1)!}cos\lambda x+(-1)^{n+1}\frac{a_1(\lambda)}{2\lambda}\frac{w^{2n}(x)}{(2n)!}K(x)sin\lambda x$$

$$+(-1)^{n+1}\frac{a_2(\lambda)}{2\lambda}\frac{w^{2n}(x)}{(2n)!}K(x)cos\lambda x+(-1)^n\frac{a_1(\lambda)}{2\lambda}\frac{w^{2n}(x)}{(2n)!}L(x)cos\lambda x$$

$$+(-1)^{n+1}\frac{a_2(\lambda)}{2\lambda}\frac{w^{2n}(x)}{(2n)!}L(x)sin\lambda x+o\left(\frac{e^{|\tau|x}}{\lambda^{1-s}}\right)$$

$$\varphi_{1,2n}(x,\lambda)=(-1)^n\frac{w^{2n}(x)}{(2n)!}sin\lambda x+(-1)^n\frac{w^{2n}(x)}{(2n)!}cos\lambda x$$

$$+(-1)^n\frac{a_1(\lambda)m}{\lambda}\frac{w^{2n-1}(x)}{(2n-1)!}cos\lambda x+(-1)^n\frac{a_1(\lambda)m^2x}{2\lambda}\frac{w^{2n-2}(x)}{(2n-2)!}cos\lambda x$$

$$+(-1)^{n+1}\frac{a_2(\lambda)m^2x}{2\lambda}\frac{w^{2n-2}(x)}{(2n-2)!}sin\lambda x+(-1)^{n+1}\frac{a_1(\lambda)}{2\lambda}\frac{w^{2n-1}(x)}{(2n-1)!}K(x)cos\lambda x$$

$$+(-1)^n\frac{a_2(\lambda)}{2\lambda}\frac{w^{2n-1}(x)}{(2n-1)!}K(x)sin\lambda x+(-1)^{n+1}\frac{a_1(\lambda)}{2\lambda}\frac{w^{2n-1}(x)}{(2n-1)!}L(x)sin\lambda x$$

$$+(-1)^{n+1}\frac{a_2(\lambda)}{2\lambda}\frac{w^{2n-1}(x)}{(2n-1)!}L(x)cos\lambda x+o\left(\frac{e^{|\tau|x}}{\lambda^{1-s}}\right)$$

$$\varphi_{2,2n+1}(x,\lambda)=(-1)^{n+1}\frac{w^{2n+1}(x)}{(2n+1)!}sin\lambda x+(-1)^{n+1}\frac{w^{2n+1}(x)}{(2n+1)!}cos\lambda x$$

$$+(-1)^{n+1}\frac{a_2(\lambda)m}{\lambda}\frac{w^{2n}(x)}{(2n)!}sin\lambda x+(-1)^{n+1}\frac{a_1(\lambda)m^2x}{2\lambda}\frac{w^{2n-1}(x)}{(2n-1)!}cos\lambda x$$

$$+(-1)^{n}\frac{a_2(\lambda)m^2x}{2\lambda}\frac{w^{2n-1}(x)}{(2n-1)!}sin\lambda x+(-1)^{n}\frac{a_1(\lambda)}{2\lambda}\frac{w^{2n}(x)}{(2n)!}K(x)cos\lambda x$$

$$+(-1)^{n+1}\frac{a_2(\lambda)}{2\lambda}\frac{w^{2n}(x)}{(2n)!}K(x)sin\lambda x+(-1)^{n}\frac{a_1(\lambda)}{2\lambda}\frac{w^{2n}(x)}{(2n)!}L(x)sin\lambda x$$

$$+(-1)^{n}\frac{a_2(\lambda)}{2\lambda}\frac{w^{2n}(x)}{(2n)!}L(x)cos\lambda x+o\left(\frac{e^{|\tau|x}}{\lambda^{1-s}}\right)$$

$$\varphi_{2,2n}(x,\lambda)=(-1)^{n+1}a_1(\lambda)\frac{w^{2n}(x)}{(2n)!}cos\lambda x+(-1)^{n}a_2(\lambda)\frac{w^{2n}(x)}{(2n)!}sin\lambda x$$

$$+(-1)^{n+1}\frac{a_2(\lambda)m}{\lambda}\frac{w^{2n-1}(x)}{(2n-1)!}cos\lambda x+(-1)^{n}\frac{a_1(\lambda)m^2x}{2\lambda}\frac{w^{2n-2}(x)}{(2n-2)!}sin\lambda x$$

$$+(-1)^{n}\frac{a_2(\lambda)m^2x}{2\lambda}\frac{w^{2n-2}(x)}{(2n-2)!}cos\lambda x+(-1)^{n+1}\frac{a_1(\lambda)}{2\lambda}\frac{w^{2n-1}(x)}{(2n-1)!}K(x)sin\lambda x$$

$$+(-1)^{n+1}\frac{a_2(\lambda)}{2\lambda}\frac{w^{2n-1}(x)}{(2n-1)!}K(x)cos\lambda x+(-1)^{n}\frac{a_1(\lambda)}{2\lambda}\frac{w^{2n-1}(x)}{(2n-1)!}L(x)cos\lambda x$$

$$+(-1)^{n+1}\frac{a_2(\lambda)}{2\lambda}\frac{w^{2n-1}(x)}{(2n-1)!}L(x)sin\lambda x+o\left(\frac{e^{|\tau|x}}{\lambda^{1-s}}\right)$$

for sufficiently large |λ|, uniformly inx. Hence, the proof of the theorem1 is completed by successive approximations method.

For defineteness, below we suppose $s_1=s_2=s$ and $r_1=r_2=r$. The other cases can be treated similarly.

Define the entire function Δ(λ) by

$$\Delta(\lambda)=b_1(\lambda)\varphi_1(\pi,\lambda)+b_2(\lambda)\varphi_2(\pi,\lambda), \qquad (5)$$

this function is called the characteristic function of the problem (1)-(3) and the zeros $\{\lambda_n\}_{n\in\mathbb{Z}}$. (counting with algebraic multipicities) coincide with the eigenvalues of the problem (1)-(3). The spectrum of the considered problem consist of eigenvalues $\{\lambda_n\}_{n\in\mathbb{Z}}$ up to $o(n^{-1})$. From (3) and (4), we get the characteristic function Δ(λ) has the following asymptotic relation for sufficiently large |λ|,

$$\Delta(\lambda)=\lambda^{s+r}\{2sin(\lambda\pi-w(\pi))-\frac{m^2\pi}{\lambda}cos(\lambda\pi-w(\pi)) \qquad (6)$$

$$+\frac{L(\pi)}{\lambda}cos(\lambda\pi-w(\pi))-\frac{K(\pi)}{\lambda}sin(\lambda\pi-w(\pi))+o\left(\frac{e^{|\tau|\pi}}{\lambda}\right)\}$$

Using this asymptotic relation, for sufficiently large $n > 0$, we get

$$\lambda_n = n - r - s + \frac{w(\pi)}{\pi} + \frac{m^2 - L(\pi)}{2n} + o\left(\frac{1}{n}\right) \tag{7}$$

Similarly, for n ≥ 1,

$$\lambda_{-n} = -n + \frac{w(\pi)}{\pi} - \frac{m^2 - L(\pi)}{2n} + o\left(\frac{1}{n}\right) \tag{8}$$

Denote the algebraic multiplicity of $\lambda_n \in \mathbb{Z}$ by ρ_n , then by virtue of (7) and (8) we have $\rho_n = 1$, for sufficiently large $|n|$.

Theorem2. For sufficiently large $|n|$, the first component $\varphi_1(x, \lambda_n)$of the eigenfunction $\varphi(x, \lambda_n)$ has exactly $n - r - s$ nodes ${x_n}^j \quad (j = 0, \dots, n - r - s - 1)$ in the interval $(0, \pi)$ i.e.,

$0<{x_n}^0 < {x_n}^1 < \cdots < {x_n}^{n-r-s-1}<\pi$. The numbers $\{{x_n}^j\}$ satisfy the following asymptotic formula:

$${x_n}^j = \frac{j\pi}{n-r-s} + \frac{w({x_n}^j) - 1}{n-r-s} - \frac{w(\pi)}{(n-r-s)\pi}\frac{j\pi}{n-r-s}$$

$$-\frac{(w({x_n}^j) - 1)w(\pi)}{(n-r-s)^2\pi} + \frac{m + m^2{x_n}^j - L({x_n}^j)}{(n-r-s)^2} + O\left(\frac{1}{n^3}\right)$$

Proof From (3), we can write

$$\varphi_1(x, \lambda_n) = a_1(\lambda_n)sin[\lambda_n x - w(x)] + a_2(\lambda_n)cos[\lambda_n x - w(x)]$$

$$+\frac{a_1(\lambda_n)m}{\lambda_n}sin[\lambda_n x - w(x)] - \frac{a_1(\lambda_n)m^2 x}{2\lambda_n}cos[\lambda_n x - w(x)]$$

$$+\frac{a_2(\lambda_n)m^2 x}{2\lambda_n}sin[\lambda_n x - w(x)] - \frac{a_1(\lambda_n)}{2\lambda_n}K(x)sin[\lambda_n x - w(x)]$$

$$-\frac{a_2(\lambda_n)}{2\lambda_n}K(x)cos[\lambda_n x - w(x)] + \frac{a_1(\lambda_n)}{2\lambda_n}L(x)cos[\lambda_n x - w(x)]$$

$$-\frac{a_2(\lambda_n)}{2\lambda_n}L(x)sin[\lambda_n x - w(x)] + o\left(\frac{e^{|\tau|x}}{\lambda^{1-s}}\right)$$

which is equivalent to

$$\varphi_1(x, \lambda_n) = (\lambda_n)^s\{\sin[\lambda_n x - w(x)] + \cos[\lambda_n x - w(x)] + \frac{m}{\lambda_n}\sin[\lambda_n x - w(x)]]$$

$$-\frac{m^2 x}{2\lambda_n}cos[\lambda_n x - w(x)] + \frac{m^2 x}{2\lambda_n}sin[\lambda_n x - w(x)]$$

$$-\frac{1}{2\lambda_n}K(x)sin[\lambda_n x - w(x)] \; -\frac{1}{2\lambda_n}K(x)cos[\lambda_n x - w(x)]$$

$$+\frac{1}{2\lambda_n}L(x)cos[\lambda_n x - w(x)] - \frac{1}{2\lambda_n}L(x)sin[\lambda_n x - w(x)] + o\left(\frac{e^{|\tau|x}}{\lambda_n}\right)$$

for sufficiently large |n|. From $\varphi_1\left({x_n}^j, \lambda_n\right) = 0$, we get

$$sin\left[\lambda_n {x_n}^j - w\left({x_n}^j\right)\right] + cos\left[\lambda_n {x_n}^j - w\left({x_n}^j\right)\right] + \frac{m}{\lambda_n}sin\left[\lambda_n {x_n}^j - w\left({x_n}^j\right)\right]$$

$$-\frac{m^{2{x_n}^j}}{2\lambda_n}cos\left[\lambda_n {x_n}^j - w\left({x_n}^j\right)\right] + \frac{m^{2{x_n}^j}}{2\lambda_n}sin\left[\lambda_n {x_n}^j - w\left({x_n}^j\right)\right]$$

$$-\frac{1}{2\lambda_n}K\left({x_n}^j\right)sin\left[\lambda_n {x_n}^j - w\left({x_n}^j\right)\right] - \frac{1}{2\lambda_n}K\left({x_n}^j\right)cos\left[\lambda_n {x_n}^j - w\left({x_n}^j\right)\right]$$

$$+\frac{1}{2\lambda_n}L\left({x_n}^j\right)cos\left[\lambda_n {x_n}^j - w\left({x_n}^j\right)\right] - \frac{1}{2\lambda_n}L\left({x_n}^j\right)sin\left[\lambda_n {x_n}^j - w\left({x_n}^j\right)\right] + o\left(\frac{e^{|\tau|x}}{\lambda_n}\right) = 0$$

divide both sides by $cos[\lambda_n {x_n}^j - w({x_n}^j)$, we get

$$tan\left[\lambda_n {x_n}^j - w\left({x_n}^j\right)\right] + 1 + \frac{m}{\lambda_n}tan\left[\lambda_n {x_n}^j - w\left({x_n}^j\right)\right] - \frac{m^{2{x_n}^j}}{2\lambda_n}$$

$$+\frac{m^2{x_n}^j}{2\lambda_n}tan[\lambda_n {x_n}^j - w({x_n}^j)] - \frac{1}{2\lambda_n}K({x_n}^j)tan[\lambda_n {x_n}^j - w({x_n}^j)] - \frac{1}{2\lambda_n}K({x_n}^j)$$

$$+\frac{1}{2\lambda_n}L\left({x_n}^j\right) - \frac{1}{2\lambda_n}L\left({x_n}^j\right)tan\left[\lambda_n {x_n}^j - w\left({x_n}^j\right)\right] + o\left(\frac{e^{|\tau|x}}{\lambda_n}\right) = 0,$$

then, we get

$$tan\left[\lambda_n {x_n}^j - w\left({x_n}^j\right)\right] = \left(1 + \frac{m}{\lambda_n} + \frac{m^2{x_n}^j}{2\lambda_n} - \frac{K({x_n}^j)}{2\lambda_n} - \frac{L({x_n}^j)}{2\lambda_n}\right)^{-1} \times$$

$$\times\left(-1 + \frac{m^2{x_n}^j}{2\lambda_n} + \frac{K({x_n}^j)}{2\lambda_n} - \frac{L({x_n}^j)}{2\lambda_n} + o\left(\frac{e^{|\tau|x}}{\lambda_n}\right)\right),$$

Taylor formula for the function arctangent yields

$${x_n}^j = \frac{1}{\lambda_n}\left(j\pi + w\left({x_n}^j\right) - 1 + \frac{m}{\lambda_n} + \frac{m^2{x_n}^j}{\lambda_n} - \frac{L({x_n}^j)}{\lambda_n} + o\left(\frac{1}{\lambda_n}\right)\right).$$

If we put

$${\lambda_n}^{-1} = \frac{1}{n-r-s}\left\{1 - \frac{w(\pi)}{(n-r-s)\pi} + o\left(\frac{1}{n}\right)\right\}; \frac{1}{{\lambda_n}^2} = \frac{1}{(n-r-s)^2}\left\{1 - \frac{2w(\pi)}{(n-r-s)\pi} + o\left(\frac{1}{n}\right)\right\}$$

then we get

$$x_n{}^j = \frac{j\pi}{n-r-s} + \frac{w(x_n{}^j)-1}{n-r-s} - \frac{w(\pi)}{(n-r-s)\pi}\frac{j\pi}{n-r-s}$$

$$-\frac{(w(x_n{}^j)-1)w(\pi)}{(n-r-s)^2\pi} + \frac{m+m^2x_n{}^j - L(x_n{}^j)}{(n-r-s)^2} + O\left(\frac{1}{n^3}\right)$$

Fix x ∈ $(0,\pi)$. Let X be the set of nodal points. One can choose a sequence $x_n{}^j \subset X$ such that $x_n{}^j$ converges to x. Then the following limits are exist and finite:

$$f(x) := \lim_{|n|\to\infty}\left(x_n{}^j - \frac{j\pi}{n-r-s}\right)(n-r-s) = w(x_n{}^j) - 1 + \frac{w(\pi)}{\pi}x \qquad (9)$$

and

$$g(x) := \lim_{|n|\to\infty}\left(x_n{}^j - \frac{j\pi}{n-r-s} - \frac{w(x_n{}^j)-1}{n-r-s} + \frac{w(\pi)}{(n-r-s)\pi}\frac{j\pi}{n-r-s}\right)(n-r-s)^2 \qquad (10)$$

$$= -\frac{(w(x_n{}^j)-1)w(\pi)}{\pi} + m + m^2x_n{}^j - L(x_n{}^j)$$

Now, we can formulate the following uniqueness theorem and establish a constructive procedure for reconstructing the potantial of the considered problem. Without loss of generality, we assume

$$L(\pi) = \int_0^\pi (\chi_{12}(t,t) - \chi_{21}(t,t))dt = 0$$

Theorem3. The given dense subset of nodal set X uniquely determines the potential V(x) of the problem, the function $L'(x) = \chi_{12}(x,x) - \chi_{21}(x,x)$ of the partial imformation of the integral part, a.e. on $(0,\pi)$. Moreover, $V(x), L'(x)$, and m can be constructed by the following algorithm:

(1) fix $x \in (0,\pi)$, choose a sequence $\left(x_n{}^{j(n)}\right) \subset$ X such that $\lim_{|n|\to\infty} x_n{}^{j(n)} = x$;

(2) find the function $f(x)$ via (9) and calculate

$$w(\pi) = \frac{f(\pi)+1}{2}$$

$$V(x) = f'(x) - \frac{f(\pi)+1}{2\pi}$$

(3) find the function $g(x)$ via (10) and calculate

$$m = g(0) - \frac{f(\pi)+1}{2\pi}$$

$$L'(x) = -g'(x) - \frac{V(x)}{\pi} + m^2$$

Acknowledgement: The work was supported by grants from CUBAP (F-568)

REFERENCES

[1] J.R. McLaughlin, Inverse spectral theory using nodal points as data a uniqueness result, J. Diff. Eq. 73 (1988) 354-362.

[2] O.H. Hald, J.R. McLaughlin, Solutions of inverse nodal problems, Inv. Prob. 5 (1989) 307-347.

[3] X-F Yang, A solution of the nodal problem, Inverse Problems, 13 (1997) 203-213.

[4] P.J. Browne, B.D. Sleeman, Inverse nodal problem for Sturm-Liouville equation with eigenparameter depend boundary conditions, Inverse Problems 12 (1996) 377-381.

[5] S.A. Buterin, C.T. Shieh, Inverse nodal problem for differential pencils, Appl. Math. Lett. 22, (2009) 1240-1247.

[6] S.A. Buterin, C.T. Shieh, Incomplete inverse spectral and nodal problems for differential pencil. Results Math. 62 (2012) 167-179.

[7] Y.H. Cheng, C-K. Law and J. Tsay, Remarks on a new inverse nodal problem, J. Math. Anal. Appl. 248 (2000) 145-155.

[8] C.K. Law, C.L. Shen and C.F. Yang, The Inverse Nodal Problem on the Smoothness of the Potential Function, Inverse Problems, 15-1 (1999) 253-263 (Erratum, Inverse Problems, 17 (2001) 361-363.

[9] A.S. Ozkan, B. Keskin, Inverse Nodal Problems for Sturm-Liouville Equation with EigenparameterDependent Boundary and Jump Conditions, Inverse Problems in Science and Engineering, 23-8 (2015) 1306-1312.

[10] C-T Shieh, V.A. Yurko, Inverse nodal and inverse spectral problems for discontinuous boundary value problems, J. Math. Anal. Appl. 347 (2008) 266-272.

[11] C-F Yang, Xiao-Ping Yang, Inverse nodal problems for the Sturm-Liouville equation with polynomially dependent on the eigenparameter, Inverse Problems in Science and Engineering, 19-7 (2011) 951-961.

[12] C-F Yang, Inverse nodal problems of discontinuous Sturm-Liouville operator, J. Differential Equations, 254 (2013) 1992-2014.

[13] C-F Yang, Z-Y.Huang, Reconstruction of the Dirac operator from nodal data. Integr. Equ. Oper. Theory 66 (2010) 539-551.

[14] C-F Yang, V.N. Pivovarchik, : Inverse nodal problem for Dirac system with spectral parameter in boundary conditions. Complex Anal. Oper. Theory 7 (2013) 1211-1230.

[15] Y. Guo, Y. Wei, Inverse Nodal Problem for Dirac Equations with Boundary Conditions Polynomially Dependent on the Spectral Parameter, Results. Math. 67 (2015) 95--110.

[16] S.A. Buterin, On an Inverse Spectral Problem for a Convolution Integro-Differential Operator, Results in Mathematics, 50 (2007) 173-181.

[17] S.A. Buterin, The Inverse Problem of Recovering the Volterra Convolution Operator from the Incomplete Spectrum of its Rank-One Perturbation, Inverse Problems, 22 (2006) 2223--2236.

[18] G. Freiling, V.A. Yurko, Inverse Sturm--Liouville Problems and their Applications, Nova Science, New York, 2001.

[19] Y.V. Kuryshova, Inverse Spectral Problem for Integro-Differential Operators, Mathematical Notes, 81-6 (2007) 767-777.

[20] B.Wu, J. Yu, Uniqueness of an Inverse Problem for an Integro-Differential Equation Related to the Basset Problem, Boundary Value Problems, 229 (2014).

[21] B. Keskin A. S. Ozkan, Inverse nodal problems for Dirac-type integro-differential operators, J. Differential Equations. 263 (2017) 8838--8847

[22] B. Keskin, H. D. Tel, Reconstruction of the Dirac-Type Integro-Differential Operator From Nodal Data, Numerical Functional Analysis and Optimization, 39-11 (2018) 1208–1220.

Cumhuriyet Science Journal
CSJ

e-ISSN: 2587-246X
ISSN: 2587-2680

Cumhuriyet Sci. J., Vol.40-4 (2019) 886-895

A Study on First-Order Fuzzy Initial Value Problems with Positive and Negative Fuzzy Number Coefficients by Fuzzy Laplace Transform

Hülya GÜLTEKİN ÇİTİL

Department of Mathematics, Faculty of Arts and Sciences, Giresun University, Giresun, Turkey.

Received: 14.10.2019; Accepted: 21.11.2019 *http://dx.doi.org/10.17776/csj.632770*

Abstract. In this paper, fuzzy initial value problems for first-order fuzzy differential equations with positive and negative fuzzy number coefficients are studied by fuzzy Laplace transform. Solutions are found under the approach of generalized differentiability. Examples are solved. Figures of the solutions are drawn using the Mathematica program. Finally, conclusions are given.

***Keywords*:** Fuzzy Initial Value Problem, Generalized Differentiability, Fuzzy Laplace Transform, Positive and Negative Fuzzy Numbers.

Fuzzy Laplace Dönüşümüyle Pozitif ve Negatif Fuzzy Sayı Katsayılı Birinci-Mertebe Fuzzy Başlangıç Değer Problemleri Üzerine Bir Çalışma

Özet. Bu çalışmada, fuzzy Laplace dönüşümüyle pozitif ve negatif fuzzy sayı katsayılı birinci-mertebe fuzzy diferansiyel denklemler için fuzzy başlangıç değer problemleri çalışıldı. Çözümler genelleştirilmiş diferansiyellenebilirlik yaklaşımı altında bulundu. Örnekler çözüldü. Çözümlerin şekilleri Mathematica programı kullanarak çizildi. Son olarak, sonuçlar verildi.

Anahtar Kelimeler Fuzzy Başlangıç Değer Problem, Genelleştirilmiş Diferansiyellenebilirlik, Fuzzy Laplace Dönüşüm, Pozitif ve Negatif Fuzzy Sayılar.

1. INTRODUCTION

The topic of fuzzy differential equations has been rapidly grown in current years. The term of ‘‘fuzzy differetial equation’’ was introduced by Kandel and Byatt [1]. The fuzzy differential equations are extensively used in applied mathematics, physics and engineering. Many researchers study fuzzy differential equation with different approach. The first approach is on the Zadeh’s extenciple [2]. The second approach is differential inclusion [3]. The third approach is Hukuhara derivative [4-5] or generalized derivative [6-8].

Fuzzy Laplace transform is very useful to solve fuzzy differential equation. In many papers, fuzzy Laplace transform was studied [9-11].

This paper is on solutions of fuzzy initial value problems for first-order fuzzy differential equations with positive and negative fuzzy number coefficients by fuzzy Laplace transform.

* Corresponding author. *Email address:* *hulya.citil@giresun.edu.tr*

Definition 1.1 [12] A fuzzy number is a function $u: \mathbb{R} \to [0,1]$ satisfying the following properties:

u is normal, u is convex fuzzy set, u is upper s
emi-continuous on $\mathbb{R}$ and $cl\{x \in \mathbb{R} | u(x) > 0\}$ is compact, where cl denotes the closure of a subset. Let $\mathbb{R}_F$ be the space of fuzzy numbers.

Definition 1.2 [12] Let be $u \in \mathbb{R}_F$. The α-level set of u is $[u]^\alpha = \{x \in \mathbb{R} | u(x) \geq \alpha\}$, $0 < \alpha \leq 1$.

If $\alpha = 0$, the support of u is $[u]^0 = cl\{x \in \mathbb{R} | u(x) > 0\}$.

Definition 1.3 [13] A fuzzy number u in parametric form is a pair $\left[\underline{u}_\alpha, \overline{u}_\alpha\right]$ of functions $\underline{u}_\alpha, \overline{u}_\alpha$, $0 \leq \alpha \leq 1$, which satisfy the following requirements:

1. $\underline{u}_\alpha$ is bounded non-decreasing left-continuous in $(0,1]$, right-continuous at $\alpha = 0$.

2. $\overline{u}_\alpha$ is bounded non-increasing left-continuous in $(0,1]$, right-continuous at $\alpha = 0$.

3. $\underline{u}_\alpha \leq \overline{u}_\alpha$, $0 \leq \alpha \leq 1$.

Definition 1.4 [14] A fuzzy number u is called positive (negative), denoted by $u > 0$ ($u < 0$), if its membership function $u(x)$ satisfies $u(x) = 0$, $\forall x < 0$ ($x > 0$).

Definition 1.5 [12] If A is a symmetric triangular number with support $\left[\underline{a}, \overline{a}\right]$, the α-level set of A is

$$[A]^\alpha = \left[\underline{a} + \left(\frac{\overline{a}-\underline{a}}{2}\right)\alpha, \overline{a} - \left(\frac{\overline{a}-\underline{a}}{2}\right)\alpha\right].$$

Definition 1.6 [15] Let be $u, v \in \mathbb{R}_F$, $[u]^\alpha = \left[\underline{u}_\alpha, \overline{u}_\alpha\right]$, $[v]^\alpha = \left[\underline{v}_\alpha, \overline{v}_\alpha\right]$, the product $u.v$ is defined by

$$[u.v]^\alpha = [u]^\alpha.[v]^\alpha, \forall \alpha \in [0,1],$$

where

$$[u]^\alpha.[v]^\alpha = \left[\underline{u}_\alpha, \overline{u}_\alpha\right]\left[\underline{v}_\alpha, \overline{v}_\alpha\right] = \left[\underline{w}_\alpha, \overline{w}_\alpha\right],$$

$$\underline{w}_\alpha = min\left\{\underline{u}_\alpha\underline{v}_\alpha, \underline{u}_\alpha\overline{v}_\alpha, \overline{u}_\alpha\underline{v}_\alpha, \overline{u}_\alpha\overline{v}_\alpha\right\}, \overline{w}_\alpha = max\left\{\underline{u}_\alpha\underline{v}_\alpha, \underline{u}_\alpha\overline{v}_\alpha, \overline{u}_\alpha\underline{v}_\alpha, \overline{u}_\alpha\overline{v}_\alpha\right\}.$$

Definition 1.7 [16] Let be $u, v \in \mathbb{R}_F$. If there exists $w \in \mathbb{R}_F$ such that $u = v + w$ then w is called the H-difference of u and v and it is denoted $u \ominus v$.

Definition 1.8 [16] Let be $f: [a,b] \longrightarrow \mathbb{R}_F$ and $t_0 \in [a,b]$. If there exists $f'(t_0) \in \mathbb{R}_F$ such that for all $h > 0$ sufficiently small, $\exists f(t_0 + h) \ominus f(t_0)$, $f(t_0) \ominus f(t_0 - h)$ and the limits hold

$$\lim_{h \to 0} \frac{f(t_0 + h) \ominus f(t_0)}{h} = \lim_{h \to 0} \frac{f(t_0) \ominus f(t_0 - h)}{h} = f'(t_0),$$

f is (1)-differentiable at t_0. If there exists $f'(t_0) \in \mathbb{R}_F$ such that for all $h > 0$ sufficiently small, $\exists f(t_0) \ominus f(t_0 + h)$, $f(t_0 - h) \ominus f(t_0)$ and the limits hold

$$\lim_{h \to 0} \frac{f(t_0) \ominus f(t_0 + h)}{-h} = \lim_{h \to 0} \frac{f(t_0 - h) \ominus f(t_0)}{-h} = f'(t_0),$$

f is (2)-differentiable.

Definition 1.9 [13] The fuzzy Laplace transform of fuzzy function f is

$$F(s) = L\big(f(t)\big) = \int_0^{\infty} e^{-st} f(t)dt = \left[\lim_{\rho\to\infty}\int_0^{\rho} e^{-st}\,\underline{f}(t)dt\,,\ \lim_{\rho\to\infty}\int_0^{\rho} e^{-st}\,\overline{f}(t)dt\right].$$

$$F(s,\alpha) = L([f(t)]^{\alpha}) = \left[L\left(\underline{f}_{\alpha}(t)\right), L\left(\overline{f}_{\alpha}(t)\right)\right],$$

$$L\left(\underline{f}_{\alpha}(t)\right) = \int_0^{\infty} e^{-st}\,\underline{f}_{\alpha}(t)dt = \lim_{\rho\to\infty}\int_0^{\rho} e^{-st}\,\underline{f}_{\alpha}(t)dt,$$

$$L\left(\overline{f}_{\alpha}(t)\right) = \int_0^{\infty} e^{-st}\,\overline{f}_{\alpha}(t)dt = \lim_{\rho\to\infty}\int_0^{\rho} e^{-st}\,\overline{f}_{\alpha}(t)dt.$$

Theorem 1.1 [9] Let $f'(t)$ be an integrable fuzzy function and $f(t)$ is primitive of $f'(t)$ on $(0,\infty]$.

1. If f is (1)-differentiable, $L\big(f'(t)\big) = sL\big(f(t)\big) \ominus f(0)$.

2. If f is (2)-differentiable, $L\big(f'(t)\big) = \big(-f(0)\big) \ominus \big(-sL\big(f(t)\big)\big)$.

2. RESULTS AND DISCUSSION

Consider the fuzzy problem

$$u'(t) + [\mu]^{\alpha}u(t) = [\rho]^{\alpha},\ t > 0 \tag{1}$$

$$\mathrm{u}(0) = [\omega]^{\alpha}, \tag{2}$$

by the fuzzy Laplace transform, where $[\mu]^{\alpha} = \left[\underline{\mu}_{\alpha}, \overline{\mu}_{\alpha}\right]$, $[\rho]^{\alpha} = \left[\underline{\rho}_{\alpha}, \overline{\rho}_{\alpha}\right], [\omega]^{\alpha} = \left[\underline{\omega}_{\alpha}, \overline{\omega}_{\alpha}\right]$ are symmetric triangular fuzzy numbers and $u(t)$ is positive fuzzy function. In this paper, (i) solution means that u is (i)-differentiable, i=1,2.

I) The case of positive fuzzy number coefficient

Let be $[\mu]^{\alpha} = \left[\underline{\mu}_{\alpha}, \overline{\mu}_{\alpha}\right]$ positive fuzzy number.

1) Let be u (1)-differentiable. Then, using the fuzzy Laplace transform, from the fuzzy differential equation (1)

$$sL\big(u(t)\big) \ominus u(0) + [\mu]^{\alpha}L\big(u(t)\big) = L([\rho]^{\alpha})$$

is obtained. Using the Hukuhara difference and fuzzy arithmetic, we have

$$sL\left(\underline{u}_{\alpha}(t)\right) - \underline{u}_{\alpha}(0) + \underline{\mu}_{\alpha}L\left(\underline{u}_{\alpha}(t)\right) = L\left(\underline{\rho}_{\alpha}\right),$$

$$sL\big(\overline{u}_{\alpha}(t)\big) - s\overline{u}_{\alpha}(0) + \overline{\mu}_{\alpha}L\big(\overline{u}_{\alpha}(t)\big) = L\big(\overline{\rho}_{\alpha}\big).$$

Also, using the initial condition (2), we obtain

$$L\left(\underline{u}_{\alpha}(t)\right) = \frac{\underline{\rho}_{\alpha}}{s\left(s+\underline{\mu}_{\alpha}\right)} + \frac{\underline{\omega}_{\alpha}}{s+\underline{\mu}_{\alpha}},$$

$$L\big(\overline{u}_{\alpha}(t)\big) = \frac{\overline{\rho}_{\alpha}}{s\big(s+\overline{\mu}_{\alpha}\big)} + \frac{\overline{\omega}_{\alpha}}{s+\overline{\mu}_{\alpha}}.$$

Taking the inverse Laplace transform of this equations, (1) solution is obtained as

$$\underline{u}_\alpha(t) = e^{-\underline{\mu}_\alpha t}\left(\underline{\omega}_\alpha - \frac{\underline{\rho}_\alpha}{\underline{\mu}_\alpha}\right) + \frac{\underline{\rho}_\alpha}{\underline{\mu}_\alpha},$$

$$\overline{u}_\alpha(t) = e^{-\overline{\mu}_\alpha t}\left(\overline{\omega}_\alpha - \frac{\overline{\rho}_\alpha}{\overline{\mu}_\alpha}\right) + \frac{\overline{\rho}_\alpha}{\overline{\mu}_\alpha},$$

$$[u(t)]^\alpha = \left[\underline{u}_\alpha(t), \overline{u}_\alpha(t)\right].$$

2) Let be u (2)-differentiable. Using the fuzzy Laplace transform, from the fuzzy differential equation (1)

$$-u(0) \ominus \left(-sL\big(u(t)\big)\right) + [\mu]^\alpha L\big(u(t)\big) = L([\rho]^\alpha),$$

that is, the equations

$$-\overline{u}_\alpha(0) + sL\big(\overline{u}_\alpha(t)\big) + \underline{\mu}_\alpha L\left(\underline{u}_\alpha(t)\right) = L\left(\underline{\rho}_\alpha\right),$$

$$-\underline{u}_\alpha(0) + sL\left(\underline{u}_\alpha(t)\right) + \overline{\mu}_\alpha L\big(\overline{u}_\alpha(t)\big) = L\big(\overline{\rho}_\alpha\big)$$

are obtained. From this, we have

$$sL\big(\overline{u}_\alpha(t)\big) + \underline{\mu}_\alpha L\left(\underline{u}_\alpha(t)\right) = \frac{\underline{\rho}_\alpha}{s} + \overline{\omega}_\alpha \tag{3}$$

$$sL\left(\underline{u}_\alpha(t)\right) + \overline{\mu}_\alpha L\big(\overline{u}_\alpha(t)\big) = \frac{\overline{\rho}_\alpha}{s} + \underline{\omega}_\alpha. \tag{4}$$

If $L\big(\overline{u}_\alpha(t)\big)$ in the equation (4) is replaced by the equation (3),

$$L\left(\underline{u}_\alpha(t)\right) = \left(\overline{\rho}_\alpha - \overline{\mu}_\alpha\overline{\omega}_\alpha\right)\left(\frac{1}{s^2 - \underline{\mu}_\alpha\overline{\mu}_\alpha}\right) + \underline{\omega}_\alpha\left(\frac{s}{s^2 - \underline{\mu}_\alpha\overline{\mu}_\alpha}\right) - \frac{\underline{\rho}_\alpha\overline{\mu}_\alpha}{s\left(s^2 - \underline{\mu}_\alpha\overline{\mu}_\alpha\right)}$$

is obtained. Taking the inverse Laplace transform of this equation, the lower solution is obtained as

$$\underline{u}_\alpha(t) = \frac{\left(\overline{\rho}_\alpha - \overline{\mu}_\alpha\overline{\omega}_\alpha\right)}{\sqrt{\underline{\mu}_\alpha\overline{\mu}_\alpha}} sin\left(\sqrt{\underline{\mu}_\alpha\overline{\mu}_\alpha}\,t\right) + \underline{\omega}_\alpha cos\left(\sqrt{\underline{\mu}_\alpha\overline{\mu}_\alpha}\,t\right) - \frac{\underline{\rho}_\alpha}{\underline{\mu}_\alpha}\left(\frac{e^{\sqrt{\underline{\mu}_\alpha\overline{\mu}_\alpha}\,t} + e^{-\sqrt{\underline{\mu}_\alpha\overline{\mu}_\alpha}\,t}}{2} - 1\right).$$

Similarly, the upper solution is obtained as

$$\overline{u}_\alpha(t) = \frac{\left(\underline{\rho}_\alpha - \underline{\mu}_\alpha\underline{\omega}_\alpha\right)}{\sqrt{\underline{\mu}_\alpha\overline{\mu}_\alpha}} sin\left(\sqrt{\underline{\mu}_\alpha\overline{\mu}_\alpha}\,t\right) + \overline{\omega}_\alpha cos\left(\sqrt{\underline{\mu}_\alpha\overline{\mu}_\alpha}\,t\right) - \frac{\overline{\rho}_\alpha}{\overline{\mu}_\alpha}\left(\frac{e^{\sqrt{\underline{\mu}_\alpha\overline{\mu}_\alpha}\,t} + e^{-\sqrt{\underline{\mu}_\alpha\overline{\mu}_\alpha}\,t}}{2} - 1\right).$$

Example 2.1 Consider the fuzzy initial value problem

$$u'(t) + [1]^\alpha u(t) = [2]^\alpha,\ t > 0 \tag{5}$$

$$\mathrm{u}(0) = [1]^\alpha, \tag{6}$$

using the fuzzy Laplace transform, where $[1]^\alpha = [\alpha, 2-\alpha],\ [2]^\alpha = [1+\alpha, 3-\alpha]$.

If u is (1)-differentiable, (1) solution is

$$\underline{u}_\alpha(t) = e^{-\alpha t}\left(\alpha - \left(\frac{1+\alpha}{\alpha}\right)\right) + \left(\frac{1+\alpha}{\alpha}\right),$$

$$\overline{u}_\alpha(t) = e^{-(2-\alpha)t}\left((2-\alpha) - \left(\frac{3-\alpha}{2-\alpha}\right)\right) + \left(\frac{3-\alpha}{2-\alpha}\right),$$

$$[u(t)]^\alpha = \left[\underline{u}_\alpha(t), \overline{u}_\alpha(t)\right].$$

If u is (2)-differentiable, (2) solution is

$$\underline{u}_\alpha(t) = \left(\frac{(3-\alpha)-(2-\alpha)^2}{\sqrt{\alpha(2-\alpha)}}\right) sin\left(\sqrt{\alpha(2-\alpha)}t\right) + \alpha cos\left(\sqrt{\alpha(2-\alpha)}t\right) - \left(\frac{1+\alpha}{\alpha}\right)\left(\frac{e^{\sqrt{\alpha(2-\alpha)}t}+e^{-\sqrt{\alpha(2-\alpha)}t}}{2} - 1\right),$$

$$\overline{u}_\alpha(t) = \left(\frac{(1+\alpha)-\alpha^2}{\sqrt{\alpha(2-\alpha)}}\right) sin\left(\sqrt{\alpha(2-\alpha)}t\right) + (2-\alpha) cos\left(\sqrt{\alpha(2-\alpha)}t\right)$$

$$-\left(\frac{3-\alpha}{2-\alpha}\right)\left(\frac{e^{\sqrt{\alpha(2-\alpha)}t}+e^{-\sqrt{\alpha(2-\alpha)}t}}{2} - 1\right),$$

$$[u(t)]^\alpha = \left[\underline{u}_\alpha(t), \overline{u}_\alpha(t)\right].$$

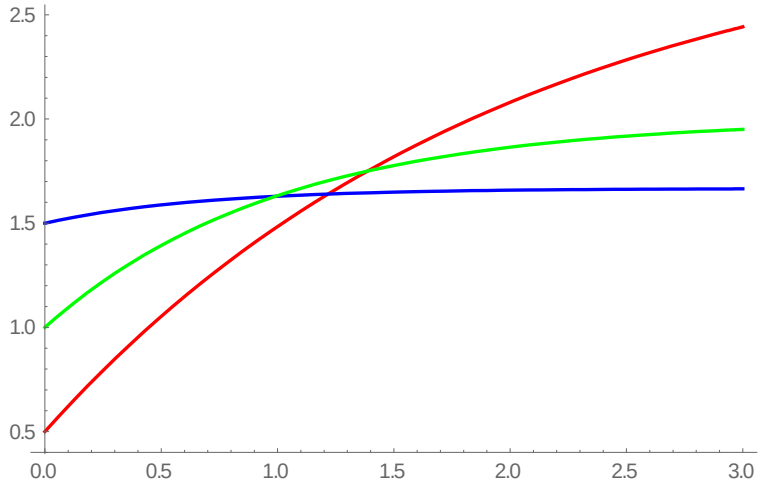

Figure 1 (1) solution for $\alpha = 0.5$

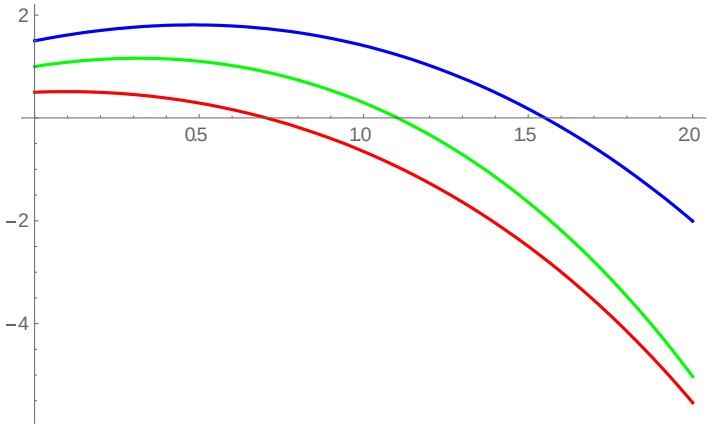

Figure 2 (2) solution for $\alpha = 0.5$

$$red \rightarrow \underline{u}_\alpha(t),\ blue \rightarrow \overline{u}_\alpha(t),\ green \rightarrow u(t)$$

From Definition 1.3 and since $[u(x)]^\alpha$ is positive fuzzy function, according to figure 1, (1) solution is a valid fuzzy number for $x\epsilon[0,1.21735]$, according to figure 2, (2) solution is a valid fuzzy number for $x\epsilon[0,0.704091]$.

II) The case of negative fuzzy number coefficient

Let be $[\mu]^\alpha = \left[\underline{\mu}_\alpha, \overline{\mu}_\alpha\right]$ negative fuzzy number.

1) Let be u (1)-differentiable. Then, using the fuzzy Laplace transform, the fuzzy differential equation (1) yields

$$sL\big(u(t)\big) \ominus u(0) + [\mu]^\alpha L\big(u(t)\big) = L([\rho]^\alpha).$$

From this, using the fuzzy arithmetic and Hukuhara difference

$$sL\left(\underline{u}_\alpha(t)\right) - \underline{u}_\alpha(0) + \underline{\mu}_\alpha L\big(\overline{u}_\alpha(t)\big) = L\left(\underline{\rho}_\alpha\right),$$

$$sL\big(\overline{u}_\alpha(t)\big) - s\overline{u}_\alpha(0) + \overline{\mu}_\alpha L\left(\underline{u}_\alpha(t)\right) = L\big(\overline{\rho}_\alpha\big)$$

are obtained. That is, we have the equations

$$sL\left(\underline{u}_\alpha(t)\right) + \underline{\mu}_\alpha L\big(\overline{u}_\alpha(t)\big) = \frac{\underline{\rho}_\alpha}{s} + \underline{\omega}_\alpha, \tag{7}$$

$$sL\big(\overline{u}_\alpha(t)\big) + \overline{\mu}_\alpha L\left(\underline{u}_\alpha(t)\right) = \frac{\overline{\rho}_\alpha}{s} + \overline{\omega}_\alpha. \tag{8}$$

If $L\big(\overline{u}_\alpha(t)\big)$ in the equation (7) is replaced by the equation (8),

$$L\left(\underline{u}_\alpha(t)\right) = \left(\underline{\rho}_\alpha - \underline{\mu}_\alpha\overline{\omega}_\alpha\right)\left(\frac{1}{s^2 - \underline{\mu}_\alpha\overline{\mu}_\alpha}\right) + \underline{\omega}_\alpha\left(\frac{s}{s^2 - \underline{\mu}_\alpha\overline{\mu}_\alpha}\right) - \frac{\overline{\rho}_\alpha\underline{\mu}_\alpha}{s\left(s^2 - \underline{\mu}_\alpha\overline{\mu}_\alpha\right)}$$

is obtained. Then, the lower solution is

$$\underline{u}_\alpha(t)=\frac{\left(\underline{\rho}_\alpha-\underline{\mu}_\alpha\overline{\omega}_\alpha\right)}{\sqrt{\underline{\mu}_\alpha\overline{\mu}_\alpha}}sin\left(\sqrt{\underline{\mu}_\alpha\overline{\mu}_\alpha}t\right)+\underline{\omega}_\alpha cos\left(\sqrt{\underline{\mu}_\alpha\overline{\mu}_\alpha}t\right)-\frac{\overline{\rho}_\alpha}{\overline{\mu}_\alpha}\left(\frac{e^{\sqrt{\underline{\mu}_\alpha\overline{\mu}_\alpha}t}+e^{-\sqrt{\underline{\mu}_\alpha\overline{\mu}_\alpha}t}}{2}-1\right).$$

Similarly, upper solution is

$$\overline{u}_\alpha(t)=\frac{\left(\overline{\rho}_\alpha-\overline{\mu}_\alpha\underline{\omega}_\alpha\right)}{\sqrt{\underline{\mu}_\alpha\overline{\mu}_\alpha}}sin\left(\sqrt{\underline{\mu}_\alpha\overline{\mu}_\alpha}t\right)+\overline{\omega}_\alpha cos\left(\sqrt{\underline{\mu}_\alpha\overline{\mu}_\alpha}t\right)-\frac{\underline{\rho}_\alpha}{\underline{\mu}_\alpha}\left(\frac{e^{\sqrt{\underline{\mu}_\alpha\overline{\mu}_\alpha}t}+e^{-\sqrt{\underline{\mu}_\alpha\overline{\mu}_\alpha}t}}{2}-1\right).$$

2) Let be u (2)-differentiable. Then, using the fuzzy Laplace transform, from the fuzzy differential equation (1)

$$-u(0)\ominus\left(-sL\left(u(t)\right)\right)+[\mu]^\alpha L\left(u(t)\right)=L([\rho]^\alpha),$$

that is,

$$-\overline{u}_\alpha(0)+sL\left(\overline{u}_\alpha(t)\right)+\underline{\mu}_\alpha L\left(\overline{u}_\alpha(t)\right)=L\left(\underline{\rho}_\alpha\right),$$

$$-\underline{u}_\alpha(0)+sL\left(\underline{u}_\alpha(t)\right)+\overline{\mu}_\alpha L\left(\underline{u}_\alpha(t)\right)=L\left(\overline{\rho}_\alpha\right)$$

are obtained. From this, we have

$$L\left(\underline{u}_\alpha(t)\right)=\frac{\overline{\rho}_\alpha}{s\left(s+\overline{\mu}_\alpha\right)}+\frac{\underline{\omega}_\alpha}{s+\overline{\mu}_\alpha},$$

$$L\left(\overline{u}_\alpha(t)\right)=\frac{\underline{\rho}_\alpha}{s\left(s+\underline{\mu}_\alpha\right)}+\frac{\overline{\omega}_\alpha}{s+\underline{\mu}_\alpha}.$$

Then, (2) solution is obtained as

$$\underline{u}_\alpha(t)=e^{-\overline{\mu}_\alpha t}\left(\underline{\omega}_\alpha-\frac{\overline{\rho}_\alpha}{\overline{\mu}_\alpha}\right)+\frac{\overline{\rho}_\alpha}{\overline{\mu}_\alpha},$$

$$\overline{u}_\alpha(t)=e^{-\underline{\mu}_\alpha t}\left(\overline{\omega}_\alpha-\frac{\underline{\rho}_\alpha}{\underline{\mu}_\alpha}\right)+\frac{\underline{\rho}_\alpha}{\underline{\mu}_\alpha},$$

$$[u(t)]^\alpha=\left[\underline{u}_\alpha(t),\overline{u}_\alpha(t)\right].$$

Example 2.2 Consider the fuzzy initial value problem

$$u'(t)+[-1]^\alpha u(t)=[2]^\alpha,\ t>0 \tag{9}$$

$$u(0)=[1]^\alpha, \tag{10}$$

using the fuzzy Laplace transform, where

$[-1]^\alpha=[-2+\alpha,-\alpha],\ [1]^\alpha=[\alpha,2-\alpha],[2]^\alpha=[1+\alpha,3-\alpha].$

If u is (1)-differentiable, (1) solution is

$$\underline{u}_\alpha(t) = \left(\frac{(1+\alpha)+(2-\alpha)^2}{\sqrt{\alpha(2-\alpha)}}\right) sin\left(\sqrt{\alpha(2-\alpha)}t\right) + \alpha cos\left(\sqrt{\alpha(2-\alpha)}t\right)$$
$$+\left(\frac{3-\alpha}{\alpha}\right)\left(\frac{e^{\sqrt{\alpha(2-\alpha)}t}+e^{-\sqrt{\alpha(2-\alpha)}t}}{2}-1\right),$$

$$\overline{u}_\alpha(t) = \left(\frac{(3-\alpha)+\alpha^2}{\sqrt{\alpha(2-\alpha)}}\right) sin\left(\sqrt{\alpha(2-\alpha)}t\right) + (2-\alpha)\alpha cos\left(\sqrt{\alpha(2-\alpha)}t\right)$$

$$+\left(\frac{1+\alpha}{2-\alpha}\right)\left(\frac{e^{\sqrt{\alpha(2-\alpha)}t}+e^{-\sqrt{\alpha(2-\alpha)}t}}{2}-1\right),$$

$$[u(t)]^\alpha = \left[\underline{u}_\alpha(t), \overline{u}_\alpha(t)\right].$$

If u is (2)-differentiable, (2) solution is

$$\underline{u}_\alpha(t) = e^{\alpha t}\left(\frac{\alpha^2+3-\alpha}{\alpha}\right) - \left(\frac{3-\alpha}{\alpha}\right),$$

$$\overline{u}_\alpha(t) = e^{(2-\alpha)t}\left(\frac{(2-\alpha)^2+1+\alpha}{2-\alpha}\right) - \left(\frac{1+\alpha}{2-\alpha}\right),$$

$$[u(t)]^\alpha = \left[\underline{u}_\alpha(t), \overline{u}_\alpha(t)\right].$$

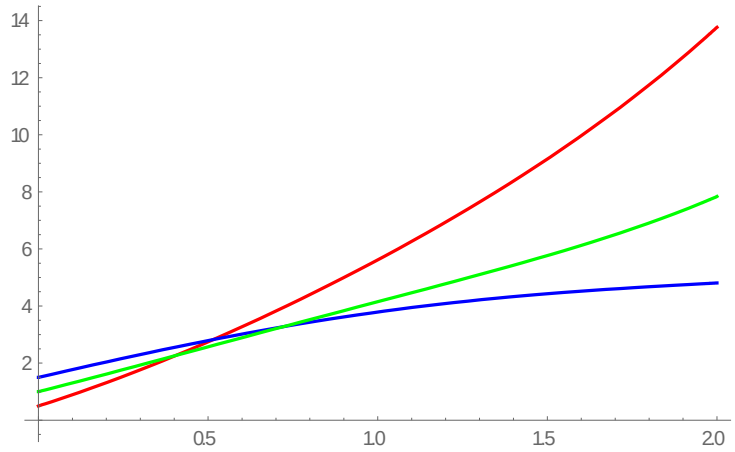

Figure 3 (1) solution for $\alpha = 0.5$

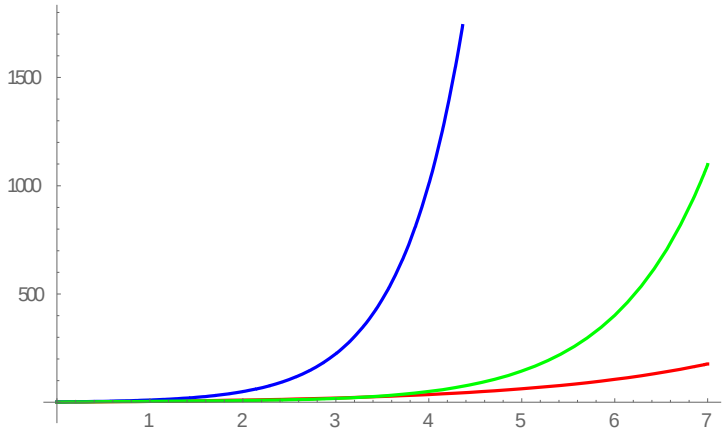

Figure 4 (2) solution for $\alpha = 0.5$

$red \rightarrow \underline{u}_{\alpha}(t)$, $blue \rightarrow \overline{u}_{\alpha}(t)$, $green \rightarrow u(t)$

From Definition 1.3 and since $[u(x)]^{\alpha}$is positive fuzzy function, according to figure 3, (1) solution is a valid fuzzy number for $x\epsilon[0,0.514863]$, according to figure 4, (2) solution i

s a valid fuzzy number for $t > 0$.

3. CONCLUSIONS

In this study, solutions of fuzzy initial value problems for first-order fuzzy differential equations with positive and negative fuzzy number coefficients are investigated by fuzzy Laplace transform. Generalized differentiability is used. Examples are solved and the figures of the solutions are drawn. It is shown that whether the solutions are valid fuzzy functions or not. Also, it is shown that solutions are valid fuzzy functions in different intervals for each α −cut.

REFERENCES

[1] Kadel A. and Byatt W.J., Fuzzy Differential Equations, in: Proceedings of International Conference Cybernetics and Society, Tokyo, (1978) 1213-1216.

[2] Zadeh L.A., The Concept of a Linguistic Variable and its Application to Approximate Reasoning, Information Sciences, 8 (1975) 199-251.

[3] Hüllermeier E., An Approach to Modelling and Simulation of Uncertain Dynamical Systems, International Journal of Uncertainty, Fuzziness and Knowledge-Based Systems, 5-2 (1997) 117-137.

[4] Kaleva O., Fuzzy Differential Equations, Fuzzy Sets and Systems, 24-3 (1987) 301-317.

[5] Gültekin H. and Altınışık N., On Solution of Two-Point Fuzzy Boundary Value Problems, The Bulletin of Society for Mathematical Services and Standards, 11 (2014) 31-39.

[6] Bede B., Rudas I.J. and Bencsik A.L., First Order Linear Fuzzy Differential Equations under Generalized Differentiability, Information Sciences, 177-7 (2007) 1648-1662.

[7] Gültekin Çitil H., The Relationship between the Solutions according to the Noniterative Method and the Generalized Differentiability of the Fuzzy Boundary Value Problem, Malaya Journal of Matematik, 6-4 (2018) 781-787.

[8] Ceylan T. and Altınışık N., Fuzzy Eigenvalue Problem with Eigenvalue Parameter Contained in the Boundary Condition, Journal of Science and Arts, 3-44 (2018) 589-602.

[9] Allahviranloo T. and Barkhordari Ahmadi M., Fuzzy Laplace Transforms, Soft Computing, 14-3 (2010) 235-243.

[10] Patel K.R. and Desai N.B., Solution of Fuzzy Initial Value Problems by Fuzzy Laplace Transform, Kalpa Publications in Computing, 2 (2017) 25-37.

[11] Patel K.R. and Desai N.B., Solution of Variable Coefficient Fuzzy Differential Equations by Fuzzy Laplace Transform, International Journal on Recent and Innovation Trends in Computing and Communication, 5-6 (2017) 927-942.

[12] Liu H.-K., Comparison Results of Two-Point Fuzzy Boundary Value Problems, International Journal of Computational and Mathematical Sciences, 5-1 (2011) 1-7.

[13] Salahshour S. and Allahviranloo T., Applications of Fuzzy Laplace Transforms, Soft Computing, 17-1 (2013) 145-158.

[14] Shirin S. and Saha G.K., A New Computational Methodology to Find Appropriate Solutions of Fuzzy Equations, Mathematical Theory and Modeling, 2-1 (2011) 1-10.

[15] Lakshmikantham V. and Mohapatra R.N., Theory of Fuzzy Differential Equations and Inclusions, Taylor and Francis, London, New York, 2003.

[16] Khastan A. and Nieto J.J., A Boundary Value Problem for Second Order Fuzzy Differential Equations, Nonlinear Analysis: Theory, Methods and Applications, 72-9-10 (2010) 3583-3593.

Cumhuriyet Science Journal
CSJ

e-ISSN: 2587-246X
ISSN: 2587-2680

Cumhuriyet Sci. J., Vol.40-4 (2019) 896-901

A Dynamic Network Model For Population Growth And Urbanization

Emir HALİKİ [1*]

[1] *EgeUniversity, Faculty of Science, Department of Physics, Izmir, Turkey*

Received: 14.10.2019; Accepted: 08.12.2019 *http://dx.doi.org/10.17776/csj.632996*

Abstract. Dynamic networks imply those states of which change over time and such changes are generally associated with the topology of a network. Dynamic models are currently needed for numerous systems which could be defined as a network model. Those related to the propagation of living organisms are also a typical example. The study has examined a sample space which has been defined in the network topology of human population as the way in which it will spread with population growth and correlated with various variables in the modeled dynamic network.

Keywords**:** Network, Population growth, Logistic differential equation, Connected component, Clustering coefficient, Correlation.

Nüfus Artışı ve Kentleşme İçin Dinamik Bir Ağ Modeli

Özet. Dinamik ağlar, zaman içinde değişiklik gösteren durumları belirtmekte ve bu değişiklikler genellikle bir ağın topolojisi ile ilişkilendirilmektedir. Ağ modeli olarak tanımlanabilecek birçok sistem için dinamik modellere ihtiyaç duyulmaktadır. Canlı organizmaların yayılması ile ilgili olanlar da bu duruma bir örnektir. Çalışmada insan nüfusunun ağ topolojisi tanımlanarak ile bir örnek uzay oluşturulmuş, nüfus artışı ile içerisinde nasıl bir yayılma görüleceği araştırılmış ve nüfus büyümesinin modellenen dinamik ağdaki çeşitli değişkenler ile aralarındaki korelasyonlar incelenmiştir.

Anahtar Kelimeler: Dönüştürülmüş iki boyutlu dağılım, Bağımlılık, İki boyutlu dağılım, Spearman sıra korelasyonu, Fréchet sınırları.

1. INTRODUCTION

When the human population was still small and when people were constantly moving from one place to another, the abandonment of the land on which they grew plants and lived was not a problem for the nature yet. However, the idea that nature had to be conquered developed later and people pass on to expansionist form of life [1]. By far the most important factor in this sense originated from the transition to settlement. So sufficient was settlement instead of immigration for sources that existing land was preserved with inevitable expansion to the new soils. It is known that Neolithic people first passed to settlement approximately 12500 years ago [2,3]. It was the major factors which played a significant role in the related transition that agricultural development, climatic changes and husbandry of animals occurred. Although it is still obscure whether those reasons triggered population growth or population growth lead to those reasons, it is a fact that population growth accelerated use up of present sources in a place and necessitated people to expand to new lands, which is currently going on.

* Corresponding author. *Email address:* *emir.haliki@ege.edu.tr*

Expansion of regions by human being under the settlement principle has caused the cities to be made up of districts and countries to be composed of cities [4]. Increasingly growing population and urbanization leads to construction shifting to rural areas and expansion is in the form of construction across natural zones by transforming them into increased settlement. Various predictions and dynamic models have been thus far developed on the growth and spread of countless plant and animal populations [5,6] while those on spreading human population are far cry from being sufficient [7,8].

The present study has modeled the human expansion accompanied by population growth using a network model to finally examine its correlation of several variables with it. A fictitious region has been defined, separated into a certain number of nodes and a precessor pattern is created in such a way that no nodes are connected with each other (disconnected graph) first and then a random starting node has been selected where the population first began to proliferate and urbanized in a sense with the identification of the location and linking a new node to the preceeding ones over time. In conclusion, the correlation between population growth and some characteristics of the growing network has been shown and the conclusions presented in the section of results and discussion.

2. MATERIALS AND METHODS

A population-related differential equation to indicate the two important concepts namely, ecology and epidemiology are as follows;

$$\dot{N} = (r - d)N, \tag{1}$$

where N is the number of individuals r birth rate and d death. If $r > d$ the population continues to grow indefinitely. In a real environment, any growth in the population will hit constraints such as in running out of nutrients or physical space, which suggests the concept of carrying capacity and a more proper population growth could be given by the logistic equation [9] below;

$$\dot{N} = rN\left(1 - \frac{N}{\kappa}\right), \tag{2}$$

where κ is the carrying capacity. When N increases, the rate of growth decreases. As $N = \kappa$, growth of the population stops. For any initial population N_0, solution of eq. 2 is presented as follows;

$$N(t) = \frac{\kappa N_0 e^{rt}}{\kappa + N_0(e^{rt} - 1)} \tag{3}$$

with N_0 being the initial population. As time passes, the population converges to its carrying capacity. Once it has reached it, growth stops. However, there may be occasional dynamic limits for the carrying capacity [10]. Ecological carrying capacity is suitable for non-human beings whereas it does not always apply to human beings, because economy, environment, culture and demography are involved [11]. Nevertheless, an average carrying capacity can be determined in order to acquire fundamental approaches to population dynamics [12,13].

The region of population distribution in the developed model as a pattern composed of 36 nodes, each of which corresponds to a zone likely to be occupied on a possible settlement map. The network growth has been defined as expanding 2-D graph distribution which represents a graph with n nodes uniformly distributed over a plane. Edges between nodes have been determined by distance d. The simulation exhibits that the d value in the network changes proportionally with the increasing population by the continuous logistic equation. The initial population for population growth model is 100 individuals and

the growth rate (r) 0.3. The carrying capacity corresponding to the situation where all the spread on the system is completed is limited to a hundred thousand. Moreover, one has calculated the global clustering coefficient (GCC) and the largest connected component (LCC) values of the cluster at each moment corresponding to the time checkpoints of the continuous logistic equation in the growing network as a 2-D graph distribution. The LCC represents the largest subset in a network [14] (reaches the total number of nodes in the network with each node having a connection), while the GCC, a measure of how much the network is connected, is the ratio of three-fold number of the triangles to that of pairs of adjacent edges in network [15]. GCC and LCC in network growth have been simulated by averaging over ten thousand experiments to reduce possible errors statistically. Figure 1 has shown the edges between nodes in the growing network at various timesteps (given checkpoints) selected from a random experiment.

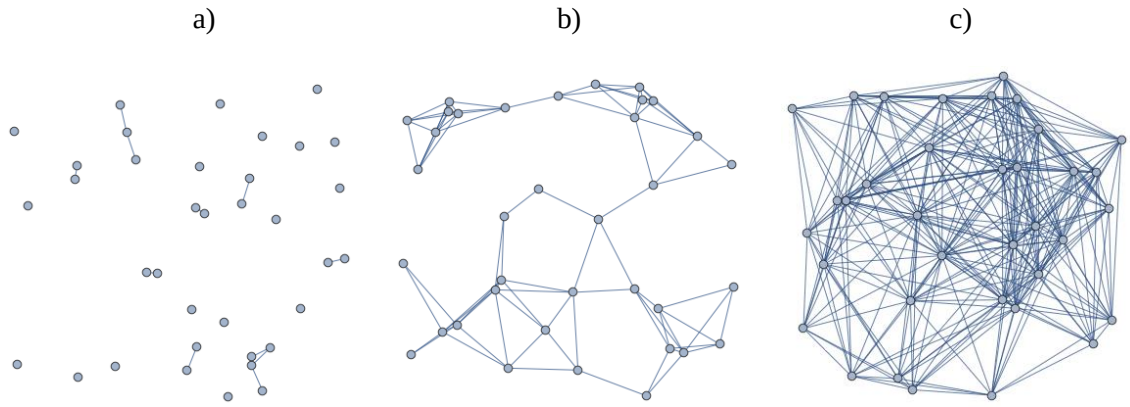

Figure 1. Three snapshots of the growing network which has a) $d = 0.07$, b) $d = 0.22$, c) $d = 0.49$.

The aforementioned times correspond to steps of 0.01 for d values with figure 2 exhibiting the graph of the GCC values versus time and logistic population growth (N) versus time. Note that the logistic population growth data have been normalized to the [0,1] range where 1 is the carrying capacity.

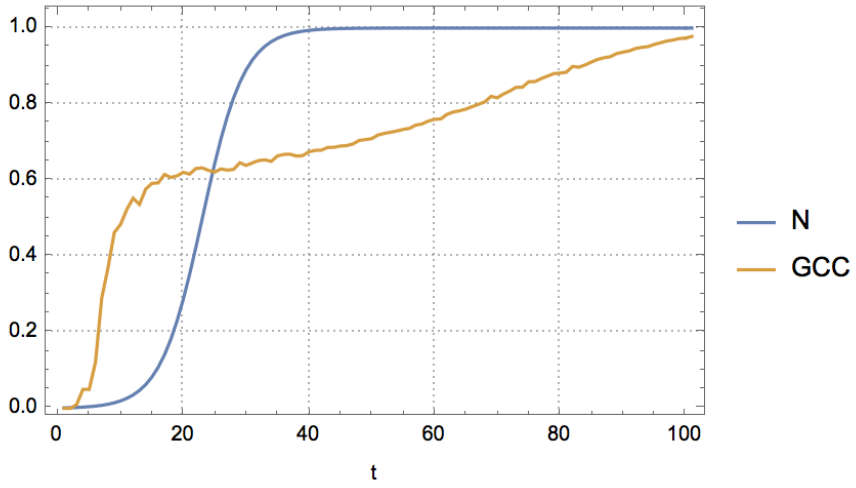

Figure 2. Behaviors of the population and the global clustering coefficient over time. When the population reaches to carrying capacity, the number of edges of the network is observed to be still increasing.

When the population reaching to the carrying capacity, the reason for the growth of the GCC is that the number of connections of each node increases due to the rise of the connection distance in the 2-D graph distribution model. Accordingly, the increase of LCC in the growth of the network over time is presented in figure 3.

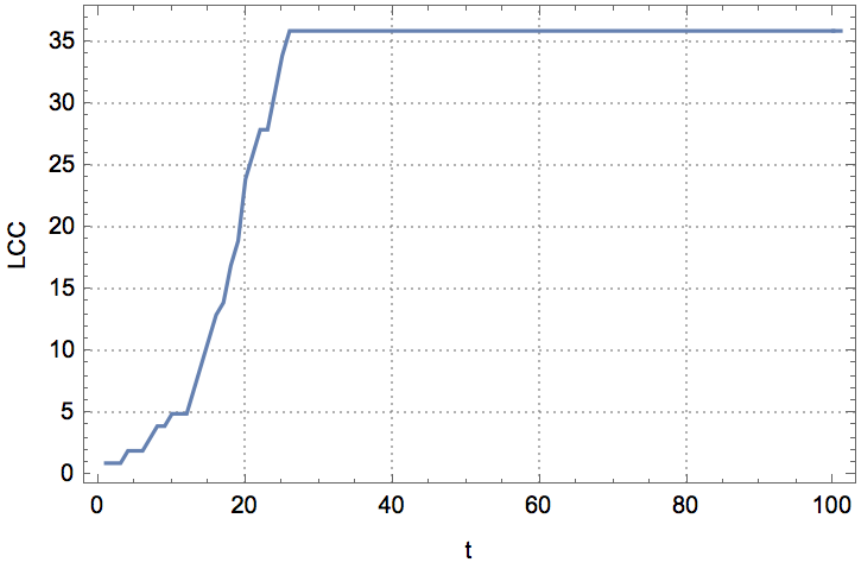

Figure 3. Growth of the largest connected component of the network. After the 26th timestep, the network has been fully connected.

Following a given period of time, the logistic growth of the population has reached to carrying capacity, the LCC value to the maximum number of nodes and the GCC to its maximum of 1, which exhibits the way the population growth and the GCC and LCC of the network correlate with the generated model. Pearson correlation coefficient [16] between two variables is given as;

$$\rho_{XY} = \frac{\sigma_{XY}}{\sigma_X \sigma_Y}, \tag{4}$$

where σ_{XY} is the covariance between variables X and Y and the denominator is also their multiplied standard deviations. Each of three variables' Pearson correlation coefficients with the other two has thus been calculated and shown in Table 1.

Table 1. Pearson correlation coefficients.

N-GCC	N-LCC	GCC-LCC
0.793	0.958	0.801

3. RESULTS AND DISCUSSION

With a certain population growing, the interconnectedness of each region spread over time is also seen in such concepts as online social, spread disease and traffic networks [17-19]. Therefore, the three quantities examined in the established model are correlated with each other. LCC is highly correlated with population growth in simulation outputs. The reason for the very strong relationship between them is the increase in LCC in a behavior similar to the population in spreading from one node to the other with population growth. On the other hand, as the population grows and spreads to other nodes, the number of connections between the nodes increases. For instance, open triplets turn into closed triangles, which has been simulated in such a way that interactions have increased between settlements as the population grows in the model. That is the explanation for the strong relationship between N and GCC. The strong relationship between the GCC and the LCC is also one of the basic networking features requiring that the growth of the connected component should depend on the number of connections, ie the clustering

coefficient [20]. They have become well correlated since the network grew from a single point in the 2-D graph distribution-based model.

The present knowledge of the world is often determined by geographical maps. In the developed model, a possible settlement on a given map has been divided into units (nodes) and extrapolated from the initial node to the others with the population. In order that the model to should show some similarity to the reality, the number of connections has continued to increase even if the carrying capacity has been reached in order to make the settlement area completely connected to each other. If different components of a human population is to have heterogeneous requirements, estimates of total carrying capacity based on a single formula could not be accurate. Similarly, it is possible that different parts of the global human population would have heterogeneous needs as well. Therefore, the developed model may seem to be simplified in terms of the increase of the human population and its limitation to a certain area. However, in future studies, carrying capacity, a variable of equations such as logistic growth, could be rendered more dynamic by having multiple variables within itself.

REFERENCES

[1] Goudie A. S., Human impact on the natural environment, 8th ed., Wiley: Hoboken, NJ, USA, 2018.

[2] Kuijt I. J., People and space in early agricultural villages: exploring daily lives, community size, and architecture in the Late Pre-Pottery Neolithic, Anthropol. Archaeol., 19 (2000) 75-102.

[3] Putterman L., Agriculture, diffusion and development: ripple effects of the neolithic revolution, Economica, 75 (2008) 729-748.

[4] Dickinson R. E., City and region: a geographical interpretation, Taylor&Francis: Oxfordshire, UK, 1998.

[5] Clark J. S., Lewis M., McLachlan J. S., HilleRisLambers J., Estimating population spread: what can we forecast and how well?, Ecology, 84 (2003) 1979-1988.

[6] Haydon D. T., Morales J. M., Yott A., Jenkins D. A., Rosatte R., Fryxell J. M. P., Socially informed random walks: incorporating group dynamics into models of population spread and growth, Roy. Soc. B. Biol. Sci., 275 (2008) 1101-1109.

[7] Wittemyer G., Elsen P., Bean W. T., Burton A. C. O., Brashares J. S., Accelerated human population growth at protected area edges, Science, 321 (2008) 123-126.

[8] Bongaarts J., Human population growth and the demographic transition, Philos. T. Roy. Soc. B., 364 (2009) 2985-2990.

[9] Nowak M. A., Evolutionary dynamics, Harvard University Press: London, UK, 2006.

[10] Meyer P. S., Ausubel J. H., Carrying capacity: a model with logistically varying limits, Technol. Forecast. Soc., 61 (1999) 209-214.

[11] Cohen J. E., Population growth and earth's human carrying capacity, Science, 269 (1995) 341-346.

[12] Graymore M. L., Sipe N. G., Rickson R. E., Sustaining human carrying capacity: a tool for regional sustainability assessment, Ecol. Econ., 69 (2010) 459-468.

[13] Hopfenberg R., Human carrying capacity is determined by food availability, Popul. Environ., 25 (2003) 109-117.

[14] Yang X., Megson G. M., Tang Y. Y., Xing Y., Largest connected component of a star graph with faulty vertices, Int. J. Comput. Math., 85 (2008) 1771-1778.

[15] Soffer S. N., Vazquez A., Network clustering coefficient without degree-correlation biases, Phys. Rev. E., 71 (2005) 057101.

[16] Benesty J., Chen J., Huang Y., Cohen I., Pearson correlation coefficient. In Noise reduction in speech processing, Springer: Berlin, Heidelberg, 2009.

[17] Centola D., The spread of behavior in an online social network experiment, Science, 329 (2010) 1194-1197.

[18] Jeger M. J., Pautasso M., Holdenrieder O., Shaw M. W., Modelling disease spread and control in networks: implications for plant sciences, New Phytol., 174 (2007) 279-297.

[19] Coclite G. M., Garavello M., Piccoli B., Traffic flow on a road network, SIAM J. Math. Anal., 36 (2005) 1862-1886.

[20] Serrano M. Á., Boguná M., Percolation and epidemic thresholds in clustered networks, Phys. Rev. Lett., 97 (2006) 088701.

Cumhuriyet Science Journal
CSJ

e-ISSN: 2587-246X
ISSN: 2587-2680

Cumhuriyet Sci. J., Vol.40-4 (2019) 902-908

Half-Inverse Problem For Dirac Operator With Boundary And Transmission Conditions Dependent Spectral Parameter Polynomially

Merve ARSLANTAŞ [1], *Yalçın GÜLDÜ* [1*]

[1] *Department of Mathematics, Faculty of Science, Cumhuriyet University 58140 Sivas, TURKEY*

Received: 25.10.2019; Accepted: 18.12.2019 *http://dx.doi.org/10.17776/csj.637861*

Abstract. In this paper, half-inverse problem is considered for Dirac equations with boundary and finite number of transmission conditions depending polynomially on the spectral parameter, if the potential is given over the half of the considered interval and if one spectrum is known then, potential function $\Omega(x)$ on the whole interval and the other coefficients of the considered problem can be determined uniquely.

***Keywords*:** Dirac equations, Transmission conditions, Spectral parameter.

Sınır ve Süreksizlik Koşulları Spektral Parametreye Polinom Olarak Bağlı Dirac Operatörü İçin Yarı-Ters Problem

Özet. Bu makalede, sınır koşulları ve sonlu sayıda süreksizlik koşulları spektral parametreye polinom olarak bağlı Dirac denklemleri için yarı-ters problem ele alınmış olup, yarı aralıkta $\Omega(x)$ potansiyel fonksiyonu biliniyorken, bir spektruma göre, aralığın tamamında $\Omega(x)$ potansiyel fonksiyonu ile ele alınan problemin katsayılarının tek olarak belirlendiği gösterilmiştir.

Anahtar Kelimeler: Dirac denklemler, Süreksizlik koşulları, Spektral parametre.

1. INTRODUCTION

Inverse problems of spectral analysis compose of retrieving operators from their spectral characteristics. For this reason, inverse spectral theory is so significant research subject in mathematics, physics, mechanics, electronics, geophysics and other branches of natural sciences.

Half-inverse problem for a Dirac operator consists in reconstruction of the operator from its spectrum and known potential in the half-interval. Half inverse problem was first studied by Hochstadt and Lieberman in 1978[1]. In study of [2],by one boundary condition and potential which is known on half the interval, the potential and other boundary condition are uniquely determined. After that, these results have been used to lots of works[3-12].

On the other hand, in 1973 Walter [13] and in 1977 Fulton [14] studied the Sturm-Liouville problem with boundary conditions dependent on spectral parameter linearly. Then, inverse problems for some classes of differential operators depending on the eigenvalue-parameter linearly or nonlinearly on boundary and also transmission conditions were studied in various papers[15-33].

The main result of this paper is that if the potential function $\Omega(x)$ is known over the half the interval and one spectrum is given, then coefficients of the following problem can be uniquely determined.

* Corresponding author. *Email address:* *yguldu@cumhuriyet.edu.tr*

In this study, we concern the boundary value problem L generated by the following system of Dirac equations

$$l[Y(x)] \coloneqq BY'(x) + \Omega(\mathrm{x})\mathrm{Y}(\mathrm{x}) = \lambda Y(x) \tag{1}$$

with the boundary conditions

$$l_1 y \coloneqq a_2(\lambda)y_2(a) - a_1(\lambda)y_1(a) = 0 \tag{2}$$

$$l_2 y \coloneqq b_2(\lambda)y_2(b) - b_1(\lambda)y_1(b) = 0 \tag{3}$$

and the transmission conditions

$$\begin{array}{ll} U_i(y) \coloneqq & y_1(\xi_i + 0) - \theta_i y_1(\xi_i - 0) = 0 \\ V_i(y) \coloneqq & y_2(\xi_i + 0) - \theta_i^{-1} y_2(\xi_i - 0) - \gamma_i(\lambda)y_1(\xi_i - 0) = 0 \end{array} \quad i = \overline{1,n} \tag{4}$$

where $B = \begin{pmatrix} 0 & 1 \\ -1 & 0 \end{pmatrix}$, $\Omega(\mathrm{x}) = \begin{pmatrix} p(x) & q(x) \\ q(x) & r(x) \end{pmatrix}$, $Y(x) = \begin{pmatrix} y_1(x) \\ y_2(x) \end{pmatrix}$, $p(x)$, $q(x)$ and $r(x)$ are real valued functions in $L_2(a,b)$, $\boldsymbol{\lambda}$ is a spectral parameter, $a_i(\lambda)$, $b_i(\lambda)$, $(i = 1,2)$ and $\gamma_i(\lambda)$ $(i = \overline{1,n})$ are polynomial with real cofficients and no common zeros, $\xi_i \epsilon (a,b)$ $(i = \overline{1,n})$, $\theta_i \epsilon \mathbb{R}^+$,

$a_1(\lambda) = \sum_{k=0}^{m_1} a_{k1}\lambda^k$, $a_2(\lambda) = \sum_{k=0}^{m_2} a_{k2}\lambda^k$, $b_1(\lambda) = \sum_{k=0}^{m_3} b_{k1}\lambda^k$, $b_2(\lambda) = \sum_{k=0}^{m_4} b_{k2}\lambda^k$ and

$\gamma_i(\lambda) = \sum_{k=0}^{r_i} \gamma_{ki}\lambda^k$, $f(\lambda) = \frac{b_1(\lambda)}{b_2(\lambda)}$, $m_a = max\{m_1, m_2\}$, $m_b = max\{m_3, m_4\}$,

$r = max_{1 \le i \le n}\{deg\, \gamma_i(\lambda)\}$.

2. UNIQUENESS THEOREM

Theorem: Suppose

$\lambda_n = \tilde{\lambda}_n$, $a_i(\lambda) = \tilde{a}_i(\lambda)$ $(i = 1,2)$, $\Omega(\mathrm{x}) = \widetilde{\Omega}(\mathrm{x})$ on $\left[a, \frac{a+b}{2}\right]$ and $U_i = \widetilde{U}_i$, $V_i = \widetilde{V}_i$ for all $i = \overline{1,n}$ with $\xi_i \le \frac{a+b}{2}$ for $dega_2(\lambda) > dega_1(\lambda)$

if $degb_2(\lambda) > degb_1(\lambda)$ $m_2 > m_4 + \sum_{i=1}^{n} r_i$

if $degb_1(\lambda) > degb_2(\lambda)$ $m_2 > m_3 + \sum_{i=1}^{n} r_i$

if $degb_1(\lambda) = degb_2(\lambda)$ $m_2 > m_b + \sum_{i=1}^{n} r_i$.

Then $\Omega(\mathrm{x}) = \widetilde{\Omega}(\mathrm{x})$ almost everywhere on $[a,b]$, $f(\lambda) = \tilde{f}(\lambda)$ and $\theta_i = \tilde{\theta}_i$, $\gamma_i(\lambda) = \tilde{\gamma}_i(\lambda)$, $\xi_i = \tilde{\xi}_i$ for $i = \overline{1,n}$.

We need the following lemma, before we prove this theorem.

Lemma: If λ^* is the zero of the polynomial $a_2(\lambda)$ with multiplicities m_{λ^*} then λ^* is also the zero of the entire function

$C\psi_1(a,\lambda) - \tilde{\psi}_1(a,\lambda)$

with at least multiplicities m_{λ^*}.

Proof: $\Delta(\lambda) = a_1(\lambda)\psi_1(a,\lambda) - a_2(\lambda)\psi_2(a,\lambda)$ and $\tilde{\Delta}(\lambda) = a_1(\lambda)\tilde{\psi}_1(a,\lambda) - a_2(\lambda)\tilde{\psi}_2(a,\lambda)$.

If λ^* is the zero of the polynomial $a_2(\lambda)$ with multiplicities m_{λ^*} at that time we attain

$\Delta(\lambda^*) = a_1(\lambda^*)\psi_1(a,\lambda^*)$ and $\tilde{\Delta}(\lambda^*) = a_1(\lambda^*)\tilde{\psi}_1(a,\lambda^*)$.
On the other hand, since $\tilde{\Delta}(\lambda)$ and $\Delta(\lambda)$ are both entire in λ, by Hadamard's factorization theorem we can $\tilde{\Delta}(\lambda) = C\Delta(\lambda)$. Then

$0 = C\Delta(\lambda^*) - \tilde{\Delta}(\lambda^*) = a_1(\lambda^*)\left[C\psi_1(a,\lambda^*) - \tilde{\psi}_1(a,\lambda^*)\right]$.
Since $a_1(\lambda)$ and $a_2(\lambda)$ do not have common zeros, we have

$C\psi_1(a,\lambda^*) - \tilde{\psi}_1(a,\lambda^*) = 0$.

Now, inductively, if for all $0 \le s < k \le m_{\lambda^*} - 1$ there holds

$\frac{d^s}{d\lambda^s}\left[C\psi_1(a,\lambda) - \tilde{\psi}_1(a,\lambda)\right]\Big|_{\lambda=\lambda^*} = 0$

then we will prove that

$\frac{d^k}{d\lambda^k}\left[C\psi_1(a,\lambda) - \tilde{\psi}_1(a,\lambda)\right]\Big|_{\lambda=\lambda^*} = 0.$

$$\frac{d^k}{d\lambda^k}\Delta(\lambda) = \frac{d^k}{d\lambda^k}[a_1(\lambda)\psi_1(a,\lambda) - a_2(\lambda)\psi_2(a,\lambda)]$$

$$= \sum_{t=0}^{k}\binom{k}{t}\left[\frac{d^t}{d\lambda^t}a_1(\lambda)\frac{d^{k-t}}{d\lambda^{k-t}}\psi_1(a,\lambda) - \frac{d^t}{d\lambda^t}a_2(\lambda)\frac{d^{k-t}}{d\lambda^{k-t}}\psi_2(a,\lambda)\right]$$

$$\frac{d^k}{d\lambda^k}\Delta(\lambda)\Big|_{\lambda=\lambda^*} = \sum_{t=0}^{k}\binom{k}{t}\frac{d^t}{d\lambda^t}a_1(\lambda)\Big|_{\lambda=\lambda^*}\frac{d^{k-t}}{d\lambda^{k-t}}\psi_1(a,\lambda)\Big|_{\lambda=\lambda^*}$$

$$\frac{d^k}{d\lambda^k}\tilde{\Delta}(\lambda)\Big|_{\lambda=\lambda^*} = \sum_{t=0}^{k}\binom{k}{t}\frac{d^t}{d\lambda^t}a_1(\lambda)\Big|_{\lambda=\lambda^*}\frac{d^{k-t}}{d\lambda^{k-t}}\tilde{\psi}_1(a,\lambda)\Big|_{\lambda=\lambda^*}$$

From the last two equations we have

$$\frac{d^k}{d\lambda^k}\left[C\Delta(\lambda) - \tilde{\Delta}(\lambda)\right]\Big|_{\lambda=\lambda^*} = \sum_{t=0}^{k}\binom{k}{t}\frac{d^t}{d\lambda^t}a_1(\lambda)\Big|_{\lambda=\lambda^*}\frac{d^{k-t}}{d\lambda^{k-t}}\left[C\psi_1(a,\lambda) - \tilde{\psi}_1(a,\lambda)\right]\Big|_{\lambda=\lambda^*}.$$

Since

$C\Delta(\lambda) - \tilde{\Delta}(\lambda) = 0$

$$\sum_{t=0}^{k}\binom{k}{t}\frac{d^t}{d\lambda^t}a_1(\lambda)\Big|_{\lambda=\lambda^*}\frac{d^{k-t}}{d\lambda^{k-t}}\left[C\psi_1(a,\lambda) - \tilde{\psi}_1(a,\lambda)\right]\Big|_{\lambda=\lambda^*} = 0.$$

Since for all $0 \le s < k$

$\frac{d^s}{d\lambda^s}\left[C\psi_1(a,\lambda) - \tilde{\psi}_1(a,\lambda)\right]\Big|_{\lambda=\lambda^*} = 0$

we have

$a_1(\lambda^*)\frac{d^k}{d\lambda^k}\left[C\psi_1(a,\lambda)-\tilde{\psi}_1(a,\lambda)\right]\Big|_{\lambda=\lambda^*}$=0.

Since $a_1(\lambda^*)$ we obtain

$\frac{d^k}{d\lambda^k}\left[C\psi_1(a,\lambda)-\tilde{\psi}_1(a,\lambda)\right]\Big|_{\lambda=\lambda^*}$=0.

Lemma is proved.

If $a_1(\lambda)\equiv 0$ and $a_2(\lambda)\equiv 1$ are taken in the boundary condition, since $M(\lambda)=-\frac{\psi_1(a,\lambda)}{\Delta(\lambda)}$ and

$\Delta(\lambda)= a_1(\lambda)\psi_1(a,\lambda)-a_2(\lambda)\psi_2(a,\lambda)=-\psi_2(a,\lambda)$

$$M_0(\lambda):=\frac{\psi_1(a,\lambda)}{\psi_2(a,\lambda)}$$

obtained.

Remark 1: For the problem L given by the conditions $a_1(\lambda)\equiv 0$ and $a_2(\lambda)\equiv 1$ if $M_0(\lambda)=\tilde{M}_0(\lambda)$ then $\Omega(\mathrm{x})=\tilde{\Omega}(\mathrm{x})$ almost everywhere on $[a,b]$, $f(\lambda)=\tilde{f}(\lambda)$ and for each $i=\overline{1,n}$ $\theta_i=\tilde{\theta}_i$,

$\gamma_i(\lambda)=\tilde{\gamma}_i(\lambda)$, $\xi_i=\tilde{\xi}_i$ applies.

Remark 2: For the Dirac operator given in the interval $\left[\frac{a+b}{2},b\right]$ with equation (1), $y_2\left(\frac{a+b}{2}\right)=0$ and the transmission conditions (4), from the above Remark 1; $M_0(\lambda)$ determines the function $\Omega(\mathrm{x})$ and θ_i, $\gamma_i(\lambda)$, ξ_i for $i=\overline{1,n}$ as one on $\left[\frac{a+b}{2},b\right]$.

Proof of Theorem : We only prove the case when $\xi_i\neq\frac{a+b}{2}$ for all i. The argument of the case when $\xi_i=\frac{a+b}{2}$ for some i is similar. Using Lagrange identity we have

$$\int_a^{\frac{a+b}{2}}\left(\tilde{\psi}_1(x,\lambda),\tilde{\psi}_2(x,\lambda)\right)\left(\Omega(\mathrm{x})-\tilde{\Omega}(\mathrm{x})\right)\begin{pmatrix}\psi_1(x,\lambda)\\ \psi_2(x,\lambda)\end{pmatrix}dx$$

$$+\left[\tilde{\psi}_1(x,\lambda)\psi_2(x,\lambda)-\tilde{\psi}_2(x,\lambda)\psi_1(x,\lambda)\right]\Big|_a^{\frac{a+b}{2}}$$

For all i satisfying $\xi_i<\frac{a+b}{2}$

$$\left[\tilde{\psi}_1(x,\lambda)\psi_2(x,\lambda)-\tilde{\psi}_2(x,\lambda)\psi_1(x,\lambda)\right]\Big|_{\xi_i-0}^{\xi_i+0}=0$$

Together with $\Omega(\mathrm{x})=\tilde{\Omega}(\mathrm{x})$ for a.e. $\left[a,\frac{a+b}{2}\right]$ we have

$$\tilde{\psi}_1\left(\frac{a+b}{2},\lambda\right)\psi_2\left(\frac{a+b}{2},\lambda\right)-\tilde{\psi}_2\left(\frac{a+b}{2},\lambda\right)\psi_1\left(\frac{a+b}{2},\lambda\right)$$

$$=\tilde{\psi}_1(a,\lambda)\psi_2(a,\lambda)-\tilde{\psi}_2(a,\lambda)\psi_1(a,\lambda).$$

Since

$\tilde{\Delta}(\lambda) = C\Delta(\lambda)$, $\Delta(\lambda) = a_1(\lambda)\psi_1(a,\lambda) - a_2(\lambda)\psi_2(a,\lambda)$ and $\tilde{\Delta}(\lambda) = a_1(\lambda)\tilde{\psi}_1(a,\lambda) - a_2(\lambda)\tilde{\psi}_2(a,\lambda)$

we get

$$\tilde{\psi}_1(a,\lambda)\psi_2(a,\lambda) - \tilde{\psi}_2(a,\lambda)\psi_1(a,\lambda) = \Delta(\lambda)\frac{C\psi_1(a,\lambda) - \tilde{\psi}_1(a,\lambda)}{a_2(\lambda)}$$

Denote

$$\mathrm{T}(\lambda) := \frac{\mathrm{G}(\lambda)}{\Delta(\lambda)}$$

$$= \frac{\tilde{\psi}_1\left(\frac{a+b}{2},\lambda\right)\psi_2\left(\frac{a+b}{2},\lambda\right) - \tilde{\psi}_2\left(\frac{a+b}{2},\lambda\right)\psi_1\left(\frac{a+b}{2},\lambda\right)}{\Delta(\lambda)}$$

The function $\mathrm{T}(\lambda)$ is entire in $\mathbb{C}$. From the assumption that $\lambda_n = \tilde{\lambda}_n$ and the term of the characteristic function $\Delta(\lambda)$ it is easy to infer that

if $degb_2(\lambda) > degb_1(\lambda)$ $m_4 = \tilde{m}_4$

if $degb_1(\lambda) > degb_2(\lambda)$ $m_3 = \tilde{m}_3$

if $degb_1(\lambda) = degb_2(\lambda)$ $m_b = \tilde{m}_b$.

From the following inequalities

$$|\Delta(\lambda)| \geq C_\delta|\lambda|^{m_2+m_4+A}exp\{|Im\lambda|(b-a)\}, \qquad degb_2(\lambda) > degb_1(\lambda)$$

$$|\Delta(\lambda)| \geq C_\delta|\lambda|^{m_2+m_3+A}exp\{|Im\lambda|(b-a)\}, \qquad degb_1(\lambda) > degb_2(\lambda)$$

$$|\Delta(\lambda)| \geq C_\delta|\lambda|^{m_2+m_b+A}exp\{|Im\lambda|(b-a)\}, \qquad degb_1(\lambda) = degb_2(\lambda)$$

and the asymptotic formulas of the functions $\psi_i(x,\lambda), (i = 1,2)$ for all intervals $(\xi_i, \xi_{i+1}), (i = \overline{0,n})$ and Phragmen-Lindelöf theorem, for all λ we get $\mathrm{T}(\lambda) \equiv 0$.

Because of $\mathrm{G}(\lambda) \equiv 0$ it yields

$$\tilde{\psi}_1\left(\frac{a+b}{2},\lambda\right)\psi_2\left(\frac{a+b}{2},\lambda\right) - \tilde{\psi}_2\left(\frac{a+b}{2},\lambda\right)\psi_1\left(\frac{a+b}{2},\lambda\right) = 0$$

which is equivalent to

$$\frac{\psi_1\left(\frac{a+b}{2},\lambda\right)}{\psi_2\left(\frac{a+b}{2},\lambda\right)} = \frac{\tilde{\psi}_1\left(\frac{a+b}{2},\lambda\right)}{\tilde{\psi}_2\left(\frac{a+b}{2},\lambda\right)}.$$

From Remark 1 and Remark 2, proof of this theorem is finished.

Acknowledgement: The work was supported by grants from CUBAP (F-543).

REFERENCES

[1] Hochstadt, H., Lieberman, B., An inverse Surm-Liouville Problem with mixed given data, Siam J. Appl. Math., 34 -4 (1978) 676-680.

[2] Hald, O. H., Discontiuous inverse eigenvalue problems, Comm. Pure Appl. Math., 37 (1984) 539-577.

[3] Buterin, S., On half inverse problem for differential pencils with the spectral parameter in boundary conditions, Tamkang J. Math. , 42 (2011) 355-364.

[4] Özkan, A. S., Half inverse problem for a class of differential operator with eigenvalue dependent boundary and jump conditions, Journal of Advanced Research in Applied Mathematics, 4 (2011) 43-49.

[5] Özkan, A. S., Half-inverse Sturm-Liouville problem with boundary and discontinuity conditions dependent on the spectral parameter, Inverse Problems in Science and Engineering. 22-5 (2013) 848-859.

[6] Sakhnovich, L., Half inverse problems on the finite interval, Inverse Probl., 17 (2001) 527-532.

[7] Wang, YP., Inverse problems for Sturm-Liouville operators with interior discontinuities and boundary conditions dependent on the spectral parameter, Math. Methods Appl. Sci., 36 (2013) 857-868.

[8] Yang, C-Fu., Uniqueness theorems for differential pencils with eigenparameter boundary conditions and transmission conditions, 255 (2013) 2615-2635.

[9] Yang, C-Fu., Inverse problems for Dirac equations polynomially depending on the spectral parameter, Applicable Analysis, (2015).

[10] Yang, C-Fu. (2011). Hochstadt-Lieberman theorem for Dirac operator with eigenparameter dependent boundary conditions, Nonlinear Anal. Ser. A: Theory Methods Appl., 74 (2011) 2475-2484.

[11] Yang, C-Fu., Determination of Dirac operator with eigenparameter dependent boundary conditions from interior spectral data, Inv. Probl. Sci. Eng., 20 (2012) 351-369.

[12] Yang, C-Fu, Huang Z-You., A half-inverse problem with eigenparameter dependent boundary conditions, Numer. Func. Anal. Opt. , 31 (2010) 754-762.

[13] Walter, J., Regular eigenvalue problems with eigenvalue parameter in the boundary conditions, Math Z., 133 (1973) 301-312.

[14] Fulton, C. T. (1977). Two-point boundary value problems with eigenvalue parameter contained in the boundary conditions, Proc. R. Soc. Edinburgh, A77 (1977) 293-308.

[15] Amirov, R. Kh.; Keskin, B.; Özkan, A. S., Direct and inverse problems for the Dirac operator with spectral parameter linearly contained in boundary condition., Ukrainian Math. J., 61-9 (2009) 1365-1379.

[16] Binding, P. A.; Browne, P. J.; Watson, B. A., Inverse spectral problems for Sturm--Liouville equations with eigenparameter dependent boundary conditions, J. London Math. Soc. 62 (2000) 161--182.

[17] Binding, P. A.; Browne, P. J.; Watson, B. A., Equivalence of inverse Sturm--Liouville problems with boundary conditions rationally dependent on the eigenparameter, J. Math. Anal. Appl. 291 (2004) 246-261.

[18] Binding, P. A.; Browne, P. J.; Seddighi, Sturm-Liouville problems with eigenparameter dependent boundary conditions, Proc. Edinb. Math. Soc. 37-2 (1993) 57-72.

[19] Browne, P. J.; Sleeman, B. D., A uniqueness theorem for inverse eigenparameter dependent Sturm-Liouville problems, Inverse Problem, 13 (1997) 1453-1462.

[20] Chernozhukova, A.; Freiling, G., A uniqueness theorem for the boundary value problems with non-linear dependence on the spectral parameter in the boundary conditions, Inverse Problems in Science and Engineering, 17-6 (2009) 777-785.

[21] Freiling, G.; Yurko, V. A., Inverse problems for Sturm-Liouville equations with boundary conditions polynomially dependent on the spectral parameter. Inverse Problems 26-5 (2010) 17.

[22] Gasymov, M. G.; Levitan, B. M., The Inverse Problem for the Dirac System, Dokl. Akad. Nauk SSR, 167 (1966) 967-970.

[23] Gasymov, M. G., The inverse scattering problem for a system of Dirac equations of order 2n. Dokl. Akad. Nauk SSSR 169 (1966) 1037-1040 (Russian); 11 676-678.

[24] Gasymov, M. G.; Dzhabiev, T. T., On the Determination of the Dirac System from Two Spectra, Transactions of the Summer School on Spectral Theory Operator, Baku/ELM., (1975) 46-71.

[25] Guliyev, N. J., Inverse eigenvalue problems for Sturm-Liouville equations with spectral parameter linearly contained in one of the boundary conditions. Inverse Problems 21-4 (2005) 1315-1330.

[26] Guseinov, IM., On the representation of Jost solutions of a system of Dirac differential equations with discontinuous coefficients, Izv. Akad. Nauk Azerb. SSR., 5 (1999) 41-45.

[27] Güldü, Y., On discontinuous Dirac operator with eigenparameter dependent boundary and two transmission conditions. Bound. Value Probl., (2016) 135- 19.

[28] Keskin, B., Inverse spectral problems for impulsive Dirac operators with spectral parameters contained in the boundary and discontinuity conditions polynomially, Neural Comput&Applic. ,23 (2013) 1329-1333.

[29] Keskin, B., Inverse problems for impulsive Dirac operators with spectral parameters contained in the boundary and multitransfer conditions, Math. Methods in Applied Sciences, (2013) 38.

[30] Mennicken, R.; Schmid, H., Shkalikov, A. A., On the eigenvalue accumulation of Sturm-Liouville problems depending nonlinearly on the spectral parameter, Math. Nachr., 189 (1998) 157-170.

[31] Schmid, H.; Tretter, C., Singular Dirac systems and Sturm-Liouville problems nonlinear in the spectral parameter, J. Differ. Eqns., 181-2 (2002) 511-542.

[32] Yurko, V. A., Boundary value problems with a parameter in the boundary conditions, Izv. Akad. Nauk Armyan. SSR, Ser. Mat., 19-5 (1984) 398-409.

[33] Yurko, V. A. (2000). An inverse problem for pencils of differential operators, Mat Sbornik, 191-10 (2000) 137-158.

Cumhuriyet Science Journal
CSJ

e-ISSN: 2587-246X
ISSN: 2587-2680

Cumhuriyet Sci. J., Vol.40-4 (2019) 909-916

Proton Therapy Simulations by GATE in the Treatment of Non-Small Cell Lung Cancer (NSCLC)

Burcu ARMUTLU [1], ***İlknur HOŞ***[2*]

[1] *Istanbul Aydın University, Graduate Education Institute, Health Physics, 34295, Istanbul, Turkey*

[2] *Istanbul Aydın University, Application and Research Center For Advanced Studies, 34295, Istanbul, Turkey*

Received: 30.10.2019; Accepted: 22.11.2019 *http://dx.doi.org/10.17776/csj.640079*

Abstract. Lung cancer is one of the leading causes of cancer - related deaths. Recently, radiotherapy is being used extensively for the treatment of patients suffering from cancer. Proton therapy is a very suitable form of radiation therapy for tumors that occur in the vicinity of critical tissues such as lung, due to the unique characteristics of the protons used in the treatment. In this study, a geometry model with lung, heart, tumor and bone structures in a water phantom is modeled with the Monte Carlo simulation tool vGATE, version of 7.2. With this simulation, the accumulated dose are calculated for each organ.

Keywords**:** GATE, Monte Carlo, Lung cancer, Proton therapy

Küçük Hücreli Olmayan Akciğer Kanseri (KHDAK) Tedavisinde GATE ile Proton Tedavi Simülasyonları

Özet. Akciğer kanseri, kansere bağlı ölümlerde ilk sırada yer almaktadır. Günümüzde kanser hastalarını tedavi etmek amacıyla yaygın bir şekilde radyoterapi kullanılmaktadır. Proton tedavisi, tedavide kullanılan protonların benzersiz karakteristik özelliklerinden dolayı akciğer gibi kritik dokuların yakınında oluşan tümörler için oldukça uygun bir radyasyon tedavisi şeklidir. Bu çalışmada, Monte Carlo simülasyon aracı GATE (vGATE 7.2) ile bir su fantomu içerisinde akciğerler, kalp, tümör ve kemik yapıların bulunduğu bir geometri modellenmiştir. Bu benzetim ile organların aldığı dozlar hesaplanmıştır.

Anahtar Kelimeler GATE, Monte Carlo, Akciğer kanseri, Proton terapi

1. INTRODUCTION

According to the case records over the world in 2018, lung and breast cancer is the most common cancer. For all cancers in Turkey in 2018, a total of 210 537 new cases and 116 710 deaths have been reported. 34 703 (16.5%) of these new cases reported as lung cancer [1].

The history of radiation therapy begins in 1895 when Rontgen discovered X-ray [2]. The existence of the proton was first introduced by Ernest Rutherford in 1919 and the first cyclotron was built in 1930 by E. O. Lawrence [3]. In 1946, Robert Wilson, from Harvard University, made the first suggestion that the use of accelerated protons should be considered [3,4] for radiation therapy. In 1954, the first patient applications were reported, and in 1955 he treated the patients with protons for the first time with Tobias and his colleagues at the Lawrence Berkeley Laboratory [3,5]. Following this, clinical treatments were started at Harvard University MGH (Massachusetts General Hospital) in USA and Uppsala University in Sweden. Hospital-based proton therapy began in 1990 at Loma Linda University, and by the end of 2008,

* Corresponding author. *Email address:* *ilknurhos@aydin.edu.tr*

approximately 13,000 patients were treated [6]. Currently, there are a total of 99 particle treatment centers in the world since 1954, of which 86 are protons and 13 are carbon-ions. Furthermore, 43 treatment centers are under construction and 24 treatment centers are under planning [7].

Radiation therapy is an important component in the treatment applications for non-small cell lung cancer (NSCLC), either alone or in combination with chemotherapy and surgery [8]. The aim of radiation therapy is to protect the normal tissues around the tumor as much as possible while delivering required radiation dose to the tumor. However, radiation causes certain side effects and secondary cancer risk in healthy tissues around the tumor. Compared to photons considering accumulated the dose throughout the tissue and exit dose, protons show a maximum dose accumulation (Bragg peak) at the desired tissue depth due to their characteristic properties, followed by a sharp dose reduction with very little exit dose. This dosimetric difference of proton treatment is a good treatment option especially for lung cancer that is close to critical structures such as adjacent lung, esophagus, heart, spinal cord, main airways, vessels, as it provides an unnecessary dose reduction to critical organs [9-12]. Proton beam therapy (PBT) has also emerged as a potential solution to improve clinical outcomes such as isolated local recurrence, toxicity and life expectancy in modern photon radiation techniques in both early and locally advanced disease [8].

Recently, the popularity of Monte Carlo (MC) techniques in the field of medical physics has increased rapidly especially for proton therapy. MC simulations are important tools in the design and commissioning of clinical facilities that provide a detailed description of the beam line and distribution system and can also potentially be used to simulate the entire Proton Therapy System [13-16]. MC uses basic laws of physics to determine the probability distributions of individual interactions of photons and particles. As the number of simulated particles increases, the accuracy of predicting their dispersion increases, but the computational time is prolonged in a prohibitive manner. The dose distribution is calculated by the accumulation of ionizing events in the boxes (voxels) causing the accumulation of energy in the medium. MC is the most accurate method of calculating dose distribution in a patient, despite uncertainties in calculation time. Sample plans with MC simulation have shown improvements in dose calculation accuracy, particularly at the interfaces of heterogeneous tissues and in the lung where particle imbalance may occur under certain conditions [3]. Furthermore, beam data simulated with MC can be used as input data to the clinical commercial treatment planning systems [17]. This can greatly improve the commissioning efficiency of the Proton Therapy system.

GATE (OpenGATE Collab.) is an open source software developed jointly by the world's leading medical physics laboratories, which simulates medical physics using the Geant4 code library. It supports output formats such as GATE, ROOT, ASCII, ECAT7 and LMF, which are commonly used for modeling, optimization and algorithm generation [18].

Geant4 is a toolkit that provides a comprehensive software package including the passage of particles through matter and their interactions with matter. Geant4 can handle complex geometries efficiently and compactly and allows visualization of the geometry and particle tracks through a variety of interfaces. Its areas of application include high energy, nuclear and accelerator physics, studies in medical and space science [19-20].

There are recent studies have been performed using the Geant4 simulation program to simulate the proton beam line and compare the simulation data with the experimental data. The first study is done by Hong Qi Tan and his friends by using the GEANT4 toolkit and MC simulations for the preliminary preparation of a new Proton Therapy Center, scheduled to open in Singapore in 2020 [21]. They have shown the energy-range comparison of the measured data the simulation for different energies and data showed compatibility is observed. A second study published by Shane Mesko and Daniel Gomez is a review of treatment options, proton doses, and outcomes for patients with non-small cell lung cancer at different stages such as early stage, locally advanced stage, relapse and postoperative NSCLC radiation [8]. This

paper conclude that proton therapy provides higher survival, better local control and less toxicity than photon radiation therapy. A paper, by Cirrone and his friends, reported proton ranges and Bragg peaks obtained from different materials (water, aluminum, copper and PMMA) in the energy range of 10-62 MeV [22]. Another study done by Cirrone and friends presents the treatment of the patients with ocular melanoma lesions of different stages using an energy of 62 MeV at the first Italian protontherapy facility called CATANA. The preliminary results were very similar to the treatment of uveal melanoma via hadrons reported in the literature, despite limited follow-up time, and showed a high percentage of tumor response with limited acute and subacute toxicity and visual outcome compared to previsions [23].

In our paper, we will report the Bragg peaks and deposited dose in the organs filled with proper materials by using vGATE. We first summarize the geometry of phantom contains lungs, heart, bones and tumor. Then Bragg peaks are shown for each organ and tumor. Later accumulated dose values are given, and results are discussed.

2. GEOMETRY DEFINITION and SIMULATION of BEAM LINE

All the relative results presented in this article and in the simulation of proton beam were obtained using QGSP_BERT_HP_EMY as the Reference Physics List. In this study, the vGATE7.2 version of GATE was used [18].

This study is primarily intended to demonstrate the proton beam, from the proton source defined in the simulation, dose distribution in the organs we positioned. 'Pencil Beam Scanning' (PBS) rays were used as proton source. Pencil beam scanning is a perfect and efficient proton beam delivery method for both traditional and Intensity Modulated Proton Therapy (IMPT) techniques. Its major advantage is not requiring any site-specific equipment such as scattering foils, field openings and physical range compensators, and that subsequent areas are automatically transmitted without the need to enter the treatment room [3]. The source was positioned at 13 0 -25 cm inside the world volume, described in next paragraph, to suit the tumor position.

As shown schematically in Figure 1, a world volume is defined, and a water phantom is placed at the center of this volume. A bone, right and left lungs, a spherical tumor with a radius of 1 cm inside the left lung, an ellipsoid heart, and a second bone were identified, respectively, according to their distance from the source into the water phantom. The simulated phantom, we use, is obtained by developing a sample which makes a range-dose comparison in water using a source of pencil beam scanning of the proton beam defined in a heterogeneous phantom (water, bones, lung). The size of simulated heart inside the phantom is determined using an average adult heart shape [24]. The lung parameters described in our study are decided by using inputs from ref [25]. This reference paper aims to determine lung sizes and volume ranges using computed tomography (CT) images to contribute to the development of the body phantom for a human. Muscle was selected as tumor material and tumor is placed in the left lung at the coordinates of 0.0 0.0 -6.0 cm. Tissues for each organ are defined in GATE as muscle, lung and bone materials. The heart with the material of muscle is placed in the phantom at 2.0 -3.0 2.0 cm. The size and positioning of each geometry are shown in Table 1. When the geometry formed, a schematic view is created to see the geometry. In Figure 1 left image shows lateral view (in the x direction), while right image represents the view from the z-axis. From the first image (left in Figure 1) one can see bone, lung, tumor within the lung, heart and second bone, respectively. When the geometry is viewed from the back, it is observed that the tumor is defined correctly in the left lung and the heart is between the two lungs along the z-axis. The source is positioned perpendicular to the phantom material (z-direction) and irradiated in this manner. 99 MeV proton energy is used to reach the target depth and 2.14×10^{7} particles are delivered to get the ~4 Gy dose (around one fraction out of 70 Gy [8]).

Table 1: Dimensions and positions of simulated water phantom, organs (inside the water phantom) and tumor (inside the left lung)

Organ	**Organ Dimensions (cm) (x, y, z)**	**Organ Locations (cm) (x, y, z)**
Water Phantom	40 × 50 × 40	0.0 0.0 0.0
Bone 1	36 × 40 × 4	0.0 0.0 -18.0
Bone 2	36 × 40 × 4	0.0 0.0 11.0
Right Lung	11.6 × 26.9 × 16.9	-11.0 0.0 -7.0
Left Lung	10 × 26.1 × 17.1	13.0 0.0 -7.0
Tumor	r = 1	0.0 0.0 -6.0
Heart	r = 6, 4, 3	2.0 -3.0 2.0

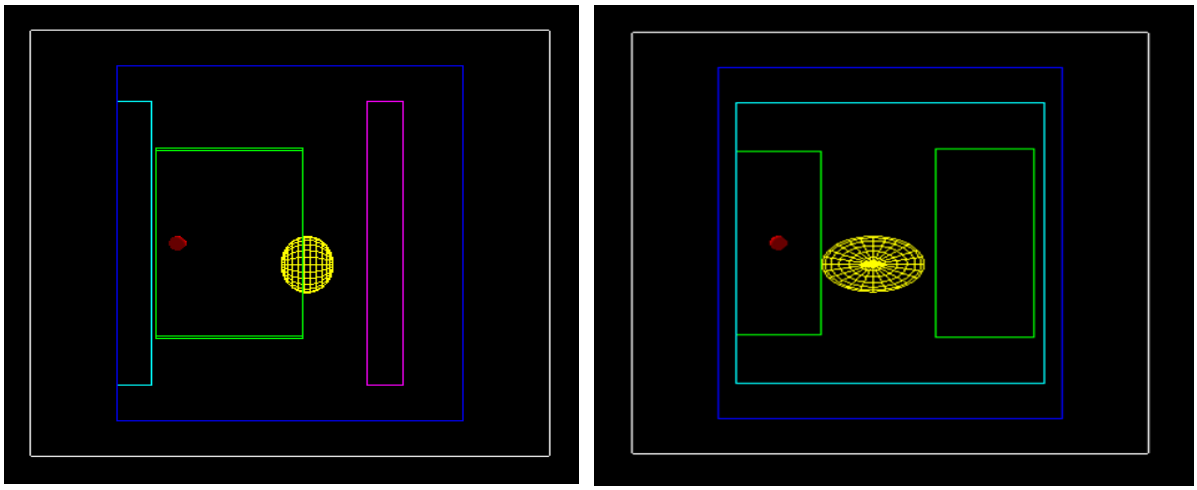

Figure 1: Schematic view of the geometry used during the simulation a) View of the simulation geometry from 270^0 (lateral). b) View of the simulation geometry from 180^0 (back). The white box is defined as world volume, blue box is the water phantom, cyan is the 1st bone, green is the right and left lung, red is the tumor, yellow is the heart and magenta is the 2nd bone.

3. BRAGG PEAKS and ACCUMULATED DOSE in ORGANS

The aim of this study is to ensure that the tumor volume receives at least 95% of the given dose, which recommended by International Commission on Radiation Units and Measurement (ICRU) and that the adjacent lungs and heart are exposed to the lowest possible dose [26]. In the simulation, the source energy was adjusted to allow the Bragg peak to peak over the tumor volume and to envelop the tumor volume. Bragg peak and dose distribution curves on the organs we defined were obtained within ROOT analysis program [27].

Figure 2 shows the dose distributions versus depth of Bragg peak for each organ obtained within the ROOT analysis program. In the simulation, when the energy is adjusted to cover the tumor volume, a peak occurs at approximately -7.7 cm (distance from the negative edge of water box in z-direction) in the water phantom. In the simulation, the tumor volume was positioned at 0.0 0.0 -6.0 cm in the left lung. As seen in Figures 2a and 2c, the beam energy is adjusted and the position of the tumor is targeted. Figure 2d shows that the entire volume of the tumor is exposed to dose. Dose distribution for right lung and heart decreases with depth. In the first bone, it is seen that the dose distribution with the range increases in proportion to the source. Finally, in the second bone, the dose distribution decreases deeply from the bone surface.

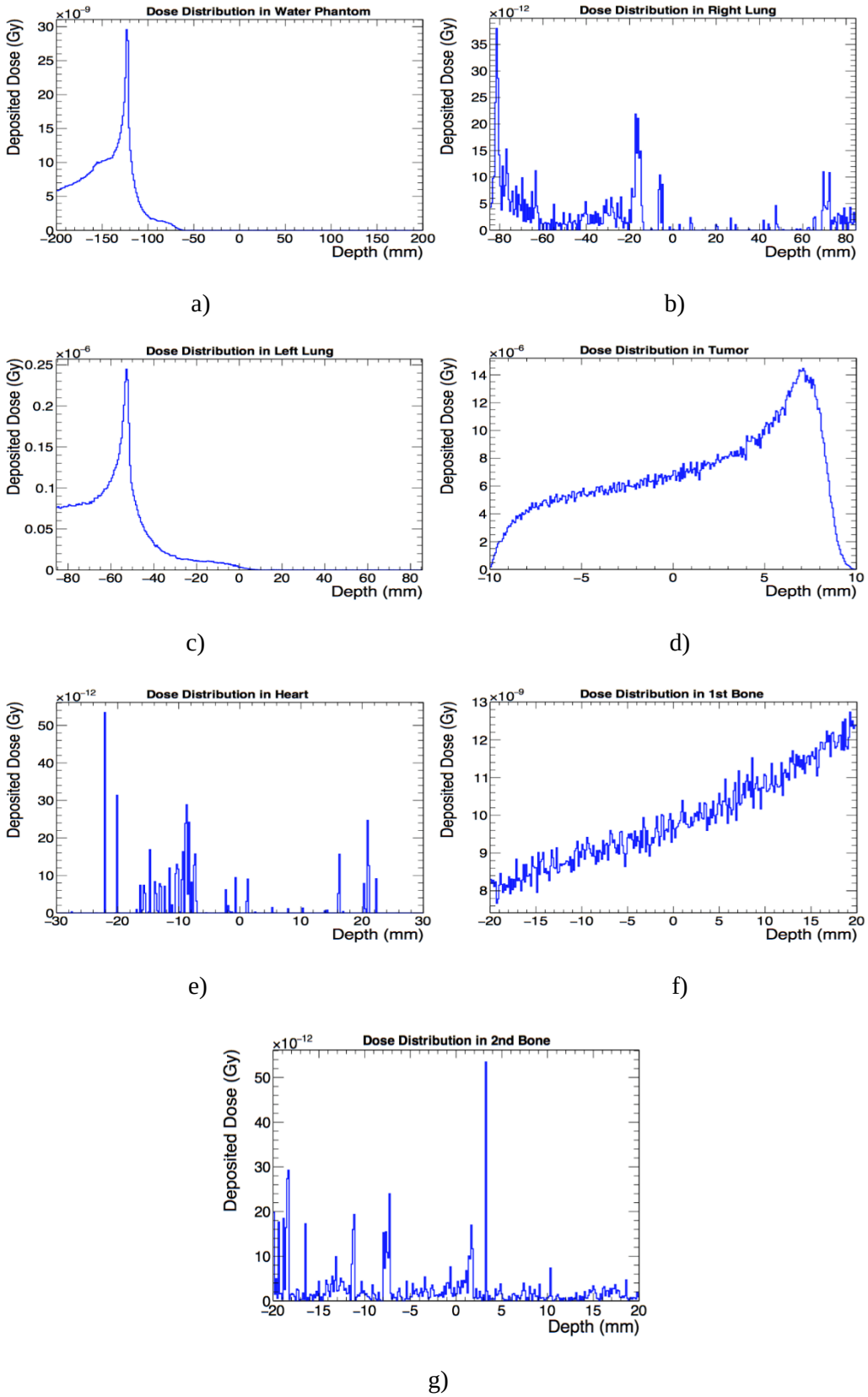

Figure 2: Proton Bragg Peaks obtained by ROOT for 99 MeV proton energy. The graph shows the stored depth in the vertical direction and the horizontal depth in the organ depth. The figure shows the dose distribution obtained for a) water phantom, b) right lung, c) left lung, d) tumor, e) heart, f) first bone, g) second bone.

Table 2 shows the amount of dose stored in each organ in Gy. The target tissue, tumor stored 4.28614 Gy, while dose of 0.0183414 Gy is stored in the left lung and 2.20925 e^{-06} Gy is stored in heart. The acumulated dose in other organs are very low and listed in Table 2.

Table 2: Total dose accumulated in each organ and tumor

Organ	**Organ Volumes (cm^3)**	**Absorbed Dose (Gy)**	**Percent (%)**
Water Box	80.000	0.00155207	%0.036
Bone 1	5760	0.00635112	%0.15
Bone 2	5760	$1.12122e^{-06}$	<%0.01
Right Lung	5273.476	$1.3463e^{-06}$	<%0.01
Left Lung	4463.1	0.0183414	%0.43
Tumor	4.19	4.28614	%99.3913
Heart	301.59	2.20925 e^{-06}	<%0.01
Total	101562.356	4.31239	%100

4. CONCLUSION

In this study, our aim is to ensure that the tumor volume defined in the simulation receives at least 95% of the total dose and that the adjacent lungs and heart are exposed to the lowest possible dose. In this study, a total dose of 4.31239 Gy was given to the phantom for one fraction. According to the simulation calculations, the dose in the tumor volume is 4.28614 Gy. This shows that tumor volume takes 99.3913% of the delivered total dose. The left lung received 0.43% of the total dose, while the right lung heart received less than 0.01%.

Cirrone and his colleagues used Geant4 simulation program to illustrate proton beam line with different scatter materials and studied lateral dose distributions for proton beams at the patient position, while we used GATE simulation program to calculate accumulated dose inside the organs. Therefore, we have shown the change of Bragg peak and dose distributions without using the proton beam line and scatters defined in their study. The 99 MeV energy used in our study is consistent with experimental peak energy-range distribution in water phantom reported in [28]. If we make a comparison of Bragg peak distributions to the ones obtained by Cirrone and colleagues, we see that the full width of the peak at half height (FWHM) is much narrower in the Bragg Peak distributions we obtained. As a result, in the absence of scattering, almost all of the delivered total dose is stored in the targeted volume and the critic organs are exposed to a very small dose, whereas a uniform dose distribution on the target tissue is not achieved since the width of the peak does not fully cover the target volume.

REFERENCES

[1] Globocan 2018 Graph production: IARC, World Health Organization. Adress: http://gco.iarc.fr/today. Retrieved September 23, 2019.

[2] Peh W.C.G., History of the discovry of x ray, part I- Rontgen and his discovery of x ray, Singapore Med. J., 36 (1995) 437-441.

[3] Khan M.F., Gibbons J.P., (2014), Khan's The Physics of Radiation Therapy (Fifth Edition), Lippincott Williams & Wilkins, Philadelphia, USA: LWW.com

[4] Wilson R.R., Radiological use of fast protons, Radiology, 47 (1946) 487-491.

[5] Lawrence J.H., Tobias C.A., Born J.L., Mccombs R.K., Roberts J.E., Anger H.O., Lowbeer B.V., Huggıns C.B., Pituitary irradiation with high energy proton beams: a preliminary report, Cancer Res., 18-2 (1958) 121-34.

[6] Gragoudas E., Li W., Goitein M., Lane A.M., Munzenrider J.E., Egan K.M., Evidence-based estimates of outcome in patients irradiated for intraocular melanoma, Arch Ophthalmol 10-12 (2002) 1665-71.

[7] Particle Therapy Co-Operative Group (PTCOG) - An organisation for those interested in proton, light ion and heavy charged particle radiotherapy. Adress:https://www.ptcog.ch/index.php/facilities-in-operatio. Retrieved September 30, 2019.

[8] Mesko S., Gomez D., Proton Therapy in Non-small Cell Lung Cancer, Curr. Treat. Options in Oncol., 19-12 (2018) 76. doi: https://doi.org/ 10.1007/s11864-018-0588-z.

[9] Cozzi L., Fogliata A., Lomax A., Bolsi A., A treatment planning comparison of 3D conformal therapy, intensity modulated photon therapy and proton therapy for treatment of advanced head and neck tumours, Radiother Oncol., 61-3 (2001) 287–297.

[10] Macdonald O.K., Kruse J.J., Miller J.M., Garces Y.I., Brown P.D., Miller R.C., Foote R.L., Proton beam radiotherapy versus three-dimensional conformal stereotactic body radiotherapy in primary peripheral, early-stage non-small-cell lung carcinoma: a comparative dosimetric analysis, Int J Radiation Oncol. Biol. Phys., 75-3 (2009) 950–958.

[11] Kadoya N., Obata Y., Kato T., Kagiya M., Nakamura T., Tomoda T., Takada T., Takayama K., Fuwa N., Dose-volume comparison of proton radiotherapy and stereotactic body radiotherapy for non-small cell lung cancer, Int J Radiat Oncol Biol Phys., 79 (2011) 1225–31.

[12] Roelofs E., Engelsman M., Rasch C., Persoon L., Quamhiyeh S., Ruysscher D.D., Verhaegen F., Pijls J.M., Lambin P., Rococo consortium, Results of a multicentric in silico clinical trial (ROCOCO): comparing radiotherapy with photons and protons for non-small cell lung cancer, J Thorac Oncol., 7-1 (2012) 165–76. doi: 10.1097 / JTO.0b013e31823529fc.

[13] Paganetti H., Jiang H., Lee S.Y., Kooy H.M., Accurate Monte Carlo simulations for nozzle design, commissioning and quality assurance for a proton radiation therapy facility, Med. Phys., 31-7 (2004) 2107–2118. doi: https://doi.org/10.1118/1.1762792.

[14] Van Goethem M.J., Van Der Meer R., Reist H.W., Schippers J.M., Geant4 simulations of proton beam transport through a carbon or beryllium degrader and following a beam line, Phys. Med. Biol., 7-54 (2009) 5831–5846. doi:https://doi.org/10.1088/0031-9155/54/ 19/011.

[15] Aso T., Kimura A., Tanaka S., Yoshida H., Kanematsu N., Sasaki T., Akagi T., Verification of the Dose Distributions With GEANT4 Simulation for Proton Therapy, IEEE Transactions on Nuclear Science, 52-4 (2005) 896–901. doi: https://doi.org/10. 1109/tns.2005.852697.

[16] Allison J., Amako K., Araujo H., Apotolakis J., Geant4 developments and applications, IEEE Trans.Nucl.Sci., 53-1 (2006) 270-278.

[17] Clasie B., Depauw N., Fransen M., Gom C., Panahandeh H.R., Seco J., et al.: Golden beam data for proton pencil-beam scanning. Phys. Med. Biol. 57-5 (2012). doi:https://doi.org/10.1088/ 0031-9155/57/5/1147.

[18] Users Guide V7.2 From GATE collaborative documentation wiki. Adress: http://www.opengatecollaboration.org/sites/default/files/GATE-UsersGuideV7.2.pdf. Retrieved September 13, 2019.

[19] Agostinelli S., Allison J., Amako K. al, Apostolakis J., Araujo H., Arce P., Asai M., Axen D., Banerjee S., Barrand G., GEANT4—a simulation toolkit, Nucl. instruments methods Phys. Res. Sect. A Accel. Spectrometers, Detect. Assoc. Equip., 506 (2003) 250–303.

[20] GEANT4 a simulation toolkit. Adress: https://geant4.web.cern.ch/. Retrieved: November 19, 2019.

[21] Tan H.Q., Phua J.H., Tan L., Ang K.W., Lee J., Bettiol A.A., Geant4 Simulation for Commissioning of Proton Therapy Centre, World Congress on Medical Physics and Biomedical Engineering 2018, IFMBE Proceedings, 68-1 (2018) 583-587. doi:https://doi.org/10.1007/978-981-10-9035-6_108.

[22] Cirrone G.A.P., Cuttone G., Nigro S.L., Guatelli S., Mascialino B., Pia M.G., Raffaele L., Russo G., Implementation of a New Monte Carlo GEANT4 Simulation Tool for the Development of a Proton Therapy Beam Line and Verification of the Related Dose Distributions, IEEE Transactions on Nuclear Science, 52-1 (2005) 262-265. doi:10.1109/TNS.2004.843140.

[23] Cirrone, G.A.P., Cuttone, G., D. Battaglia L., Calabbretta L., Celona F., Di R., Lojacono P., Maggiore M., Mongelli V., Nigro L.S., Piazza L.A.C., Patti V.I., Raffaele L., Re M., Rifuggiato D., Russo G.,Sabini M.G, Salamone V., Valastro L.M., A 62 MeV Proton beam for the treatment of ocular melanoma at Laboratori Nazionali del Sud-INFN (CATANIA), IEEE Nuclear Science Symposium. Conference Record, 5 (2003) 3658-3662. doi:https://doi.org/10.1109/NSSMIC.2003.1352701.

[24] Gray H., Gray's Anatom, 39th ed. Londo: Churchill; (2005) 997-1003.

[25] Kramer G.H., Capello K., Bearrs B., Lauzon A., Normandeau L., Linear dimensions and volumes of human lungs obtained from CT images. Health Phys., 102-4 (2012) 378-83. doi:10.1097/HP.0b013e31823a13f1.

[26] International Commission on Radiation Units and Measurement)(ICRU). Adress:https://icru.org/. Retrieved September 13, 2019.

[27] Rene B. and Fons R., ROOT An Object Oriented Data Analysis Framework, Proceedings AIHENP'96 Workshop, Lausanne, Nucl. Inst. & Meth. in Phys. Res. A., 389 (1997) 81-86.

[28] Rinecker Proton Therapy Center Third Annual Report Establishing Proton Cancer Therapy in Europe. Adress: https://www.rptc.de/en/information/latest-news/progress-reports/news-progress-reports-detail/rinecker-proton-therapy-center-third-annual-report-establishing-proton-cancer-therapy-in-europe.html. Retrieved September 10 (2019).

Cumhuriyet Science Journal
CSJ

e-ISSN: 2587-246X
ISSN: 2587-2680

Cumhuriyet Sci. J., Vol.40-4 (2019) 917-925

The Development of pH Modulated Solidified Homogeneous Liquid Phase Microextraction Methodology for Preconcentration and Determination of Nickel in Water Samples

Demirhan ÇITAK [1,*], ***Rabia DEMİROK*** [1]

[1] *Tokat Gaziosmanpaşa University, Faculty of Science and Arts, Chemistry Department, 60250 Tokat, Turkey*

Received: 04.11.2019; Accepted: 19.12.2019 *http://dx.doi.org/10.17776/csj.642319*

Abstract. In this work, a new, fast and green pH assisted solidified homogeneous liquid phase microextraction method (pH-MS-HLPME) was developed. Initially, the complex formation of Ni-1-Phenylthiosemicarbazide (Ni-PTC) and the dissolution of the extraction solvent (caprylic acid) in water were achieved by addition of NaOH. After base addition caprylic acid (CA) become completely soluble as sodium caprylate in model solution. The phase separation of extraction solvent was accessed by addition of HCl. The analyse of nickel concentrations was carried out by micro-sampler adapted flame atomic absorption spectrometer. Under optimized parameters, linear range (10.0-450 µg L-1), detection limit (3.2 µg L-1), limit of quantification (10.0 µg L-1), relative standard deviation (2.0 %), relative error (-3.9 %), and preconcentration factor (45) were calculated, respectively. Finally, the developed pH-MS -HLPME methodology was successfully applied to LGC 6010 hard drinking water (CRM) and some water samples.

***Keywords*:** Nickel, pH, liquid phase microextraction, drinking water samples, microsampler system.

Su Örneklerinde Nikelin Zenginleştirilmesi ve Tayini için pH Modülasyonlu Katılaştırılmış Homojen Sıvı Faz Mikroekstraksiyon Metodunun Geliştirilmesi

Özet. Bu çalışmada yeni, hızlı ve yeşil bir pH destekli katılaştırılmış homojen sıvı faz mikroekstraksiyon metodu (pH-MS-HLPME) geliştirildi. İlk olarak, Ni-1-feniltiyosemikarbazit (Ni-PTC) kompleksinin oluşumu ve ekstraksiyon çözücüsünün (kaprilik asit) su içinde çözülmesi, NaOH ilave edilerek sağlandı. Baz ilave edildikten sonra kaprilik asit (CA), model çözeltide sodyum kaprilat halinde tamamen çözünür hale geldi. Ekstraksiyon çözücüsü fazının ayrılması HC1 ilavesiyle gerçekleştirildi. Nikel konsantrasyonlarının tayini, mikro örnekleyici uyarlanmış alevli atomik absorpsiyon spektrometresi ile gerçekleştirildi. Optimize edilmiş parametreler altında, doğrusal çalışma aralığı (10.0-450 µg L-1), gözlenebilme sınırı (3.2 µg L-1), tayin sınırı (10.0 µg L-1), bağıl standart sapma (% 2.0), bağıl hata (-3.9 %) zenginleştirme faktörü (45) hesaplandı. Son olarak, geliştirilen pH-SFO-HLPME yöntemi LGC 6010 sert içme suyu standard referans maddesine ve bazı su örneklerine başarıyla uygulandı.

***Anahtar Kelimeler*:** Nikel, pH, sıvı faz mikroekstraksiyon, içme suları, mikro örnek verici sistem.

1. INTRODUCTION

Nickel is widely used industrial element for making many products such as batteries, coins, keys, cooking equipments and cell phones etc. In addition, natural waters, foods, fruits and vegetables include trace amount of nickel and nickel compounds. It is also very important for

* Corresponding author. *Email address:* *demirhan.citak@gop.edu.tr*

hormonal activity and lipid metabolism [1–4]. However, the excessive amount uptake of nickel can cause cancer, allergic skin problems and psychological disorders. Because of these harmful effects determination of nickel is an essential obligation for analytical chemists. Many modern instrumental methods like inductively coupled plasma mass spectrometry (ICP-MS), inductively coupled plasma optical emission spectrometry (ICP-OES, electrothermal atomic absorption spectrometry (ETAAS), flame atomic absorption spectrometry (FAAS) can be used for determination of nickel in various samples. FAAS is the most favourable and used technique when it is compared to the other spectroanalytical techniques. However, for sensitive and reliable determination of nickel a sample pretreatment procedure is needed before FAAS measurements [5–9].

The aim of many analytic chemists is to develop high- performance, away from environmental pollution and matrix effects, less time consuming and economically feasible sample pretreatment methods. Nowadays, the popularity of liquid phase microextraciton (LPME) methods is increasing day by day when we compare with the other sample pretreatment methods. LPME was presented as a simpler and cheaper alternative to conventional liquid-liquid extraction in 1990s [10–12]. Many kinds of modified LPME techniques were reported in literature for separation and preconcentration of metals [13–18] such as dispersive liquid–liquid microextraction (DLLME) [19], single-drop microextraction (SDME) [20–22], hollow-fiber liquid-phase microextraction (HF-LPME) [23,24], solidification of floating organic droplets liquid phase microextraction (SFO-LPME) [25,26].

The use of two types of solvent (disperser and extraction solvent) at DLLME, the instability of the extraction solvent drop at SDME, the use of expensive membranes at HF-LPME restrict the application of these methods [27]. Among these techniques, SFO-LPME draws more attention due to advantages such as easy removal of extraction solvent, use of less toxic extraction solvents and simplicity [28]. In this technique usually a low toxic extraction solvent with appropriate melting point (near room temperature) is mixed with a disperser solvent and injected into water sample for providing short extraction time and fast mass transfer. After phase separation by centrifugation, the sample tubes are placed in an ice bath for solidification of organic drop floats on the surface. The solidified organic drop including analyte removed with a spatula to a conical tube than the melted extraction solvent introduced to appropriate analytic techniques [29–31].

The aim of this work was to develop a modified SFO-LPME called pH modulated solidified homogeneous liquid phase microextraction (pH-MS-HLPME) method for determination of nickel. The concentration levels of nickel in various water samples were determined by microsampler adapted flame atomic absorption spectrometer. This method offers more green and economic alternative when compared to the other SFO-LPME methods. Because the dissolution of the extraction solvent (caprylic acid) and complex formation of Ni-1-Phenylthiosemicarbazide (Ni-PTC) was achieved by using any disperser solvent and buffer solution. Both were achieved by addition of appropriate amount of NaOH-HCl.

2. EXPERIMENTAL

2.1 Instruments and chemicals

A hand made micro-sampler adapted Perkin-Elmer Analyst 700 (Norwalk, CT, USA) atomic absorption spectrometer was used for Ni (II) determination. The operation conditions of FAAS were chosen according to manufacturer guides. A Sartorius pp-15 (Gottingen, Germany) model pH meter with glass-electrode and a Nüve NF 200 (Ankara, Turkey) model centrifuge were used for pH measuring and centrifuging test solutions, respectively.

All chemicals used during the pH-MS-HLPME were analytical reagent grade. Caprylic acid, 1-phenylthiosemicarbazide were purchased from Merck chemical company (Darmstadt, Germany). 0.1 % (w/v) PTC solution was prepared daily by dissolving in methanol. Sodium hydroxide and hydrochloric acid (E. Merck, Darmstadt, Germany) solutions at various concentrations were prepared by dissolving appropriate amount in deionized water. 1000 mg L^{-1} Ni (II) standard solution were prepared from $Ni(NO_3)_2.6H_2O$ (Sigma-Aldrich) and nickel solutions at other concentrations for test solutions were prepared by diluting from 1000 mg L^{-1} Ni (II) standard solution.

2.2 pH-MS-HLPME procedure

130 µL CA was added to conical test tube containing 9 mL test solution (containing 30 µg L^{-1} Ni(II), 1 ml PTC from 0.1 %) by a micropipette . Than 1.0 mL NaOH (1 mol L^{-1}) was added to test

solution and vortexed 20-30 seconds. CA became completely soluble as its salt form (sodium caprylate) and test solution was seen completely homogeneous. After addition of 1.0 mL HCl (1 mol L^{-1}), cloudy solution was appeared and complexes of Ni-PTC were extracted to CA phase. This cloudy solution was centrifuged for 3 min. at 3500 rpm and transferred to refrigerator for solidification. The solidified CA phase was removed by spatula and diluted to 200 µL with an acidified ethanol. The diluted CA phase was introduced to microsampler adapted flame atomic absorption spectrometer for determining Ni (II) concentrations.

2.3 Sample preparation procedure of pH-MS-LPME

The water samples (tap waters, hot spring water and river water) were filtered and acidified after collection (different places from TURKEY). The bottled samples were collected from local markets of Tokat, TURKEY. The samples were stored at refrigerator before application of procedure.

3. RESULTS AND DISCUSSION

3.1 Effect of added base-acid amount

The pH of sample is one of the most effective factor in metal enrichment studies for the formation of metal complexes with the high efficiency. In this work, the complex formation of Ni-PTC and the dissolution of the CA was achieved by addition of NaOH. After HCl addition a cloudy solution was appeared. For that purpose, the varied concentrations and volumes of NaOH and HCl in the range of 0.0-1.5 mol L^{-1} and 0.0-1.5 mL were added to test solutions. The recoveries of Ni (II) for pH-MS-LPME were not quantitative (< 95 %) for added NaOH and HCl in the range of 0.0-0.75 mol L^{-1} and 0.0- 0.75 mL. The quantitative recoveries (≥ 95 %) of Ni(II) were obtained after addition of 1 mol L^{-1} and 1.0 mL NaOH and HCl, respectively. As it can be seen table 1, addition of 1 mol L^{-1} and 1.0 mL NaOH and HCl were chosen as an optimal added base-acid amount for further studies.

Table 1. Effect of added base-acid concentration and volume (N=3)

The concentration of NaOH-HCl (mol L^{-1})	Added base-acid (mL)	Recovery of Ni(II), %
0.25	0.25	28±2*
0.50	0.50	49±3
0.75	0.75	73±3
1.00	1.00	95±4
1.25	1.25	96±2
1.50	1.50	96±3

*mean ± standard deviation

3.2 Effect of PTC amount

The type and amount of the ligand is one of the important step that should be optimized for the formation of hydrophobic chelates with high efficiency. We noticed that PTC has not been used before for extraction of nickel in the solidification based microextraction processes. For that purpose the amount of PTC were investigated to obtain high complex yield. As shown in figure 1, the increase in recovery was seen by the addition PTC in the range of 0-1.0 mL (0.1 %, w/v). As a result of the obtained data, the amount of ligand was optimized as 1 mL.

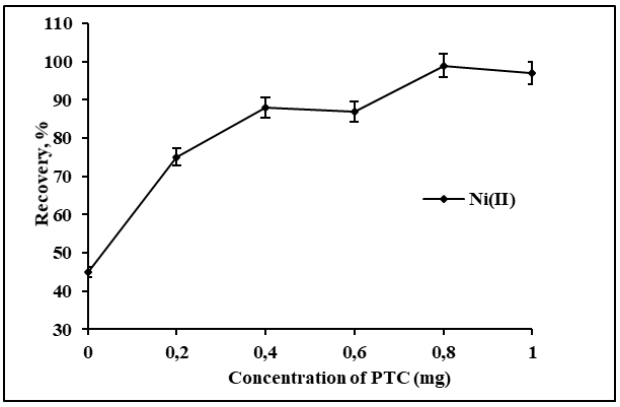

Figure.1 Effect of PTC concentration on pH-MS-HLPME (N:3)

3.3 Effect of volume of CA

Many extraction solvents (1-Undecanol, 1-Dodecanol, 1-Decanol, 1-Undecanoic acid) for SFO-LPME procedures were used in literature [32]. According to our literature survey we saw that caprylic acid was not yet used for extraction of Ni (II) solidification based studies in water samples. For that purpose, effects of volume of CA were tested in the range of 80-150 µL. the resuls were shown in figure 2. According to our results, the recoveries of Ni (II) were not quantitative up to

volume 120 µL. It was quantitative in the range of 120-130 µL. After volume of 130 µL a decrease was seen. Therefore 130 µL CA volume was chosen for other experimental parameters.

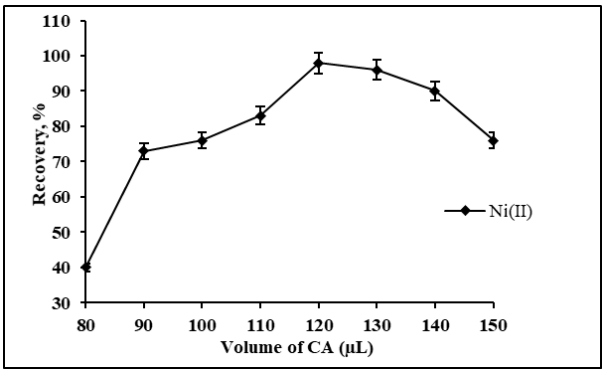

Figure.2 Effect of volume of CA (N:3)

3.4 Optimization of the other experimental parameters

The mixing time is an important parameter that plays a major role for increasing the extraction efficiency and reducing the extraction time. The effective mixing of the aqueous and organic phases is very important to ensure the mass transfer of the solution. The mass transfer coefficient of the aqueous phase increases with increasing mixing ratio. Therefore, in this study, the effects of shaking and centrifugation times on recovery rates of 1 to 5 minutes were examined. As it can be seen from figure 3, it was found that the best recovery was achieved the 20-30 seconds vortex time and 3 minute centrifugation time for the experimental conditions and all of the studies were completed at this time period.

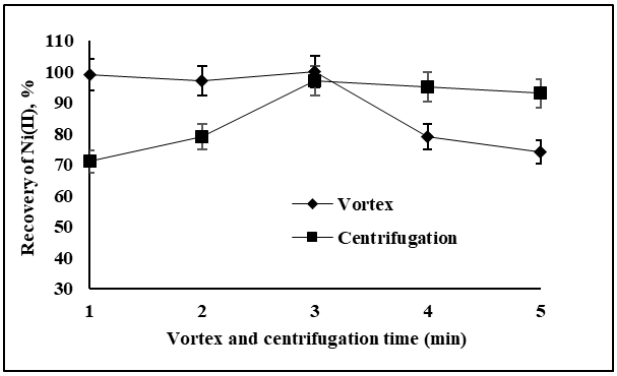

Figure 3. The effects of vortex and centrifugation and vortex time on recovery Ni (II) (N:3)

The increase in the ratio of the aqueous phase volume to the organic phase will increase the preconcentration factor, but this can reduce the extraction efficiency in a given extraction time. The effects of sample volume on the recovery of Ni (II) were investigated in the range of 8-14 mL in this study. The results are shown in figure 4. The recovery of 95 % and higher than 95 % was achieved between 8-9 mL. Therefore, the sample volume was chosen as 9 mL. In addition, the final volume was completed with 1M HNO3 (in ethanol) to 200 mL before the analysis step.

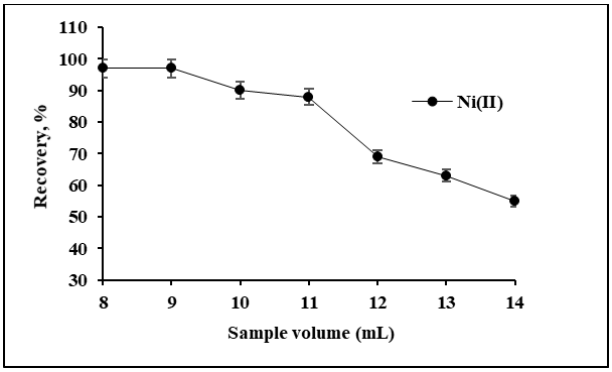

Figure 4. The effect of sample volume on pH-MS-HLPME (N:3)

3.5 Effect of interferences on pH-MS-HLPME

Some components which can be present in the water samples may interfere and cause negative or positive errors during the preconcentraiton studies. Therefore, the effects of some ions in different concentrations and types were investigated for pH-MS-HLPME technique. The results (table 2.) showed that ions had no effect until added concentrations. It demonstrates that our pH-MS-HLPME method was applicable for water samples.

Table 2. Effect of interferes on pH-MS-HLPME (N=3)

Ion	Interference/metal ratio	Recovery of Ni(II),%
Na^+	400	99±3*
K^+	500	96±2
Ca^{2+}	200	96±2
Mg^{2+}	200	99±4
Cl^-	800	102±3
NO_3^-	500	102±5
SO_4^{2-}	500	96±3
PO_4^{3-}	600	103±3

* mean ± standard deviation

3.5 Analytical performance criteria of the proposed method

To evaluate analytical performance criteria of the proposed method, limit of detection, calibration curve equation, linear range, reproducibility and preconcentration factor were calculated under optimized conditions. The limit of detection (3Sb, Sb is the standard deviation of ten replicates of the blank measurement) and limit of quantification (10Sb) were found as 3.2 μg L^{-1} and 10 μg L^{-1}, respectively. The linear range was found as 10.0-450 μg L^{-1}. The calibration curve equation was $A=1.73x10^{-2}C + 3.2x10^{-3}$ ($r^2=0.9993$). The reproducibility defined as relative standard deviation (R.S.D.) was calculated as 2.0 % after application (N=11) of pH-MS-LPME to model solutions containing 30 μg L^{-1} of Ni (II). The preconcentration factor of 45 was calculated from the ratio of the highest sample volume (9 mL) to final completed volume (200 μL).

3.6 Accuracy and application of optimized pH-MS-HLPME

In order to test the accuracy of the developed method, the method was applied to standard reference material (LGC 6010 hard drinking water). The experimental obtained value was found 49 ± 2 μg L^{-1} and the certificate value was 51 μg L^{-1}. The values of SRM shoved that pH-MS-HLPME method was found to be applicable to water samples. The relative error was calculated as -3.9 %.

Also, the developed method was applied to two different tap water samples, river water, hot spring water, sea water and 7 different bottled water samples purchased from local markets in Tokat city (TURKEY) for the determination of Ni (II). The obtained results were given in Table 3. together with the recoveries. The recovery values were quantitative. The results of pH-MS-HLPME shoved that the method was applicable for the determination of Ni (II) in natural and bottled water samples.

3.7 Comparison of pH-MS-HLPME with the other solidification based microextraction methods in literature

The developed pH-MS-HLPME was compared with some SFODME based studies for preconcentration of Ni (II) in the literature (Table 4). In many DLLME and SFODME studies, a disperser solvent was often used to mix the extraction solvent in the samples. However, the dissolution of the extraction solvent, the formation of the Ni-PTC complex and the phase separation of extraction solvent were carried out only with the addition of NaOH-HCl in our study. This showed that the developed method reduces use of the amount of organic toxic solvent during the sample preparation step and because of this reason, the developed pH-MS-HLPME was a more environmentally and economically efficient method.

Table 3. Application of optimized pH-MS-HLPME (N:3)

Element	Added (µg L^{-1})	SAMPLES			
		Tap water 1		**Tap water 2**	
		Found (µg L^{-1})	Recovery (%)[a]	Found (µg L^{-1})	Recovery (%)
Ni(II)	0	ND[b]	-	ND	-
	50	49.6±1.5	99±3	48.5±1.4	97±3
	100	98.2±2.6	98±3	96.5±3.4	97±3
		River water		**Spring water**	
		Found (µg L^{-1})	Recovery (%)	Found (µg L^{-1})	Recovery (%)
Ni(II)	0	ND	-	17±0.4	-
	50	48.0±2.0	96±3	65.2±3.1	96±4
	100	98.3±3.1	98±3	114±3.0	97±4
		Sea water		**Bottled water 1**	
		Found (µg L^{-1})	Recovery (%)	Found (µg L^{-1})	Recovery (%)
Ni(II)	0	ND	-	ND	-
	50	48.0±1.3	96±1	47.5±1.9	95±1
	100	95.0±3.4	95±3	96.3±2.7	96±3
		Bottled water 2		**Bottled water 3**	
		Found (µg L^{-1})	Recovery (%)	Found (µg L^{-1})	Recovery (%)
Ni(II)	0	ND	-	ND	-
	50	49.1±1.1	98±2	48.6±1.2	97±2
	100	96.6±3.2	97±3	95.2±3.4	95±3
		Bottled water 4		**Bottled water 5**	
		Found (µg L^{-1})	Recovery (%)	Found (µg L^{-1})	Recovery (%)
Ni(II)	0	ND	-	ND	-
	50	48.3±2.0	99±3	49.1±1.4	98±2
	100	97.5±2.7	98±3	98.5±2.2	99±2
		Bottled water 6		**Bottled water 7**	
		Found (µg L^{-1})	Recovery (%)	Found (µg L^{-1})	Recovery (%)
Ni(II)	0	ND	-	ND	-
	50	47.5±3.0	95±3	49±2.0	98±3
	100	97.8±3.3	98±4	99.2±2.0	99±2

a: mean ± standard deviations
b: Not detected

Table 4. Comparison of pH-MS-HLPME with the other solidification based microextraction procedures

Element	Method	Extraction solvent	Disperser agent	LOD	PF	R.S.S %	Ref.
Ni(II), Co(II), Pb(II), Cr(III)	GFAAS	1-dodecanol	Ethanol	1.3 ng L^{-1}	800	7.20	[33]
Ni	FAAS	1-dodecanol	Ethanol	1.27 µgL^{-1}	-	2.55	[34]
Ni, Co	GFAAS	1-undecanol	-	0.3 ng L^{-1}	497	3.60	[35]
Ni, Co	FAAS	1-dodecanol	Ultrasonication	1.7 µg L^{-1}	65	3.60	[36]
Ni,Co, Cu	GFAAS	1-undecanol	Acetone	1.2 ngL^{-1}	277	3.20	[37]
Ni,Cd	FAAS	1-dodecanol	Ultrasonication	0.20 µgL^{-1}		2.10	[38]
Ni	FAAS	Caprylic acid	-	3.2 µg L^{-1}	45	2.0	This work

4. CONCLUSIONS

In this study, a new, fast, useful and sensitive pH modulated solidified homogeneous liquid phase microextraction method for preconcentration and determination of nickel in water samples was developed for determination of Ni (II) in water samples. The developed pH-MS-LPME method had many advantages such as having a lower detection limit, better reproducibility and higher preconcentration factor compared to some established studies. Moreover the established methodology provides greener microextraction procedure with using any disperser solvent. Because, the dispersing of the extraction solvent, the formation of the Ni-PTC complex and the phase separation of extraction solvent were provided by only addition of NaOH-HCl. Under optimized conditions, the developed pH-MS-HLPME successfully applied to water samples for determination of Ni (II).

ACKNOWLEDGEMENT

The authors are grateful for the financial support of the Unit of the Scientific Research Projects of Tokat Gaziosmanpaşa University (project number: 2018/41).

References

[1] Barreto J.A., dos Santos de Assis R., Cassella, R.J., and Lemos, V.A., A novel strategy based on in-syringe dispersive liquid-liquid microextraction for the determination of nickel in chocolate samples, Talanta, 193 (2019) 23–28.

[2] Zdrojewicz Z., Popowicz E., and Winiarski J., Nickel - role in human organism and toxic effects, Polski Merkuriusz Lekarski : Organ Polskiego Towarzystwa Lekarskiego, (2016) 115–118.

[3] Baytak S., and Türker A., Determination of lead and nickel in environmental samples by flame atomic absorption spectrometry after column solid-phase extraction on Ambersorb-572 with EDTA. Journal of Hazardous Materials, 129-1,3 (2006) 130–136.

[4] Arkhipova A.A., Statkus M.A., Tsizin G.I., and Zolotov Y.A., Preconcentration of elements as hydrophobic complexes with low-polar adsorbents, Journal of Analytical Chemistry, 70-12 (2015) 1413–1431.

[5] Hashemi B., Zohrabi P., Kim K.H., Shamsipur M., Deep, A., and Hong J., Recent advances in liquid-phase microextraction techniques for the analysis of environmental pollutants, TrAC Trends in Analytical Chemistry, 97 (2017) 83–95.

[6] Lemos V., Baliza P., Santos J., Nunes L., Jesus A., and Rocha M., A new functionalized resin and its application in preconcentration system with multivariate optimization for nickel determination in food samples, Talanta, 66-1 (2005) 174–180.

[7] Yalçın M.S., Özdemir S., and Kılınç E., Preconcentrations of Ni(II) and Co(II) by using immobilized thermophilic Geobacillus stearothermophilus SO-20 before ICP-OES determinations, Food Chemistry, 266 (2018) 126–132.

[8] Naghizadeh M., Taher M.A., Abadi L.Z., and Moghaddam F.H., Synthesis, characterization and theoretical investigation of magnetite nanoclay

modified as a new nanocomposite for simultaneous preconcentration of lead and nickel prior to ETAAS determination, Environmental Nanotechnology, Monitoring & Management, 7 (2017) 46–56.

[9] ALOthman Z.A., Habila M.A., Yilmaz E., Soylak M., and Alfadul S.M., Ultrasonic supramolecular microextration of nickel (II) as N,N′-Dihydroxy-1,2-cyclohexanediimine chelates from water, tobacco and fertilizer samples before FAAS determination, Journal of Molecular Liquids, 221 (2016) 773–777.

[10] He Y. and Lee H.K., Liquid-Phase Microextraction in a Single Drop of Organic Solvent by Using a Conventional Microsyringe. Analytical Chemistry, 69-22 (1997) 4634–4640.

[11] Rykowska I., Ziemblińska J., and Nowak I., Modern approaches in dispersive liquid-liquid microextraction (DLLME) based on ionic liquids: A review, Journal of Molecular Liquids, 259 (2018) 319–339.

[12] De Almeida O.N., Luzardo F.H.M., Amorim F.A.C., Velasco F.G., and González L.N., Use of fiberglass support in the application of dried-spot technique with dispersion liquid-liquid microextraction for the determination of Co, Cr, Cu, Ni and Pb by Energy Dispersive X-Ray Fluorescence Spectrometry, Spectrochimica Acta Part B: Atomic Spectroscopy, 150 (2018) 92–98.

[13] Kocot K., Pytlakowska K., Zawisza B., and Sitko R., How to detect metal species preconcentrated by microextraction techniques, TrAC Trends in Analytical Chemistry, 82 (2016) 412–424.

[14] Giakisikli G. and Anthemidis A.N., An automatic stirring-assisted liquid–liquid microextraction system based on lab-in-syringe platform for on-line atomic spectrometric determination of trace metals, Talanta, 166 (2017) 364–368.

[15] Habila M.A., Yilmaz E., ALOthman Z.A., and Soylak M., Combination of dispersive liquid–liquid microextraction and multivariate optimization for separation-enrichment of traces lead by flame atomic absorption spectrometry, Journal of Industrial and Engineering Chemistry, 37 (2016) 306–311.

[16] Zhang S., Chen B., He M., and Hu B., Switchable solvent based liquid phase microextraction of trace lead and cadmium from environmental and biological samples prior to graphite furnace atomic absorption spectrometry detection, Microchemical Journal, 139 (2018) 380–385.

[17] Biata N.R., Nyaba L., Ramontja J., Mketo N., and Nomngongo P.N., Determination of antimony and tin in beverages using inductively coupled plasma-optical emission spectrometry after ultrasound-assisted ionic liquid dispersive liquid-liquid phase microextraction, Food Chemistry, 237 (2017) 904–911.

[18] Khazaeli E., Haddadi H., Zargar B., Hatamie A., and Semnani A., Ni(II) analysis in food and environmental samples by liquid-liquid microextraction combined with electro-thermal atomic absorption spectrometry, Microchemical Journal, 133 (2017) 311–319.

[19] Altunay N., Yıldırım E., and Gürkan R., Extraction and preconcentration of trace Al and Cr from vegetable samples by vortex-assisted ionic liquid-based dispersive liquid–liquid microextraction prior to atomic absorption spectrometric determination, Food Chemistry, 245 (2018) 586–594.

[20] Manzoori J.L., Amjadi M., and Abulhassani, J., Ultra-trace determination of lead in water and food samples by using ionic liquid-based single drop microextraction-electrothermal atomic absorption spectrometry, Analytica Chimica Acta, 644-1,2 (2009) 48–52.

[21] Xia L., Li, X., Wu Y., Hu B., and Chen R., Ionic liquids based single drop microextraction combined with electrothermal vaporization inductively coupled plasma mass spectrometry for determination of Co, Hg and Pb in biological and environmental samples. Spectrochimica Acta Part B: Atomic Spectroscopy, 63-11 (2008) 1290–1296.

[22] Dadfarnia S., and Haji Shabani A.M., Recent development in liquid phase microextraction for determination of trace level concentration of metals—A review, Analytica Chimica Acta, 658-2 (2010) 107–119.

[23] Jiang H., Hu B., Chen B., and Xia L., Hollow fiber liquid phase microextraction combined with electrothermal atomic absorption spectrometry for the speciation of arsenic (III) and arsenic (V) in fresh waters and human hair extracts, Analytica Chimica Acta, 634-1 (2009) 15–21.

[24] Ghambarian M., Yamini Y., and Esrafili A.,

Developments in hollow fiber based liquid-phase microextraction: principles and applications, Microchimica Acta, 177-3 (2012) 271–294.

[25] Shamsipur M., Ramezani M., and Miran Beigi A.A., Floating Organic Drop Microextraction Combined with Electrothermal Atomic Absorption Spectrometry for Trace Determination of Cobalt in Oil Refining Wastewaters, Energy Sources, Part A: Recovery, Utilization, and Environmental Effects, 37-11 (2015) 1164–1171.

[26] Mohammadi S.Z., Sheibani A., Abdollahi F., and Shahsavani E., Speciation of Tl(III) and Tl(I) in hair samples by dispersive liquid–liquid microextraction based on solidification of floating organic droplet prior to flame atomic absorption spectrometry determination, Arabian Journal of Chemistry, 9 (2016) 1510–S1515.

[27] Haji Shabani A.M., Dadfarnia S., and Nozohor M., Indirect spectrophotometric determination of ultra trace amounts of selenium based on dispersive liquid–liquid microextraction–solidified floating organic drop, Spectrochimica Acta Part A: Molecular and Biomolecular Spectroscopy, 116 (2013) 1–5.

[28] Karadaş, C., and Kara, D., Dispersive liquid–liquid microextraction based on solidification of floating organic drop for preconcentration and determination of trace amounts of copper by flame atomic absorption spectrometry, Food Chemistry, 220 (2017) 242–248.

[29] Mohamadi M., and Mostafavi A., A novel solidified floating organic drop microextraction based on ultrasound-dispersion for separation and preconcentration of palladium in aqueous samples. Talanta, 81-2 (2010) 309–313.

[30] Pérez-Outeiral J., Millán E., and Garcia-Arrona, R., Determination of phthalates in food simulants and liquid samples using ultrasound-assisted dispersive liquid–liquid microextraction followed by solidification of floating organic drop, Food Control, 62 (2016) 171–177.

[31] Pelit F.O. and Yengin Ç., Application of solidified floating organic drop microextraction method for biomonitoring of chlorpyrifos and its oxon metabolite in urine samples, Journal of Chromatography B, 949–950 (2014) 109–114.

[32] Mansour F.R. and Danielson N.D., Solidification of floating organic droplet in dispersive liquid-liquid microextraction as a green analytical tool, Talanta, 170 (2017) 22–35.

[33] Mirzaei M., Behzadi M., Abadi N.M., and Beizaei A., Simultaneous separation/preconcentration of ultra trace heavy metals in industrial wastewaters by dispersive liquid–liquid microextraction based on solidification of floating organic drop prior to determination by graphite furnace atomic absorption spectrometer Journal of Hazardous Materials, 186-3 (2011) 1739–1743.

[34] Wang Y., Zhang J., Zhao B., Du X., Ma J., and Li J., Development of Dispersive Liquid–Liquid Microextraction Based on Solidification of Floating Organic Drop for the Determination of Trace Nickel, Biological Trace Element Research, 144-3 (2011) 1381–1393.

[35] Bidabadi M.S., Dadfarnia S., and Shabani A.M.H., Solidified floating organic drop microextraction (SFODME) for simultaneous separation/preconcentration and determination of cobalt and nickel by graphite furnace atomic absorption spectrometry (GFAAS), Journal of Hazardous Materials, 166-1 (2009) 291–296.

[36] Arpa Ç. and Arıdaşır I., Ultrasound assisted ion pair based surfactant-enhanced liquid–liquid microextraction with solidification of floating organic drop combined with flame atomic absorption spectrometry for preconcentration and determination of nickel and cobalt ions in vegeta, Food Chemistry, 284 (2019) 16–22.

[37] Amirkavei M., Dadfarnia S., and Shabani A.M.H., Dispersive liquid-liquid microextraction based on solidification of floating organic drop for simultaneous separation/preconcentration of nickel, cobalt and copper prior to determination by electrothermal atomic absorption spectrometry. Química Nova, 36-1 (2013) 63–68.

[38] Ezoddin M., Taghizadeh T., and Majidi B., Ultrasound-assisted surfactant-enhanced emulsification microextraction for the determination of Cd and Ni in tea and water samples. Environmental Technology, 35-19 (2014) 2401–2409.

Cumhuriyet Science Journal
CSJ

e-ISSN: 2587-246X
ISSN: 2587-2680

Cumhuriyet Sci. J., Vol.40-4 (2019) 926-927

Correction

Antikanser İlaç Olan Epirubicin'in DNA ile Etkileşiminin DNA Biyosensörleri ile Elektrokimyasal Tayini

Adil ELİK [1], Gültekin GÖKÇE [2], Ebru BOSTANCI [2], Derya KIZILOLUK [3]*

[1] *Cumhuriyet Üniversitesi Fen Fakültesi Kimya Bölümü, 58140 Sivas, TÜRKİYE*
[2] *Cumhuriyet Üniversitesi Eğitim Fakültesi, 58140 Sivas, TÜRKİYE*
[3] *Cumhuriyet Üniversitesi Fen Fakültesi Biyokimya Bölümü, 58140 Sivas, TÜRKİYE*

Correction to: *Cumhuriyet Sci. J., Vol.38-3 (2017) 525-534*; http://dx.doi.org/10.17776/csj.340503; Received: 21.04.2017; Accepted: 30.05.2017

The original version of this article contained errors in Fig. 2, 3, 8(b) and 9(b). The correct figure is below.

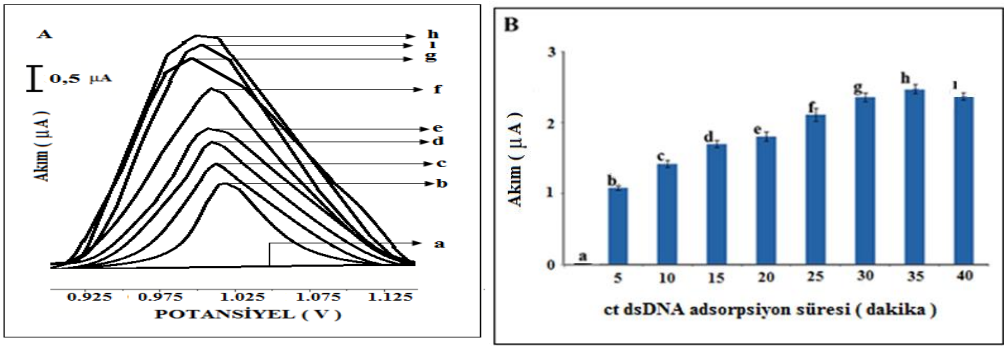

Şekil 2. PGE yüzeyine immobilize edilen ct ds-DNA'ların **(a)**ct ds-DNA yokken **(b)**5**(c)**10 **(d)**15 **(e)**20 **(f)**25 **(g)**30 **(h)**35 **(ı)**40 dakika gibi farklı sürelerde etkileşim sonrasında DPV tekniği ile ölçülen guanin sinyallerini gösteren voltamogramlar **(A)** ve histogramlar **(B)**

* Corresponding author. *Email address:* *elik@cumhuriyet.edu.tr*

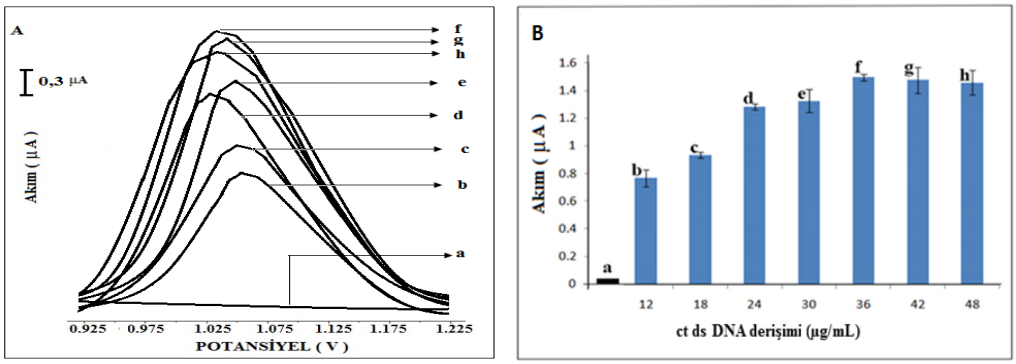

Şekil 3. PGE yüzeyine immobilize edilen **(a)**ct ds-DNA yokken **(b)**12 **(c)**18 **(d)**24 **(e)**30 **(f)**36 **(g)**42 **(h)**48 µg/mL gibi farklı derişimlerdeki ct ds-DNA'lara ait DPV tekniği ile ölçülen guanin sinyallerini gösteren voltamogramlar **(A)** ve histogramlar **(B)**

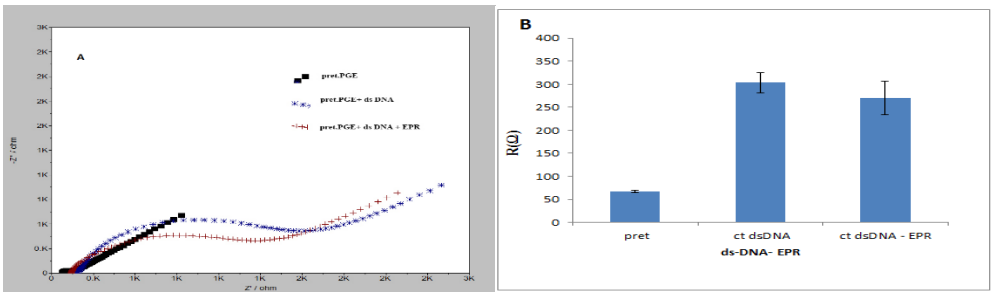

Şekil 8. (A) Niquist eğrisi **(B)**PGE yüzeyinde gerçekleşen ct ds-DNA-EPR etkileşiminin transfer edilen akımyüküne karşı gösterdiği direnç; **(a)** aktivasyonu gerçekleştirilen PGE 'lerin direnci, **(b)** ct ds-DNA immobilize edilen PGE'lerin direnci, **(c)** PGE yüzeyine immobilize edilen ct ds-DNA-EPR etkileşiminin direnci.

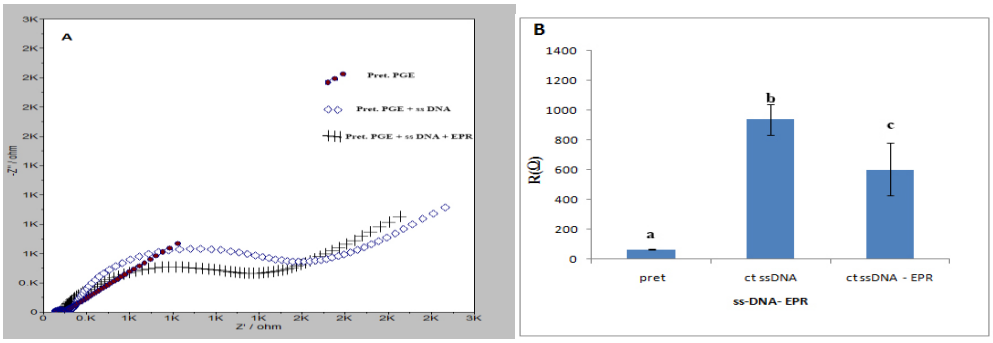

Şekil 9. (A) Niquist eğrisi (B)PGE yüzeyinde gerçekleşen ct ssDNA-EPR etkileşiminin transfer edilen akım yüküne karşı gösterdiği direnç; (a) aktivasyonu gerçekleştirilen PGE'lerin direnci, (b) ct ss-DNA immobilize edilen PGE 'lerin direnci, (c) PGE yüzeyine immobilize edilen ct ss-DNA-EPR etkileşiminin direnci

Cumhuriyet Science Journal
CSJ

e-ISSN: 2587-246X
ISSN: 2587-2680

Cumhuriyet Sci. J., Vol.40-4 (2019) 917-925

Reactive Extraction of Propionic Acid Using Tributyl Phosphate in Imidazolium-Based Ionic Liquids: Optimization Study Using Response Surface Methodology

Nilay BAYLAN [1,*]

[1] *Department of Chemical Engineering, İstanbul University-Cerrahpaşa, Avcılar 34320, İstanbul, Turkey*

Received: 04.07.2019; Accepted: 12.10.2019 *http://dx.doi.org/10.17776/csj.586822*

Abstract. In this work, the reactive extraction of propionic acid from aqueous solutions using imidazolium-based ionic liquids was examined. Ionic liquids, 1-butyl-3-methylimidazolium bis(trifluoromethylsulfonyl)imide ([BMIM][Tf_2N]), and 1-butyl-3-methylimidazolium hexafluorophosphate ([BMIM][PF_6]) were utilized as diluents. Tributyl phosphate (TBP) as an extractant in ionic liquids was used. D-optimal design based on the response surface methodology (RSM) has been exerted to specify the effect of different variables on the reactive extraction process. Initial propionic acid concentration (2-10% w/w), extractant (TBP) concentration (0-3.00 mol.L^{-1}) and temperature (25-45 °C) were chosen as numerical variables, and type of ionic liquid was chosen as a categorical variable. Extraction efficiency, selected as a dependent variable, was calculated from the experimental data. In addition to, the model equation for the extraction efficiency was created. The optimum extraction conditions were obtained as the initial propionic acid concentration of approximately 5% (w/w), TBP concentration in ionic liquids of 3 mol.L^{-1} and temperature of 45°C**.** Under these conditions, the values of extraction efficiency were determined as 85.64% for [BMIM][PF_6], and 81.91% for [BMIM][Tf_2N]. This study has indicated that the systems of TBP in ionic liquids is an efficient and green reactive extraction method for the removal of propionic acid from the aqueous media.

Keywords**:** Propionic acid, Imidazolium-Based Ionic Liquids, Tributyl phosphate, Reactive extraction, Response surface methodology.

İmidazolyum Bazlı İyonik Sıvılarda Trıbutil Fosfat Kullanarak Propyonik Asitin Reaktif Ekstraksiyonu: Yanıt Yüzey Metodolojisi İle Optimizasyon Çalışması

Özet. Bu çalışmada, propiyonik asidin sulu çözeltilerden imidazolyum bazlı iyonik sıvılar kullanılarak reaktif ekstraksiyonu incelenmiştir. İyonik sıvılar, 1-butil-3-metil imidazolyum bis(triflorometilsülfonil)imid ([BMIM][Tf_2N]), ve 1-butil-3-metil imidazolyum hekzaflorofosfat ([BMIM][PF_6]) seyreltici olarak kullanılmıştır. İyonik sıvılarda ekstraktan olarak tributil fosfat (TBP) kullanılmıştır. Farklı değişkenlerin reaktif ekstraksiyon işlemi üzerindeki etkisini belirlemek için yanıt yüzey metodolojisi (RSM) temelli D-optimal tasarım kullanılmıştır. Başlangıç propiyonik asit konsantrasyonu (ağırlıkça % 2-10), ekstraktan (TBP) konsantrasyonu (0-3.00 mol.L^{-1}) ve sıcaklık (25-45 °C) sayısal değişkenler olarak, ve iyonik sıvı türü ise kategorik değişken olarak seçilmiştir. Bağımlı değişken olarak seçilen ekstraksiyon etkinliği deneysel verilerden yararlanarak hesaplanmıştır. Ayrıca, ekstraksiyon etkinliği için model denklem oluşturulmuştur. Optimum ekstraksiyon koşulları, yaklaşık %5 (ağ/ağ) başlangıç propiyonik asit konsantrasyonu, 3 mol.L^{-1} iyonik sıvılar içerisinde TBP konsantrasyonu ve 45 °C sıcaklık olarak elde edildi. Bu koşullar altında, ekstraksiyon etkinliği değerleri [BMIM][PF_6] için %85.64 ve [BMIM][Tf_2N] için %81.91 olarak belirlenmiştir.

* Corresponding author. *Email address:* *nilay.baylan@istanbul.edu.tr*

Bu çalışma, iyonik sıvılar içerisindeki TBP sistemlerinin, propiyonik asidin sulu ortamdan uzaklaştırılması için verimli ve yeşil reaktif ekstraksiyon yöntemi olduğunu göstermiştir.

***Anahtar Kelimeler*:** Propiyonik asit, İmidazolyum Bazlı İyonik Sıvılar, Tributil fosfat, Reaktif ekstraksiyon, Yanıt yüzey Metodolojisi.

1. INTRODUCTION

Propionic acid has large amount of using in different chemical applications and industries. Especially it is widely used in production of cellulose plastics, ester solvents, perfume bases, arthritis drugs, herbicides, and plasticizers. Also, it is utilized to prevent the growth of mold and rope in cakes and breads in food industry and it is used as mold preventives in hay and silage [1]. Propionic acid is generally obtained by the fermentation process and is acquired not only as a single product, but as by-product with aqueous solutions. The by-product formation is a major problem that reduces the production efficiency. It must be removed from the fermentation broths for the continuous fermentation process. [2, 3]. Hence, the removal of propionic acid from waste streams or aqueous media or fermentation broths has great importance.

A variety of separation methods such as solvent extraction [4, 5], electrodialysis [6], reverse osmosis [7], adsorption [8-10], ion exchange [11], membrane system [12] are utilized for the removal of propionic acid from aqueous media. In addition to these methods, reactive extraction is commonly used for the propionic acid removal from aqueous media or fermentation broths or industrial wastewaters [13-15].

Reactive extraction can be defined as a process in which solvent extraction occurs simultaneously with the chemical complexation [16]. The removal of carboxylic acid by reactive extraction from aqueous solutions ensures a higher distribution coefficient and removal yield [17]. Aliphatic amines such as trioctylamine (TOA), tributylamine (TBA), and organophosphorous compounds like tributyl phosphate (TBP), trioctylphosphine oxide (TOPO), are broadly utilized as extractants for the removal carboxylic acids from aqueous. These extractants exhibit a high selectivity and solvent capacity [16]. The traditional organic solvents, such as alcohols, aliphatic hydrocarbons, ketones, ethers, are frequently used as diluents in the reactive extraction process [18].
Ionic liquids are organic molten salts which composed of specific anions and cations. Anions can be composed of organic or inorganic groups like bis (trifluoromethanesulfonyl) imide, hexafluorophosphate, tris (trifluoromethylsulfonyl) methyl, tetrafluoroborate, halides, acetate and nitrate. Cations are composed of organic groups like pyrrolidinium, ammonium pyridinium, sulfonium, phosphonium and imidazolium. Ionic liquids have negligible vapor pressure, and so they do not contribute to the atmosphere. Ionic liquids are non-flammable, good thermal stability, recyclable and good solubility for diverse compounds. Considering the substantial features of ionic liquids, they are also entitled “green solvents”. They have received great interest as an alternative to traditional solvents in many applications [19, 20].

Reactive extraction systems investigated in the literature for the uptake of propionic acid from aqueous solutions are summarized in Table 1. As shown in Table 1, the traditional organic solvents have been tested for the removal of propionic acid by reactive extraction. Nevertheless, these organic solvents cause environmental pollution due to they have toxic, volatile and flammable features. Therefore, the search for environmentally friendly solvent has emerged in the extraction. In this regard, ionic liquids have attention as alternative green solvents for the extraction processes instead of the traditional solvents [21].

Response surface methodology (RSM) is a technique consisting of mathematical and statistical methods used to determine the relation between independent variables and response, construct an experimental plan, build the model equation and specify the optimal conditions for response. RSM gives the minimum number of experiments that the maximum information about process behavior can be detected. Factorial Design, Box-Behnken, Central Composite and D-optimal designs are experimental design methods mostly used in RSM [36-38].

In this study, the use of imidazolium-based ionic liquids were investigated in the reactive extraction of propionic acid. TBP was utilized as an extractant in ionic liquids. D-optimal design based on RSM

has been applied to specify the effect of initial propionic acid concentration, TBP concentration, temperature and ionic liquid type on the reactive extraction process. The mathematical model equation was created and the experimental data were evaluated using analysis of variance (ANOVA). And also, optimal conditions were determined for the reactive extraction process.

Table 1: Reactive extraction systems investigated in the literature for the removal of propionic acid.

Extractants	Diluent solvents	References
Amberlite LA-2	Cyclohexane, 1-octanol, 2-octanone, isooctane, toluene, methyl isobutyl ketone and hexane	[22]
TOA	1-octanol, methyl isobutyl ketone, chloroform and tetrachloromethane	[18]
TOA	Heptane, oleyl alcohol, ethyl acetate and petroleum ether	[23]
TOA	1-decanol and 2-octanol	[13]
TOA	Dichloromethane, n-butyl acetate and n-heptane	[24]
TBP	1-dodecanol, toluene, benzene, hexane, heptane, butyl acetate, paraffin liquid and petroleum ether	[25]
TBP	Kerosene and 1-decanol	[26]
TBP	Heptane, petroleum ether and toluene	[27]
TBP, TOA and Aliquat 336	1-octanol	[28]
TBP, TOA	Hexane	[29]
TOPO	Hexane	[30]
TRPO	Kerosene	[31]
Alamine 336	Toluene	[32]
Aliquat 336	Methyl isobutyl ketone	[33]
Aliquat 336	2-octanol	[34]
Aliquat 336	Cyclohexane, methyl isobutyl ketone, ethyl acetate hexane and toluene	[15]
Primary amine (N1923)	Hexane, n-octanol and butyl acetate	[35]

2. MATERIALS AND METHODS

Propionic acid solutions were prepared by dissolving of a certain amount of propionic acid (Merck, >99%) in distilled water. Organic solutions were prepared by dissolving of tributyl phosphate (TBP; Sigma-Aldrich, >99%) in ionic liquids. Imidazolium-based ionic liquids, 1-butyl-3-methylimidazolium bis(trifluoromethylsulfonyl)imide ([BMIM][Tf_2N]; Iolitec, >99%) and 1-butyl-3-methylimidazolium hexafluorophosphate ([BMIM][PF_6]; Iolitec, >99%), were utilized as diluents.

The volumes of propionic acid and organic solutions were 2 mL. Experiments were performed by shaking in a water bath (Nüve ST 30) at 150 rpm for 1 h. Then, the samples were centrifuged in 3000 rpm for 10 min to separate the phases. The propionic acid concentration in the aqueous phase was determined using an automatic Schott Titroline titrator with NaOH solution of 0.1 N. The concentration of propionic acid in the organic phase was calculated from the material balance.

The experimental results were appraised with using the distribution coefficient, extraction efficiency and loading factor [39]:

The distribution coefficient (D) is defined as the propionic acid extracted from the aqueous phase into the organic phase. It is declared as follows:

$$D = \frac{C_{A,org}}{C_A} \quad (1)$$

The extraction efficiency (E) is clarified as the ratio of extracted propionic acid to initial propionic acid

concentration. It can be written in the following form:

$$E = \left(1 - \frac{C_A}{C_{Ao}}\right) * 100 \quad (2)$$

The loading of extractant (Z), known as loading factor, is described as the total propionic acid concentration in the organic phase divided by the total extractant concentration in the organic phase. It is remarked as below:

$$Z = \frac{C_{A,org.}}{C_{E,org.}} \quad (3)$$

where C_{A0} (mol.L^{-1}) is the initial propionic acid concentration in the aqueous phase, C_A (mol.L^{-1}) is the propionic acid concentration in the aqueous phase at the end of the extraction and $C_{A,org.}$ (mol.L^{-1}) is the propionic acid concentration in the organic phase at the end of the extraction. $C_{E,org.}$ (mol.L^{-1}) is the extractant concentration in the organic phase.

3. RESULTS AND DISCUSSION

3.1. Response Surface Methodology

D-optimal design based on RSM has been exerted to determine the effect of different variables on the reactive extraction process, specify the relation between the variables and response and create the mathematical model equation representing the extraction system. For the purposes, Design-Expert® Software Trial Version 11 (Stat-Ease, Inc.) was utilized. Design variables (numerical and categorical variables) and their levels were indicated in Table 2. The independent variables were selected as initial propionic acid concentration (X_1), initial TBP concentration in ionic liquid (X_2), and temperature (X_3). These variables were numerical variables. Other independent variable was ionic liquid type (X_4) and this variable was categorical variable. Dependent variable or response was selected as extraction efficiency. The variables and their levels given in Table 2 were entered into Design-Expert® Software. The experiment plan was determined according to four variables, namely three numerical variables and one categorical variable. As shown in Table 3, Design-Expert® Software proposed 24 experiment points and these experiments were carried out experimentally. Table 3 shows D-optimal design plan and experimental data obtained.

Table 2. D-optimal design variables and levels.

Variables	Unit	Code	Categorical / Numerical	Levels		
				1	2	
				-1	0	1
Initial propionic acid concentration	%	X_1	Numerical	2	6	10
TBP concentration	mol.L^{-1}	X_2	Numerical	0	1.5	3
Temperature	°C	X_3	Numerical	25	35	45
Ionic liquid type		X_4	Categorical	[BMIM][PF_6]	[BMIM][Tf_2N]	

Table 3. D-optimal design plan and experimental responses.

Experiment Number	Independent variables				Dependent variable
	Initial propionic acid concentration X_1	TBP concentration X_2	Temperature X_3	Ionic liquid type X_4	Extraction efficiency (%) Y_1
1	2	3	25	[BMIM][PF_6]	76.97
2	6	1.5	25	[BMIM][PF_6]	60.04
3	10	0	25	[BMIM][PF_6]	29.92
4	10	3	25	[BMIM][PF_6]	77.68
5	10	3	35	[BMIM][PF_6]	78.64
6	8	2.25	35	[BMIM][PF_6]	70.88
7	2	0	35	[BMIM][PF_6]	28.12
8	6	1.5	40	[BMIM][PF_6]	63.28
9	2	3	45	[BMIM][PF_6]	84.06
10	10	0	45	[BMIM][PF_6]	35.15
11	2	3	45	[BMIM][PF_6]	83.11
12	10	0	45	[BMIM][PF_6]	35.52
13	10	1.5	25	[BMIM][Tf_2N]	61.12
14	6	3	25	[BMIM][Tf_2N]	80.25
15	2	0	25	[BMIM][Tf_2N]	30.77
16	10	1.5	25	[BMIM][Tf_2N]	61.31
17	6	3	25	[BMIM][Tf_2N]	79.92
18	2	0	25	[BMIM][Tf_2N]	31.32
19	6	0.75	30	[BMIM][Tf_2N]	51.62
20	10	0	35	[BMIM][Tf_2N]	38.06
21	2	3	35	[BMIM][Tf_2N]	75.89
22	6	1.5	45	[BMIM][Tf_2N]	63.67
23	2	0	45	[BMIM][Tf_2N]	36.71
24	10	3	45	[BMIM][Tf_2N]	78.83

3.1.1. Analysis of Experimental Results

ANOVA table with numerous useful data is utilized to interpret of experimental results. The experimental results obtained were evaluated statistically using ANOVA. ANOVA table for extraction efficiency (Y) were indicated in Table 4. In ANOVA table, F-value and p-value of the model shows whether the model is significant or not [40]. As can be seen in Table 4, F-value of 1473.52 and p-value of < 0.0001 were obtained, these values showed that the model was significant for the extraction efficiency (Y). ANOVA table also shows effective parameters according to p-value. P-values of parameters less than 0.05 are important model terms and have an effect on the response [41]. In this case, X_1, X_2, X_3 and X_4 terms had the linear effects on the extraction efficiency; X_1X_2, X_1X_3, X_1X_4, X_2X_4 and X_3X_4 terms had the interaction effects on the extraction efficiency; X_1^2, X_2^2 and X_3^2 terms had exponential effects on the extraction efficiency. In other words, these terms had influential model terms and the model equation characterizing the extraction efficiency consists of these model terms. As a result, the model equation in coded factors was created with RSM as below:

$$Y = 61.78 + 1.17\,X_1 + 22.47\,X_2 + 2.11\,X_3 + 0.72\,X_4 - 0.97\,X_1X_2 - 0.77\,X_1X_3 + 0.58\,X_1X_4 - 1.93\,X_2X_4 - 0.81\,X_3X_4 - 3.54\,X_1^2 - 3.05\,X_2^2 + 1.06\,X_3^2$$

Table 4. ANOVA data for the extraction efficiency (Y).

Source	Sum of Squares	df	Mean Square	F-value	p-value Prob>F
Model	9493.66	13	730.28	1473.52	< 0.0001
X_1	17.19	1	17.19	34.69	0.0002
X_2	6623.59	1	6623.59	13364.69	< 0.0001
X_3	68.11	1	68.11	137.43	< 0.0001
X_4	10.14	1	10.14	20.46	0.0011
X_1X_2	10.97	1	10.97	22.13	0.0008
X_1X_3	6.22	1	6.22	12.54	0.0053
X_1X_4	4.12	1	4.12	8.32	0.0163
X_2X_3	2.05	1	2.05	4.13	0.0696
X_2X_4	47.96	1	47.96	96.78	< 0.0001
X_3X_4	9.91	1	9.91	19.99	0.0012
X_1^2	27.70	1	27.70	55.90	< 0.0001
X_2^2	18.26	1	18.26	36.85	0.0001
X_3^2	4.65	1	4.65	9.38	0.0120
Residual	4.96	10	0.4956		
Lack of Fit	4.21	5	0.8425	5.67	0.0400
Pure Error	0.7435	5	0.1487		
Cor. Total	9498.62	23	730.28	1473.52	< 0.0001

The model equation showed that all independent variables affect the extraction efficiency. Due to having the highest coefficient in the model equation, TBP concentration (X_2) was the most effective parameter on the extraction efficiency.

Table 5. Statistical parameters obtained in D-optimal design for extraction efficiency (Y).

Statistical parameters			
R^2	0.9995	**SD**	0.7040
Adjusted R^2	0.9988	**AP**	102.3903
Predicted R^2	0.9919	**CV %**	1.20

A number of statistical parameters are utilized to determine the adequacy and accuracy of model equation. Table 5 indicates the statistical parameters like the correlation coefficients (R^2, predicted R^2 and adjusted R^2), the coefficient of variation (CV), the standard deviation (SD) and adequate precision (AP). R^2 can be described as a measure of the grade of compliance. As can be seen in Table 6, R^2 value (0.9995) was found to be quite high. This has been proved that the experimental data was compatible with the model equation. R^2_{Adj} can be defined as a measure of the amount of variation around the average. If R^2 and adjusted R^2 (R^2_{Adj}) values are close to each other, it shows that the experimental data were represented sufficiently by the model. The difference between the predicted R^2 (R^2_{Pred}) and R^2_{Adj} is desirable to be less than 0.2. It indicates that these values are in reasonable agreement with each other. If the standard deviation is low, the model fit is better. Adequate precision (AP) measures the signal to noise proportion. It is desirable to be greater than 4. On the other hand, the coefficient of variation (CV) describes as the measure of proportion of the standard deviation of the average and is expected to be quite low [36, 37]. All statistical data indicate that the acquired model equation was accurate and adequate to design the reactive extraction of propionic acid.

Other control points for the verification of the experimental results are the analysis of diagnostic plots (predicted vs. actual plot or residuals vs. predicted plot) [42, 43]. The predicted vs actual plot and residuals vs. predicted plot were depicted in Figure 1. As depicted in Figure 1.a, the experimental data,

namely actual values were aligned as a straight line. As indicated in Figure 1.b, all residual points were distributed within the range. Diagnostic plots denoted that the predicted values by the model equation were consistent with the experimental data.

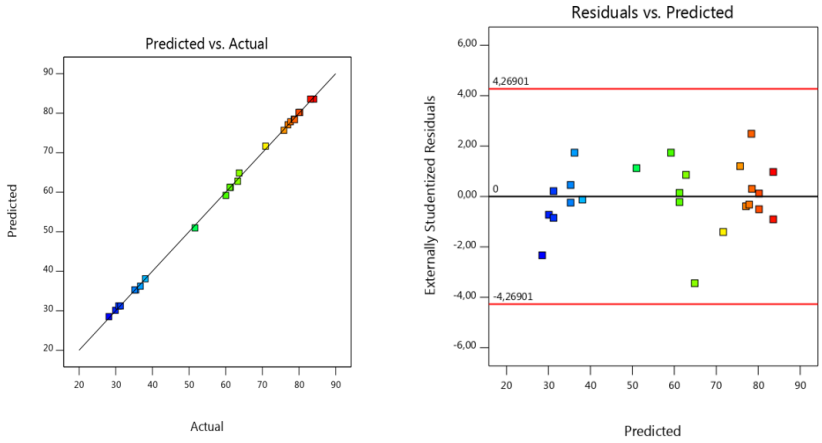

Figure 1. Diagnostic plots of D-optimal design model. (a) predicted vs actual plot (b) residuals vs. predicted plot.

3.1.2. Response Surface Plots

Response surface plots (3D plots) were depicted to specify the relation between the numerical variables and extraction efficiency. 3D plots were illustrated between two selected numerical variables. Other numerical variable was held at center levels. Figure 2 shows the effect of numerical variables on the extraction efficiency for both ionic liquids. As can be seen in Figures 2.a and 2.b, the extraction efficiency increased significantly with increasing TBP concentration in ionic liquids. When TBP is utilized as an extractant in the ionic liquid, the grade of extraction of propionic acid increases. So, more propionic acid molecules are extracted from the aqueous phase [44]. The trend observed acquired from this work were consistent with the reported studies in the literature [45]. From Figures 2.a and 2.c, the extraction efficiency slightly increased as the initial propionic acid concentration increased from 2% to 10%. In the literature, the reactive extraction of propionic acid with Aliquat 336 was investigated by Uslu and İnci [32]. Similarly, they observed that the extraction efficiency increased with increasing initial propionic acid concentration. In addition to, as the temperature was increased, the extraction efficiency increased slightly. From Figure 2.c, it increased from 60.04% to 63.67% with increasing the temperature varied range 25-45 °C. Athankar et. al. investigated gallic acid extraction with tri-n-caprylylamine and they reported that the extraction efficiency was only slightly increased (from 62% to 65%) with increasing temperature [46].

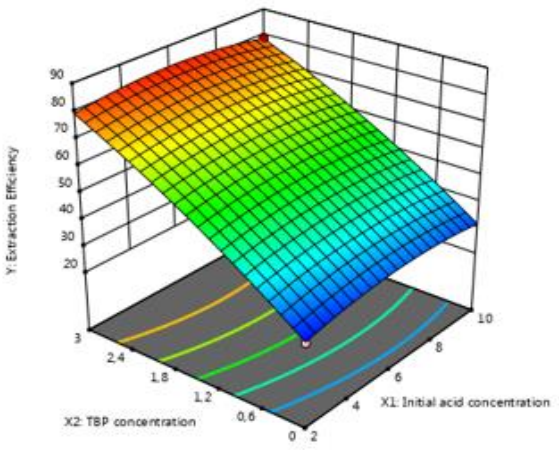

(a) [BMIM][PF_6]

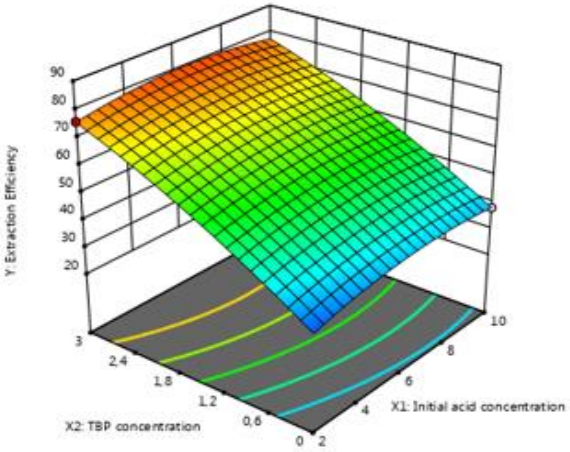

(a) [BMIM][Tf_2N]

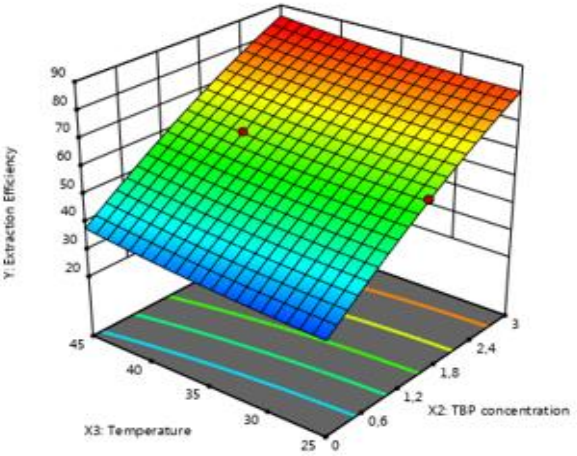

(b) [BMIM][PF_6]

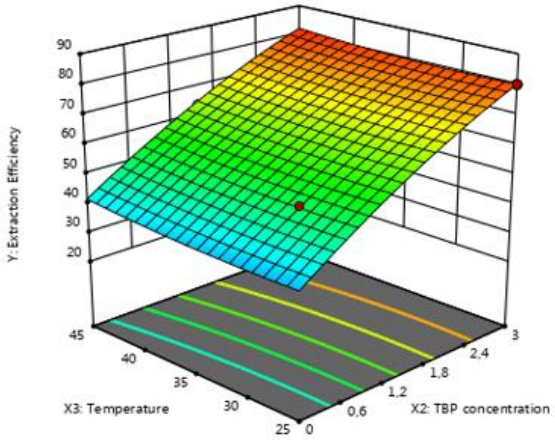

(b) [BMIM][Tf_2N]

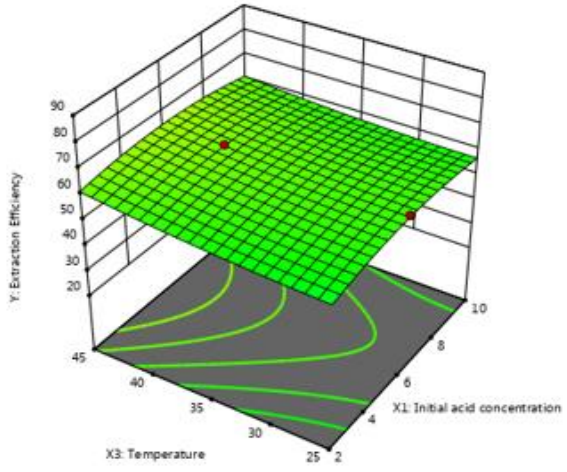

(c) [BMIM][PF_6]

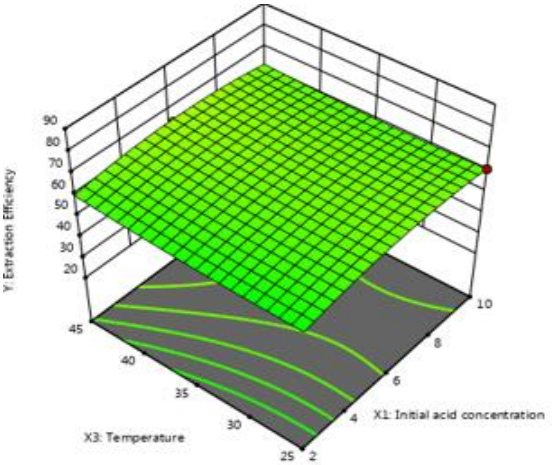

(c) [BMIM][Tf_2N]

Figure 2. 3D plots for the extraction efficiency in the reactive extraction of propionic acid with ionic liquids **(a)** the effect of initial propionic acid concentration (X_1) and TBP concentration (X_2) in case of temperature of 35 °C. **(b)** the effect of TBP concentration (X_2) and temperature (X_3) in case of initial propionic acid concentration of 6%. **(c)** the effect of initial propionic acid concentration (X_1) and temperature (X_3) in case of TBP concentration of 1.5 mol/L.

The final step of the design is the specification of the criteria for optimization. The optimization criterion was is to maximize the extraction efficiency. And also, all independent variables were kept within in the investigated range. These conditions were entered into Design-Expert® Software and the optimum conditions were obtained as shown in Table 6.

Table 6. Optimum reactive extraction conditions obtained by D-optimal design.

Ionic liquid type	Initial propionic acid concentration (% w/w)	TBP concentration (mol/L)	Temperature (°C)	Predicted Extraction efficiency (%)	Desirability
[BMIM][PF_6]	5.511	2.989	44.428	85.640	1.000
[BMIM][Tf_2N]	5.984	3.000	45.000	81.911	0.962

4. CONCLUSION

In the present design study, imidazolium-based ionic liquids, namely [BMIM][PF_6] and [BMIM][Tf_2N] were examined in the reactive extraction of propionic acid by using TBP. D-optimal design was conducted to determine the effect of various parameters on the extraction efficiency. The second-order model equation representing process parameters and extraction efficiency was obtained. The validity of model equation was evaluated by ANOVA and graphical analysis. The acquired model equation was in good agreement with the experimental data. The model equation indicated that all independent variables affect the extraction efficiency. Among independent variables, TBP concentration was obtained as the most effective parameter on the extraction efficiency. The optimum conditions were obtained as the initial propionic acid concentration of approximately 5% (w/w), TBP concentration in ionic liquids of 3 $mol.L^{-1}$, temperature of 45°C**.** Under optimum conditions, the values of extraction efficiency were determined as 85.64% for [BMIM][PF_6], and 81.91% for [BMIM][Tf_2N]. This study has also shown that ionic liquids [BMIM][PF_6] and [BMIM][Tf_2N] as green extraction solvents can be used in the reactive extraction of propionic acid.

ACKNOWLEDGEMENT

This study was funded by Istanbul University-Cerrahpaşa with the Project Number BYP-2018-32041.

REFERENCES

[1] A. Keshav, K.L. Wasewar, Back extraction of propionic acid from loaded organic phase, Chemical Engineering Science, 65 (2010) 2751-2757.

[2] S. Kumar, B. Babu, Process intensification for separation of carboxylic acids from fermentation broths using reactive extraction, Journal on Future Engineering & Technology, 3 (2008) 19-26.

[3] H. Song, S.Y. Lee, Production of succinic acid by bacterial fermentation, Enzyme and Microbial Technology, 39 (2006) 352-361.

[4] S. Çehreli, B. Tatlı, P. Bagˇman, (Liquid+ liquid) equilibria of (water+ propionic acid+ cyclohexanone) at several temperatures, The Journal of Chemical Thermodynamics, 37 (2005) 1288-1293.

[5] V. Taghikhani, G. Vakili-Nezhaad, M. Khoshkbarchi, M. Shariaty-Niassar, Liquid− Liquid Equilibria of Water+ Propionic Acid+ Methyl Butyl Ketone and of Water+ Propionic Acid+ Methyl Isopropyl Ketone, Journal of Chemical & Engineering Data, 46 (2001) 1107-1109.

[6] A.J. Weier, B.A. Glatz, C.E. Glatz, Recovery of propionic and acetic acids from fermentation broth by electrodialysis, Biotechnology Progress, 8 (1992) 479-485.

[7] R.A. Diltz, T.V. Marolla, M.V. Henley, L. Li, Reverse osmosis processing of organic model compounds and fermentation broths, Bioresource Technology, 98 (2007) 686-695.

[8] A.H. da Silva, E.A. Miranda, Adsorption/desorption of organic acids onto different adsorbents for their recovery from fermentation broths, Journal of Chemical & engineering data, 58 (2013) 1454-1463.

[9] A. Freitas, M. Mendes, G. Coelho, Thermodynamic study of fatty acids adsorption on different adsorbents, The Journal of Chemical Thermodynamics, 39 (2007) 1027-1037.
[10] İ. İnci, Ş.S. Bayazit, H. Uslu, Investigation of adsorption equilibrium and kinetics of propionic acid and glyoxylic acid from aqueous solution by alumina, Journal of Chemical & Engineering Data, 56 (2011) 3301-3308.
[11] H. Uslu, İ. İnci, S.S. Bayazit, G.K. Demir, Comparison of solid− liquid equilibrium data for the adsorption of propionic acid and tartaric acid from aqueous solution onto Amberlite IRA-67, Industrial & Engineering Chemistry Research, 48 (2009) 7767-7772.
[12] R. Wodzki, J. Nowaczyk, M. Kujawski, Separation of propionic and acetic acid by pertraction in a multimembrane hybrid system, Separation and Purification Technology, 21 (2000) 39-54.
[13] A. Keshav, K.L. Wasewar, S. Chand, Reactive extraction of propionic acid using tri-n-octylamine, Chemical Engineering Communications, 197 (2009) 606-626.
[14] S. Kumar, D. Datta, B. Babu, Estimation of equilibrium parameters using differential evolution in reactive extraction of propionic acid by tri-n-butyl phosphate, Chemical Engineering and Processing: Process Intensification, 50 (2011) 614-622.
[15] H. Uslu, İ. İnci, (Liquid+ liquid) equilibria of the (water+ propionic acid+ Aliquat 336+ organic solvents) at T= 298.15 K, The Journal of Chemical Thermodynamics, 39 (2007) 804-809.
[16] M. Rodriguez, S. Luque, J. Alvarez, J. Coca, Extractive ultrafiltration for the removal of valeric acid, Journal of Membrane Science, 120 (1996) 35-43.
[17] M.O. Ruiz, J.L. Cabezas, I. Escudero, J. Coca, Valeric Acid Extraction with Tri-N-butyl Phosphate Impregnated in a Macroporous Resin. I. Equilibrium and Mass Transfer Rates, Separation Science and Technology, 39 (2005) 77-95.
[18] Z. Li, W. Qin, Y. Dai, Liquid− liquid equilibria of acetic, propionic, butyric, and valeric acids with trioctylamine as extractant, Journal of Chemical & Engineering Data, 47 (2002) 843-848.
[19] K. Ghandi, A review of ionic liquids, their limits and applications, Green and Sustainable Chemistry, 4 (2014) 44-53.
[20] K. Mikami, Green reaction media in organic synthesis, Wiley Online Library, 2005.
[21] L. Sprakel, B. Schuur, Solvent developments for liquid-liquid extraction of carboxylic acids in perspective, Separation and Purification Technology, 211 (2019) 935-957.
[22] Y.S. Aşçı, İ. İnci, Extraction equilibria of propionic acid from aqueous solutions by Amberlite LA-2 in diluent solvents, Chemical Engineering Journal, 155 (2009) 784-788.
[23] A. Keshav, K.L. Wasewar, S. Chand, Extraction of propionic acid with tri-n-octyl amine in different diluents, Separation and Purification Technology, 63 (2008) 179-183.
[24] A.I. Galaction, A. Carlescu, M. Turnea, D. Caşcaval, Direct Extraction of Propionic Acid from Propionibacterium acidipropionici Broths with Tri-n-octylamine, Chemical Engineering & Technology, 35 (2012) 1657-1663.
[25] A. Keshav, S. Chand, K.L. Wasewar, Equilibrium studies for extraction of propionic acid using tri-n-butyl phosphate in different solvents, Journal of Chemical & Engineering Data, 53 (2008) 1424-1430.
[26] S. Kumar, D. Datta, B. Babu, Differential evolution approach for reactive extraction of propionic acid using tri-n-butyl phosphate (TBP) in kerosene and 1-decanol, Materials and Manufacturing Processes, 26 (2011) 1222-1228.
[27] A. Keshav, K.L. Wasewar, S. Chand, Recovery of propionic acid from an aqueous stream by reactive extraction: Effect of diluents, Desalination, 244 (2009) 12-23.
[28] A. Keshav, K.L. Wasewar, S. Chand, Extraction of propionic acid using different extractants (tri-n-butylphosphate, tri-n-octylamine, and Aliquat 336), Industrial & Engineering Chemistry Research, 47 (2008) 6192-6196.
[29] M. Matsumoto, T. Otono, K. Kondo, Synergistic extraction of organic acids with tri-n-octylamine and tri-n-butylphosphate, Separation and Purification Technology, 24 (2001) 337-342.
[30] A. Keshav, K.L. Wasewar, S. Chand, Equilibrium and Kinetics of the Extraction of Propionic Acid Using Tri-n-Octylphosphineoxide, Chemical Engineering & Technology: Industrial Chemistry-Plant Equipment-Process

Engineering-Biotechnology, 31 (2008) 1290-1295.
[31] Y. Wang, Y. Li, Y. Li, J. Wang, Z. Li, Y. Dai, Extraction equilibria of monocarboxylic acids with trialkylphosphine oxide, Journal of Chemical & Engineering Data, 46 (2001) 831-837.
[32] H. Uslu, Linear solvation energy relationship (LSER) Modeling and kinetic studies on propionic acid reactive extraction using Alamine 336 in a toluene solution, Industrial & Engineering Chemistry Research, 45 (2006) 5788-5795.
[33] A. Keshav, K.L. Wasewar, S. Chand, Reactive extraction of propionic acid using Aliquat 336 in MIBK: Linear solvation energy relationship (LSER) modeling and kinetics study, Journal of Scientific and Industrial Research 2009; 68: 708-713.
[34] A. Keshav, K. Wasewar, S. Chand, H. Uslu, Reactive extraction of propionic acid using Aliquat-336 in 2-octanol: Linear solvation energy relationship (LSER) modeling and kinetics study, Chemical and Biochemical Engineering Quarterly, 24 (2010) 67-73.
[35] K. Wang, Z. Chang, Y. Ma, C. Lei, S. Jin, Y. Wu, I. Mahmood, C. Hua, H. Liu, Equilibrium study on reactive extraction of propionic acid with N1923 in different diluents, Fluid Phase Equilibria, 278 (2009) 103-108.
[36] N. Baylan, S. Çehreli, Ionic liquids as bulk liquid membranes on levulinic acid removal: A design study, Journal of Molecular Liquids, 266 (2018) 299-308.
[37] N. Baylan, S. Çehreli, Removal of acetic acid from aqueous solutions using bulk ionic liquid membranes: A transport and experimental design study, Separation and Purification Technology, 224 (2019) 51-61.
[38] D. Granato, V.M. de Araújo Calado, The use and importance of design of experiments (DOE) in process modelling in food science and technology, Mathematical and statistical methods in food science and technology, 1 (2014) 1-18.
[39] İ. İnci, Linear solvation energy relationship modeling and kinetic studies on reactive extraction of succinic acid by tridodecylamine dissolved in MIBK, Biotechnology Progress, 23 (2007) 1171-1179.
[40] C.-C. Chen, K.-T. Chiang, C.-C. Chou, Y.-C. Liao, The use of D-optimal design for modeling and analyzing the vibration and surface roughness in the precision turning with a diamond cutting tool, The International Journal of Advanced Manufacturing Technology, 54 (2011) 465-478.
[41] M.D. Turan, Statistical Approach to Mineral Engineering and Optimization, Contributions to Mineralization, IntechOpen, 2018.
[42] A. Asghar, A. Raman, A. Aziz, W.M.A.W. Daud, A comparison of central composite design and Taguchi method for optimizing Fenton process, The Scientific World Journal, 2014 (2014) 1-14.
[43] T. Rajmohan, K. Palanikumar, Modeling and analysis of performances in drilling hybrid metal matrix composites using D-optimal design, The International Journal of Advanced Manufacturing Technology, 64 (2013) 1249-1261.
[44] M. Djas, M. Henczka, Reactive extraction of carboxylic acids using organic solvents and supercritical fluids: a review, Separation and Purification Technology, 201 (2018) 106-119.
[45] K.L. Wasewar, D. Shende, A. Keshav, Reactive extraction of itaconic acid using tri-n-butyl phosphate and aliquat 336 in sunflower oil as a non-toxic diluent, Journal of Chemical Technology & Biotechnology, 86 (2011) 319-323.
[46] K.K. Athankar, K.L. Wasewar, M.N. Varma, D.Z. Shende, Reactive extraction of gallic acid with tri-n-caprylylamine, New Journal of Chemistry, 40 (2016) 2413-2417.

Cumhuriyet Science Journal
CSJ

e-ISSN: 2587-246X
ISSN: 2587-2680

Cumhuriyet Sci. J., Vol.40-4 (2019) 939-945

CT and MRI Medical Image Fusion Using Discrete Wavelet Transform

Molham Moshantat [1], ***Saeid Karamzadeh*** [2] *

[1] *Electrical and Electronics Engineering, Istanbul Aydın University, Istanbul, TURKEY*

[2] *Electrical and Electronics Engineering Department, Faculty of Engineering and Natural Sciences, Bahçeşehir University, Istanbul, TURKEY*

Received: 04.04.2019; Accepted: 24.05.2019 http://dx.doi.org/10.17776/csj.549192

Abstract. In these days, using medical image is very important in hospitals. These medical images give a lot of data about human body for example Computed Tomography (CT) identifies the bone structure, Magnetic Resonance Image (MRI) image gives information about tissue data, Positron on Emission Tomography (PET) and Single photon release computed tomography (SPECT) give human body functionality data. but these images can't give clear data image for disease diagnosis and treatment planning. So, these different modality complementary data for effective disease analysis is required. In this work we fused two images (CT and MRI) by using discrete wavelet transform then applied this transform on all types of wavelets (haar, Daubechies, Mexican Hat, Symlets, Morlet, Shannon).

Keywords**:** Image fusion, DWT, PSNR, IDWT, CT, MRI, Entropy.

Ayrık Dalgacık Dönüşümü ile CT ve MRI Medikal Görüntü Füzyonu

Özet. Günümüzde medikal görüntülerin teşhis ve tedavide büyük bir rol oynadığı aşikardır. Daha fazla bilgi taşıyan ve birden fazla görüntünün füzyonundan ulaşan bir görüntü bu sürece katkı sağlayacaktır. Bu çalışmada ise, CT ve MRI görüntülerinin füzyonu için, literatürde bilinen en iyi füzyon yöntemlerinden bir olan dalgacık dönüşümü uygulanmıştır. Farklı dalgacık dönüşümleri kullanılıp sonuçları sunulmuştur. Çıkan sonuçların karşılaştırılması için entropi ve sinyal, gürültü oranı (SNR) ölçülüp verilmiştir.

Anahtar Kelimeler**:** Dalgacık Dönüşümü, Görüntü Füzyonu, Entropi.

1. INTRODUCTION

These days, with the accelerate advancement in high-technology and contemporary instrumentation, medical imaging is now an essential part of a high number of applications, such as diagnosis, research, and treatment, for medical examination, just one sort of image might not be enough to supply accurate clinical prerequisite for doctors. Consequently, the combination of this multi-modal medical images is required [1]. Medical imaging provides many modes of images information for the clinical examination including CT, X-ray, DSA, MRI, PET, SPECT etc. Different medical images have different features, which may provide structural knowledge of distinct organs. By way of instance, CT (Computed tomography) and MRI (Magnetic resonance image) with high spatial resolution might offer anatomical construction info of organs. Thus, an assortment of imaging to get the exact same organ, they're contradictory but interrelated and complementary. As a result, the right image fusion of distinct features becomes an urgent

* Corresponding author. *Email address:* *karamzadeh@itu.edu.tr*

necessity for clinical examination [2]. in this work we designed a program to merge two medical image (MRI and CT) using wavelet transform (Discrete Wavelet Transform) and discussed the best result when applied to all types of wavelets on this image and we used image fusion technique are performed on medical image utilizing wavelets like db, coif, sym, dmey, bior, rbio and haar. These fusion Algorithms are analyzed using different performance parameters like Entropy, PSNR, SD, SNR to choose the better methods.

2. MEDICAL IMAGE FUSION USING WAVELET TRANSFORM

MRI and CT images usually contain individual information such as the condition and spread of the disease or details of the tissues in the human body, this section we briefly explain Digital imaging and communication in medicine (DICM) images and discusses the application of DWT fusion rule in complex wavelet domain as an approach to combine the complementary information from both the images into a single one for precise diagnosis [3-4].

2.1. Digital Imaging and Communication in Medical

Through the last thirty decades, there has been a huge development of digital technology. Computers have entered almost every part of their lives, so of course they have become increasingly important in medical applications. Much medical imaging methods utilized today mostly rely on computer processing. Computers are used not merely to show or store pictures but to make pictures or 3D models from the input of data. Data are obtained from imaging apparatus that use complicated processes, including CT, MRI, SPECT, PET. Furthermore, there's turned into a large, less or more powerful, development of computer-aided diagnosis (CAD) methods [5, 6]. Due to many directions in the evolution of medical imaging equipment, it was quite essential to creating a standard for connection and information flow between appliances. As there are numerous manufacturers that produce medical imaging equipment with numerous approaches, obtaining a standard makes use of the picture and healthcare information easier. This standard is made by workgroups a year to fulfill any medical branch [7]. DICOM (Digital Imaging and Communication) Standard consists of many layers in regard to ISO (international standers organization) OSI (open systems interconnection) network design. DICOM is independent of the surface since it doesn't establish a physical link. upper layer protocol (ULP) is described within the DICOM standard. It's an abstract protocol which defines information encapsulation and is greater than level five of the ISO OSI model.

2.2. Medical Image Fusion Using Discrete Wavelet Transform

Modalities like CT and MRI generally contain solitary information i.e. either demonstration of disease extent or the details of soft tissues. It's practically not possible to capture each detail from 1 imaging modality that will ensure clinical precision and robustness of the investigation and consequent identification. Figure 1 shows the 3 major concentrated areas of research in medical image combination: (a) Identification, improvement and development of imaging modalities useful for medical image fusion (b) Development of different techniques for medical image fusion (c) Application of medical image fusion for studying human organs of interest in assessments of medical condition Various approaches are available for graphic mix applications, but image fusion techniques are essentially categorized into two broad classes i.e. spatial domain Fusion and Transform domain-based fusion.

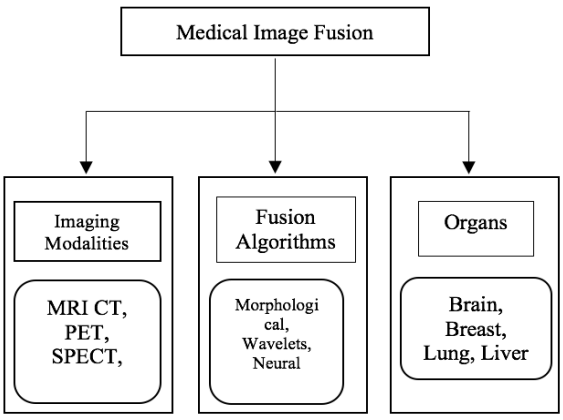

Figure 1: Nature of modalities, methods and organs used in medical image fusion [11].

The first idea and concept of wavelet-based multiresolution analysis came from Mallat. A wavelet transform is a mathematical tool which could detect local attributes in a signal process. Additionally, it may be utilized to segregate two dimensional (2D) signs like 2D gray-scale image signals into various varying levels for multiresolution analysis. Wavelet transform has been heavily utilized in several locations, including texture analysis, data compression, feature detection, and image fusion.

In one dimension (1D) the basic idea of the DWT is to represent the signal as a superposition of wave lets. Suppose that a discrete signal is represented by f(t) the wavelet decomposition is then defined as

$$f(t) = \sum_{m,n} c_{m,n}\ \psi_{m,n}(t) \quad (1)$$

Where $\psi m,\ n\ (t) = 2{-}m/2\ \psi\ [2{-}m\ t - n]$ and m and n are integers. Wavelet transform for image fusion the schematic diagram for wavelet based fusion techniques is shown in figure 2.

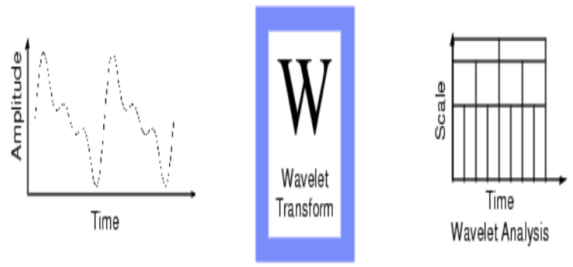

Figure 2: Wavelet Transform on a signal [10].

In all wavelet-based image fusion techniques the wavelet transforms W of the two registered input images are computed and these transforms are combined using some kind of fusion rule Ø. This is given by equation (2) below:

$$I(x,y) = w^{-1}(\phi\left(W\left(I_1(x,y)\right), W\left(I_2(x,y)\right)\right) \quad (2)$$

where W-1 is the inverse discrete wavelet transform (IDWT).

Generally, the fundamental idea of image fusion based on wavelet transform would be to execute a multiresolution decomposition on every source image; the coefficients of the low-frequency band and high-frequency bands are subsequently performed with a particular mix rule. Following that, the fused image is accessed by doing the inverse DWT (IDWT) for its corresponding combined wavelet coefficients [8, 9].

2.3. Algorithm:

Following algorithm has been developed and implemented in MATLAB software:

1. Read the image I1 and find its size.

2. Read the second image I2 and find its size.

3. Compute and match the size if not same, make it same.

4. The indexed image should be DICOM.

5. Perform multilevel wavelet decomposition using any wavelet (haar, db, bior…). Generate the coefficient matrices of the level-three approximation and horizontal, vertical and diagonal details.

6. Now fuse the wavelet coefficients using discrete wavelet transform.

7.Generate a final matrix of fused wavelet coefficients.
8. Compute the inverse wavelet transform to get the fused image.
9. Finally compute the entropy, SD, PSNR, SNR and display the results

The block diagram for image fusion is shown in figure 3.

3. RESULT AND DISCUSSION PERFORMANCE ANALYSIS

This paper aims to present a new algorithm to improve the quality of multimodality medical image fusion using discrete wavelet transform (DWT) approach. performance of fusion is calculated on the basis of entropy, SD and PSNR. The total processing time and the results demonstrate the effectiveness of fusion scheme based on wavelet transform. MRI and CT images are taken as source images (figure 4). MATLAB is used for the simulation.

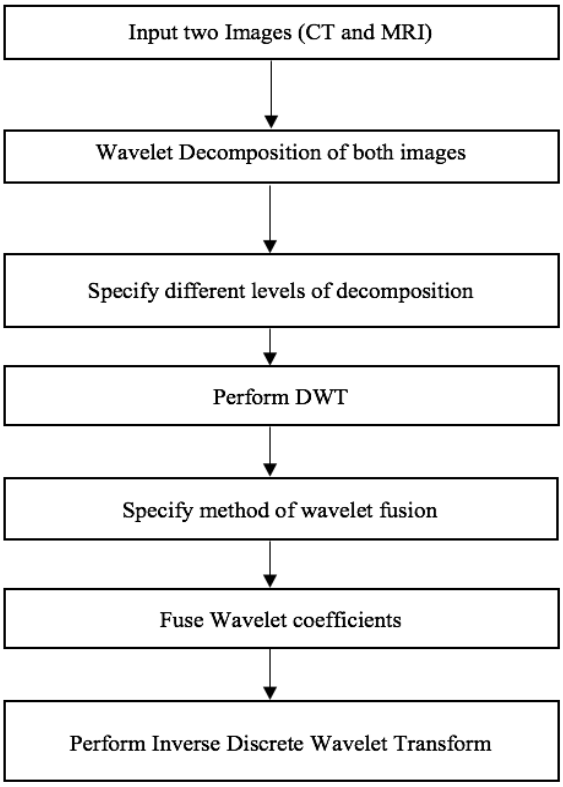

Figure 3: Block diagram for image fusion.

Fusion is performed on source images using different wavelets like db, coif, sym, dmey, bior, rbio and haar. The MRI & CT medical images (figure 4) are used for the fusion experiment. The simulations are performed on these MRI and CT Medical images for 7 different wavelets transform methods (Bior, coif, db, dmey, haar, rbio and sym). In the whole work the Max– Max wavelet coefficient with level-1 has been used.

3.1. Entropy

Entropy has been used in several scientific areas in addition to in image processing procedures and it includes the data content of image. Entropy is a parameter to value the information quantity in image. Entropy defines the info in the electronic numbers in images because of a frequency of modification.

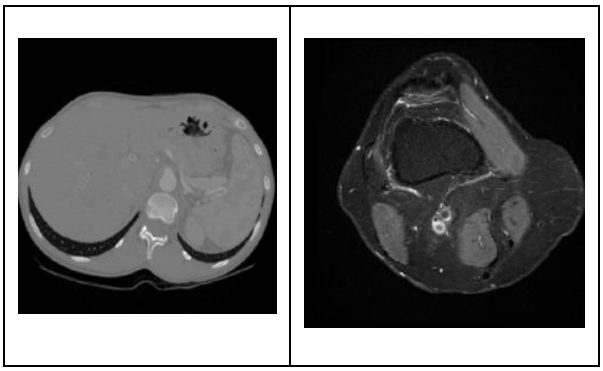

(a) (b)

Figure 4: a) MRI image that we used in our program, b): CT image that we used in our program [7].

When every grey level has the exact same frequency, then the entropy gets the highest value. Quality evaluation is essential as Imaging techniques such as the fusion algorithm can present a few quantities of artifacts or distortion in the signal. For quality evaluation, entropy is employed to appraise the data quantity in image. The greater value of entropy suggests the revised image is far better than the benchmark image that has more contrast and clarity and is your best image to use for medical purposes. In case entropy of fused image is greater than the source image then it suggests the revised image contains more info than source image and the fused performances are enhanced [12]. Entropy Provides the amount of Data contained in the image, the Further information it Comprises, entropy is defined as:

$$H = -\sum_{i=1}^{M}\sum_{j=1}^{N} p_{ij} log_2\, p_{ij} \quad (3)$$

$$p_{ij} = \frac{f(i,j)}{\sum_{i=1}^{M}\sum_{i=1}^{N} f(i,j)} \quad (4)$$

Where H represents the regional information entropy, pij is the gray value probability of point (i, j) in the regional image, f (i, j) is the gray value of point (i, j) in the regional image. The size of the region is M*N. The entropy value is 0 when no texture is in the image. The entropy is maximized when full of texture is in the image. The entropy value in our proposed work is shown in table 1 shown that fused image using biorthogonal wavelets have the highest value compering with other wavelet which mean this result will give us more details than source image.

3.2. Standard Deviation:

Standard deviation calculates the quantity of grey values which are dispersed in image. In the event of the image fusion, standard deviation measures the comparison of the fused image. [13] High quality of standard deviation is obtained from the absence of noise.

3.3. Peak Signal To Niose Ratio (PSNR):

PSNR is your measure of ratio between the highest value of image and the size of the noise present in the image background. Normally PSNR is utilized to assess the reconstruction quality of fused image It suggests that the similarity between two images, the PSNR defined as:

$$PSNR = 10\frac{log_{10}(255)^2}{MSE}\ dB \quad (5)$$

$$MSE = \frac{1}{MN}\sum_{i=1}^{M}\sum_{k=1}^{N}(x_{j,k} - \tilde{x_{j,k}}) \quad (6)$$

MSE is the mean square error representing the difference between the original cover image sized N x N and the stego image sized N x N, and the x(j,k) and x'(j,k) are pixel located at the jth row the kth column of images x and x', respectively.

A large PSNR value means that the stego image is most similar to original image and vice versa. It is hard for the human eyes to distinguish between original cover image and stego image when the PSNR ratio is larger than 30dB.

The PSNR value our proposed work is shown in table 1 shown that biorthogonal wavelets value is 21.7275 which is the highest result and less than 30dB which mean the human eyes can recognition the different between the resulting images.

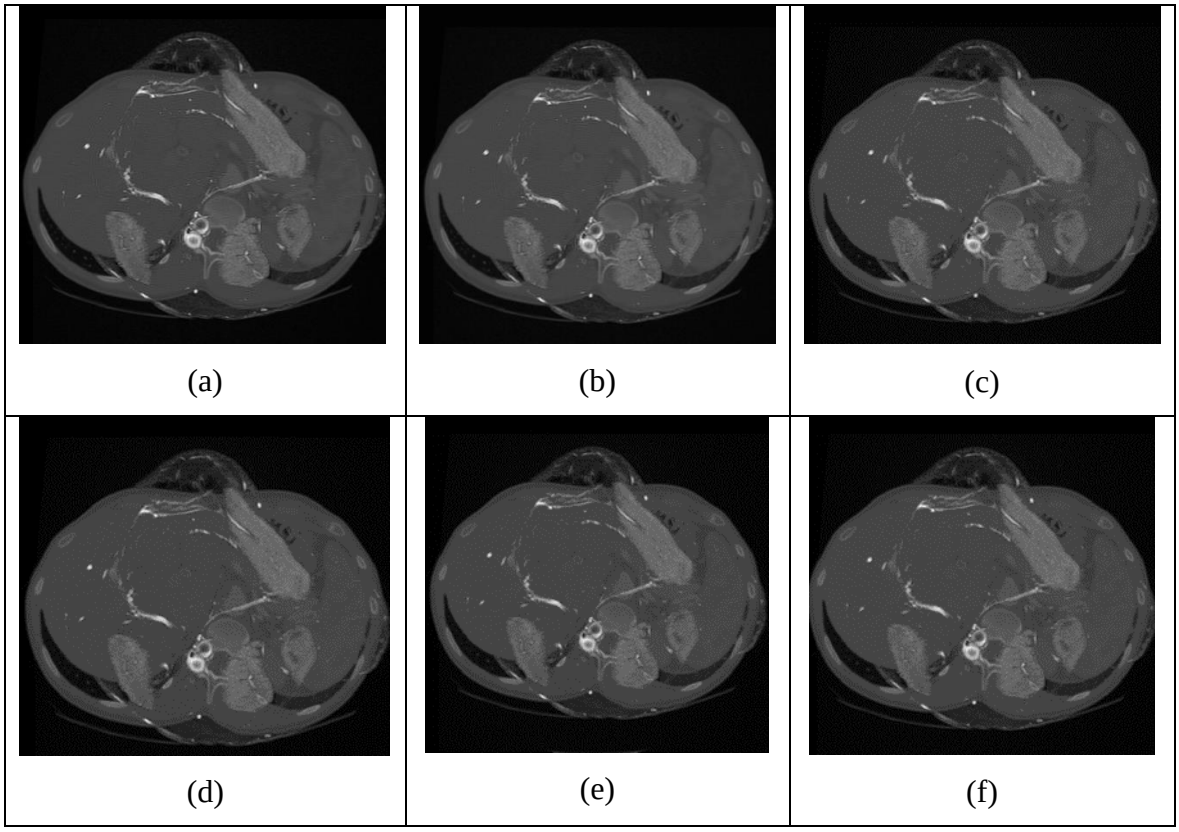

Figure (5): The image resulting from the application a): haar wavelet, b): application Discrete approximation of Meyer wavelet c): Daubechies Wavelets , d): Symlets wavelets, e): Biorthogonal wavelets, f): Reverse biorthogonal wavelets.

3.3 signal-to-noise ratio (SNR):

Quantification of this signal-to-noise ratio (SNR) is important in image acquisition processes in electron microscopy and other areas where the image is degraded by noise. Specifically, together with scanning electron microscopy (SEM), the tradeoff with image resolution is usually SNR. The definition of SNR varies based on this area [14]. In electrical engineering and statistical optics, it's defined as the power (variance) ratio between noise and signal, whilst at the electron microscopy that the square root of the amount is usually believed, it is given by

$$SNR = 10\ log_{10}\ \frac{\sigma_x^2}{\sigma_s^2} \qquad (7)$$

The SNR value in our proposed work is shown in table 1 shown that best result is biorthogonal wavelets compare with another wavelet.

Table 1: The result for merged image

Wavelet	Analyze Performance			
	Entropy	***PSNR***	***SD***	***SNR***
Haar	5.7060	21.1426	0.1423	7.9962
dmey	5.6236	21.2663	0.1410	8.1435
Db9	5.6523	21.1470	0.1424	8.0877
Conif1	5.6611	21.3843	0.1419	8.2876
Sym3	5.6857	21.2875	0.1414	8.2626
Bior1.3	5.7202	21.2949	0.1424	8.1692
Rbio3.1	5.7598	21.7265	0.1431	10.264

4. CONCLUSİONS

In this paper, the image fusion of MRI & CT medical images is done using fully automated wavelet transforms in MATLAB environment. 3The different fusion methods used are - Bior, coif, db, dmey, haar, rbio and sym. Further the comparative analysis of image fusion techniques helps in selecting the best fused image and therefore can provide better visualization of the fused image. The synthesized image has the qualities of both MRI & CT fused images. After the fusion of the images, it is concluded that the best synthesized image at level 1 with max-max method is Rbio3.1. Using the entropy method as a measuring assessment it is found that the resultant Rbio3.1 image has highest entropy (5.7598), so it is considered as the best fused image having the best quality, clarity and contrast. The worst entropy is obtained for dmey wavelet transforms. The best fused image is distinctively clear, easy to observe and thus, can be analyzed by the doctors for prescribing the proper medication for the shown ailment, in this thesis only (DWT) were investigated in Two-Dimensional. There are more tools like ridgelet transform bandelet transform grouplet transform etc. and we can use that need to be explored for image fusion and also, we can use Three-Dimensional.

REFERENCES

[1] A. Soma Sekhar, Dr.M.N. Giri Prasad., A Novel Approach of Image Fusion on MR and CT Images Using Wavelet Transforms, 3rd International Conference on Electronics Computer Technology, April (2011) 12 -86 DOI: 10.1109/ICECTECH.2011.5941881.

[2] H. H. Wang., A new multiwavelet-based approach to image fusion, Journal of Mathematical Imaging and Vision, 21 (2004) 177-180.

[3] Bernd Fischer, Jan Modersitzki., Curvature Based Image Registration, Journal of Mathematical Imaging and Vision, 18-1 (2003) 81–85.

[4] Peter Rogelj and Stanislav Kovacic., Similarity Measures for Non- Rigid Registration, Ministry of Science and Technology of the Republic of Slovenia, Research program, feb. (2001) 82-91.

[5] Ligia Chiorean, Mircea-Florin Vaida., Medical Image Fusion Based on Discrete Wavelet Transform Using Java Technology, 31st Int. Conf. on Information Technology Interfaces, June (2009).

[6] NEMA Publications., Digital Imaging and Communications in Medicine (DICOM), journal of digtal medcicin , Ver. 8.0 (2008) 8-16.

[7. https://www.dicomlibrary.com 12.11.2018 11:45.

[8] M. Hub, M.L. Kessler, and C.P. Karger., A stochastic approach to estimate the uncertainty involved in B-spline image registration, MedImg, 28-11 (2009) 1708–1716.

[9] J.V.Chapnick, M.E.Noz, G.Q. Maguire, E.L.Kramer, J.J.Sanger, B.A.Birnbaum, A.J.Megibow., Techniques of Multimodality Image Registration, Proceedings of the IEEE nineteenth Annual North East Bioengineeering conference, 18-19 March (1993) 221-222.

[10] J. B. Antoine Maintz and Max A. Viergever., A Survey of Medical Image Registration, Medical Image Analysis 2-1 (1998) 1-36.

[11] Brown Gottesfeld L., A survey of image Registration Techniques, ACM Computing surveys, 24-4 (1992) 325-376.

[12] Rahul S.Shınde, Altaaf O.Mulani., Bıomedıcal Image Fusıon Usıng Wavelet Transform, 2-10 (2015) 50-53.

[13] P. A. Van Den Elsen, E. J. D. Pol and M. A. Viergever., Medical image matching: a review with classification, IEEE Engineering in medicine and biology, march (1993) 26-39.

[14] Pelizzari CA, Chen GTY, Spelbring DR, Weichselbaum RR, Chen CT. Accurate 3-dimensional registration of CT, PET, and/or MR images of the brain. J Comput Assist Tomogr, Jan-Feb. (1989) 13-20.

Cumhuriyet Science Journal
CSJ

e-ISSN: 2587-246X
ISSN: 2587-2680

Cumhuriyet Sci. J., Vol.40-4 (2019) 946-957

Correlation of the entrainment factor with frother types and their mixtures in the column flotation

Hulya KURŞUN[1,*]

[1] *Department of Material and Metallurgical Engineering, Sivas Cumhuriyet University, TR-58140 Sivas, Turkey*

Received: 16.09.2019; Accepted: 11.11.2019 *http://dx.doi.org/10.17776/csj.620798*

Abstract. In flotation, entrainment is a mechanical mass transfer process and it is based on the changes depending on the establishment of linear relationship between water and solid recovery. The present paper presents results obtained in investigating the effect of frother mixture concentrations on the entrainment of fine particles' during the column flotation. The aim of the present study was to investigate more specifically the relationship between the recovery via entrainment of a range of different hydrophilic calcite particles. For this, to determine entrainment factor of fine particle was used a mixture of artificial ore (celestite/calcite; 1:1). The results showed that the frother mixtures had important effect on the grade and recovery, superficial air rate, gas hold-up and entrainment of fine gangue particles. Entrainment factors for frother mixtures were compared in flotation column. Kirjaveinen (1989) model was used for explaining the specific entrainment factor (Pi) of hydrophilic particles and it has been observed that this model supports the results of this study. This, together with the increased recovery, resulted in higher celestite grades of valuable mineral recovered to the concentrate when using the frother mixtures (Pine Oil+MIBC).

***Keywords*:** Entrainment, Column flotation, Frothers, Celestite, Calcite.

Sürüklenme faktörünün kolon flotasyonunda kullanılan köpürtücü tür ve karışımlarıyla ilişkisi

Özet. Flotasyonda, su ile taşınım mekanik bir kütle transfer işlemidir ve katı-su kazanımı arasında doğrusal bir ilişki kurulmasına bağlı değişim gösterir. Bu çalışmada, kolon flotasyonunda ince tanelerin sürüklenmesi üzerine farklı miktarlarda köpürtücü karışımlarının etkisi incelenmektedir. Çalışmanın amacı, hidrofilik kalsit tanelerinin sürüklenmesi yoluyla geri kazanım arasındaki ilişkiyi daha spesifik olarak incelemektir. İnce tanelerin sürüklenme faktörünü belirlemek için yapay cevher karışımı (selestit / kalsit; 1: 1) kullanılmıştır. Deneysel sonuçlar, köpürtücü karışımlarının tenör-verim, yüzeysel hava hızı, gaz tutunumu ve ince gang tanelerinin sürüklenmesi üzerinde önemli bir etkiye sahip olduğunu göstermiştir. Farklı tür ve miktarlarda köpürtücü karışımları için sürüklenme faktörleri, kolon flotasyonunda karşılaştırılmıştır. Hidrofilik tanelerin spesifik sürüklenme faktörünü (Pi) açıklamak için Kirjaveinen (1989) modeli kullanılmış ve bu modelin bu çalışmanın sonuçlarını desteklediği görülmüştür. Çamyağı + MIBC köpürtücü karışımı kullanıldığında, konsantrede verim artmış ve daha yüksek tenörlü selestit konsantresi elde edilmiştir.

***Anahtar Kelimeler*:** Su ile taşınım, Kolon flotasyonu, Köpürtücüler, Selestit, Kalsit

1. INTRODUCTION

In entrainment, particles suspended in the water between bubbles enter froth zone from the collection zone and are conducted to the concentrate. Both hydrophobic and hydrophilic mineral particles in pulp can experience entrainment. Entrainment is widely accepted to be

* Corresponding author. *Email address:* *hkursun@cumhuriyet.edu.tr, hlykursun@gmail.com*

the dominant mechanism of during enrichment of fine-sized ores, particularly in the size range below 45 μm. Entrainment starts in the pulp phase. Since entrainment has a harmful effect on the grade of the concentrate, a number of studies have been performed to understand entrainment mechanisms. Many researchers have developed models with an objective of predicting entrainment in a flotation cell. They have worked on understanding the factors affecting entrainment, the mechanisms, measurement techniques and the modelling [2-23]. There is a direct relationship between entrainment and water recovery, which is generally dependent on froth characteristics. Therefore, water recovery plays an important role in recovering gangue minerals by entrainment [3,10,24]. Wang et al. [25] commented the literature on flotation entrainment and both theoretical and empirical models that have been developed to simulate entrainment and explaining the various mechanisms of interest. Zheng et al. [26] and Kirjavainen [1,27] developed models to define and estimate the recovery of hydrophilic particles by entrainment. Kirjavainen [27] suggested a mathematical model for the degree of entrainment of hydrophilic particles in a continuous laboratory flotation system. Experiments were carried out using quartz and phlogopite minerals at different slurry densities with only frother added. The relationship between the water and the gangue recovery was defined for continuous flotation system at steady state by Kirjavainen [1,6,27] in Eq. (1):

$$P = W^{0.7} / (W^{0.7} + b\Psi\eta^{-0.5\Psi} m^{0.5\Psi-0.4}) \quad (1)$$

where P is the entrainment factor (the ratio of the recovery of gangue and water), W is the water recovery (kg/m^2 /s), m is the particle mass (pg), g is the slurry viscosity (mPas), Ψ is a dynamic shape factor, while b is a constant. Kirjavainen [6] can be replaced for batch flotation system in Eq. (2):

$$R_i = 1-exp(-P_i R_w) \ , \ P_i = ln(1-R_i)/-R_w \quad (2)$$

where R_i is the relationship between recovery of the ith gangue fraction, P_i is the entrainment factor that depends on the particle characteristics and process variables.

The entrainment process is affected by a number of factors in the pulp and froth during flotation. Among them; frother types and concentrations, superficial air rate, superficial feed rate, superficial wash water rate, air-hold-up, bias rate, collection and cleaning zone height, residance time, collector types and concentrations, etc. have been parameters. Many of these parameters have been studied by many researchers [1,5,6,27-38].

Kursun [39] presented a problem of entrainment in conventional and column flotation. The results demonstrated that the frother concentration and particle size had important effect on the grade and recovery, flotation time and fine gangue entrainment. Kursun [40] was defined that the frother types and concentrations and superficial air rates had significant effects on calcite and water recoveries and entrainment behaviour of calcite in column flotation. The results have shown that MIBC improved the recovery and grade of celestite concentrate and entrainment factor was obtained as the lowest for MIBC frother (celestite grade and recovery, 89.95%, 87.11%, entrainment factor (Pi: 0.365)) and 4 minute is determined as optimum residence time since the lowest entrainment factor has provided. Kirjaveinen [1] model was used for the determination of specific entrainment factor of hydrophilic particle in both studies [30,31].
Unlike the course of the study in Kursun 2017 [40], within paper presents results obtained in investigating the effect of frother mixtures (Pine Oil+MIBC, Pine Oil+Aerofroth 88, MIBC+Aerofroth 88) concentrations (ratio 1:1) on the entrainment factor. The effect of frothers on the degree of entrainment is important for selective flotation, but the mechanism causing the effect is still poorly known. The purpose of the present study should be maximum recovery with the minimum gangue contamination in the laboratuary type column flotation. Hence, determination of entrainment factors using only calcite (97.78% $CaCO_3$) and celestite (97.20% $SrSO_4$) ore mixtures in different frother mixtures were aimed.

2. EXPERIMENTAL

2.1. Materials and reagents

In the current study, in order to obtain accurate entrainment factor, entrainment tests were performed, under the identical operating conditions using MIBC (metil izobütil karbinol -$C_6H_{14}O$), Pine Oil (complex mixtures of monoterpene hydrocarbons (alpha, beta-pinene) and oxygenated monoterpenes (terpineol, borneol, bornyl acetate)), Aerofroth 88 (2-Ethylhexanol- $C_8H_{18}O$) and Pine Oil+MIBC, Pine Oil+Aerofroth 88, MIBC+Aerofroth 88 mixtures frothers. The minerals to the experiments, calcite and celestite were supplied from BMT Gypsum Co. (Sivas-Turkey) and Barit Mining Co.

(Sivas-Turkey), respectively (Table 1). A similar particle size distribution of the celestite and calcite as shown in Figure 1 was achieved by a ball mill grinding. Celestite samples were prepared to several particle size ranges (-106+75µm, 75+53µm, -53+38µm) by screening and calcite samples were screened to size fraction of -38µm.

Table 1. Chemical analysis of the samples [39-40]

	Component	%
Celestite	$SrSO_4$	97.20
	$CaSO_4.2H_2O_4$	2.32
	Others (Fe_2O_3+Al_2O_3+MgO)	0.48
Calcite	CaO	54.42
	LOI	43.36
	Others (MgO, Fe_2O_3, Al_2O_3, Na_2O, SO_3, K_2O, SiO_2<0.01)	2.22

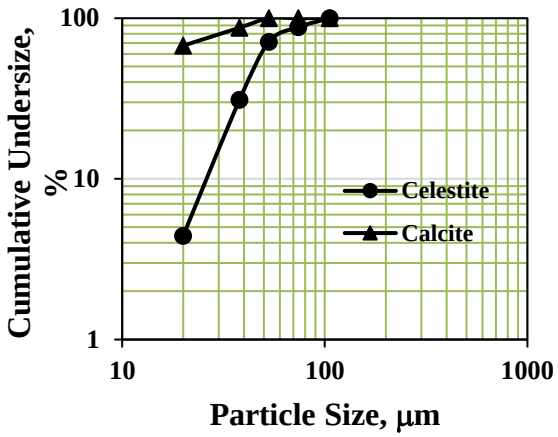

Figure 1. Particle size distributions of the celestite and calcite after grinding

NaOH (sodium hydroxide) was used to adjust the pH (WTW INO LAB 740, Germany) of the slurry to 10.0. The anionic collector used was Na-oleate (600 $g.t^{-1}$) and Pine Oil, MIBC and Aerofroth 88 were added to the pulp as frother. On the other hand, Pine Oil, MIBC and Aerofroth 88 were used as 40 $g.t^{-1}$, 80 $g.t^{-1}$, 120 $g.t^{-1}$, 160 $g.t^{-1}$, respectively. These reagents were prepared daily prior to the tests using distilled water. Table 2 shows the ranges of dosages for these reagents along with major operating parameters used of experiments.

Table 2. Operating conditions used in column flotation test [39-40]

Operating parameters	
pH	10.0
Pulp density (%)	20
Na-oleate ($g.t^{-1}$)	600
Frother dosage ($g.t^{-1}$)	40-80-120-160
Superficial air velocity ($cm.sec^{-1}$)	0.5-1.0-1.5-2.0
Superficial feeding velocity ($ml.min^{-1}$)	400
Superficial wash water velocity ($ml.min^{-1}$)	150

2.2. Entrainment tests

Entrainment tests using the fully liberated celestite and calcite were performed in column cell. The column flotation system consists of a plexiglas circular column 750 mm in height and 50 mm in a diameter, a conditioner 12.75 liter (300x240x200 mm) in volume, a flowmeter, two peristaltic pumps (Watson Marlow 323U/D, UK) for feeding and tailing exit, a compressor supplying air to the column. The column was mounted on a chassis, and a universal shower attached on the top was used as the washing system. A universal shower-type wash water system that is located from 20 mm above the top of the column. Wash water was introduced through a perforated plexiglas container situated just above the froth zone. Bubbles were produced using air spargers and a pump having a maximum pressure greater than 0.012 MPa with 1.8 rpm. The air feed to column was organized by a flow at different air rates. During the experiments, extra care was taken in order not to disturb the froth by the wash water added. The volume of the feed tank was five times the volume of the column. The feed to column was introduced from the upper section of the collection zone by pumping the slurry from a mixing thank that was agitated at 60 rpm (a mechanical stirrer-IKA-WERK RW 20 (Anke&Kunkel, Germany)). In order to obtain concentrates and tailing, certain period of time was allowed for the system to reach

steady state after testing the parameters. Tap water (pH: 7.8) was used in the experiments.
Bubble diameters were moderated by recording the bubbles for 40 sec. from the air-water phases (45 cm above the column base) using a camera (CANON EOS 5D-Mark II, Japan). Images were seized by illuminating the column and putting a black panel behind the wall. Camera was focused on midpoints of (both height and width) the front cross section of the column. Bubble diameters were measured on the milli-metric scale using a capture program running on the computer.

3. RESULTS and DISCUSSION

3.1. The effect of bubble diameters, superficial air rates and air-hold up on entrainment

In Figure 2, the variation of gas holdup with the superficial air rates using different frother types and mixtures (15 g.t^{-1}) is illustrated in a two-phase system (water/air). In the experiments, Pine Oil, MIBC, Aerofroth 88, Pine Oil + MIBC (1:1), Pine Oil + Aerofroth 88(1:1) and MIBC + Aerofroth 88 (1:1) were used as frother and frother fixed. The lowest value of gas holdup (ε_g: 3.70%) was provided by using Pine Oil at the superficial air rate of 0.5 cm.sec^{-1}, while the highest value (ε_g: 33.00 %) was achieved at the superficial air rate of 2.5 cm.sec^{-1} with the Aerofroth 88.
In the case of the use of frother mixtures, the the lowest value of gas holdup (ε_g: 4.6 %) was obtained by using Pine Oil+MIBC at the superficial air rate of 0.5 cm.sec^{-1}. On the other hand, the highest value (ε_g: 30.12 %) was reached at the superficial air rate of 2.5 cm.sec^{-1}. with the MIBC+Aerofroth 88 mixture. The gas hold-up was increased when superficial air rate were increased.

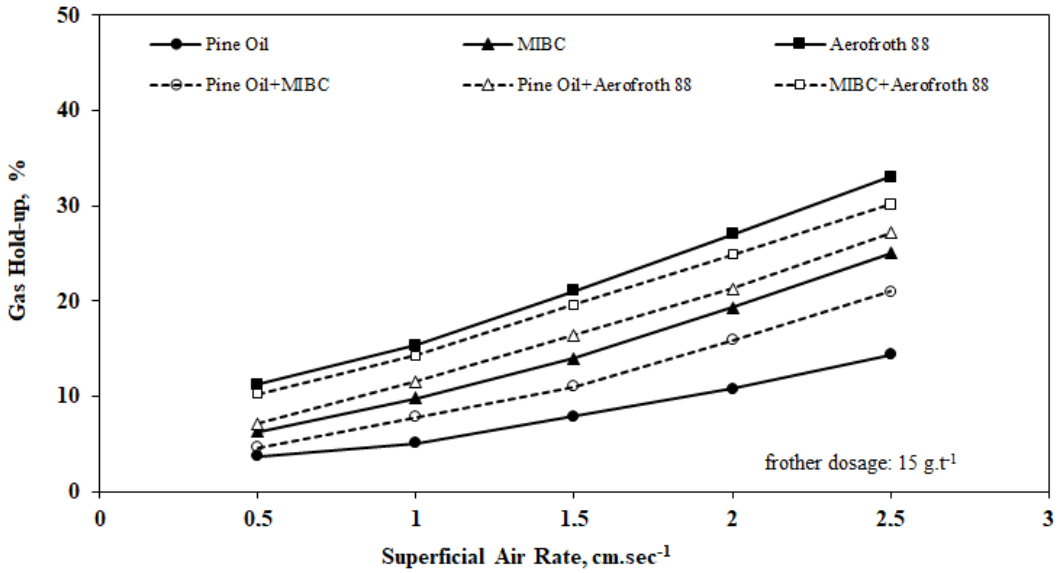

Figure 2. Variation of gas holdup with superficial air rate for different frother types and frother mixtures (1:1)

Three different frothers and mixtures were tested in this research: Pine Oil, MIBC, Aerofroth 88, Pine Oil+MIBC (1:1), Pine Oil+Aerofroth 88 (1:1) and MIBC+Aerofroth 88 (1:1). Variation of average bubble diameter with superficial air rate for the combinations of different frother types and frother mixtures were given in Figure 3.
For instance, at 15 g.t^{-1} frother concentration and 0.5 cm.sec^{-1} of superficial air rate with Pine Oil, MIBC and Aerofroth 88, the average bubble diameter was 1.26, 1.20 and 1.01 mm, respectively. When the air rate was increased to 2 cm.sec^{-1}, the average bubble diameter was decreased to 1.75, 1.68 and 1.40 mm for Pine Oil, MIBC and Aerofroth 88, respectively. On the other hand, the same situation was observed in the frother mixture. When the air rate was increased to 0.5 cm.sec^{-1}, the average bubble diameter was decreased to 1.22, 1.18 and 1.30 mm for Pine Oil+MIBC, Pine Oil+Aerofroth 88, MIBC+Aerofroth 88, respectively. 2.0 cm.sec^{-1} of superficial air rate with Pine Oil+MIBC, Pine Oil+Aerofroth 88, MIBC+Aerofroth 88 the average bubble diameter was 1.26, 1.20 and 1.01 mm, respectively.
In a two-phase system (water/air), bubble pictures photographed at different superficial air rates when using Pine Oil, MIBC, Aerofroth 88, Pine Oil+MIBC (1:1), Pine Oil+Aerofroth 88 (1:1) and

MIBC+Aerofroth 88 (1:1) as frother are illustrated in Figure 4.

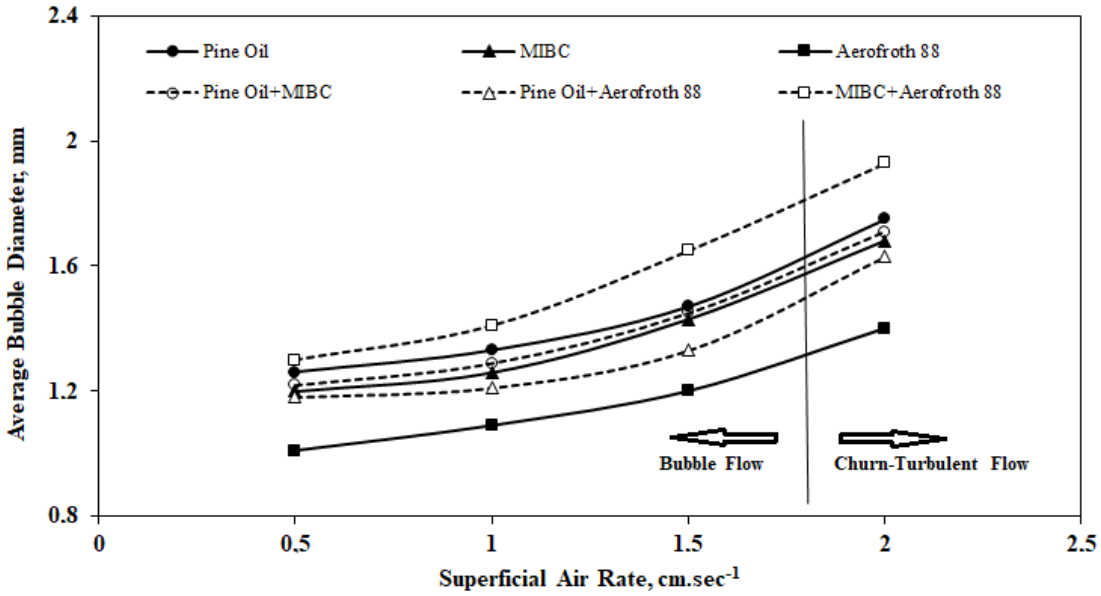

Figure 3. Variation of average bubble diameter with superficial air rate for the combinations of different frother types and frother mixtures (1:1) at frother concentration 15 g.t^{-1}

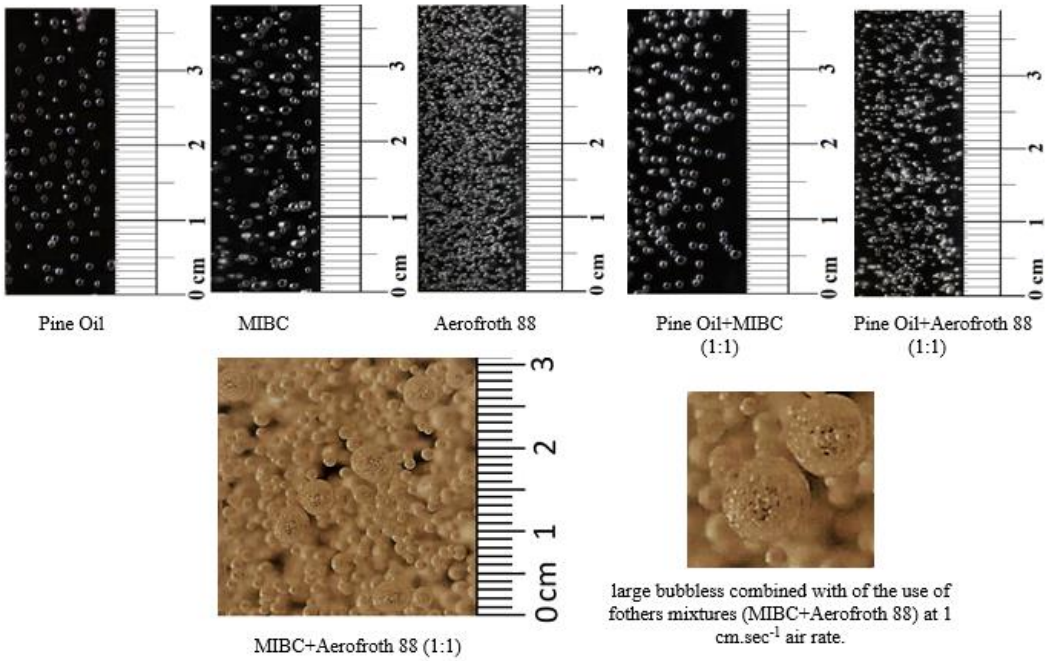

Figure 4. Bubble pictures photographed at different air rates when using Pine Oil, MIBC, Aerofroth 88 [40], Pine Oil+MIBC, Pine Oil+Aerofroth 88, MIBC+Aerofroth 88 as frother (1 cm.sec-1)

3.2. The effect of frother types-dosages and frother mixtures types-dosages on entrainment

The celestite and calcite used in these tests was fully liberated, and will therefore be recovered into the concentrate solely by entrainment. In a three-phase system (water/air/particle), the superficial air rates using different frother types, concentration, frother mixtures and flotation times is illustrated in Table 3 (a-b).

Table 3 (a-b). Entrainment factor and recoveries of celestite, calcite and water as a function of flotation time with various frother types-concentration and mixtures frother in column flotation (celestite (-106+38μm), calcite (-38μm))

Frother Concentration ($g.l^{-1}$)	Time (min)	Pine Oil						MIBC						Aerofroth 88					
		Recovery (%)			Grade (%)			Recovery (%)			Grade (%)			Recovery (%)			Grade (%)		
		Celestite	Calcite	Water	Celestite	Calcite	p_t	Celestite	Calcite	Water	Celestite	Calcite	p_t	Celestite	Calcite	Water	Celestite	Calcite	p_t
40	1	39.74	6.51	12.44	58.63	41.37	0.541	51.41	5.91	14.02	71.52	28.48	0.434	52.21	8.21	13.36	52.44	47.56	0.641
	2	42.11	8.84	14.83	61.24	38.76	0.624	54.80	8.78	20.63	73.24	26.76	0.445	56.68	10.36	15.07	54.92	45.08	0.652
	3	48.96	14.04	26.49	63.52	36.48	0.571	57.63	11.55	24.92	78.55	21.45	0.493	57.92	15.65	26.80	55.21	44.79	0.635
	4	52.21	16.79	35.76	66.11	33.89	***0.514***	67.36	12.07	33.81	76.82	23.18	***0.380***	65.80	19.21	34.24	57.83	42.17	***0.623***
80	1	62.41	11.25	21.13	71.88	28.12	0.492	75.52	9.21	23.41	81.41	18.59	0.413	73.51	14.05	21.57	57.50	52.50	0.702
	2	70.24	13.41	25.67	75.21	24.79	0.561	77.28	11.32	27.48	83.34	16.66	0.437	77.80	16.63	26.59	59.25	40.75	0.684
	3	74.11	17.20	33.96	79.12	20.88	0.519	83.48	13.33	35.51	83.25	16.75	0.403	79.21	20.18	34.94	59.92	40.08	0.645
	4	77.92	19.09	44.13	82.05	17.95	***0.480***	87.11	16.06	47.89	89.95	10.05	***0.365***	82.93	23.72	43.60	61.48	38.52	***0.622***
120	1	62.64	12.61	24.37	74.81	25.19	0.553	71.51	11.92	24.97	84.31	15.69	0.484	75.11	15.54	24.82	53.49	46.51	0.774
	2	64.73	15.26	28.95	75.24	24.76	0.572	72.93	13.78	28.63	81.12	18.88	0.518	77.28	17.99	27.65	54.66	45.34	0.761
	3	66.21	18.49	37.01	77.02	22.98	0.564	74.18	17.23	36.97	80.21	19.79	0.511	79.41	22.34	36.13	56.05	43.95	0.743
	4	70.38	23.23	48.86	78.20	21.80	***0.541***	78.82	21.74	49.21	84.51	15.49	***0.498***	80.24	25.88	45.86	56.98	43.02	***0.733***
160	1	66.44	15.94	26.02	65.74	34.26	0.694	73.04	15.52	30.81	79.61	20.39	0.547	77.64	29.41	42.27	59.41	40.59	0.824
	2	72.24	20.11	32.82	63.12	36.88	0.684	75.67	16.83	32.24	78.55	21.45	0.571	78.11	30.34	41.99	59.12	40.88	0.861
	3	72.09	21.74	39.32	62.83	37.17	0.678	76.41	20.37	38.11	79.14	20.86	0.598	79.86	33.05	46.12	56.95	43.05	0.870
	4	65.13	27.37	51.50	62.16	37.84	***0.621***	73.26	24.08	51.11	75.59	24.41	***0.539***	82.23	36.88	57.95	54.88	45.12	***0.794***

Constant Conditions; pulp density: 20%, collector concentration: 600 $g.t^{-1}$ Na-oleate, superficial feed rate: 400 $ml.min^{-1}$, superficial wash water rate: 150 $ml.min^{-1}$, superficial air rate: 1 $cm.sec^{-1}$

(a) Pine Oil, MIBC and Aerofroth 88 [39,40]

Frother Concentration ($g.t^{-1}$)	Time (min)	Pine Oil+MIBC (1:1)						Pine Oil+Aerofroth 88 (1:1)						MIBC+ Aerofroth 88 (1:1)					
		Recovery (%)			Grade (%)			Recovery (%)			Grade (%)			Recovery (%)			Grade (%)		
		Celestite	Calcite	Water	Celestite	Calcite	p_t	Celestite	Calcite	Water	Celestite	Calcite	p_t	Celestite	Calcite	Water	Celestite	Calcite	p_t
40	1	51.20	6.70	15.11	74.88	25.12	0.459	43.12	7.21	11.97	54.72	45.28	0.625	50.66	9.81	15.10	49.69	50.31	0.683
	2	57.48	8.25	17.19	75.29	24.71	0.501	49.72	10.41	17.96	56.88	43.12	0.612	55.21	13.77	21.44	51.88	48.12	0.691
	3	64.24	10.41	23.39	76.81	23.19	0.470	52.41	14.36	24.18	57.58	42.42	0.641	56.48	16.41	26.67	53.01	46.99	0.672
	4	70.13	11.24	35.49	77.30	22.70	***0.336***	58.88	19.51	35.99	59.72	40.28	***0.603***	66.71	21.44	32.40	53.31	46.69	***0,745***
80	1	67.88	7.51	18.46	84.59	15.41	0.423	60.41	9.41	17.20	49.77	50.23	0.574	70.51	12.24	17.56	44.72	55.28	0.743
	2	72.68	8.28	19.87	86.06	13.94	0.435	66.16	12.03	24.00	50.88	49.12	0.534	76.48	16.48	24.82	52.79	49.21	0.723
	3	85.10	11.63	30.18	89.49	10.51	0.410	69.84	16.05	30.20	55.82	44.18	0.579	81.14	23.48	35.96	53.06	46.94	0.744
	4	89.13	12.08	53.68	91.82	8.18	***0.239***	75.15	21.32	46.02	66.59	33.41	***0.521***	85.11	35.21	61.04	60.29	39.71	***0.721***
120	1	69.41	10.23	20.83	85.52	14.48	0.518	59.65	12.05	18.42	57.80	42.20	0.697	68.24	15.48	22.51	56.79	43.21	0.747
	2	72.11	11.02	22.50	83.59	16.41	0.519	63.51	17.72	27.59	56.90	43.10	0.707	70.83	24.48	37.39	55.72	44.28	0.751
	3	79.47	15.75	31.68	85.18	14.82	0.541	69.07	20.98	34.14	54.01	45.99	0.690	74.21	31.67	50.44	54.61	45.39	0.755
	4	83.71	22.31	55.37	87.34	12.66	***0.456***	73.04	28.80	49.75	64.21	35.79	***0.683***	79.07	38.77	65.76	55.49	44.51	***0.746***
160	1	70.99	11.95	22.36	81.38	18.62	0.569	56.21	16.45	25.03	60.22	39.78	0.718	69.47	21.07	29.12	58.19	41.81	0.812
	2	71.17	13.16	24.20	80.17	19.83	0.583	59.48	20.11	30.97	59.76	40.24	0.725	71.07	27.69	39.82	56.16	43.84	0.814
	3	74.08	19.41	35.32	82.06	17.94	0.611	67.77	23.48	35.83	54.93	45.07	0.747	71.98	36.78	56.82	53.79	46.21	0.807
	4	75.98	25.44	56.35	81.59	18.41	***0.521***	69.94	30.05	50.76	60.44	39.56	***0.704***	73.03	45.31	75.15	50.88	49.12	***0.803***

Constant Conditions; pulp density: 20%, collector concentration: 600 $g.t^{-1}$ Na-oleate, superficial feed rate: 400 $ml.min^{-1}$, superficial wash water rate: 150 $ml.min^{-1}$, superficial air rate: 1 $cm.sec^{-1}$

(b) Pine Oil+MIBC, Pine Oil+Aerofroth 88 and MIBC+Aerofroth 88

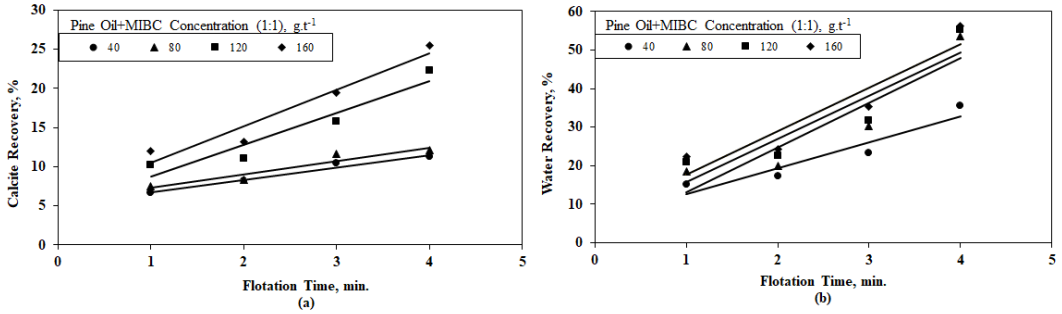

Figure 5(a-b). Calcite and water recoveries as a function of flotation time with various Pine Oil+MIBC concentration

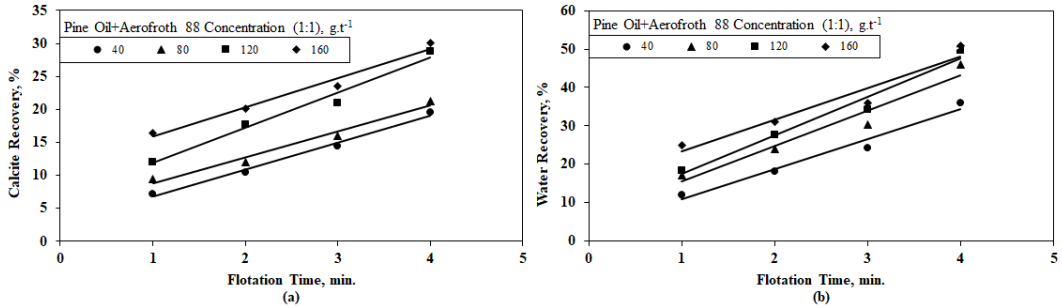

Figure 6(a-b). Calcite and water recoveries as a function of flotation time with various Pine Oil+Aerofroth 88 concentration

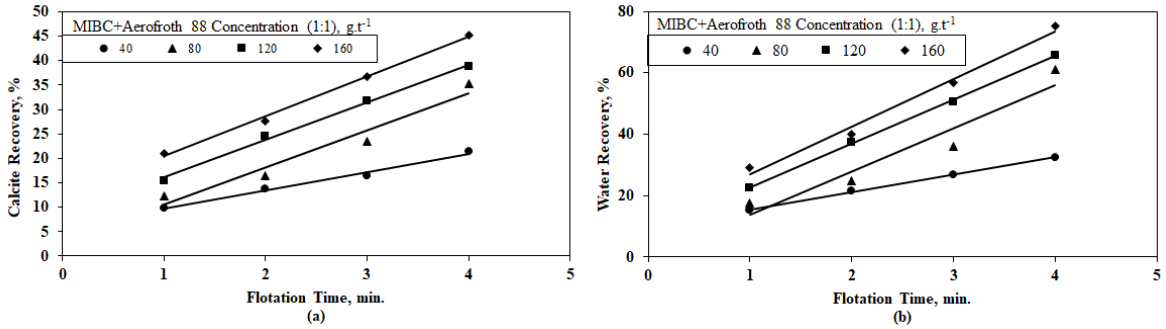

Figure 7(a-b). Calcite and water recoveries as a function of flotation time with various MIBC+Aerofroth 88 concentration

In general, calcite and water recovery were increased with increased frother concentration [39,40]. Since the recovery of fine gangue increases with water recovery, lower product grades were expected for 80 $g.t^{-1}$ Pine Oil, MIBC, Aerofroth 88, concentration. Above 80 $g.t^{-1}$ frother concentration, the celestite grade was decreased with increasing Pine Oil, MIBC, Aerofroth 88, Pine Oil+MIBC, Pine Oil+Aerofroth 88 and MIBC+Aerofroth 88 concentration. In the frother concentration 80 $g.t^{-1}$, the celestite grade and recovery (4 min) was reached high value using different frother types Pine Oil, MIBC, Aerofroth 88 (Pine Oil: 71.88% grade; 62.41% recovery, MIBC: 81.41% grade; 75.52% recovery, Aerofroth 88: 57.50% grade; 73.51% recovery). The same findings were also obtained in Pine Oil+MIBC,

Pine Oil+ Aerofroth 88 and MIBC+Aerofroth 88 frother mixtures (Pine Oil+MIBC: 91.82% grade; 89.13% recovery, Pine Oil+Aerofroth 88: 66.59% grade; 75.15% recovery, MIBC+Aerofroth 88: 60.29% grade; 85.11% recovery). As shown in Figure 8, the highest grade and recovery values

were obtained by using a mixture of Pine Oil+MIBC frother mixture at 80 $g.t^{-1}$.

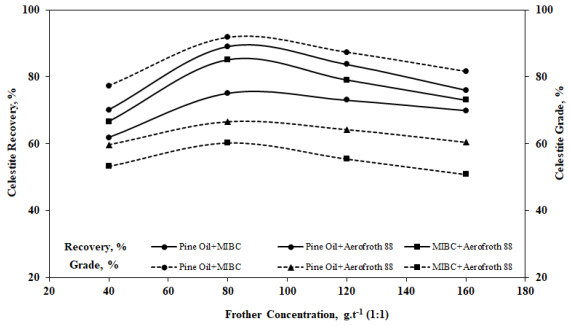

Figure 8. Celestite recoveries and grades as a function of flotation time with various frother type-concentration and frother mixtures (at 4 minutes of flotation time)

As can be seen (Figure 9), the entrainment factor increased with increasing concentration of both single frother (Pine Oil, MIBC, Aerofroth 88) and frother mixtures (Pine Oil+MIBC, Pine Oil+Aerofroth 88, MIBC+Aerofroth 88). When increasing the concentration of Pine Oil, MIBC and Aerofroth 88, from 40 $g.t^{-1}$ to 160 $g.t^{-1}$, the entrainment factor increased from 0.514 to 0.621, from 0.380 to 0.539 and from 0.623 to 0.794, respectively (Table 3a). For the same change in the concentration of PineOil+MIBC, Pine Oil+Aerofroth 88 and MIBC+Aerofroth 88, entrainment factor increased from 0.336 to 0.521, from 0.603 to 0.704 and from 0.745 to 0.803, respectively (Table 3b).

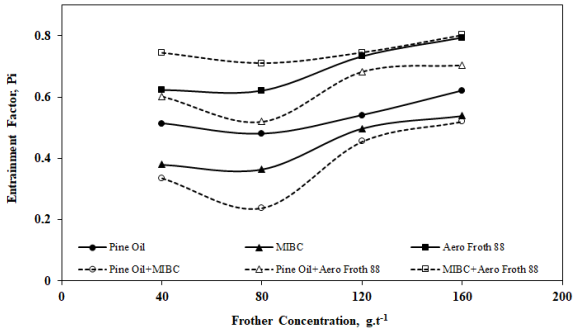

Figure 9. Variation of entrainment factor with various frother types-concentrations and frother mixtures (1:1)

The highest entrainment (ε_g: 0.711) factor value was obtained with MIBC+Aerofroth 88 while the lowest entrainment factor (ε_g: 0.239) was obtained by using Pine Oil+MIBC frother mixture at 80$g.t^{-1}$ (Figure 10). This was supported by the traced linear relationship between the entrainment factor and solid/water recovery acquired from the tests performed using different frother types, frother concentrations and frother mixtures.

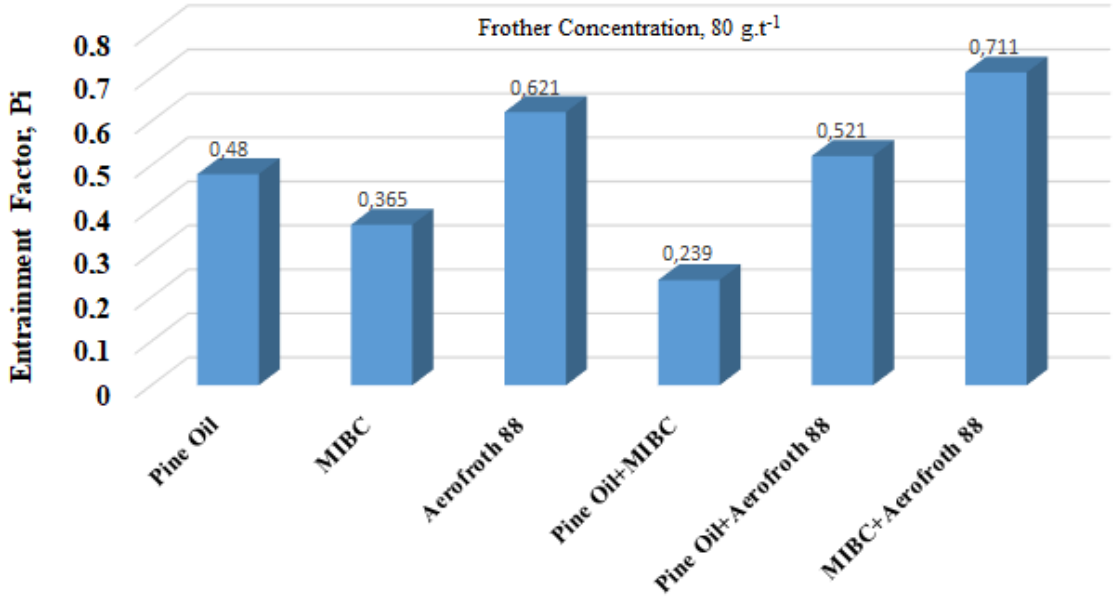

Figure 10. Variation of entrainment factor with various frother types and frother mixtures (1:1)

4. CONCLUSION

The column flotation experiment was performed using a mixture of liberated celestite as the valuable mineral and as the gangue mineral calcite, to indicate the primary factors affecting the entrainment factor. The obtained experimental results performed allow the following conclusions to be drawn:

. Superficial air rates, air hold-up and frother concentrate are three parameters that directly effective each other. When superficial air rate and the frother concentration were increased, the bubble diameter was decreased. Above a certain superficial air rate value, bubbly flow conditions were destroyed and turbulence flow conditions were formed producing large bubbles. When frother concentration was increased, bubble size was demonstrate to decrease importantly at the pulp/froth interface, which resulted in an increase in gas holdup (ε_g).

. In the MIBC Aerofroth 88 frother mixture, small bubbles collided in the pulp/froth interface and occured form large bubbles. In this case, bubbly flow conditions were lost and churn-turbulent flow conditions prevailed accompanied by large bubbles. This case, the amount of particles that can overcome the downward gravitational force to be recovered by the entrainment mechanism to the final concentrate increased, and the entrainment factor increased. As a result, the concentrate was contaminated by fine calcite minerals.

This was explained by the observed linear relationship between the entrainment factor and liquid velocity at the pulp/froth interface obtained from the tests performed using different frother types and concentrations. It has been seen that there is a linear relationship between calcite and water recoveries. Beside, the type, concentration and mixture of frother had exceptional effect on calcite. The recovery was increased, but the selectivity was decreased. The lowest entrainment factor was obtained with 80 $g.t^{-1}$ of frother concentration for Pine Oil+ MIBC frother mixture (εg: 0.239).

. Experimental results show that the entrainment factor varied significantly frother type, frother concentration and frother mixture. The recovery of calcite by entrainment was affected by Pine Oil+MIBC, Pine Oil+Aerofroth 88 and MIBC+Aerofroth 88 frother mixture. These results suggest that the frother types, frother concentration and frother mixtures at the flotation is a key factor which affects the entrainment factor. Kirjaveinen Model's [1] has been seen supported the results of this study.

REFERENCES

[1] Kirjavainen V.M., Application of a probability model for the entrainment of hydrophilic particles in froth flotation. Int. J. of Miner. Process., 27 (1) (1989) 63–74.

[2] Jowett, A., Gangue mineral contamination of froth, Brazilian J. of Chem. Eng. 2:5 (1966) 330–333.

[3] Johnson, N.W., MC Kee D.J., Lynch A.J., Flotation rates of non-sulphide minerals in chalcopyrite processes, Trans. of the American Inst. of Mining, Metall. and Petrol. Eng., 256 (1974) 204–226.

[4] Bisshop J.P and White M.E., Study of particle entrainment in flotation froths. Trans. of the Inst. of Mining and Metall. Section C: Miner. Process. and Extract. Metall., 85 (1976) 191– 194.

[5] Smith P.G. and Warren L.J., Entrainment of particles into flotation froths, Miner. Process. and Extract. Metall. Rev. 5 (1989), 123–145.

[6] Kirjavainen V.M., Review and analysis of factors controlling the mechanical flotation of gangue minerals. Int. J. of Miner. Process. 46 (1996) 21– 34.

[7] Savassi O.N., Alexander J.P., Franzidis J.-P., Manlapig E.V., An empirical model for entrainment in industrial flotation plants, Min. Eng., 11 (3) (1998) 243–256.

[8] Zheng X., Franzidis J.P., Johnson N.W., An evaluation of different models of water recovery in flotation, Miner. Eng., 19 (2006) 871–882.

[9] Yianatos J.B., Contreras F., Díaz F., Villanueva A., Direct measurement of entrainment in large flotation cells, Powder Technol., 189 (2009) 42–47.

[10] Yianatos J. and Contreras F., Particle entrainment model for industrial cells, Powder Technol. 197 (2010) 260–267.

[11] Konopacka Z. and Drzymala J., Types of particles recovery-water recovery entrainment plots useful in flotation research, Adsorption, 16 (2010) 313–320.

[12] Warren L.J., Determination of the contributions of true flotation and entrainment in batch flotation test, Int. J. of Miner. Process., 14 (1985) 33–34.

[13] Ross V.E., Flotation and entrainment of

particles during batch flotation, Miner. Eng., 3(3/ 4) (1990) 254–256.
[14] Wang L., Runge K., Peng Y., Vos C., An empirical model for the degree of entrainment in froth flotation based on particle size and density, Miner. Eng., 98 (2016) 187–193.
[15] Wang L., Peng Y., Runge K., The mechanism responsible for the effect of frothers on the degree of entrainment in laboratory batch flotation, Miner. Eng., 100 (2017) 124–131.
[16] Wiese J., Becker M., Yorath G., O'Connor C., An investigation into the relationship between particle shape and entrainment, Miner. Eng., 83 (2015) 211–216.
[17] Wiese J. and Harris P., The effect of frother type and dosage on flotation performance in the presence of high depressant concentrations, Miner. Eng. 36– 38 (2012) 204–210.
[18] Wiese J.G. and O'Connor C.T., An investigation into the relative role of particle size, particle shape and froth behaviour on the entrainment of chromite, Int. J. of Miner. Process., 156 (2016) 127–133.
[19] McFadzean B., Marozva T., Wiese J., Flotation frother mixtures: Decoupling the sub-processes of froth stability, froth recovery and entrainment, Miner. Eng., 85 (2016) 72–79.
[20] Little L., Wiese J., Becker M., Mainza A., Ross V., Investigating the effects of particle shape on chromite entrainment at a platinum concentrator, Miner. Eng., 96–97 (2016) 46–52.
[21] Lima N.P., de Souza Pinto T.C., Tavares A.C., Sweet J., The entrainment effect on the performance of iron ore reverse flotation, Miner. Eng. 96–97 (2016) 53–58.
[22] Neethling S.J. and Cilliers J.J.. The entrainment factor in froth flotation: Model for particle size and other operating parameter effects, Int. J. Miner. Process., 93 (2009) 141–148
[23] Mao Y., Peng Y., Bu X., Xie G., Wu E., Xia W., Effect of ultrasound on the true flotation of lignite and its entrainment behavior, Part A: Recovery, Utilization, and Environmental Effects, Energy Sources, 40 (8) (2018) 940–950
[24] Neethling S.J., Lee H.T, Cilliers J.J., Simple relationships for predicting the recovery of liquid from flowing foams and froths, Miner. Eng., 16 (2003) 1123–1130.
[25] Wang L., Peng Y., Runge K., Bradshaw D. A review of entrainment: Mechanisms, contributing factors and modelling in flotation, Miner. Eng., 70 (2015) 77-91.
[26] Zheng X., Johnson N.W., Franzidis J.P., Modelling of entrainment in industrial flotation cells: water recovery and degree of entrainment, Miner. Eng., 19 (2006) 1191–1203.
[27] Kirjavainen V.M., Mathematical model for the entrainment hydrophilic particles in froth flotation, Int. J. of Miner. Process., 35 (1992) 1–11
[28] Maachar A. and Dobby G.S., Measurement of feed water recovery and entrainment solids recovery in flotation columns, Canadian Metall. Quarterly, 31 (3) (1992) 167–172.
[29] Tao D., Luttrell G.H., Yoon R.H., A parametric study of froth stability and its effect on column flotation of fine particles, Int. J. Miner. Process., 59 (2000) 25–43.
[30] Liang L., Tan J., Li B., Xie G., Reducing quartz entrainment infine coalflotation by polyaluminumchloride, Fuel, 235 (2019) 150-157.
[31] Tuteja R. K., Spottıswood D. J., Mısra V. N., Column parameters: Their effect on entrainment in froth, Miner. Eng., 8 (1995) 1359–1368.
[32] Rahal K., Manlapig E., Franzidis J.-P., Effect of frother type and concentration on the water recovery and entrainment recovery relationship, Miner. & Metall. Process., 18(3) (2001) 138–141.
[33] Johnson N.W., A Review of the entrainment mechanism and its modelling in ındustrial flotation processes. Proceedings-Centenary of Flotation Symposium, Brisbane, 2005,5 Australia.
[34] Yianatos J., Contreras F., Díaz F., Villanueva A., Direct measurement of entrainment in large flotation cells, Powder Technol., 189 (2009) 42–47.
[35] Nguyen A.V. and Schulze H.J., Colloidal science of flotation. Surfactant Science Series, 118. Marcel Dekker Inc. New York, (2004) 709–775.
[36] Kursun H., Influence of superficial air rate on entrainment in column flotation, J. of Eng. and Earth Sci., 2(1) (2017) 8-16
[37] Runge K., Laboratory flotation testing – an essential tool for ore characterisation. Flotation plant optimisation: A metallurgical guide to identifying and solving problems in

flotation plants, 16. Australasian Inst. of Mining and Metall. Spectrum Series, Carlton, Vic, (2010) 55–173.

[38] Shabalala N.Z.P., Harris M., Leal Filho L.S., Deglon D.A., Effect of slurry rheology on gas dispersion in a pilot-scale mechanical flotation cell, Miner. Eng., 24 (2011) 1448–1453.

[39] Kursun H., Effect of fine particles' entrainment on conventional and column flotation, Particulate Sci. and Technol. 32 (2014) 251–256.

[40] Kursun H., The influence of frother types and concentrations on fine particles' entrainment using column flotation, Sep. Sci. and Technol., 4 (2017) 722–731.

Cumhuriyet Science Journal
CSJ

e-ISSN: 2587-246X
ISSN: 2587-2680

Cumhuriyet Sci. J., Vol.40-4 (2019) 958-966

Comparative Analysis of the Feature Extraction Performance of Augmented Reality Algorithms

Umut TOSUN [1*]

[1] *Alanya Alaaddin Keykubat University, Faculty of Engineering, Department of Computer Engineering, Alanya, TURKEY*

Received: 25.10.2019; Accepted: 21.11.2019 *http://dx.doi.org/10.17776/csj.638297*

Abstract. The algorithms that extract keypoints and descriptors in augmented reality applications are getting more and more important in terms of performance. Criterions like time and correct matching of points gain more impact according to the type of application. In this paper, the performance of the algorithms used to identify an image using keypoint and descriptor extraction is studied. In the context of this research, main criterion like the number of keypoints and descriptors that the algorithms extract, algorithm execution time, and the quality of keypoints and descriptors extracted are considered as the performance metrics. Same data stacks were used for obtaining comparison results. In addition to comparisons for a group of well-known augmented reality applications, the best performing algorithms for varying applications were also suggested. C++ language and OpenCV library were used for the implementation of the augmented reality algorithms compared.

Keywords**:** Augmented Reality, Image Processing, Key Point, Descriptor.

Artırılmış Gerçeklik Algoritmalarının Öznitelik Çıkarma Performanslarının Karşılaştırmalı Analizi

Özet. Artırılmış gerçeklik uygulamalarında kullanılan anahtar nokta ve öznitelik çıkaran algoritmalar performansları açısından önem teşkil etmektedirler. Uygulamanın türüne göre zaman, noktaların doğru eşleşmesi gibi kriterler önem kazanmaktadır. Bu makalede artırılmış gerçeklik uygulamalarında kullanılan ve bir resmi tanımak amacı ile resim üzerinde anahtar nokta ve öznitelik bulunması için uygulanan algoritmaların performansları incelenmiştir. Çalışma kapsamında, algoritmaların çıkarabildiği anahtar nokta sayısı, öznitelik sayısı, algoritmanın çalışması sırasında geçen süre, iki resmin eşleştirilmesi sırasında çıkartılan anahtar nokta ve özniteliklerin kaliteleri gibi ana kriterler incelenmiştir. Karşılaştırma sonuçlarının elde edilmesinde, aynı veri kümeleri kullanılmıştır. Bu çalışmada, iyi bilinen bir grup artırılmış gerçeklik algoritması incelenerek performanslarının karşılaştırılmasının yanında, farklı uygulamalar için kullanılabilecek algoritmalar hakkında da önerilerde bulunulmuştur. Artırılmış gerçeklik algoritmalarının karşılaştırılması için C++ dili ve OpenCV kütüphaneleri kullanılmıştır.

Anahtar Kelimeler Artırılmış Gerçeklik, Görüntü İşleme, Anahtar Nokta, Öznitelik.

1. INTRODUCTION

Augmented reality is the result of combining real data and computer generated sound, images, graphics and location information in the world we live in. [1]. In other words, it is the enrichment of reality with virtual data in computer environment [2, 3]. Various methods

* Corresponding author. *Email address:* *umut.tosun@alanya.edu.tr*

are used to recognize the actual images in the virtual environment. In order to recognize an image from the real world, there are qualified points on the image.

Descriptors of a feature are extracted with respect to some of the basic properties of this point (pixels) and other points around it. The dots on the image that have the feature value for that image are then used for virtual recognition of this image. Thus, in the virtual environment, a person has the values of the picture that they want to be recognized. The user can compare the picture that he has previously extracted and wanted to recognize with the other pictures taken from the camera. A “threshold" value should be determined during the matching phase. Otherwise, if the features taken from the camera and extracted from a picture that we do not want to recognize actually match the features of the picture that is intended to be recognized, a wrong match will be made. After setting the threshold value, it is possible to match the image to be recognized with the images taken from the camera. One of the methods used to extract key points and features on the image is the Oriented Fast and Rotated Brief (ORB) algorithm [4].

ORB is a binary algorithm. Within the scope of this paper, one of the reasons why ORB algorithm is compared with other methods is the opinion that it is faster than basic algorithms in the literature which extract some key points and features. The fact that ORB is based on binary descriptor and that pairing between two pictures happens while performing matching, supports the idea that it is faster than other methods.

In the literature, fps (frame per second), the number of key points extracted on one image, the number of features extracted on one image and the number of features matched correctly between the two images are used to compare the algorithms used in the extraction of key points and features [5-10]. This work will be based on the criteria mentioned. At the end of this study, the algorithms used for augmented reality an developed for the recognition of an image will be compared and their performance will be benchmarked. At the end of the study, the algorithms used for augmented reality and developed for the recognition of an image will be compared and their performance will be benchmarked. Moreover, some suggestions on the usage areas will be made.

2. COMPARED ALGORITHMS

Keypoint is a pixel that has a specific meaning on an image. In calculating the key point, various algorithms can be applied depending on the type of application. The ORB algorithm [4] uses the FAST [11, 12] algorithm in the background when calculating the key points on the image. The FAST algorithm basically calculates the key points by targeting the corners on the image. There may be many meaningless pixels on the picture. These insignificant pixels cause loss of performance within augmented reality. Therefore, it is important to identify and process key points. However, in some cases, key points may not make sense alone. Feature values should be calculated while matching the key points on the picture taken from the real world with the picture that is required to be recognized within the context of augmented reality. Thus, when pairing the two images, more accurate matches can be made with the feature values of the key points extracted from the objects to be recognized.

Feature can be defined as scalable and observable information obtained from the image [13, 14]. Feature extraction removes a significant set of features by discarding unnecessary information [15]. Feature extraction aims to reduce processing time by reducing the size of high-dimensional data. Using this data as it is in image processing applications increases processing complexity. Feature extraction is an important part of augmented reality applications in terms of application performance [16]. It aims to increase the recognition success by expressing the information of the pattern in the smallest dimension with the most prominent features [17]. Dimension reduction is performed by extracting unnecessary information that is irrelevant to the pattern and obtaining specific properties. This process aims to create a more selective set by

obtaining a subset of the feature set using different methods. The algorithms to be compared in this study will perform feature extraction. As a result of feature extraction, algorithms will be compared according to criteria such as time, correct matching, number of features.

2.1. Method Oriented Fast & Rotated BRIEF

Oriented Fast and Rotated Brief (ORB) [4], proposed by Ethan Rublee, Vincent Rabaud, Kurt Konolige, and Gary R. Bradski, is an effective algorithm alternative for SIFT [18] or SURF [19]. ORB is basically a combination of the FAST [11, 12] key point and BRIEF [20] descriptor, but it also incorporates many performance-enhancing modifications. Oriented FAST and rotated BRIEF techniques are interesting because of their good performance and low costs. ORB first finds key points using FAST, then applies the Harris corner measure to find the top N points between them [21]. ORB also uses the pyramid to produce multi-scale features. With the method called rBRIEF [22], it searches for all possible binary tests to find high variance, as well as averages close to 0.5, as well as non-correlated ones.

2.2. Scale-Invariant Feature Transform

Scale-Invariant Feature Transform (SIFT) [18] is an algorithm proposed by David Lowe for identifying and describing regional features in an image. The key points are extracted by the SIFT sensor and their descriptors are calculated by the SIFT descriptor. The SIFT sensor or SIFT descriptor can also be used independently of each other (such as calculating key points without descriptors or calculating descriptors without special key points) [23]. Along with linked descriptors, SIFT has created a new field of research on image-based matching and recognition with many application areas. Multi-image matching, object recognition, object category classification and robotics are among the known uses of this algorithm [24].

2.3. Speeded Up Robust Feature

The Speed Up Robust Feature (SURF) is a powerful regional feature sensor presented by Herbert Bay and friends, which can be used in computer image tasks such as object recognition or 3D reconstruction [19]. SURF is partly inspired by the SIFT [18] descriptor, but the standard versions of SURF work much faster than SIFT. It is also stated that SURF is more powerful than SIFT against different image transformations. SURF is based on the sum of 2D Haar small wave elements and enables the effective use of integral images [19]. In addition, SURF was advanced over SIFT by applying box filter approximation to the convolution kernel of the Gaussian derivative operator. Experiments on camera calibration and object identification also reveal that SURF has a large potential for computer vision applications [25].

2.4. Fast Retina Keypoint

Fast Retina Keypoint (FREAK) is a key point descriptor presented by Alexandre Alahi and friends. [26]. The creation of FREAK was inspired by the human visual system and the retina. The cascading of binary sequences is calculated by effective comparison of image densities on the retinal sampling pattern. In their experiments, Alexander Alahi and colleagues showed that FREAK was generally more powerful and faster in computing with lower memory load than SIFT [18], SURF [19] or BRISK [27]. FREAK is therefore considered to be a competitive alternative to existing algorithms, especially for embedded applications [27].

3. EXPERIMENTS AND RESULTS

In order to analyze the performance of the algorithms, a framework has been developed in Visual Studio 2012 using C ++ language and OpenCV library. This application can run the algorithms ORB [4], SURF [19], SIFT [18] and FREAK [26]. The application first reads a fixed image and extracts key points and features from that image. The key values and features of this image will then be used for comparison for each image (frame) taken from a video taken with the camera. In the next step, the application reads a video for use in comparing algorithms. The prepared video is a video of the first fixed picture taken from different heights and angles.

The prepared video is used separately for each algorithm. Thus, it was considered to obtain the correct values. After reading the prepared video, the application takes individual pictures (frames). The key points and feature values are extracted from these images (frames) as in the fixed image. These extracted feature values are then assigned to a matching function with the feature values extracted from the fixed image. This allows you to see if the features match correctly. The application calculates the duration of each function for all algorithms.

Figure 1. Fixed Image with Key Points Features Used in Testing

The image to be used as a fixed image is shown in Figure 1 and it is taken to video to be used in augmented reality subjects. In the testing phase and taken into the video is an image used in augmented reality subjects. The number of edges on the image, the plurality of curves, the richness of key points and features are the main reasons for the selection of said image.

Figure 2. Screen Shot Taken During Application Run

During the operation of the application, key points and features are extracted from the fixed picture (Figure 1) and the pictures are taken from the video (frame) to be given to the matching function. In addition, key points that provide the threshold value are shown (Figure 2). Moreover, the number of the picture (frame) taken from the video, the number of key points and features that the algorithm generates for that picture (frame), and the number of features matching the threshold value are shown. There are 576 images (frames) in the video used to compare the algorithms. The threshold values 50, 100, 120 and 150 were used in the test procedures. The bit-based features are included in the comparison process, and as a result, the fs below the threshold value are calculated. Features below the threshold value correspond to a more accurate comparison result. As the threshold value increases, the number of matching features increases for algorithms.

As can be seen from the results in Table 1, the SIFT algorithm is the longest-running algorithm when the threshold is 50. However, the SIFT algorithm also provides the most accurate matchings. ORB algorithm is the fastest working algorithm according to the results. However, in the matching of features, SIFT and SURF algorithms gave worse results. From the results, the FREAK algorithm is both relatively slow and has poor results in the feature matching phase. One of the main reasons why the SIFT and SURF algorithms are slower than the ORB algorithm is the time it takes to extract key points and features. In Figure 3, the application algorithm is run for threshold 50 and the slowest running algorithm is observed as SIFT. ORB is the fastest completing algorithm. While the SIFT algorithm takes 1.182 seconds, the ORB algorithm performs key point and feature extraction in an average of 0.016 seconds, or the SURF algorithm it is 0.172 seconds and for the FREAK algorithm it is 0.655 seconds. Figure 4 shows the key and feature extraction times of the algorithms for threshold 50. According to the results, while the fastest running algorithm is ORB, the slowest running algorithm is SIFT. Figure 5 shows that the SIFT algorithm is most prominent with matching. The SURF algorithm has the most features matching after SIFT. Because the threshold value is 50; while the ORB algorithm performed 0.458 matching in an average picture (frame), the FREAK algorithm performed 0 matching. As can be seen from the results in Table 2, when the threshold value is given 120, the algorithm that runs the slowest and performs the highest number of matches, such as the

results obtained at the threshold value 50, is SIFT.

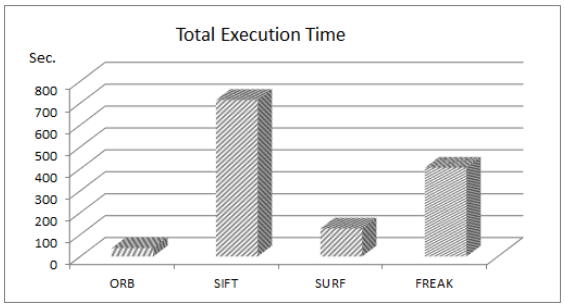

Figure 3: Total Execution Time for Threshold Value 50.

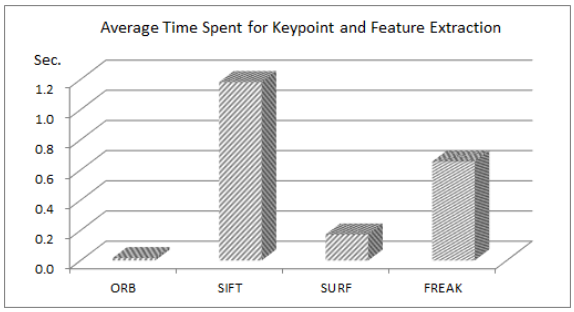

Figure 4: Average Time Spent for Key Point and Feature Extraction for Threshold Value 50

Table 1: Algorithm Performance for Threshold Value 50

	ORB	SIFT	SURF	FREAK
Base image keypoint size:	NULL	251	268	251
Base image time for keypoint extracting (seconds):	NULL	0.761	0.114	0.764
Base image descriptor size:	253	251	268	227
Base image time for descriptor extracting (seconds):	0.018	0.496	0.113	0.085
Base Image Total Feature & Descriptor Extracting Time (seconds):	0.018	1.257	0.227	0.849
Total Time (seconds):	38.120	714.094	127.543	404.836
Average Execute Time (seconds):	0.066	1.239	0.221	0.702
Total Feature Extracting Time (seconds):	NULL	393.397	52.961	371.75
Average Feature Extracting Time (seconds):	NULL	0.682	0.091	0.645
Total Descriptor Extracting Time (seconds):	9.259	287.975	46.550	5.821
Average Descriptor Extracting Time (seconds):	0.016	0.499	0.080	0.010
Total Feature & Descriptor Extracting Time (seconds):	9.259	681.372	99.511	377.571
Average Feature & Descriptor Extracting Time (seconds):	0.016	1.182	0.172	0.655
Total Match Time (seconds):	5.075	6.415	4.773	4.574
Average Match Time (seconds):	0.008	0.011	0.008	0.007
Total Draw Time (seconds):	7.216	9.625	6.895	5.895
Average Draw Time (seconds):	0.012	0.016	0.011	0.010
Average Match Size:	0.458	68.151	17.644	0

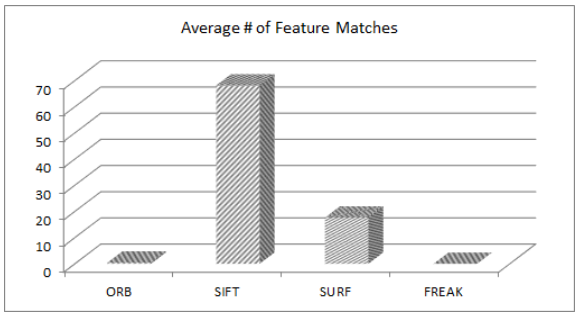

Figure 5: Average Number of Feature Matches for Threshold Value 50.

The ORB has more number of matches than SURF, according to the results observed at the threshold 50. ORB is seen to run faster than the other three algorithms. When matching numbers are compared, SURF has more feature matching numbers than other algorithms. FREAK was unable to match the feature in addition to running slowly. According to the results in the threshold value 50, the number of SURF algorithm matching features decreased. In Figure 6, the application algorithm threshold is run for 100 and the slowest running algorithm is observed as SIFT. ORB was the fastest completing algorithm. ORB completes the application in 38.541 seconds, while SIFT completes the application in 701.598 seconds (~ 11 minutes). For SURF, this time is 129.537 seconds, while FREAK finishes the application in 405.680 seconds. In order to obtain the results shown in Figure 7, the application worked with the threshold 100. SIFT takes an average of 1.159 seconds to extract key points and features from a picture (frame). This time directly affects the performance of the application. ORB is the fastest algorithm, as in the results with a threshold of 50, and takes an average of 0.015 seconds to extract key points and features from an image. SURF performs the processing in an

acceptable time of 0.169 seconds. FREAK, like SIFT, has been working for a long time to affect performance. In Figure 8, the application threshold is run for 100 and the features extracted by the algorithms are compared with the features extracted from the base image and divided by the total number of frames, the average feature matching numbers are obtained. SIFT demonstrates the advantage of slow operation here. SIFT obtained an average number of feature matching of 123.11 images from the end of the video. ORB and SURF have very close matches. The SURF gave results close to the threshold value 50, while ORB increased the number of feature matching from 0.458 to 18.946.

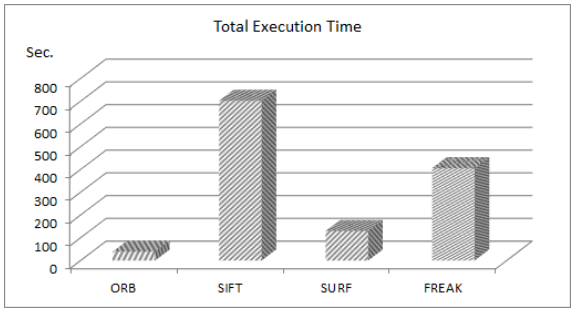

Figure 6: Total Execution Time for Threshold Value 100.

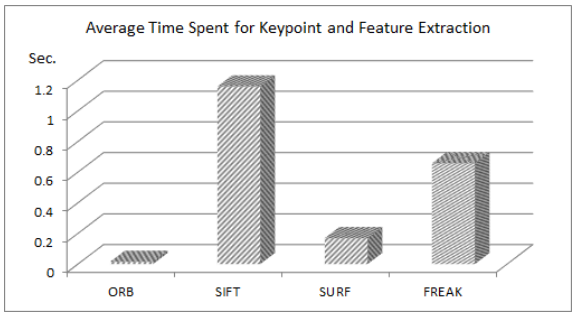

Figure 7: Average Time Spent for Key Point and Feature Extraction for Threshold Value 100

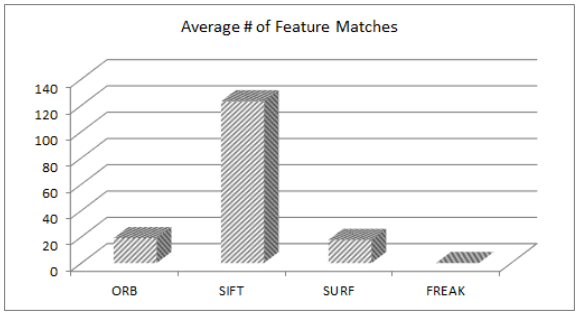

Figure 8: Average Number of Feature Matches for Threshold Value 100

As can be seen from the results in Table 2, when the threshold value is given 120, the slowest running algorithm is the SIFT as in the other threshold values. ORB, as the fastest running algorithm, has also increased the number of feature matchings obtained at threshold 100. FREAK was unable to match the feature in addition to running slowly. SURF completed the implementation within a reasonable time and again achieved an acceptable number of matches. In Figure 9, the application threshold is run for 120 and the slowest running algorithm is observed as SIFT. ORB is the fastest completing algorithm. ORB completed the application in 42,048 seconds, while SIFT completed the application in as long as 719.802 seconds (~ 11 minutes). SURF has completed the application in a suitable time of 125.222 seconds. FREAK completed the application in 423,282 seconds.

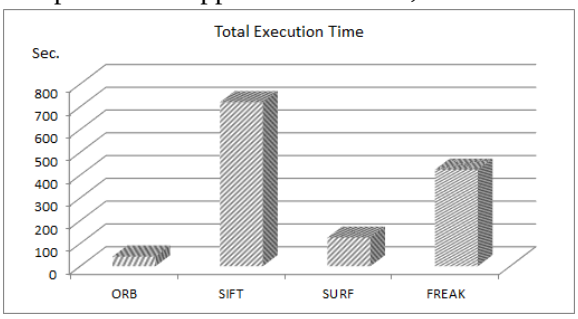

Figure 9: Total Execution Time for Threshold Value 120.

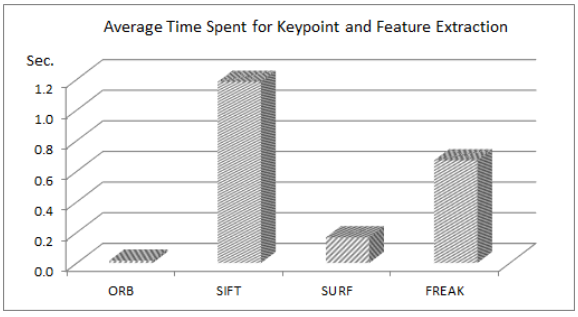

Figure 10: Average Time Spent for Key Point and Feature Extraction for Threshold Value 120

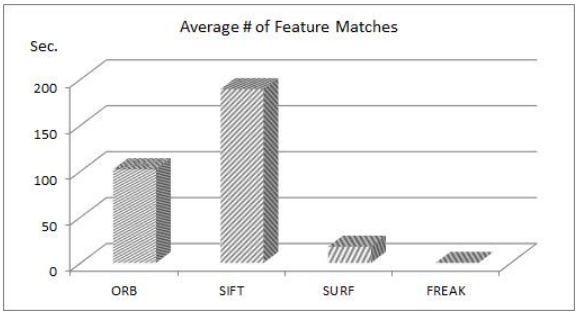

Figure 11: Average Number of Feature Matches for Threshold Value 120

Table 2: Algorithm Performance for Threshold Value 120.

	ORB	SIFT	SURF	FREAK
Base image keypoint size:	NULL	251	268	251
Base image time for keypoint extracting (seconds):	NULL	0.782	0.088	0.079
Base image descriptor size:	253	251	268	227
Base image time for descriptor extracting (seconds):	0.018	0.512	0.073	0.085
Base Image Total Feature & Descriptor Extracting Time (seconds):	0.018	1.294	0.161	0.864
Total Time (seconds):	42.048	719.802	125.222	423.282
Average Execute Time (seconds):	0.073	1.249	0.217	0.734
Total Feature Extracting Time (seconds):	NULL	390.273	50.569	380.600
Average Feature Extracting Time (seconds):	NULL	0.677	0.087	0.660
Total Descriptor Extracting Time (seconds):	9.429	291,465	45.786	5.875
Average Descriptor Extracting Time (seconds):	0.016	0.506	0.079	0.010
Total Feature & Descriptor Extracting Time (seconds):	9.429	681.738	96.355	386.475
Average Feature & Descriptor Extracting Time (seconds):	0.016	1.183	0.167	0.670
Total Match Time (seconds):	5.972	5.870	4.389	5.136
Average Match Time (seconds):	0.010	0.010	0.007	0.009
Total Draw Time (seconds):	11.876	15.504	7.010	6.026
Average Draw Time (seconds):	0.020	0.026	0.012	0.010
Average Match Size:	101.916	189.159	17.644	0.000

In Figure 10, the application is run and divided by the total number of frames (frames), the average time taken for a picture taken from the video is calculated for the key point and feature. While ORB completed key-point and feature extraction operations in a very small average time of 0.016, SIFT performed this operation on average for 1.183 seconds for an image, which means that an SIFT-powered application would run slowly. SURF completes key point and feature extraction in an acceptable average time of 0.167 seconds. FREAK completes key point and feature extraction in approximately 0.670 seconds. In Figure 11, the application is operated for the threshold 120. ORB increased the number of feature matches from 18.946 to 101.916 compared to the threshold 100. ORB removes an average of 253 features from an image and matches 101,916 of these features. SIFT can match an average of 189,159 features. SURF has maintained the 17,644 feature matching counts of threshold 100 for threshold 120. FREAK did not match any features. As the results in Table 3 show, when the threshold is set to 150, the slowest running algorithm is SIFT. ORB, as the fastest running algorithm, has increased the number of feature matches at threshold 120. FREAK has a very low number of features as well as slow operation. SURF completed the application within an acceptable time and matched the number of features obtained at the threshold 120.

Table 3: Algorithm Performance for Threshold Value 150.

	ORB	SIFT	SURF	FREAK
Base image keypoint size:	NULL	251	251	251
Base image time for keypoint extracting (seconds):	NULL	0.782	0.759	0.766
Base image descriptor size:	253	251	251	227
Base image time for descriptor extracting (seconds):	0.018	0.512	0.493	0.086
Base Image Total Feature & Descriptor Extracting Time (seconds):	0.018	1.294	1.252	0.852
Total Time (seconds):	49.391	719.802	699.518	412.129
Average Execute Time (seconds):	0.085	1.249	1.214	0.715
Total Feature Extracting Time (seconds):	NULL	390.273	371.997	378.546
Average Feature Extracting Time (seconds):	NULL	0.677	0.645	0.657
Total Descriptor Extracting Time (seconds):	9.241	291,465	286.577	5.875
Average Descriptor Extracting Time (seconds):	0.016	0.506	0.497	0.010
Total Feature & Descriptor Extracting Time (seconds):	9.241	681.738	658.574	384.421
Average Feature & Descriptor Extracting Time (seconds):	0.016	1.183	1.143	0.667
Total Match Time (seconds):	8,017	5.870	5.096	4.896
Average Match Time (seconds):	0.013	0.010	0.008	0.008
Total Draw Time (seconds):	18.369	15.504	18.826	6.104
Average Draw Time (seconds):	0.031	0.026	0.032	0.010
Average Match Size:	248.876	189.159	250.737	0.029

4. CONCLUSIONS

According to the results obtained, ORB is the fastest working algorithm. SIFT has the highest value in feature extraction criteria. Increasing the threshold value causes the fall of feature matching quality. In other words, increasing the threshold value causes the number of matching features generated by the algorithms to increase. As a result of this work, it was observed that SIFT and SURF performed more accurate feature matches. ORB has better results than the other three algorithms in terms of FPS (frame per second) time. In addition to being a slow algorithm like SIFT, FREAK is not successful in feature matching. Although SURF is relatively slow compared to ORB, it cannot provide feature matches such as SIFT. If it is an application where the simultaneous pictures taken from a camera are processed or pictures taken from a video are processed; extracting features for each image may cause a slowdown. If the desired number of features is matched on the picture, the feature may not be matched again on the next picture to be processed. Instead, features matched in the previous picture can be given to the follow-up phase depending on the type of application; thus, time can be saved as the follow-up phase runs faster than the feature matching phase. At this point, it is important to note that the key points that are processed as a result of feature matching during the follow-up phase are correctly matched key points. As a result, ORB works faster than the other three algorithms compared, and fewer features match with SIFT and SURF. Algorithm selection with respect to the application area of the augmented reality application to be implemented would be beneficial. For example, if a mobile application is to be realized, time will be an important criterion and ORB will give a good performance in this regard. SIFT or SURF will be more appropriate in high performance applications where time is not critical and correct feature matching is more important.

REFERENCES

[1] Graham M., Zook M., and Boulton A., Augmented Reality in Urban Places: contested content and the duplicity of code, Trans. Inst. Br. Geogr., 38-3 (2013) 464-479.

[2] Steuer J., Defining Virtual Reality: Dimensions Determining Telepresence, J. Commun., 42-4 (1992) 73-93.

[3] If You're Not Seeing Data You're Not Seeing, Wired.https://www.wired.com/2009/08/augmented-reality/. Retrieved October 25 (2009).

[4] Rublee E., Rabaud V., Konolige K., and Bradski G., ORB An Efficient Alternative to SIFT or SURF, Proceedings of 7th IEEE International Conference on Computer Vision, (2011) 2564-2571.

[5] Wagner D., Reitmayr G., Mulloni A., Drummond T., and Schmalstieg D., Pose Tracking from Natural Features on Mobile Phones, Proceedings of 7th IEEE and ACM International Symposium on Mixed and Augmented Reality, (2008) 125-134.

[6] Wagner D., Schmalstieg D., and Bischof H., Multiple Target Detection and Tracking with Guaranteed Framerates on Mobile Phones, International Symposium on Mixed and Augmented Reality, (2009) 57-64.

[7] Wagner D., Mulloni A., Langlotz T., and Schmalstieg D., Real-Time Panoramic Mapping and Tracking on Mobile Phones, Proceedings of IEEE Virtual Reality, (2010) 211-218.

[8] Klein G. and Murray D., Parallel Tracking and Mapping on a Camera Phone, Proceedings of 8th IEEE International Symposium on Mixed and Augmented Reality, (2009) 83-86.

[9] Ta D. N., Chen W. C., Gelfand N., and Pulli K., SURFTrac: Efficient Tracking and Continuous Object Recognition using Local Feature Descriptors, IEEE Computer Society Conference on Computer Vision and Pattern Recognition, (2009) 2937-2944.

[10] Takacs G., Chandrasekhar V., Tsai S., Chen D., Grzeszczuk R., and Girod B., Rotation-invariant fast features for large-scale recognition and real-time tracking, Signal Process. Image, 28-4 (2013) 334-34.

[11] Rosten E. and Drummond T., Machine learning for high-speed corner detection, European Conference on Computer Vision, (2006) 430-443 .

[12] Rosten E., Porter R., and Drummond T., Faster and better: A machine learning approach to corner detection, IEEE T. Pattern Anal., 32-1 (2010) 105–119.

[13] Trzcinski T., Christoudias M., Lepetit V., and Fua P., Learning Image Descriptors with the

Boosting-Trick, Advances in Neural Information Processing Systems, (2012) 1-9.
[14] Winder S. and Brown M., Learning Local Image Descriptors, IEEE Conference on Computer Vision and Pattern Recognition, (2007) 1-8.
[15] Brown M., Hua G., and Winder S., Discriminative Learning of Local Image Descriptors, IEEE T. Pattern Anal., 33-1 (2011) 43-57.
[16] Ke Y. and Sukthankar R., PCA-SIFT: A More Distinctive Representation for Local Image Descriptors, IEEE Computer Society Conference on Computer Vision and Pattern Recognition, (2004) 506-514.
[17] Simonyan K., Vedali A., and Zisserman A., Descriptor Learning Using Convex Optimisation, European Conference on Computer Vision (2012), 243-256.
[18] Lowe D. G., Distinctive Image Features from Scale-Invariant Keypoints, Int. J. Comput. Vis., 60-2 (2004) 91-110.
[19] Bay H., Ess A., Tuytelaars T., and Gool L.V., Speeded-Up Robust Features (SURF), Comput. Vis. Image Und., 110-3 (2008), 346-359.
[20] Calonder M,, Lepetit V, Strecha C, and Fua P. Brief: Binary Robust Independent Elementary Features, European Conference on Computer Vision, Heraklion, (2010) 778-792.
[21] Harris C. and Stephens M., A combined corner and edge detector, Fourth Alvey Vision Conference, (1988) 147-151.
[22] Huang W., Wu L. D., Song H. C., and Wei Y. M. "RBRIEF: a robust descriptor based on random binary comparisons". IET Comput. Vis,, 7-1 (2013) 29-35.
[23] Scale Invariant FeatureTransform, Scholarpedia.http://www.scholarpedia.org/article/SIFT. Retrieved October 18, 2013.
[24] Scale Invariant Feature Transform (SIFT), VLFeat. http://www.vlfeat.org/api/sift.html. Retrieved October 18, 2013.
[25] Schaeffer C., A Comparison of Keypoint Descriptors in the Context of Pedestrian Detection: FREAK vs. SURF vs. BRISK (2013).
[26] Alahi A., Ortiz R., and Vandergheynst P., FREAK: Fast Retina Keypoint, Proceedings of the IEEE Computer Society Conference on Computer Vision and Pattern Recognition, (2012) 510-517.
[27] Leutenegger S., Chli M., and Siegwart R. Y., BRISK: Binary Robust invariant scalable keypoints, Proceedings of the IEEE International Conference on Computer Vision, (2011) 2548-2555.

Cumhuriyet Science Journal
CSJ

e-ISSN: 2587-246X
ISSN: 2587-2680

Cumhuriyet Sci. J., Vol.40-4 (2019) 967-977

Investıgatıon of Natural Mycoflora and Aflatoxin Formation in Hazelnuts and Products

Z. Seba KESKIN [1], ***Nevcihan GURSOY*** [2]

[1] *Cumhuriyet University, Yildizeli Vocational School, Department of Food Technology Sivas / TURKEY*

[2] *Cumhuriyet University, Faculty of Engineering, Dept. of Food Engineering, Sivas/TURKEY*

Received: 08.11.2019; Accepted: 11.12.2019 *http://dx.doi.org/10.17776/csj.644503*

Abstract. In this study, natural mycoflora of 30 raw and 50 roasted hazelnut, 20 hazelnut paste and 50 inner membrane samples and their total aflatoxin contents were determined. In mycological isolations, 1.8-2.56% of *Aspergillus flavus* and 42.7-65.44% of *A. niger* were determined in the raw hazelnut samples. *A. flavus* (2.2-12.2%) and *A. niger* (33.3-74.5%) were also detected in roasted hazelnut, while the percentages of these microorganisms in hazelnut paste samples were 0-13.1% and 43.5-100.0%, respectively. The ratio of *A. flavus* and *A. niger* in inner membranes was found to be 2.6-16.2% and 44.6-89.4%, respectively. Aflatoxin analysis showed that the levels of aflatoxin were 2.11–10.03 ppb in raw hazelnut, 0.1–4.04 ppb in roasted hazelnut, 0.2-6.02 ppb in hazelnut paste samples and 0.7-38.2 ppb in inner membrane samples. While only one of the raw hazelnut, roasted hazelnut and hazelnut paste samples had toxin above the legal limit, 100% of the inner membrane samples showed different levels of aflatoxin contamination. Since there is no limitation in the Turkish Food Codex on hazelnut inner membrane, the amount of aflatoxin, which is higher than 10 ppb in 25 of the samples, was considered to be high contamination. Kruskal Wallis and Mann Whitney U analyses were used for statistical evaluation of the samples. There was a significant difference in aflatoxin formation and moisture content between the samples in different groups ($p < 0.05$).

***Keywords*:** Aflatoxin, hazelnut, hazelnut products, mycoflora.

Fındık ve Fındık Ürünlerinde Doğal Olarak Oluşan Mikoflora İle Aflatoksin Oluşumlarinin Araştirilmasi

Özet. Bu çalışmada, 30 çiğ, 50 kavrulmuş fındık, 20 ezme ve 50 iç zar örneğinde oluşan doğal mikoflora ve toplam aflatoksin içerikleri belirlenmiştir. Yapılan mikolojik izolasyonlarda çiğ fındıkta %1,8-2,56 Aspergillus flavus, %42,7-65,44 A. niger; kavrulmuş fındıkta %2,2-12,2 A. flavus, %33,3-74,5 A. niger; ezme örneklerinde %0-13,1 A. flavus, %43,5-100 A. niger; iç zarda ise %2,6-16,2 A.flavus, %44,6-89,4 A. niger belirlenmiştir. Aflatoksin analizlerinde çiğ fındıkta 2.11–10.03 ppb, kavrulmuş fındıkta 0,1–4,04 ppb, ezme örneklerinde 0,2-6,02 ppb ve iç zar örneklerinde ise 0,7-38,2 ppb seviyelerinde aflatoksin içerikleri saptanmıştır. Çiğ fındık, kavrulmuş fındık ve ezme örneklerinin sadece 1'inde yasal sınırın üzerinde toksin içeriği bulunurken, iç zar örneklerinin % 100' ünde değişik seviyelerde aflatoksin bulaşıklığı bulunmuştur. Fındık iç zarı ile ilgili Türk Gıda Kodeksinde bir sınırlama olmadığı için örneklerin 25' in de 10 ppb 'den yüksek olan aflatoksin oluşumları yüksek bulaşıklık olarak değerlendirilmiştir. Çalışılan örneklerin istatistikî değerlendirmelerinde Kruskal Wallis ve Mann Whitney U analizleri kullanılmıştır. Farklı gruplardaki örnekler arasında aflatoksin oluşumu ve nem içerikleri arasındaki değişim istatistiki açıdan önemli bulunmuştur ($p<0.05$).

***Anahtar Kelimeler*:** Aflatoksin, fındık, fındık ürünleri, mikoflora.

* Corresponding author. *Email address:* *ngursoy@cumhuriyet.edu.tr, ngursoy2@gmail.com*

1. INTRODUCTION

Hazelnut (*Corylus avellana* L.) forms the basis for the more important commercial cultivars and is belonging to *Betulaceae* family. The hazelnut (*Corylus avellana* L.) forms the more important commercial cultivars. *C. maxima* and *C. colurna* (Turkish hazel) are also common others. Hazelnut is grown in the Blacksea Region of Turkey, especially in Trabzon, Ordu, Giresun and Akçakoca. Although vary depending on the year, Turkey ranks the first in the world with approximately 600 thousand tonnes of hazelnut production [1].

Hazelnut is a food rich in proteins, lipids, carbohydrates, vitamins, minerals, dietary fibers, tocopherols, phytosterols and phenolic compounds [2,3]. Monounsaturated fatty acids (especially oleic acid) and polyunsaturated fatty acids in hazelnut have been reported to have beneficial effects on human health [3]. Hazelnut oil has been found to reduce cholesterol levels in the blood [4]. Hazelnut contains tocopherols, phytosterols, squalene and phenolic compounds that help prevent chronic diseases such as cancer and cardiovascular diseases [5,6].

There are biological, chemical and microbiological factors limiting hazelnut production. The most important microbiological factors limiting hazelnut production are fungal contamination and aflatoxins, one of the metabolites produced by these fungi. Aflatoxins are secondary metabolites produced by *Aspergillus* species. To date, more than 20 different aflatoxins have been reported. However, B_1, B_2, G_1, G_2 were reported to be four naturally occurring main forms. *A. flavus* produces only AFB_1 and B_2, while *A. parasiticus* produces AFB_1, B_2, G_1 and G_2 [7-9].

Aflatoxins produced by *Aspergillus* spp. in field conditions, transportation, processing and storage can be found in oilseeds such as nuts, pistachios, peanuts, almonds, sunflowers, in cereals and cereal products, pulses, spices, milk, dairy products, meat, meat products and animal products such as eggs [10-12].

Aflatoxins have been reported to have several effects on human and animal health such as mutagenic, carcinogenic, teratogenic (embryonal damage), tremorgenic (problems of tremor and reflex loss), hemoralgic (tissue and organs bleeding problems), dermatitic (skin lesions), hepatoxic (liver damage), nephrotoxic (kidney system damage), and neurotoxic (nervous system damage) [13-15]. Aflatoxins are known to be the most effective hepatocarcinogen in many animal species. In many countries, aflatoxins are included in the class 1A carcinogens by the International Organization for Cancer Research, since there is a positive correlation between consumption of aflatoxin-contaminated food and an increased risk of liver cancer [16].

The maximum limits of aflatoxins in many foodstuffs have been established and published in each country. In order to protect public health, importing countries, especially the European Union countries, aim to reduce the legal values of aflatoxins to zero in risky products. To this end, aflatoxin B_1 limit in many countries has been reduced from 5 ppb to 2 ppb and the total aflatoxin (B_1+B_2+G_1+G_2) in hazelnuts has been reduced from 10 ppb to 4 ppb (Commission Regulation EC No 194/97). In the Turkish Food Codex, the total aflatoxin content in hazelnut and its products is determined to be 10 ppb and Aflatoxin B_1 content is maximum 5 ppb [17,18].

As mentioned above, although vary depending on the year, Turkey ranks first in the world with approximately 600 thousand tonnes of hazelnut production [1]. In addition, Aflatoxin contamination is one of the most important problems in hazelnut and hazelnut products. Due to the aflatoxin values in nuts exported by Turkey are sometimes above the legal limits, these products are rejected by the countries, which leads to huge economic losses. Additionally, producers and industrialists are struggling economically, Turkey's reputation in foreign trade is damaged and marketing problems arise.

After the occurrence of aflatoxin, which is a problem in food all over the world, they cannot be controlled [19-21].Therefore, the most effective method for the formation of aflatoxins produced by fungi is to harvest, dry, store and process food under conditions that reduce the risk of contamination and limit the development of fungi. These conditions can only be achieved by determining the natural mycoflora that is formed in the product and can cause toxin formation.

In this study, it was aimed to determine the naturally occurring mycoflora in raw hazelnut,

roasted hazelnut, hazelnut paste and hazelnut inner membrane and to investigate the total aflatoxin formation in these products.

2. MATERIALS AND METHODS

2.1. Supply of Hazelnut Samples

The samples used in the study were obtained from various factories and retail stores in Trabzon, Ordu, Giresun and Akçakoca regions where hazelnut production is intense in the Blacksearegion. In the sampling, raw hazelnut (n = 30), roasted hazelnut (n = 50), hazelnut paste (n = 20), and inner membrane (n = 50) samples were used. The hazelnut samples were provided immediately after harvest, the inner membrane samples were obtained during the drying period and the hazelnut paste samples were provided during the processing stages of the product. Samples were brought to the laboratory under appropriate conditions and kept in labelled cloth bags and refrigerated at 4 °C until tested.

2.2. Determination of Moisture Content of Samples

The moisture content of the hazelnut, hazelnut paste and membrane samples used in the study was determined by a precision balance and halogen lamp moisture analyzer according to the method reported by Bakker [22]. 5.0 ± 0.1 g of raw and roasted hazelnut samples were taken and shredded in hand blender and moisture contents were determined at 140 °C. In order to determine the moisture content of hazelnut membrane and hazelnut paste samples, 1 g of each sample was weighed directly without any process and evaluated according Özkaya [23] equation (1).

$$\%\text{Moisture content: } \frac{M_1 - M}{M_1 - M_0} \quad (1)$$

M_0: Weight of continer (Tare) (g)
M: Weight of the container and sample after drying
M_1 : Weight of sample with container

2.3. Mycological Isolations

Raw hazelnut, roasted hazelnut and inner membrane samples were sterilized with 2.0% (v/v) NaOCl solution and washed with distilled water. After surface sterilization, of dried hazelnut, roasted hazelnut and inner membrane samples, hazelnut paste samples were added directly to Potato Dextrose Agar (PDA). After surface sterilization was performed, raw hazelnut, roasted hazelnut and inner membrane samples were dried and then planted in PDA while surface sterilization process was not applied for the cultivation of hazelnut paste samples. A total of 100 plantings were made for each sample using 10 petri dishes. Cultivated petri dishes were incubated at 24 °C for 4-5 days and thus colony development was ensured. At the end of incubation, the fungal colonies were differentiated based on macroscopic criteria such as size, colour, surface or overhead development, and colonies showing different growth were purified by classifying as *Fusarium* (F1, F2,…), *Aspergillus* (A1, A2, …) and *Penicillium* (P1, P2,…).

After purification, single spore isolation was made on water and Czapek Dox Agar. Single spore isolates were incubated at 25 °C for 7 days by transferring them to a suitable growth medium. Cultures were examined under microscope during the incubation and general morphological definitions were made, colony number and characteristics were recorded.

Specific diagnostic keys have been used for the fungi species identified intensively as a result of mycological isolations. While the diagnostic keys developed by Raper and Fennel [24] and Samson and Pitt [25] is used for the identification of *Aspergillus* species, *Penicillum* species were identified according to the diagnostic keys of Samson et al. [26] and Pitt [27]. In identifying *Fusarium* and other species, diagnostic key developed by Barnett and Hunter [28] was used.
In species identification of fungi; growth rates at certain temperatures (colony diameter and properties), overhead mycelium formation (colour and structure), the presence or absence of chlamidospores, sporodosium development, fialitic properties, conidial cap (color and shape), conidial sequencing, colony colours, presence or absence of sclerotes, and presence of macro and micro conidia were evaluated.

2.4. Aflatoxin Analysis

CD-ELISA (Competitive Direct Enzyme-Linked Immuno Sorbent Assay) method was used to investigate the total amount of aflatoxin in raw hazelnut, roasted hazelnut, inner membrane and hazelnut paste samples. 5 different aflatoxin standards were used in CD-ELISA at 0, 1, 2, 4 and 8 ppb levels. Samples were prepared and extracted according to the procedure of Neogen Veratox®. CD-ELISA results were obtained by reading at 650 nm in a microwell reader. Veratox Software for Windows, Log/Logit and Single Test Format v3.02 software were used to calculate the toxin values in ppb.

3. RESULTS AND DISCUSSION

Moisture measurement analyzes were carried out to determine how moisture content of raw hazelnut, roasted hazelnut, inner membrane and hazelnut paste affect natural mycoflora and aflatoxin formation in these samples.
The moisture content of samples obtained from Trabzon, Ordu, Giresun and Akçakoca regions are given in Figure 1.

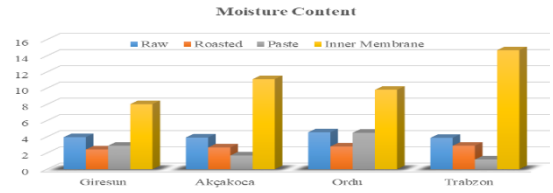

Figure 1. Moisture content of samples obtained from different regions

As can be seen from Figure 1, the moisture values of the raw hazelnuts were determined as 3.88-4.56%. It is recommended that the maximum moisture content in raw hazelnuts should be max. 4.5% [29]. It was observed that the moisture values of our samples were close to or higher than the recommended maximum value. Aluç and Aluç [30] found the moisture values of 186 Akcakoca, 177 Ordu and 160 Giresun raw hazelnut samples to be 4.2-6.8%. According to meteorological data, the rainfall of the 4 regions is approximately 61.6-75.9 mm per year. Samples of raw nuts with the highest moisture content were obtained from Ordu region. This is due to the fact that the average annual rainfall in the Ordu region is generally higher than the other three regions.

As a result of mycological isolation of raw hazelnut, roasted hazelnut, hazelnut paste and inner membrane samples, *Aspergillus* species were observed as the most dominant fungal ones. Natural mycoflora determined as a result of mycological isolations in samples obtained from different regions is presented in Table 1 and Figure 2. *Aspergillus* and *Penicillium* species are predominant in the studies conducted on the determination of raw and roasted hazelnut mycoflora, however, *Rhizopus*, *Fusarium*, *Cladosporium*, *Trichothecium*, *Mucor*, *Alternaria* and *Trichoderma* species have also been reported to be isolated [31, 32]. No studies have been found in the literature on the determination of mycoflora in hazelnut paste and inner membrane samples.

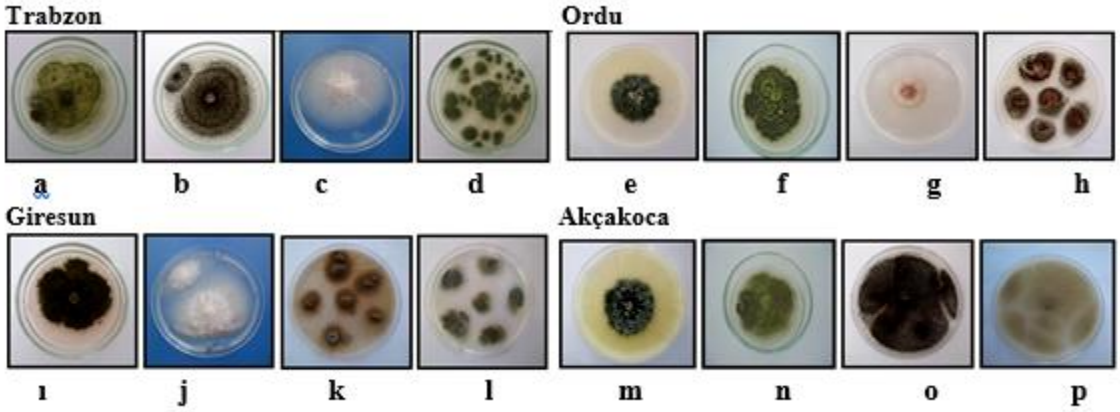

a. *A. flavus* from raw nuts; **b.** *A. niger* from roasted nuts; **c.** *Fusarium* spp. from hazelnut butter; **d.** *Penicillium* spp. from the inner membrane; **e.** *Trichoderma* spp. from raw nuts; **f.** *A. flavus* from roasted hazelnuts; **g.** *Fusarium* spp. from hazelneut butter; **h**. *A. niger* isolated from the inner membrane **ı.** *A. flavus* from raw nuts; **j.** *Fusarium* spp. from roasted hazelnuts; ***k.****Trichoderma* spp. isolated hazelnut butter; **l.** *Penicillium* spp. isolated from inner membrane; **m.** *Tricoderma* spp. from raw nuts; **n.** *A. flavus* from roasted hazelnuts; ***o***. *A. niger* from hazelneut butter; **p.** *Tricoderma* spp. from the inner membrane.

Figure 2. Isolated fungal species from sample groups.

Table 1. Natural mycoflora determined as a result

Regions	Sample Type	Fungus Species	% Isolation	Regions	Sample Type	Fungus Species	% Isolation
Trabzon	Raw	*Aspergillus*	68.0	Ordu	Raw	*Aspergillus*	63.0
		Penicillium	19.2			*Penicillium*	23.3
		Rhizopus	12.8			*Rhizopus*	9.4
	Roasted	*Aspergillus*	57.8			*Fusarium*	2.6
		Penicillium	26.6			*Trichoderma*	1.7
		Fusarium	8.4		Roasted	*Aspergillus*	44.5
		Alternaria	4.6			*Penicillium*	33.5
		Rhizopus	2.6			*Fusarium*	16.5
	Butter	*Aspergillus*	50.3			*Rhizopus*	5.5
		Penicillium	43.5		Butter	*Aspergillus*	51.0
		Fusarium	6.2			*Penicillium*	20.6
	İnner Membrane	*Aspergillus*	60.6			*Rhizopus*	18.0
		Penicillium	33.0			*Fusarium*	10.4
		Rhizopus	4.0		İnner Memb.	*Aspergillus*	95.0
		Trichoderma	1.4			*Penicillium*	4.4
Giresun	Raw	*Aspergillus*	45.0			*Rhizopus*	0.6
		Penicillium	21.0	Akçakoca	Raw	*Aspergillus*	54.2
		Rhizopus	21.0			*Penicillium*	14.6
		Fusarium	13.0			*Rhizopus*	14.6
	Roasted	*Aspergillus*	78.5			*Fusarium*	8.3
		Penicillium	17.5			*Trichoderma*	8.3
		Fusarium	4.0		Roasted	*Aspergillus*	45.2
	Butter	*Aspergillus*	63.7			*Rhizopus*	27.0
		Penicillium	23.7			*Penicillium*	18.3
		Trichoderma	10,0			*Fusarium*	9.5
		Rhizopus	2,0		Butter	*Aspergillus*	81.3
		Fusarium	0,6			*Penicillium*	18.7
	İnner Membrane	*Aspergillus*	4.8		İnner Membrane	*Aspergillus*	85.1
		Penicillium	34.4			*Penicillium*	9.3
		Trichoderma	12.2			*Trichoderma*	4.7
		Rhizopus	5.6			*Rhizopus*	0.9

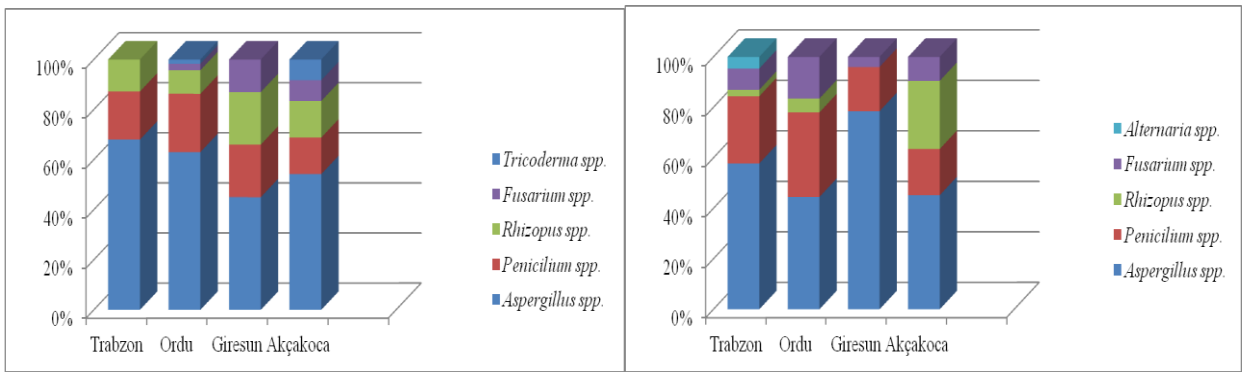

Figure 3. Fungus genus isolated from raw and roasted hazelnut samples.

Mycoflora in raw hazelnut was determined to be 45-68% of *Aspergillus* spp., 14.6-23.3% of *Penicillium* spp., 9.4-21% of *Rhizopus* spp., 2.6-13.0% of *Fusarium* spp., and 1.7-8.3% of *Trichoderma* spp. These ratios were found to be as follows in the mycoflora of roasted hazelnuts: 44.5-78.5% *Aspergillus* spp., 17.5-33.5% *Penicillium* spp., 2.6-27.0% *Rhizopus* spp., 4.0-16.5% *Fusarium* spp., 0.0-4.0% *Alternaria* spp. (Figure 3).

Various studies on the determination of natural microflora in raw and roasted hazelnuts yield similar results to the present study. In these studies, although *Aspergillus* and *Penicillium* species were dominant, *Rhizopus*, *Fusarium*, *Cladosporium*, *Trichothecium*, *Mucor*, *Alternaria* and *Trichoderma* species were also isolated [31-34]. *Aspergillus* spp. was found to be high in natural mycoflora of raw and roasted hazelnuts in many studies [35-37].Other fungi genus and their proportions isolated from raw nuts are as follows: 12.8-23.3% *Rhizopus* spp., 9.4-19.2% *Penicillium* spp., 2.6-13% *Fusarium* spp. and 1.7-8.3% *Trichoderma* spp. According to a study carried out by Demir et al. [38] on 30 raw hazelnut samples, the most commonly isolated fungi genus have been reported as follows: 2.2- 100.0% *Aspergillus* spp., 4.0-67.4% *Penicillium*, 2.0-62.0% *Rhizopus*, 2.0-82.0% *Mucor* and 2.0-56.0% other fungus genera. Simsek et al. [39], identified 96.6% *Aspergillus* spp., 93.3% *Penicillium*, 96.6% *Rhizopus* and 83.3% *Mucor* in 30 hazelnut samples obtained from Giresun. It is thought that the reason of high observation of the *Aspergillus* spp. in many of our samples is that the hazelnut was exposed to fungal contamination in the tree and during harvest. Furthermore, this indicates that although the product is harvested early and the shell forms a protective layer, there is a risk of contamination from cracks that may occur during harvest. In addition, high moisture content of hazelnut growing areas is one of the important factors that promote the development of *Aspergillus* spp.

According to our literature search could ascertain, no study is available on natural mycoflora formed in hazelnut inner membrane and hazelnut paste. However, it is thought that the data obtained from this study will serve as an example for other scientific studies in the future. As can be seen from Figure 4, 47.8-95.0% *Aspergillus* spp., 4.4-34.4% *Penicillium* spp., 1.4- 12.2% *Trichoderma* spp., and 0.6-4.0% Rhizopus spp. was determined in the inner membranes of hazelnuts samples collected from 4 regions. Unidentified fungi species were ignored. From hazelnut paste samples, 50.3-81.3% *Aspergillus* spp., 18.7-43.5% *Penicillium* spp., 2.0-18.0% *Rhizopus* spp., 0.0-10.0% *Trichoderma* spp. and 0.6-10.4% *Fusarium* spp. were isolated.

Although *Aspergillus* spp. species that can synthesize aflatoxin in hazelnut paste samples are different according to regions, they have been isolated and identified as the most dominant species in the present study by 50.3-81.3%. *Penicillium*, *Rhizopus*, *Fusarium* and *Trichoderma* strains were isolated in 18.7-43.5%, 2.0-18.0%, 0.6-10.4% and 0.0-10.0%, respectively in mycoflora of hazelnut paste samples.

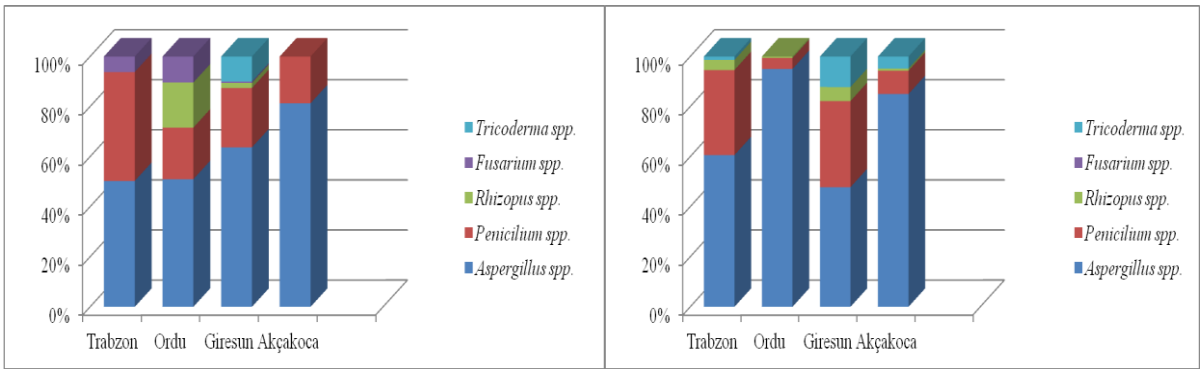

Figure 4. Fungus genus isolated from hazelnut paste and inner membrane samples.

The high rate of *Aspergillus* spp. species in most of our samples suggests that hazelnut is exposed to fungal contamination in the tree and during harvest.

This is because the development of *Aspergillus* spp. species in shelled hazelnuts starts on the surface of the shell when it is still in the tree, and it can increase during the contact of the product with the soil and harvesting. *Aspergillus* spp. are not seen in shelled hazelnuts that come into contact with the ground, while *A. flavus-parasiticus* develops in the hazelnut which is damaged in the outer shells [31]. This is because the hard shell of hazelnut is a good protector against fungal contamination and bacteria.

50% of the total 150 raw hazelnuts, roasted hazelnuts, hazelnut paste and inner membranes, aflatoxin contamination was found to be at levels of 0.1-38.2 ppb. Aflatoxin levels of 2.11-10.03 ppb were determined in 9 of 30 raw hazelnut samples and only one sample had aflatoxin content above the legal limit. Aflatoxin contamination (14.0%) and aflatoxin levels (0.1-4.04 ppb) were below the legal limit in roasted hazelnut samples (Table 2).

Table 2. Toxin contents and contamination rates determined in the samples

Sample	Number of Samples	Aflatoxin (ppb)	Contaminated Samples	Exceeding Legal Limit	% Contamination
Raw	30	2,11-10,03	9	1	30
Roasted	50	0,1-4,04	7	-	14
Hazelnut Butter	20	0,2-6,02	9	-	45
Inner Membran	50	0,7-38,2	50	25	100

As a result of statistical evaluations between the moisture contents and aflatoxin formation of 4 different hazelnut samples obtained from different regions, the relationship between moisture content and aflatoxin formation was found to be significant (p<0.05) (Figure 5).

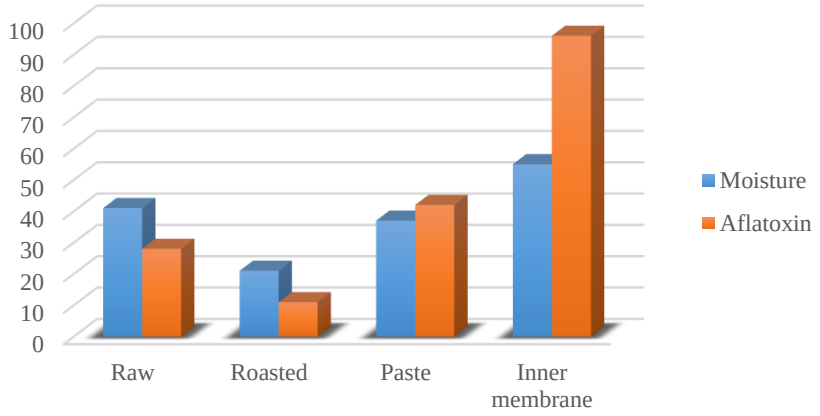

Figure 5. The relationship between moisture content and aflatoxin formation.

While the amount of aflatoxin was found to be 30% in the studied hazelnut samples, in only one of the samples obtained from 4 regions, total aflatoxin levels exceeded 10 ppb, which is the legal limit of aflatoxin determined by the Turkish Food Codex. Aycicek et al. [40] have studied the total aflatoxin levels in raw hazelnuts. According to this study, only one of 51 raw hazelnut samples has been reported to exceed this legal limit. Especially in raw hazelnut samples, high moisture content and therefore aflatoxin content were detected in high rainfall areas, indicating that climatic data play an important role. Aluç and Aluç [30] determined the

levels of aflatoxins in raw nuts obtained from Akçakoca, Ordu and Giresun. In 10 of 186 lots raw nuts from Akcakoca region B_1 = 2.66-75.08 ppb, total = 4.77-78.93 ppb, 20 of 160 lots raw nuts from Giresun region B_1 = 2.17-75.68 ppb, total = 4.34-150, 08 ppb, and 16 of 177 lots raw nuts from Ordu region B_1 = 2.1-29.44 ppb, total = 3.61-135.51 ppb aflatoxin contamination. Due to the high rainfall in the regions where raw hazelnuts are grown, factors such as high moisture values and the fact that hazelnuts are not fully developed while in the tree cause aflatoxin formation. In addition, mistakes made during the production, processing and storage stages lead to an increase in the amount of aflatoxin.

Aflatoxin was determined in 7 of the 50 roasted hazelnut samples and total amount of aflatoxin was between 0.1-4.04 ppb. The amount of aflatoxin found in the samples was found to be below the legal limit specified in the Turkish Food Codex. Heperkan [31] has investigated the mycotoxins in foods and their importance in terms of our country. In this study, 140 samples obtained from Ordu, Giresun and Tirebolu in Blacksearegion were examined and aflatoxin was determined in 5 of 25 hazelnut samples. Deabes and Al-Habib [34] reported that *Aspergillus* species, which are capable of producing aflatoxin, were predominant in mycoflora of hazelnut samples and aflatoxin levels were found to be between 41-55 ppb.

Aflatoxin content was found to be 14.0% in roasted hazelnut samples. This value was found to be lower than in raw hazelnut. Raw nuts are more risky in terms of aflatoxin, while roasted nuts are more stable [41]. The reason for this is that some fungi in the mycoflora become ineffective and the moisture content decreases as a result of heat treatments applied to roasted hazelnuts. Because fungal contamination is more common due to the high rate of free water required for the development of fungi. In addition, as the fat content of the products increases, the rate of mold and aflatoxin increase [42].

In a study, aflatoxin levels were investigated in hazelnuts. *Aspergillus* species capable of producing aflatoxin in the mycoflora of hazelnut samples analyzed have been reported to be predominant and aflatoxin levels vary between 41-55 ppb [34].

In a study investigating natural mycoflora and aflatoxin contamination in 25 raw and 25 roasted hazelnut samples, aflatoxin contamination was reported in 33 (66%) of 50 hazelnut samples at 0.1–155 ppb levels. In this study, aflatoxin formation above the legal limit was determined at 14.2-155 ppb levels in 2 raw and 6 roasted hazelnut samples [32].

Baltacı et al. [43], have collected samples during 3 years from companies exporting raw and roasted hazelnuts. According to the results of this study,

aflatoxin levels were found to be between 0.02-78.98 ppb in 3188 samples. It was determined that 3147 of these samples had aflatoxin below the legal limits and 41 of them were well above the legal limits.

The amount of aflatoxin was found to be 100% in hazelnut inner membrane. It is noteworthy that aflatoxin levels reach a high rate of 0.7-38.2 ppb. However, since there is no limitation of aflatoxin in the inner membrane in Turkish Food Codex, our samples could not be evaluated in this respect. Hazelnut membrane is a thin and brown perisperm layer that completely encapsulates the hazelnut grain and is released as a by-product during roasting process. The antioxidant capacity of hazelnut membrane is high and it is also considered as dietary fiber [44,45]. In the Blacksearegion, hazelnut inner membrane is used for different purposes such as animal feed and soil fertilizer. The absence of a legal limitation for aflatoxin contamination in the hazelnut membrane is highly risky for the health. Therefore, it is thought that it should be controlled with legal restrictions. While studies have been conducted to determine whether the hard shell protects the hazelnut against fungal contamination and thus aflatoxin formation, there is not enough work on the inner membrane. However, in a study by Özer [46] the aflatoxin content of the membrane was examined after roasting and peeling of the hazelnuts. In addition to natural contaminated hazelnuts, hazelnuts were artificially contaminated with *Aspergillus flavus* to contain aflatoxin at levels 10 and 20 ppb. According to the data obtained from the study, roasting, manual separating, mechanical separating and membrane peeling were found to reduce aflatoxin contamination and Aflatoxin B_1 content in hazelnuts. Aflatoxin B_1 level before the first roasting process was 11.28 ppb. this value was found to be 11.11 ppb after roasting. This value decreased to 0.23 ppb after peeling of the membrane. In the membrane, Aflatoxin B_1 (12.71 ppb) was reported to be higher than hazelnut. It has been reported that aflatoxin is concentrated in the membrane and damaged hazelnuts and the average reduction in aflatoxin contamination after operations is reported to be 98%.

Aflatoxin levels of 0.2-6.02 ppb were determined in 9 of 20 hazelnut paste samples used in the study. Although the rate of aflatoxin contamination in the samples was 45%, none of them exceeded the legal limit specified in the Turkish Food Codex (max.5 ppb for aflatoxin B1, max. 10 ppb for total aflatoxin). Vural et al. [47] examined 180 hazelnut paste samples consumed in Istanbul in terms of aflatoxin B_1 and total aflatoxin and found that 6.59% of the samples exceeded the legally acceptable maximum level. Günşen and Büyükyörük [48] reported that there were an average of 1076.5 ± 194.4 ppb aflatoxin B_1 in 25 cocoa hazelnut paste obtained from various markets in Bursa. Yu et al., [49] reported that the majority of aflatoxins are better produced by fungi in glucose, fructose-containing media. It is thought that hazelnut, which is a good substrate for *Aspergillus* species and sugar added as an additive in hazelnut paste may have increased aflatoxin production in hazelnut paste. The rate of contamination in the hazelnut paste analysed cannot be ignored. This situation makes us think that businesses producing hazelnut paste, which is a food consumed especially by young people and children, should be more careful in hazelnut intake, operational hygiene and storage.

4. CONCLUSION

The weather in the Black Sea region is rainy and continuously the harvesting season is very humid, increasing the risk of Aflatoxins contamination. Fungal contamination and consequently aflatoxins formation can occur in hazelnuts, at pre-harvest, harvest, during post-harvest applications and also in storage. According to this study results indicate that, although the risk of aflatoxin formation is present in hazelnuts and products, the most important stages to prevent aflatoxin occurrence are harvesting and drying methods including storage.

ACKNOWLEDGMENTS

This study was accepted by the Institute of Science and Technology of Sivas Cumhuriyet University and supported financially by the Scientific Research Council of Sivas Cumhuriyet University (CUBAP M-434).

REFERENCES

[1] TUIK., Agricultural production values. www.tuik.gov.tr (2016). (Access date: 09/09/2018).

[2] Alasavar C., Shahidi F., Liyanapathirana C.M., Oshima T., Turkish Tombul Hazelnut (Corylus Avellena L.) 1. Compositional Characteristics, Journal of Agricultural and Food Chemistry, 51(2003) 3790–3796.

[3] Alasalvar C, Amaral JS, Shahidi F.. Functional lipid characteristics of Turkish Tombul hazelnut (Corylus avellana L.). J Agric Food Chem. 54 (2006) 10117–10183.
[4] Durak I., Köksal I., Kacmaz M., Büyükkocak S., Cimen B.M.Y., Ozturk H.S., Hazelnut supplementation enhances plasma antioxidant potential and lowers plasma cholesterol levels. Clinica Chimica Acta. 284 (1999) 113–115.
[5] Maguire L.S., O'Sullvian S.M., Galvin K., O'Connor T.P., Brien N.M., Fatty acid profile, tocopherol, squalene, and phytosterol content of walnut, almonds, peanuts, hazelnuts, and macadamia nut. Int J Food Sci. 3 (2004) 171–178.
[6] Shahidi F., Alasalvar C., Liyana-Patharina C.M., Antioxidant and phytochemicals in hazelnut kernel (Corylus avellana L.) and hazelnut by-products. J Agric Food Chem. 55 (2007) 1212–1220.
[7] Quillien J.F., Mycotoxins. (2002) http://www.fevia.be/pdf/20pagers/synth/mycotoxins.pdf.
[8] Hussain I., and Anwar J., A study on contamination of aflatoxin M1 in raw milk in the Punjab province of Pakistan. Food Control 19 (2008) 393–395.
[9] Samuel M.S., Sivaramakrishna A., Mehta, A., Degradation and detoxification of aflatoxin B1 by Pseudomonas putida. Int. Biodeterioration and Biodegradation, 86 (2014) 202-209.
[10] Bullerman L.B., Schroeder L. L., Park K.Y., Formation and Control of Mycotoxins in Food, Journal of Food Protection, 47 (1984) 637-646.
[11] Severns D. E., Clements M. J., Lambert R. J., and White D. G., Comparison of Aspergillus ear rot and aflatoxin contamination in grain of high oil and normal oil corn hybrids. J. Food Prot. 66 (2003) 637–643.
[12] Alsuhaibani, A.M.A., Effects of Storage Periods and Temperature on Mold Prevalence and Aflatoxin Contamination in Nuts. Pak. J. Nutr., 17 (2018) 219-227.
[13] Amaike S.A., and Keller N.P., Aspergillus flavus. Annu.Rev.Phytopath. 49 (2011)107–133.
[14] Kensler T.W., Roebuck B.D., Wogan G.N., and Groopman J.D., Aflatoxin: a 50-year odyssey of mechanistic and translational toxicology. Toxicol.Sci.120 (2011) 28–48.
[15] Roze L.V., Hong S.Y., and Linz J.E., Aflatoxin biosynthesis: current frontiers. Annu. Rev. Food Sci.Technol.4 (2013) 293–311.
[16] IARC., Some Naturally Occurring Substances: Food Items and Constituents, Heterocyclic Aromatic Amines and Mycotoxins, in IARC Monographs on The Evaluation of Carcinogenic Risks to Humans, 56 (1993) 489–521.
[17] Afsah-Hejri L., Jinap S., Arzandeh S., Mirhosseini H., Optimization of HPLC conditions for quantitative analysis of aflatoxins in contaminated peanut. Food Control, 22 (2011) 381-388.
[18] Ding X., Peiwu L., Bai Y., Zhou H., Aflatoxin B1 in post-harvest peanuts and dietary risk in China. Food Control, 23 (2012) 143-148.
[19] Chen Y.C., Liao C.D., Lin H.Y., Chiueh L.C., Survey of aflatoxin contamination in peanut products in Taiwan from 1997 to 2011. Journal of Food and Drug Analysis, 21 (2013) 247-252.
[20] Torres A.M., Barros G.G.. Palacios S.A. Chulze S.N., Battilani P., Review on pre- and post-harvest management of peanuts to minimize aflatoxin contamination. Food Research International, 62 (2014) 11-19.
[21] Kumar P., Dipendra K.M., Madhu K., Tapan K.M., and Sang G.K., Aflatoxins: A Global Concern for Food Safety, Human Health and Their Management. Frontiers in Microbiology, 2 (7) (2017) 2170.
[22] Bakker F.W., Grains and Grain Quality. CIGR Handbook of Agricultural Engineering, Volume IV Agro-Processing Engineering. The American Society of Agricult. Eng. (1999) 1-3.
[23] Özkaya H., Analitik Gıda Kalite Kontrolü, Ankara Üniv. Ziraat Fak. Yay. 108 s., Ankara.
[24] Raper K.B. and Fennell, D.I., The Genus Aspergillus. Robert E. Krieger Publishing Company Huntington, New York, (1977) 686.
[25] Samson R.A. and Pitt I.J., Modern Concepts in Penicillium and Aspergillus Classification, NATO ASI Series, Plenum Press, New York and London, 185 (1990) 478.
[26] Samson R.A, Stolk A.C., Hadlock R., Revision of The Subsection Fasciculata of Penicillium and Some Allied Species, Stud. Mycol. Baarn, 11 (1976) 1-47.

[27] Pitt J.I. A Laboratory Guide to Common Penicillium Species, Food Science, Australia, Mycologia, 93 (2000) 689–703.
[28] Barnet H.L. and Hunter B.B., Illustrated Genera of Imperfect Fungi, Third Edition, Burgess Publishing Company (1997).
[29] Çetin Ö., Nazlı B., Bostan K., Alperden İ., Depolamanın Çiğ İç Fındığın Kalitesi Üzerine Etkileri, İst. Vet. Fak. Der., 26 (2000) 413-419.
[30] Aluç M., Aluç S., Akçakoca, Ordu ve Giresun Yörelerinde Yetiştirilen Fındıklarda Aflatoksin Düzeyinin Belirlenmesi Üzerine Bir Çalışma, Ulusal Mikotoksin Sempozyumu. İstanbul (2003) 60-67.
[31] Heperkan D., The Importance of Mycotoxins and a Brief History of Mycotoxin Studies in Turkey, The Bulletin İstanbul Tech. Uni.,54 (2003) 18-27.
[32] Gürsoy, N., Çiğ ve Kavrulmuş Fındıklardaki Mikoflora ve Aflatoksin Bulaşıklıklarının Değerlendirilmesi, Türkiye 10. Gıda Kongresi (2008) Erzurum.
[33] Jimenez M., Mateo R., Quero, A., Huerta T., Hernandez E., Mycotoxins and Mycotoxigenic Moulds in Nuts and Sunflower Seeds for Human Consumption, Mycopathologia,115 (1991) 121-7.
[34] Deabes M,. and Al- Habib R., Toxigenic Fungi and Aflatoxin Associated to Nuts in Saudi Arabia, Journal of American Science, 7 (2011) 658-665.
[35] Gürses M., Mycoflora and Aflatoxin Content of Hazelnuts, Walnuts, Peanuts, Almonds and Roasted Chickpeas (Leblebi) Sold in Turkey, J. of Food Properties, 9 (2006) 39-399.
[36] Ostadrahimi A., Ashrafnejad F., Kazemi A., Sargheini N., Mahdavi R., Farshchian M., Aflatoxin in raw and salt-roasted nuts (pistachios, peanuts and walnuts) sold in markets of Tabriz, İran. Jundishapur. J Microbiol. 7 (2014) 8674.
[37] Abdel Hafez A.I.I., Saber S.M., Mycoflora and Mycotoxin of Hazelnut (Corylus Avellana L.) and Walnut (Juglans Regia L.) Seeds in Egypt, 148 (1993) 137-147.
[38] Demir C., Şimşek O., Hamzacebi H ., Fındıkta Küf Florası ve Aflatoksin Oluşumlarının Araştırılması. Gıda 22 (2002) 291-295.
[39] Şimşek O., Arici M., Demir C., Mycoflora of Hazelnut (Corylus avellana L.) and Aflatoxin Content in Hazelnut Kernels Artifically Infected with Aspergillus parasiticus, Food Science and Technology, 46 (2002) 194-196.
[40] Ayçiçek H., Aksoy A., Saygı S., Determination of Aflatoxin Levels in Some Dairy and Food Products Which Consumed in Ankara, Turkey, Food Control, 16 (2005) 263-266.
[41] Sanchis V., Quilez M. L., Viladrich R., Vinas I., Canela R., Hazelnuts as Possible Substrate for Aflatoxin Production, Journal Food Protection, 51 (1988) 289-292.
[42] Reddy M.J., Shetty H.S., Role of Seed Lipids in Aspergillus parasiticus Growth and Aflatoxin Production, Journal of the Science of Food and Agriculture, 59 (1992) 177 - 181.
[43] Baltaci C., İlyasoğlu H., Cavrar S., Aflatoxin levels in raw and processed hazelnuts in Turkey. Food Additives and Contaminants: Part B 5 (2012) 83–86
[44] Çöpür Y., Tozluoglu A., Özkan M., Evaluating pretreatment techniques for converting hazelnut husks to bioethanol. Bioresource Technology, 129 (2013) 182–90.
[45] Velioğlu S.D., Güner K.G., Velioğlu H.M., Çelikyurt G., Fındık Zarının Fırıncılık Ürünlerinde Kullanımı. Journal of Tekirdag Agricultural Faculty, 14 (2017) 34-38.
[46] Özer H., Fındıklara Uygulanan Fiziksel ve Isıl Süreçlerde Aflatoksinler Üzerinde Etkisi, Doktora Tezi, Yıldız Teknik Üniversitesi Fen Bilimleri Enstitüsü, İstanbul (2009) 119.
[47] Vural A., Çakmak Ö., Erkan M. E., Aydın A. İstanbul Bölgesinde Tüketime Sunulan Fındık Ezmelerinde Aflatoksin Düzeylerinin Belirlenmesi, II. Ulusal Mikotoksin Sempozyumu Bildiriler Kitabı (2005) 178.
[48] Günşen U. and Büyükyörük I., Aflatoxins in Retail Food Products in Bursa, Turkey, Veterinary and Human Toxicology, 44 (2002) 289–290.
[49] [49] Yu J., Chang, P.K., Bhatnagar, D., Cleveland, T.E., Cloning of a sugar utilization gene cluster in Aspergillus parasiticus. Biochim. Biophys. Acta 1493 (2000) 211–214.